Encapsulation of hydratable salt for advanced thermochemical energy storage

Zheng Du

A thesis submitted to the University of Birmingham for the degree of

DOCTOR OF PHILOSOPHY

Birmingham Centre of Energy Storage
School of Chemical Engineering
College of Engineering and physical Sciences
The University of Birmingham
December 2022

UNIVERSITY OF BIRMINGHAM

Note: Please sign this form and present it to the Bindery with your thesis, so that it can be bound at the front of the Library deposit copy

RESEARCH THESIS
Author's Declaration

Full name (block capitals, surname first): ZHENG DU

Full title of thesis/dissertation (block capitals): ENCAPSULATION OF HYDRATABLE SALT FOR ADVANCED THERMOCHEMICAL ENERGY STORAGE

College/School/Department (block capitals): SCHOOL OF CHEMICAL ENGINEERNING

Date of award of degree (leave blank):

1. I understand that one printed and one electronic copy of my thesis/dissertation (the Work) will be deposited in the University Library (the Library) and in a suitable electronic repository, for permanent retention.
2. Without changing the content, the Library or any third party with whom it has an agreement to do so, may convert either copy into a format or medium for the purpose of long-term retention, accessibility and preservation.
3. The Library will publish, and/or arrange with appropriate third parties for the non-exclusive publication of, a bibliographic description of the thesis/dissertation, and the author's abstract.
4. Unless arrangements are made to the contrary, (see paragraph 6. below), the Library is authorised to make the Work available for consultation in the Library, and via a recognised inter library loans system. The Library is authorised to make the electronic copy of the Work freely accessible to individuals and institutions - including automated agents - via the Internet.
5. Rights granted to the University of Birmingham through this agreement are entirely non-exclusive. I retain all my rights in the Work in its present version or future derivative works.
6. I understand that I may apply to the University to retain the right to withhold access to the content of my thesis/dissertation. Access to the paper version may be withheld for a period which shall not normally exceed four calendar years from the congregation at which the degree is conferred. The actual length of the period will be specified in the application, together with the precise reasons for making that application. The electronic copy may be withheld from dissemination via the web or other networks for any period.
7. I have obtained permission for any use made of substantial amounts of published or unpublished copyright material (text, illustrations, etc) where the rights are owned by a third party, other than as permitted under either The Copyright Designs and Patents Act 1988 (as modified by any related or successor legislation) or the Terms and Conditions of any Licence governing its use.
8. The content of the copies I shall deposit with the Library will be the final version of my thesis, as approved by the Examiners.
9. I understand that the Library and administrators of any electronic theses repository do not hold any obligation to take legal action on behalf of myself, or other rights holders, in the event of a breach of intellectual property rights, or any other right, in the material deposited.
10. I understand that, in the event of my thesis/dissertation being not approved by the Examiners, this declaration will become null and void.

Signature: .....  ..... **Date:** 15th June 2023

For Library use (please leave blank):

Classmark: **Accession number:** **Control number:**

eTheses Repository url:

Abstract

The rapid growth in renewable energy brings significant challenges in managing the mismatch between intermittent supply and demand. Thermal energy storage (TES) provides a potentially highly effective solution to address such challenges. As one of three TES methods, thermochemical energy storage (TCS) has attracted increasing attention due to its high energy density, good scalability, and suitability for long-term energy storage. This thesis concerns TCS materials and devices, two crucially important aspects for bringing the TCS technology to real-world applications. The focus of the work is the use of hydratable salt as the TCS material for low-to-medium-temperature storage of solar heat. Such TCS store the thermal energy in chemical bonds of inorganic salts in anhydrous state, and release heat from the gas-solid reaction with water absorbed in those salts. It is one of the most promising types of TCS for its favourable thermochemical properties and low cost. However, pure salt has insufficient stability due to deliquesces, coalesce, and caking, resulting to a significant degradation in reactivity after cycles. It is thus essential to be enhanced by forming composites. The salt-based composites are being developed at an early stage, focusing mainly on the study of “salt-in-matrix” structures, which the salt fill the continue pores in a porous matrix. However,

the existing structure has barriers to increasing energy density above 1000kJ/kg and improving stability. In addition, most of those composites are designed for the packed-bed device, which lacks the flexibility of charging/discharging, and has an unfavourable flow resistance in the cases of large storage capacity and high airflow rate. So far, it is still challenging to find an effective solution for TCS with high density, highly flexible, and high power. This forms the major motivation of this research.

This PhD study aims to address the gaps in hydratable salt-based composite by developing an encapsulation of salt. The key novelties lie in the incorporation of solar-absorbing materials in encapsulated salt manufactured via optimized water-in-oil (W/O) Pickering emulsions. The use of Pickering emulsions as the template to manufacture the functional materials is an emerging technology, benefiting from the tailorable, facile, robust, and potentially scale-up. This work brings a fundamental understanding of Pickering emulsions, especially using commercial raw materials. A general method to manufacture encapsulation of hydratable salt is successfully developed. To the best of my knowledge, this work is the first report of the encapsulated salt with size adjustable from the nanoscale to microscale and energy storage density above 1700kJ/kg. Notably, this work first demonstrates the use of encapsulated salt in fluidized bed device. Furthermore, the integration of solar harvesting ability to encapsulate salt is also achieved for the first time in this work. All the innovations in this work

develop a breakthrough solution towards an advanced TCS with high energy density, large storage capacity, high flexibility, and the capability of storing renewable energy.

Both fundamental and experimental work was performed in this work, with the experimental including lab-scale demonstrations and some of the highlights are summarized in the following:

- The formation mechanism of Pickering emulsions with hydrophobic fumed silica nanoparticles is studied, which explains how the nanoparticle is adsorbed at the W/O interface to stabilize the emulsion and what is the preferable conditions for W/O emulsions.
- A comprehensive study is carried out on the W/O Pickering emulsions as a template for tailoring the structure of the capsules and establishing a relationship between emulsion and encapsulation sizes.
- The size effect on the thermal performance of the encapsulated salt is studied, and a performance index is proposed to evaluate the efficiency of the encapsulation.
- Upon optimization, nanoscale encapsulated salt is found to have superior reactive kinetics, high-energy density, and good stability.
- The fluidised bed device demonstrates the fluidisation of encapsulated salt, showing higher thermal performance and more flexibility compared to the conventional packed beds.

- The introduction of solar-absorbing materials to the encapsulated salt is shown to significantly improve the solar absorption of the materials.
- The solar charging device with the solar absorption-enhanced encapsulated salt demonstrates the directly coupled TCS and renewable energy, realising the solar direct charging, long-term storage with zero loss, and on-demand discharging to supply instant warm air.

Acknowledgements

I would like to express profound gratitude to my supervisor, Prof. Yulong Ding, for his invaluable support, endless encouragement, enthusiastic supervision, and illuminating suggestions throughout this research work. His moral support and continuous guidance enabled me to process my work successfully. I am also deeply indebted to Prof. Zhubing He (Southern University of Science and Technology) for his detailed and constructive advising, and his important support for the experimental facility throughout this work.

I gratefully acknowledge Southern University of Science and Technology (SUSTECH) for the financial support. Very special thanks are also due to the Birmingham Centre of Energy Storage (BCES) for the provision of a fantastic research environment. My colleagues in both Prof. Ding's and Prof. He's research groups have supported me in various aspects of my research work and living. I want to thank them for all their help, support, interest, and valuable comments.

A special thanks to my family, my mother and father. Their support to me has sustained me thus far. Finally, and most importantly, a huge thank you to my wife, Tong Wu, who met me in Birmingham and started a fantastic life with me.

Table of Contents

Abstract ..... **i**

Acknowledgements ..... **v**

List of Figures ..... **xi**

List of Tables ..... **xxii**

Abbreviations ..... **xxiii**

Nomenclature ..... **xxv**

1 Introduction **1**

1.1 Background 1

1.2 Aims and objectives 5

1.3 The structure of this thesis 6

2 Literature review **8**

2.1 Thermochemical energy storage technologies 9

2.1.1 Fundamentals of Thermal energy storage (TES) 9

2.1.2 The concepts of thermochemical energy storage 10

2.1.3 The developments of thermochemical energy storage 11

2.2 The sorption TCS with hydratable salt 16

2.2.1 Terminology 16

2.2.2 Inorganic salts as the chemisorption materials 22

2.2.3 Material issues limiting the thermal performances 28

2.3 Composite materials for enhancing the thermal performance 34

2.3.1 Overview 34

2.3.2 Salt-in-matrix 35

2.3.3 Encapsulated salt 40

2.4 Thermochemical storage system for solar heat 45

2.4.1 System and reactors design 45

2.4.2 Coupled sorption heat storage with solar heat harvesting 52

2.5 Summary of the literature review 53
3. Formation of the W/O Pickering emulsion for encapsulating thermochemical salt 55
3.1. Introduction 56
3.2. Experimental section 59
3.2.1. Materials 59
3.2.2. Preparation and characterizations of the nanoparticle and suspensions 60
3.2.3. Study for the formation of a Pickering emulsion 62
3.2.4. Fabrication of the empty silica encapsulation from emulsion 63
3.2.5. Study for the Interactions between nanoparticle and W/O interface 64
3.3. Result and discussion 67
3.3.1. Nanoparticle and suspensions 67
3.3.2. Screening the protocol of encapsulating from emulsion 71
3.3.3. Assembly behaviour of hydrophobic nanoparticle to W/O interface 74
3.3.4. Interactions between nanoparticles and droplets 77
3.4. Conclusion 91
4 Tailored Pickering emulsions for encapsulating salt 93
4.1 Introduction 94
4.2 Experimental section 96
4.2.1 Materials 96
4.2.2 Emulsions preparation 97
4.2.3 Encapsulations from Pickering emulsions 98
4.2.4 Morphology characterizations 99
4.3 Result and discussion 100

4.3.1 Effect of particle dosage and emulsification energy on emulsions 100
4.3.2 Stability of Pickering emulsions 104
4.3.3 Influence of Rhodamine B 105
4.3.4 Encapsulation from the emulsions 106
4.3.5 Pickering and network structures of the emulsions 109
4.3.6 Nanoparticle dosage effect on the size of the droplet 110
4.3.7 Salt effect on structure of encapsulation 112
4.3.8 Salt effect on the encapsulation sizes 113
4.4 Conclusion 120
5 Thermal performance and optimization of encapsulated salt 122
5.1 Introduction 123
5.2 Experimental section 124
5.2.1 Materials 124
5.2.2 Fabrication of encapsulated $CaCl_2$ 124
5.2.3 Morphology characterization 125
5.2.4 Thermal performance characterized by STA 125
5.2.5 Dynamic vapour sorption 126
5.3 Result and discussion 127
5.3.1 Effect of shell thickness on thermal performance 127
5.3.2 Effect of encapsulation size on thermal performance 132
5.3.3 Effects of encapsulation on energy storage efficiency 136
5.4 Conclusion 140
6 Encapsulated salt for thermochemical energy storage with fluidised bed reactor 142
6.1 Introduction 143
6.2 Experimental section 147

6.2.1 Materials 147
6.2.2 Emulsion template preparation 147
6.2.3 Fabrication of the NanoCaCl2 and MicroCaCl2 148
6.2.4 Fabrication of the composite of CaCl2-in-silica gel 148
6.2.5 Morphology of NanoCaCl2 capsules 149
6.2.6 XPS study of NanoCaCl2 Capsules 150
6.2.7 In-situ XRD and Raman microscopy study 150
6.2.8 Characterization of kinetic and thermal performance 150
6.2.9 The conversion profile model fitting for reaction kinetic 153
6.2.10 Demonstration of a fluidised bed reactor for NanoCaCl2 154
6.3 Result and discussion 157
6.3.1 Pickering-emulsion templated yolk-shell silica nanocapsules for thermochemical energy storage 157
6.3.2 Thermochemical energy storage in the nanocapsules 168
6.3.3 Thermal performance of NanoCaCl2 171
6.3.4 Reaction kinetic and mass transfer in capsules 179
6.3.5 The fluidisation of encapsulated salt 184
6.3.6 Evaluation on the overall performance of NanoCaCl2 186
6.4 Conclusion 188
7 Encapsulated salt for solar heat storage 190
7.1 Introduction 191
7.2 Experimental section 191
7.2.1 Materials 191
7.2.1 Preparing the Solar-NanoCaCl2 192
7.2.2 The solar heat storage device and test rig 192
7.3 Result and discussion 195
7.3.1 Encapsulated salt with enhanced solar absorption 195

7.3.2 Device test for coupled TCS and solar heat harvesting 199
7.4 Conclusion 203
8 Conclusion 205
8.1 Summary of the main conclusions 205
8.2 Recommendations & future work 209
Bibliography 212

List of Figures

Figure 1-1 Total energy supply of low emissions sources in the Net Zero Emissions by 2050 Scenario (NZE). 2

Figure 1-2 Global TES installation by September 2022 (statistics by LDES council). 3

Figure 1-3 a) The Austrian solar district heating system in Friesach, with a capacity of 4.1MWth flat plate solar collector (non-concentrated), was installed in 2021. b) Parabolic trough collectors (low-concentrated) installed at Comercial Forrajera de Lagos (COMFOSA) in Mexico.... 5

Figure 2-1 The most studied TCS reactions, classified by reaction principle. 15

Figure 2-2 Classification of chemical storage and sorption heat storage. 17

Figure 2-3 Energy potential change and heat of adsorption during physical adsorption, a) Lennard-Jones (L-J) potential and b) Total heat of physisorption according to the water uptake in Zeolite 13X. 20

Figure 2-4 One-dimensional energy potential of chemisorption (chemical absorption). 21

Figure 2-5 Crystallographic structures changed from $CaCl_2$ [73] to $CaCl_2 \cdot 6H_2O$ [74]; dark grey-Ca, green-Cl, red-O, white-H; The dash lines in $CaC_2 \cdot 6H_2O$ represent hydrogen bonds. 23

Figure 2-6 estimates the lattice enthalpy $UPOT$ of anhydrous ($n = 0$) and hydrated salt based on Born-Haber cycle. 24

Figure 2-7 Screening the hydrated substrates for TCS, reproduced from [81]. 26

Figure 2-8 Illustration of mass transfer routines in solid absorption,

reproduced from [99]. 30
Figure 2-9 Intrinsic mass diffusivity of H2O in air, in $MgCl_2$ solution[107] and in perfect $MgCl_2$ crystal [103]. 31
Figure 2-10 Two possible pathways of hydration: (I) a direct solid−solid transition; (II) a solution-mediated transition, reproduced from [109]. 32
Figure 2-11 Photos of salt after hydration for 24 hours in an atmosphere of 22°C and 60%RH [113]. 33
Figure 2-12 The photo images and schemes show the dehydration of $MgCl_2 \cdot 6H_2O$ on a heating plate [116]. 34
Figure 2-13 The principle of salt-in-matrix materials: a) Illustration of the charging-discharging cycle; b) Theoretical thermodynamic cycle presented in P-T diagram. 36
Figure 2-14 Reported encapsulated salt capsules material at the different size scales. 41
Figure 2-15 Schematic illustration of emulsion-templated in-situ polymerization for encapsulating the PCMs. 45
Figure 2-16 Configurations of the thermochemical heat storage systems, reproduced from [189]. 46
Figure 2-17 The experiments of “open-sorption pipe”. 49
Figure 2-18 Basic of fluidised bed, the pressure drops according to flow regimes [214]. 51
Figure 2-19 The TCS fluidised bed reactor prototype. 52
Figure 3-1 Schematic representation of surfactant stabilised emulsion and solid nanoparticle stabilised Pickering emulsions [230]. 56
Figure 3-2 Position of the particle at a fluid-water interface for different contact angles θ and the corresponding positioning of the particle at a

curved fluid-water interface [236]. 57
Figure 3-3 Synthetic silica nanoparticle with the different functional groups on the surface via flame pyrolysis [243], [244]. 60
Figure 3-4 Two kinds of emulsification route to create micro-emulsions. 62
Figure 3-5 Schematic diagram of the gel trapping technique “GTT” for measuring contact angles of a nanoparticle at an oil-water interface. 66
Figure 3-6 The SEM images of the nanoparticles a) R972 and b) A200. c) The FT-IR spectrum of the nanoparticles. 68
Figure 3-7 Size of raw and sonication dispersed R972 nanoparticle measured by DLS. 69
Figure 3-8 SEM images of raw and dispersed R972 nanoparticle. 70
Figure 3-9 Rheological study of suspensions, a) linear test and b) oscillation test. 70
Figure 3-10 Photo images of prepared emulsions. 72
Figure 3-11 Result of silica encapsulation from bare W/O emulsion, a) the size distribution of fresh emulsion, b) the CLSM image of the emulsion after settling for 30 mins, c) the SEM image of silica encapsulation, d) the Energy-dispersive X-ray spectroscopy (EDX) colour mixed elements mapping of silica encapsulation, blue for carbon (substrate was carbon tape), yellow for silicon and red for oxygen. 73
Figure 3-12 The SEM images of encapsulation from the aqueous phase with different pH, a) pH=2, b) pH=7, c) pH=12. 74
Figure 3-13 a) The SEM image of encapsulations from Pickering emulsion containing aqua phase with pH=2, 10mg nanoparticle in 10mL oil for 100uL water, b) zoomed-in image of the small droplet, c) the large droplet. 75

Figure 3-14 Images captured with CLSM, a) the bright field image b) laser-induced fluorescence (LIF) imaging, the nanoparticle and interface were labelled by Rhodamine B. 76
Figure 3-15 encapsulations from Pickering emulsion with high nanoparticle concentration, 100mg nanoparticle in 10mL oil for 100μL water, a) Low-magnification, b) High-magnification SEM image..... 76
Figure 3-16 Sessile drop measurement for determining the contact angle of nanoparticle aggregates. 78
Figure 3-17 “GTT” measurement for the three-phase contact angle of individual nanoparticle, a) observation configuration, b) SEM image with tilt angle at 15°, C) SEM image with tilt angle at 30°. 78
Figure 3-18 Pendant drop measurement for dynamic absorption of nanoparticle to the W/O interface 80
Figure 3-19 The illustration of nanoparticle-interface interactions: a) the typical progress with water (pH=2), b) the proposed progress with water (pH=7 or 12)..... 81
Figure 3-20 The physical model for the DLVO framework. 82
Figure 3-21 Zeta potentials of R972 nanoparticles in ethanol and cyclohexane (both with a concentration at 8mg/ml), also the result of the water drops in cyclohexane as a reference. 85
Figure 3-22 The estimated DLVO contributions of a nanoparticle with a diameter at 16nm approaching to a spheric water drops with a diameter of 1000nm..... 90
Figure 3-23 Behaviour of nanoparticles near a water drop with the different charged surfaces. 91
Figure 4-1 Illustration of emulsification devices and principles: a) rotor-stator mixer [315]; b) sonication [316]..... 98

Figure 4-2 Hydrolysis-Condensation reaction of TEOS for encapsulation [269].....99
Figure 4-3 CSLM images of W/O emulsions prepared with different conditions. From the first to the third row are the emulsions of 1ml water in 20mL Cyclohexane with 10mg R972 NP, 50mg NP, and 100mg NP, respectively. Different colours represent the different emulsification: green is for emulsified by rotor-stator at 2800 rpm (linear velocity at ~1.0m/s), blue is 8000 rpm (~2.8m/s) and red is sonicated at 500W, respectively.....101
Figure 4-4 Size distributions of droplets in emulsions, fitted in lognormal distributions. 103
Figure 4-5 Photo Images of emulsions prepared by different emulsification conditions. From left to right is processed at 2800rpm in the rotor-stator mixer, at 8000rpm in the same mixer, and sonication with 500W. The NP dosage was constant at 50mg/ml and the water volume was also the same. 104
Figure 4-6 CLSM images of pristine emulsions and aged after a week. 105
Figure 4-7 The chemical structure of Rhodamine B.....106
Figure 4-8 CLSM images of the Pickering emulsion template and corresponding SEM images of the consolidated encapsulations. The NP dosage was 200mg/ml (mass of NP to the volume of water), and the water-to-oil volumetric ratio is 1:20, from left to right column is the sample prepared from water with pH=2, 7, 12, respectively. 107
Figure 4-9 SEM images of capsules prepared from emulsions without RhB, a) water phase was adjusted to pH=2, and b) pH=12. The NP dosage is consisting of 200mg/ml (mass of NP to the volume of water). ...109

Figure 4-10 SEM images of encapsulations from emulsions containing water at pH=4, 7, and 10 (without RhB)..... 109
Figure 4-11 Photo images of emulsions containing water phase with different pH (left to right 2,7,12. The NP dosage was constant at 200mg/ml and the water-to-oil ratio is 1:25 in volume. 110
Figure 4-12 Fitting for capsule sizes prepared from pH=2 emulsions. The value in the legend represents the NP dosage (mg/mL water volume) 111
Figure 4-13 SEM images of consolidated structure from emulsions containing different salt solutions as water phase: a) 1mM NaCl, b) 1M NaCl, c) 4M NaCl, and d) 1M $CaCl_2$. The NP dosage was constant at 200mg/ml and the pH was constant at 7..... 112
Figure 4-14 Illustration of a) Network (pH=7) and b) Pickering (pH=2) type emulsions, and SEM images of capsules derived from the corresponding emulsion template, the NP dosage is 400mg/ml, and the water phase contains 1M NaCl. 113
Figure 4-15 Size distribution of capsules prepared from different water phases with a constant 400mg/ml NP dosage..... 114
Figure 4-16 The illustration of the nanoparticle absorbed in the W/O interface. 117
Figure 4-17 NP concentration C on interface estimated from all the possible conditions. 118
Figure 4-18 The relationship between droplet radius and particle wettability with the number of absorbed particles is fixed, the Gibbs free energy is labelled on the lines, unit in J/ml for water. a) the number of absorbed fixed at the lowest $C = 1.4 \times 1014$, and b) fixed at the highest $C = 5.2 \times 1016$. 119

Figure 4-19 The relationship between droplet radius and the number of absorbed particles with particle contact angle is fixed, the Gibbs free energy is labelled on the lines, unit in J/ml for water. a) the particle contact angle is 120°, and b) the particle contact angle is 135°..... 119
Figure 4-20 The illustration of NP absorbed in a bare Water/Oil interface and Brine/Oil interface, both the number of absorbed particles and contact angle changed..... 120
Figure 5-1 temperature and airflow profile used in STA. 126
Figure 5-2 The profile of pressure-jumping DVS measurement and the result of pure $CaCl_2$ (solid symbol). 127
Figure 5-3 SEM images of encapsulated $CaCl_2$ with ~800nm diameter and shell thickness of (a) 25nm, (b) 50nm, (c) 100nm. 128
Figure 5-4 STEM-HAADF images and STA of the encapsulated $CaCl_2$ with ~800nm diameter and shell thickness at (a, b) 25nm, (c, d) 50nm, (e, f) 100nm. The insertion in a, c, and e is the EDX colour-mixed mapping of the local shell, blue represents the elements of Ca and Cl, and red is for Si and O. 129
Figure 5-5 Water uptake kinetic of 800nm capsules with different shell thicknesses, a) dehydration, b) hydration. 132
Figure 5-6 SEM and STA results of $CaCl_2$ capsules with different diameters: a, b) capsules of 8μm mean diameter with ~300nm thick shell, 5.12mg for STA measurement, and c, d) unconfined pure $CaCl_2$, 5.2mg for STA measurement. 133
Figure 5-7 Breakthrough curves of encapsulated salt and unconfined pure salt at each P/P_0 stage in DVS measurement. 134
Figure 5-8 the conversion-conversion rate curves of hydration at different vapour pressure..... 135

Figure 5-9 The efficiency of encapsulated salt compared to pure salt ..139
Figure 6-1 The SEM images and corresponding EDX colour mixed mapping of $CaCl_2$-in-silica gel composite. 149
Figure 6-2 Temperature and reactive gas profile in STA 151
Figure 6-3 Setup of Microscopic dynamic observation. 152
Figure 6-4 Design of fluidised bed thermochemical test rig. 155
Figure 6-5 Details of reactor and PTFE membrane filter 156
Figure 6-6 Synthesis pathway, and Illustration of Pickering emulsion templated encapsulation and structure of the designed capsules. 157
Figure 6-7 SEM and TEM images of R972 Pharma fumed silica nanoparticle. 158
Figure 6-8 Contact Angle of R972 Pharma coated wafer: a) DI Water; b) Solution of 20%wt $CaCl_2$ in Water; c) Cyclohexane; d) Solution of 20%wt $CaCl_2$ in Ethanol.....158
Figure 6-9 Photo images of a) Silica NP suspension (15mg/ml in cyclohexane) and b) inversed emulsion of $CaCl_2$ aqueous solution in cyclohexane (10%v/v)。 159
Figure 6-10 The relation between the size of droplets and nanoparticles dosage, with the Laser Scanning Confocal Microscopic (LSCM) images of emulsions. 160
Figure 6-11 SEM images of different thermochemical salt capsules: a) $CaCl_2$; b) LiCl; c) K_2CO_3; d) $MgSO_4$. 161
Figure 6-12 a) Scanning Electronic Microscope (SEM) image of Nano$CaCl_2$. b) Size distribution of as-fabricated Nano$CaCl_2$. 163
Figure 6-13 Scanning Transmission Electronic Microscope (STEM) bright-field image of a single Nano$CaCl_2$ capsule, the insertion is the zoom-out image of functional silica nanoparticles whisker attached on the

shell. 164
Figure 6-14 Contact angle of water on NanoCaCl2. 165
Figure 6-15 High-angle annular dark-field STEM (HAADF-STEM) with overlayed Energy-dispersive X-ray spectroscopy (EDX) elemental distribution mappings (in atom%) for Si and Ca in a single capsule. 165
Figure 6-16 X-ray photoelectron spectroscopy (XPS) spectrum of Ca 2p core-level at different depths (deeper with increased ion etch time). 166
Figure 6-17 XPS depth Investigation of other elements in NanoCaCl2: a) Si2p; b) O1s; c) Cl2p; d) C1s. 167
Figure 6-18 XPS spectrum of Si 2p core-level of the capsule shell. 168
Figure 6-19 Illustration of a thermochemical energy storage cycle and analysis. a) Illustration of a thermochemical cycle consisting of 4 states. b) In-situ X-ray diffraction (XRD) analysis of NanoCaCl2 in a thermochemical cycle. c) In-situ Raman Microscope analysis of NanoCaCl2 in a thermochemical cycle, the scale in insertion is 20μm. 169
Figure 6-20 Simultaneous Thermal Analysis (STA) of NanoCaCl2 172
Figure 6-21 Isotherm water sorption capacity of TCS composite materials at 30°C 173
Figure 6-22 Dynamic Vapour Sorption (DVS) stability test with 50 cycles of NanoCaCl2 and ground pure CaCl2. 175
Figure 6-23 Results of MicroCaCl2 in DVS stability test. 175
Figure 6-24 a) Dynamic microscopic images of pure CaCl2 during a cycle and SEM Images of cycled pure salt. b) SEM Image of cycle NanoCaCl2 with EDX quantitative evaluation. 176

Figure 6-25 SEM and EDX Images of Fresh and Cycled NanoCaCl$_2$. ..177
Figure 6-26 Microscopy images during the charging/discharging cycle, a) NanoCaCl$_2$. ..178
Figure 6-27 Microscopic dynamic of MicroCaCl$_2$. ..179
Figure 6-28 Hydration breakthrough curves of encapsulated and pure CaCl$_2$, under P/P$_0$ jump from 0.0 to 0.1, and 0.1 to 0.2 at 30°C. ...180
Figure 6-29 Reaction kinetic of hydration, low vapour pressure. ..182
Figure 6-30 Reaction kinetic of hydration, high vapour pressure. ..182
Figure 6-31 Dehydration kinetics of encapsulated and pure CaCl$_2$ with the same mass of the sample. ..183
Figure 6-32 TGA with different sample mass. ..184
Figure 6-33 Application of NanoCaCl$_2$. a) A proposed open TCS system with a fluidised bed reactor and a separate storage tank. b) Fluidisation behaviour of NanoCaCl2. c) Thermal charging/dehydration and discharging/hydration of NanoCaCl2 with a lab-scale fluidised-bed reactor. ..186
Figure 6-34 Comparison of state-of-art materials for thermal energy storage (scale is in logarithmic) ..187
Figure 7-1 Design of solar thermochemical test rig. ..193
Figure 7-2 CAD drawing of the thermochemical solar reactor. ..194
Figure 7-3 Morphology and size distribution of as-received TiN Nanoparticle a) SEM images and b) DLS show the size distribution. ..196
Figure 7-4 SEM images of TiN Nanoparticle dispersed in Water, a) 1mg/ml TiN without PVA; b) 1mg/ml TiN in 30mg/ml PVA; c) 0.1mg/ml TiN in 30mg/ml PVA. ..197
Figure 7-5 SEM Image of NanoCaCl$_2$ with different TiN solar absorber

loading, a), 5mg/ml TiN, b), 20mg/ml TiN.....197
Figure 7-6 TEM bright field of as fabricated capsules with TiN solar absorber (called Solar-NanoCaCl$_2$) and corresponding STEM-EDX mapping.....198
Figure 7-7 Integration of Solar-Charged Thermochemical energy storage. a) Photo image of NanoCaCl$_2$ and Solar-NanoCaCl$_2$ with 5 and 20 mg/ml TiN dosage; b), UV-VIS-IR absorptance spectrum of above powders.....199
Figure 7-8 Designed conditions for solar-charging thermochemical storage processes with Solar-NanoCaCl$_2$.....200
Figure 7-9 a) Photo of the designed thermochemical solar reactor while tested under solar irradiation. 201
Figure 7-10 a) Temperature and vapour pressure history in solar charging. b) Temperature and vapour pressure history in discharging. 202
Figure 7-11 Pressure drop across reactive bed during a), dehydration and b), hydration.....203

List of Tables

Table 2-1 Three technologies of thermal energy storage. 9

Table 2-2 Comparison of physisorption and chemisorption 18

Table 2-3 Estimated lattice enthalpy of $CaCl_2$ by the different models, values in brackets is the enthalpy change from anhydrous salt. 25

Table 2-4 Summary of the candidate salts for thermochemical energy storage..... 28

Table 2-5 The composites of “salt-in-matrix” 39

Table 2-6 open system for sorption heat storage 47

Table 3-1 The conditions and results of emulsions preparation protocol 71

Table 4-1 parameters used in calculation. 117

Table 5-1 Studied encapsulated $CaCl_2$. 125

Table 6-1 Models used in the profile fitting. 154

Table 6-2 Estimation of the theoretical energy density of different salt encapsulated from Pickering emulsions. 162

Table 6-3 Cost Estimation on Nano$CaCl_2$ 188

Abbreviations

ATR	Attenuated total reflectance
CLSM	Confocal Laser Scanning Microscope
DLS	Dynamics Light Scattering
DLVO	Derjaguin–Landau–Verwey–Overbeek
EDX	Energy-dispersive X-ray spectroscopy
FT-IR	Fourier-transform infrared spectroscopy
GSD	Gravimetric storage density
GTT	Gel Trapping Technique
HTF	Heat transfer fluid
HVAC	Heating Ventilation and Air Conditioning
LCSM	Laser scanning confocal microscope
LHS	Latent heat storage
LIB	Li-ion battery
LIF	Laser-induced fluorescence
L-J	Lennard-Jones
MD	Molecular dynamic
MOF	Metal-organic framework
NP	Nanoparticle
NZE	Net Zero Emissions by 2050 Scenario
O/W	Oil-in-Water (emulsions)
PALS	Phase Analysis Light Scattering

PCM	Phase change material
PXRD	Powder X-ray diffraction
SEM	Scanning electron microscope
SHS	Sensible heat storage
STA	Simultaneous Thermal Analysis
TCM	Thermochemical energy storage material
TCS	Thermochemical heat storage
TEM	Transmission electron microscope
TES	Thermal energy storage
vdW	van der Waals
VSD	Volumetric storage density
W/O	Water-in-Oil (emulsions)

Nomenclature

Λ^0	Molar conductance of electrolyte
C_p	Specific heat capacity at constant pressure
E_a	Activation energy
U_{POT}	Lattice enthalpy in Haber-Bosch cycle
c_s	Concentration of free ion
k^{-1}	Debye screening length
k_B	Boltzmann constant
λ_B	Bjerrum length
G’	Storage modulus in rheology
G”	Loss modulus in rheology
h	Gapped distance
γ	Deformation rate
θ	Contact angle
ρ	Density
A	Area
C	Concentration
D	Electrical conductivity
D	Diffusivity
E	Energy in interfacial study
F	Interaction force
G	Gibbs free energy

H	Enthalpy
N	Number
Q	Energy
R	Radius
S	Entropy
S	Surface area
T	Temperature
U	Electric potential
V	Potential energy in L-J potential
V	Volume
W	Total free energy
a	Particle radius
m	Mass
n	Reflective index
q	Power
r	Particle-particle distance in L-J potential
s	Surface area
t	Time
z	Centre-to-centre distance
γ	Surface or interfacial tension
ζ	Zeta potential
η	Viscosity
η	Efficiency

θ	Rection enthalpy in Haber-Bosch cycle
σ	Particle-particle distance where potential is zero in L-J potential
σ	Current density
ψ	Surface potential
ϵ	energy potential
ϵ	Dielectric constant

subscripts

d	Droplet
g	gaseous
o	oil
p	particle
s	solid
w	water
wo	Water-oil

1 Introduction

1.1 Background

Approximately 90% of the world's energy use today involves the production or manipulation of thermal energy over a wide range of temperatures. Currently, thermal energy is mainly supplied by fossil fuels, which are also the dominant source of carbon emissions. The decarbonisation of thermal energy, therefore, represents one of the biggest challenges for achieving the net-zero target around 2050 [1]. Rising to the challenge, recent years have seen the urgent need for low-emission energy transition, and the demands of advancing the ability to transport, store, convert and efficiently utilize thermal energy [2].

With the accelerating trend of energy transition from fossils to renewables (Figure 1-1 from [3]), energy storage is essential for coping with the supply-demand mismatches by smoothing the fluctuating generation. The frequencies of fluctuations are in the range of minute to seasonal, determined by the natures of different renewable energy and the flexible demand. The preliminary results of a recent study by the Royal Society suggest the need for short-, medium-, and long-term energy storage technologies [4], distinguished by the storage duration of minutes-to-hours, days-to-weeks, and months-to-seasons, respectively. For the UK alone, a future renewable-energy dominant energy system requires ~100-120GW/100-200GWh, ~100-130GW/2-6TWh and ~70-80GW/~35-40TWh for short-, medium- and long-term storage, respectively. A significant amount of work addresses short-term energy storage e.g., lithium-ion & sodium-ion batteries, supercapacitors, and flywheels [5]; a much smaller

amount of effort has been made on medium- and long-term energy storage [6]. For medium- and long-term energy storage technologies with high economic efficiency, it is essentially to provide a long-duration (10-100hours) charging/discharging at an appropriate power [7], [8]. Therefore, it has been seen the emerging attention on energy storage technologies for long-term storage with affordable large capacity.

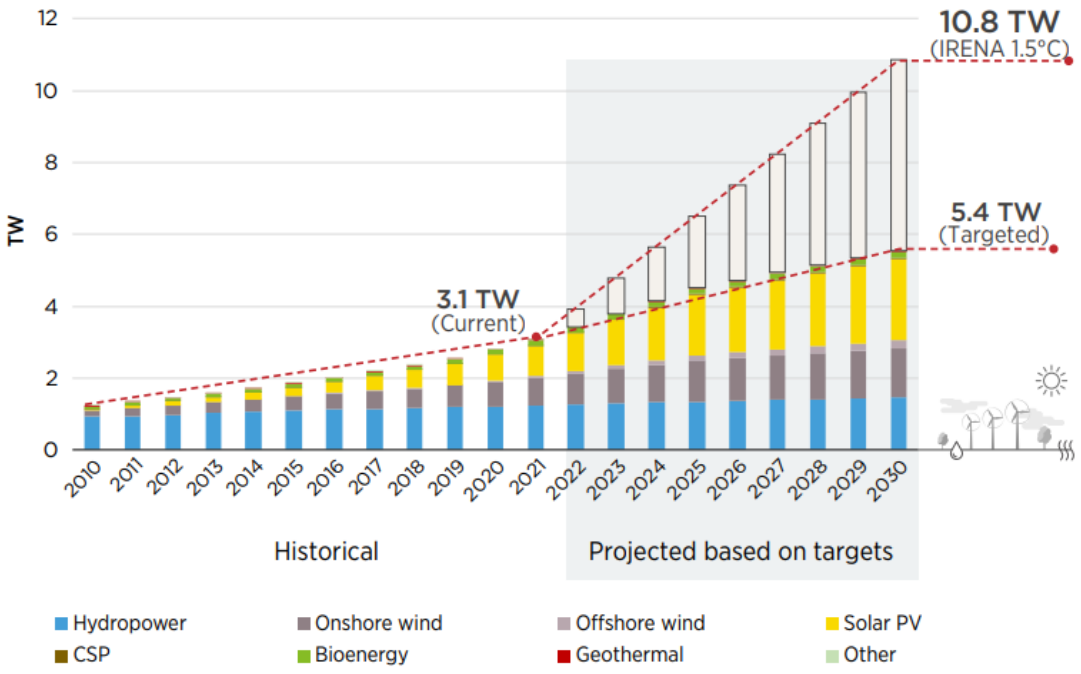


Figure 1-1 Total energy supply of low emissions sources in the Net Zero Emissions by 2050 Scenario (NZE).

Thermal energy storage (TES) has several advantages including high scalability, no geographical/geological constraints, and cost-effectiveness, thus, has the potential to meet the requirements for long-duration large-capacity energy storage [9]. Compared to the total energy storage installations of 200GW/700GWh (2021 data from [10]), the currently installed and projected TES are only ~20GWh around the world (see Figure 1-2, be cited from [11]), far behind other energy storage technologies.

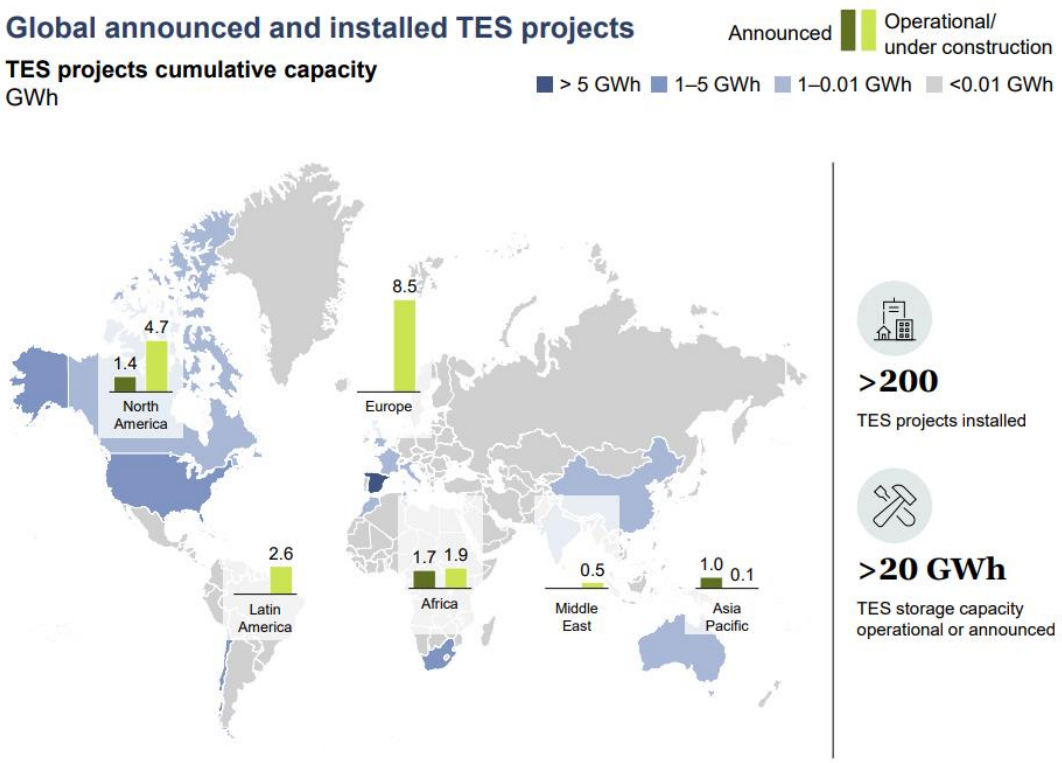


Figure 1-2 Global TES installation by September 2022 (statistics by LDES council).

Most of those TES are sensible heat storage (SHS) and latent heat storage (LHS), which have limitations in storage term due to spontaneous heat dissipation. So far, the developed TES is challenged by medium- and long-term energy storage. As another TES technology, thermochemical heat storage (TCS) is particularly suitable for high-capacity, large-scale, and long-term energy storage. The TCS technology is based on reversible reactions and/or sorption processes. This work concerns the TCS with inorganic hydratable salts, with the charging/discharging process based on solid-gas reactions with sorption and the charging temperatures below ~150°C. The advantages of such a technology include high energy density, low raw material cost, and zero energy loss during storage. However, the technical challenges of this type of technology have been and remain associated with TCS materials and devices,

particularly poor mass transfer in solid grains, and low heat generation rate in devices. In terms of materials, lots of work has been reported in the literature on the development of composites of salt hydrates. So far, the literature work has been concentrated on “salt-in-matrix” composites, where the salt is filled in a porous host material. This structure is characterised by connecting macro-, meso- and micro-pores to maintain the size of the salt particles. However, its apparent drawbacks are the slow mass transfer due to the tortuous flow path in the porous host medium and the possibility of salt leakage from the open pores. An alternative composite is the encapsulation of salt, confining salt particles within a shell. This structure not only helps to improve mass transfer by reducing and confining the diffusion length inside salt particles but also by providing additional paths for moisture diffusion outside the encapsulation. Besides, this structure provides good stability as well as the flexibility to be integrated into various devices. Little has been done in this area, which forms a motivation of this work.

Another rationale for this work is that the working temperature range of salt hydrate based TCS materials matches well that of solar heat harvested by non- or low- concentrated solar systems (Figure 1-3, be cited from [12]), making the salt hydrate based TCS a natural choice for this type of applications.

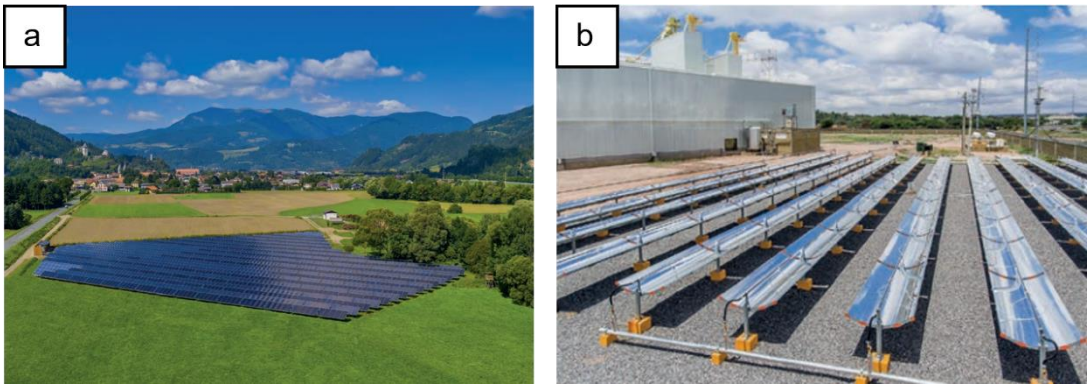


Figure 1-3 a) The Austrian solar district heating system in Friesach, with a capacity of 4.1MWth flat plate solar collector (non-concentrated), was installed in 2021. b) Parabolic trough collectors (low-concentrated) installed at Comercial Forrajera de Lagos (COMFOSA) in Mexico

Furthermore, conventional solar heat systems use solar receivers to collect thermal energy [13] and a heat transfer fluid (HTF) [14] to carry the collected heat to a separate storage device [15]. The use of thermochemical storage can potentially reduce the system complexity, improve the system efficiency and make the system suitable for long-duration and long-term heat storage. These form additional motivation of this work.

1.2 Aims and objectives

The aim of this PhD work is to develop an encapsulated inorganic salt-based technology with an enhanced charging/discharging performance to thermochemically store solar heat. The focus is on the encapsulation method, fabrication and characterisation of the encapsulated salt, optimisation of the performance of the encapsulated salt, and demonstration of the use of the encapsulated salt for large-capacity system and storing solar energy. The specific objectives are:

1) To identify the research gap in the current material research for inorganic salt-based sorption thermochemical energy storage technologies.
2) To understand the method for encapsulating inorganic salt.
3) To optimise the thermal performance of encapsulated salt.

4) To demonstrate the fluidisable encapsulated salt for a flexible long-duration energy storage

5) To integrate the encapsulated salt storage with the solar energy input.

1.3 The structure of this thesis

This thesis consists of eight chapters of which:

- Chapter 1 introduces the background, thermochemical heat storage using encapsulated salt, and the integration with solar heat system, and presents the aim and outline of the thesis.
- Chapter 2 overviews the fundamentals, developments, and state-of-art in thermochemical energy storage technologies, especially in sorption-based thermochemical heat storage technology using inorganic salt. It is given in a comprehensive review, covering the principles/concepts, inorganic salts/composite materials, and devices/systems.
- Chapter 3 studies the method for encapsulating salt, focusing on the encapsulation from the Pickering emulsions, and experimentally discovers the formation mechanism of water-in-oil (W/O) Pickering emulsions containing hydrophobic fumed silica nanoparticles as the Pickering particle.
- Chapter 4 investigates the effects of the protocol on the W/O Pickering emulsions containing a high volume of salt, especially sorts out the measures for tailoring the size of the droplet in Pickering emulsions.
- Chapter 5 discovers and optimises the thermal performance of

encapsulated salt with the geometries on a multi-scale.

- Chapter 6 describes a novel technology for using the encapsulated salt in a fluidised-bed reactor, realising a flexible TCS with high-performance.
- Chapter 7 describes a lab-scale devices using a solar absorption enhanced encapsulated salt, demonstrating the potential of storing renewable energy with the developed TCS materials.
- Chapter 8 concludes the findings, and contributions of this thesis, and provides recommendations for future work.

2 Literature review

This chapter carries out a comprehensive review of thermochemical energy storage technologies, covering the concepts, the materials, and the devices/systems. The chapter is organized as follows.

- Section 2.1 introduces the fundamentals and development of thermochemical energy storage, especially thermochemical heat storage technologies.
- Section 2.2 reviews the advanced thermochemical heat storage technology concerned in this thesis, which is the chemical absorption of water in inorganic salt via hydration/dehydration.
- Section 2.3 presents the developments and state-of-the-art composite materials used in thermochemical energy storage with hydratable salt.
- Section 2.4 presents the related thermochemical energy storage device/system, especially for storing solar heat.

2.1 Thermochemical energy storage technologies

2.1.1 Fundamentals of Thermal energy storage (TES)

Thermal energy storage is the essential technology to cop the mismatch between renewable energy production and demand. Thermochemical energy/heat storage (TCS) is one of three thermal energy storage technologies, which the others are sensible heat storage (SHS) and latent heat storage (LHS) [16], [17]. The following table summarises and compares the main features of these technologies:

Table 2-1 Three technologies of thermal energy storage.

	SHS	**LHS**	**TCS**
Fundamentals [18]	Temperature gradient $Q = mC_p\Delta T$	Phase change $Q = m\Delta H_{phase\ change}$	Reversible reaction $A + \Delta H_r \longleftrightarrow B + C$ $Q = Xn_B\Delta H_r$
Energy density [19], [20]	~150 J/g ($\Delta T = 100°C$) ~ 200 MJ/m^3	~200 J/g 300 to 500 MJ/m^3	>1000 J/g 500 to 3000 MJ/m^3
Operating temperature [21]	-150 to 800°C	-150 to 600°C	20 to 1000°C
Storage term [21]	Hours to days	Hours to days	Hours to months
Operating duration (capacity) [21]	Hours	Hours	Hours to days
Materials	Water, sand, rocks, cermet	Phase change material (PCM): organic, molten salt, hydrated salt	Metal Oxides, inorganic salt, SO_2, silica gel, zeolite,
Materials Cost (Based on energy)	Low	High	Mid
System Cost	Low	Low	High
Development	Demonstrati	Large prototype -	Concept needs

stage (by 2020) [22]	on – Commercial (TRL 8-9)	Commercial (TRL 5-9)	validation – pre-commercial prototype (TRL 3-7)

Compared to the SHS and LHS, the TCS is the lately developed, but the most promising technology for thermal energy storage. The TCS have a high gravimetric energy storage density (GSD) based on pure material. It is approximately an order of magnitude over SHS, and two times higher over LHS [23]. This superiority of TCS makes a cost-competitive in large-capacity energy storage for a long-duration charging/discharging. Differing to the spontaneous heat dissipation in SHS and LHS, TCS benefits energy loss-free during storage, thus TCS become a potential solution for medium- and long-term energy storage. An extra advantage of TCS is the controllable charging/discharging, allowing the flexible schedule for storing intermittent energy. In a summary, all the benefits make the TCS showing a great potential for long-term seasonal energy storage [24]–[28], and renewable energy storage such as solar heat [29]–[32].

2.1.2 The concepts of thermochemical energy storage

The TCS is based on storing chemical energy making use of the reversible endothermic/exothermic reactions [18]. This concept of TCS technology was first proposed fundamentally by Goldstein in 1961 [33]. He analysed several candidate reactions for storing heat and figured out the thermodynamic relationship to determine the amount of heat generated from a thermochemical reaction, as below:

$$\Delta G = \Delta H - T\Delta S \qquad \text{Equation 2-1}$$

This describes the relationship between Gibbs free energy ΔG , reaction enthalpy change ΔH, the reaction temperature T, and the entropy change ΔS. The positive ΔG represent the reaction is going forward and become zero in case of at equilibrium. The reactive enthalpy change, as well as the stored heat, is determined by a product of equilibrium temperature and entropy change ($\Delta H = T^* \Delta S$). It is favourable that a reaction with high temperature and large entropy change [34]. Therefore, most of the practical TCS reactions are carried out in the form of decomposition reactions from a condensed matter and producing gases, as illustrated by:

$$A_{solid\ or\ liquid} + \Delta H \longleftrightarrow B_{solid\ or\ liquid\ or\ gas} + C_{gas} \qquad \text{Equation 2-2}$$

Where the A and B are the in the discharged and charged TCS material (TCM), respectively. For charging process, the thermal energy input brings A to a temperature above T^*, triggering the forward reaction. The production C can be extracted from the reaction. The energy is stored as chemical potential in B, which is stored separately from C. Discharging then accounts for the reversible process, in which C are introduced to B at $T < T^*$ and recombined to release thermal energy.

2.1.3 The developments of thermochemical energy storage

In 1977, Ervin first reviewed the existing studies of the TCS at that time [35] and discussed the serval reactions, such as alkaline earth metals halides salts/NH_3,

alkaline earth metals oxides/H_2O or CO_2, metals oxides redox, SO_3/SO_2, NH_3/NH_4HSO_4 cycle, and reforming-methanation cycle. Most of them are well-known decomposition reactions, that service the high-temperature (>300°C) solar heat storage. In following years, many early-stage studies among materials characterization [36], reactor design [37], and system modelling [38] were carried out. In the 1980s, the first few proof-of-concept experiments were designed and some devices/facilities were installed, including the 20kW test rig for catalysed SO_3/SO_2 cycle by McCrary [39], a 1.6kW high-temperature solar reactor for SO_3/SO_2 cycle by De Maria [40], and a 110L packed bed-based test rig for $Ca(OH)_2/CaO$ by Fujii [41]. Although all the prototypes successfully demonstrated the feasibility of TCS, the measured energy storage density was far below the theoretical values. Besides, those TCS systems were complicated that large in floor space and were not robust due to the devices always damaged by the TCM corrosion.

Besides the TCS for high-temperature, another simple concept was proposed by Close in the same period, that adsorption is a method of storing heat in mid- and low temperature [42], [43]. It is most readily achieved by introducing water vapour as the adsorbate to the porous sorbent, such as silica gel, zeolite. The heat is generated by the water vapour condenses from the humid air and water molecular bonds at the surface of solid sorbent. His study demonstrated that the dry warm air with a temperature lift of around 10°C was obtained at the outlet of the packed bed with a volume of 0.1m^3 [44]. In the following years, to

examine candidate materials for adsorption energy storage, another experimental study was designed and conducted by Shigeishi [45], who also discussed the possibility of using zeolite molecular sieves as the adsorbent. The measurements showed the highest heat of adsorption is around 531J/g in zeolite 13X, which initially regenerated at 110°C for 48 hours and adsorbed 0.12 $g/g_{dry\ sorbent}$ water in discharging. Moreover, other researchers proposed using chabazitic tuff in place of the expensive synthetic zeolite [46]. This mineral is a kind of natural zeolite rock distributed in Italy. That rock was measured in-house, and the result showed a $193J/g_{dry\ sorbent}$ or $268MJ/m^3$ in energy storage density when operating between 20°C to 80°C. In their following studies, they pointed out that the thermal performance is highly dependent on the geometry of the material [47]. Moreover, they tested the first heat pump with solid adsorption energy storage for domestic heating [48]. Beyond silica gel and zeolite, other commercial materials were also considered at that time, including activated alumina (~$329J/g_{dry\ sorbent}$), anhydrous calcium sulphate (~$292J/g_{dry\ sorbent}$) [49] and ettringite ($Ca_3Al(OH)_6)_2(SO_4)_3{\cdot}26H_2O$ ($997J/g_{dry\ sorbent}$) [50]. Those theoretical energy storage densities are several times higher than in SHS and LHS materials. However, the major disadvantages were the high cost and large temperature hysteresis between discharge/charge.

As another principle besides adsorption on a solid surface, energy storage by absorption in bulk or liquid was proposed [51], [52]. Such systems generate exothermic reactive heat by a sorbent absorbing another working fluid [53]. One

successful case was shown as the low-temperature liquidised $CaCl_2/NH_3$ TCS integrated vapour compression heat pump by Riffat [54]. The use of liquidised $CaCl_2$ sorbent improves the heat and mass transfer, but the problems of salt crystallization and corrosion were significantly reducing the system reliability. Another example system of using salt-absorbing working fluid (NH_3) to form a complex compound is demonstrated by Rockenfeller [55]. Because salt absorption is slow in a solid-gas reaction, which is typically limited by mass diffusion. To enhance the mass transfer, they dispersed the salt particles in an immiscible organic solvent to form a slurry. The demonstration proved the potential of scale-up, but the challenge had been and remains in the design and optimization of material and reactor.

In the following decade of the 1990s, a new concept of storing low-temperature energy by reversible hydration reactions with the solid salts was proposed. Selvidge compared an inorganic salt LiBr with the sorbents materials listed above [56] and found it has a heat of hydration overcome $600J/g_{sorbent}$, which was two times higher than the tested zeolites 13X at the same regenerated condition of 350°C and 24 hours. Levitskij [57] presented a screening study of salts for heat storage systems with hydration/dehydration, in which systems are so-called “chemical heat accumulators (CHA)”. In his study, there were 10 candidate salts, which have a specific enthalpy of dehydration between $50kJ/mol_{water}$ to $70kJ/mol_{water}$, and corresponding water loss capability from 1 to $7mol/mol_{salt}$. The result shows the $MgSO_4 \cdot 7H_2O$ and $MgCl_2 \cdot 6H_2O$ positioned at

the highest and the second in the heat of dehydration, which are 4162J/$g_{dry\ salt}$ and 3405J/$g_{dry\ salt}$, respectively.

As for that time, most of the mechanisms and reactions subjected to thermochemical energy storage had been proposed, as summarised below.

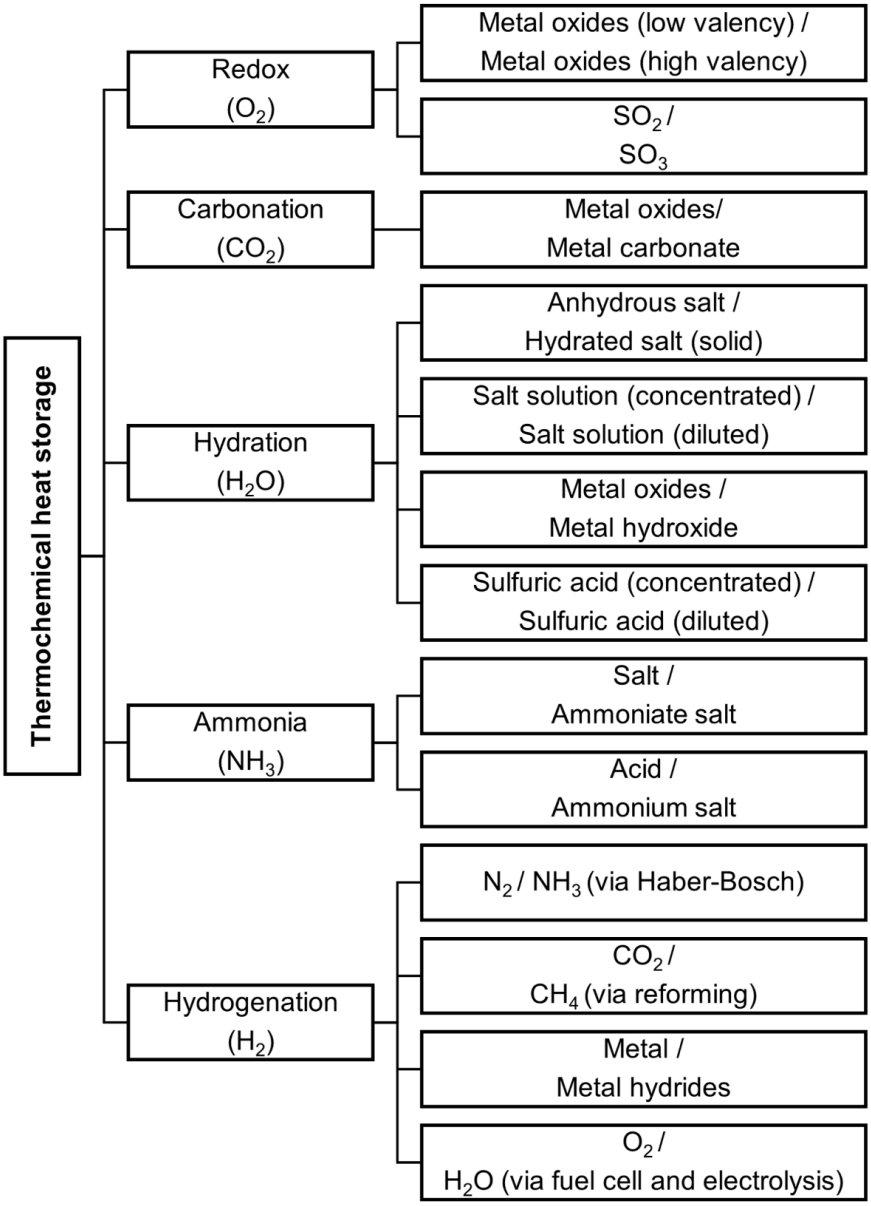


Figure 2-1 The most studied TCS reactions, classified by reaction principle.

In this thesis, the focus is on the solid hydratable salt based TCS with sorption.

This is the lately proposed concept among all the TCS techniques. The advantage of this kind of reaction contains high energy density, uses of abundant material, and a suitable temperature for low-grade heat sources, such as solar heat. In the following section, a review of this type of TCS is given in detail.

2.2 The sorption TCS with hydratable salt

2.2.1 Terminology

In the literatures, the use of the expressions “thermochemical energy/heat storage”, “sorption heat storage”, “chemical storage” and “hydration/dehydration heat storage” differs from one author to another and might be confusing to the audients. Thus, a short discussion of terminology is given in first. Here, as shown in Figure 2-2, we suggests a principle-based terminology, which inherits the classification by N’Tsoukpoe [58]. There are two types of major catalogues: “the chemical energy storage” in the first column, and “the sorption heat storage” in the last row. Chemical energy storage involves either electricity, chemicals, or heat as the product. In this study, attention is given to chemical heat storage, which is further divided into thermochemical heat storage with sorption and without sorption.

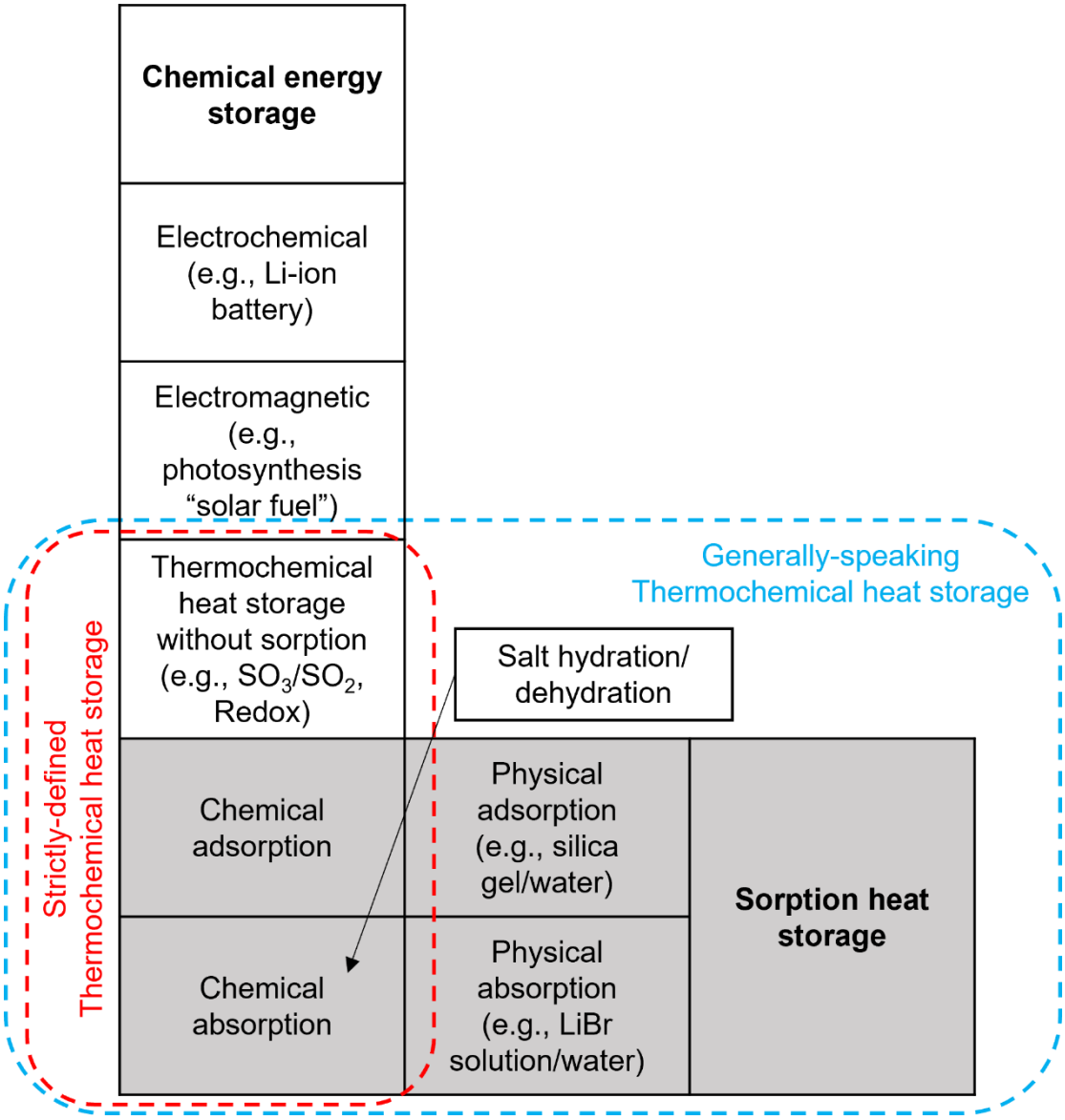


Figure 2-2 Classification of chemical storage and sorption heat storage.

From another aspect, sorption heat storage is defined as a sorption/desorption process to store thermal energy during the binding of a gas or a vapour (sorbate) by a substance in another condensed state (solid or liquid) [59]. The major types of sorption are adsorption and absorption, classified by where the sorption takes place. The former is regarding the sorption on the surface, and the latter is the sorption inside the bulk. Depending on the major difference in attractive

forces, this sorption phenomenon is categorized into: a thermo-physical (physisorption), a thermo-chemical (chemisorption) [60], [61]. A comparison of those sorption is listed below.

Table 2-2 Comparison of physisorption and chemisorption

	Physisorption	Chemisorption
Sorption force	Intermolecular force: van der Waals force (vdW), electrostatic force, hydrogen bond	Chemical bonds rupture and formation: Ionic bond, coordination bond, hydrogen bond
Typical sorption site	Multilayer absorption on the surface, condensation in pores	Bulk absorption in monomolecular
Sorption capacity	Depends on the specific surface area	Depends on volume
Sorption rate	High	Low
Sorption heat	Low	High
Cycle stability	Good	Poor
Materials	Silica gel, Zeolite, Metal-organic frameworks (MOFs)	Inorganic salt

The physisorption is the simplest sorption phenomena, which is mainly contributed by attractive van der Waals (vdW) forces. Typically, the sorbates are adsorbed on the surface of the sorbent, so-called “physical adsorption”. Another physisorption is the absorption of vapour in liquid in a specific cavity, such as water condensation in the pores of zeolite, which is called “physical absorption”. The nature of physisorption energy storage is the reversible conversions between heat and intermolecular potential, which is approximately described by the Lennard-Jones (L-J) potential [62], as written in:

$$V(r) = 4\epsilon\left[\left(\frac{\sigma}{r}\right)^{12} - \left(\frac{\sigma}{r}\right)^{6}\right] \qquad \text{Equation 2-3}$$

Where the ϵ is the depth of the potential well, r is the distance between two interacting particles, and σ is the distance at which the particle-particle potential energy $V(r)$ is zero. In the right hand of L-J potential, the first term $(\sigma/r)^{12}$ is regarding the short-range repulsive force caused by Pauli's exclusion principle between their electrons, and another term $(\sigma/r)^{6}$ represents the long-range vdW attractive force.

A general result of L-J potential is shown in Figure 2-3a. When a molecule is approaching the surface of the sorbent from the position at the red dot, they spontaneously fall into an energy well (blue dot), which is distanced from the surface in a few Ångstroms to a few nanometres. The amount of released heat is therefore equal to the decreased energy potential. Figure 2-3b presents an example of the total heat of physisorption according to the water uptake in Zeolite 13X [59], including binding energy on surface and condensation energy in pores. One can see the binding energy of adsorbates on the sorbent surface as well as the change of energy potential ϵ in Figure 2-3a, decreases to zero at a critical water uptake. It is indicating that all the surface area is occupied by the adsorbates. Additional capillary condensation energy, regarding the phase change latent heat between vapour and liquid water, is shown as a constant value in the dashed zone of Figure 2-3b. The water uptake reaches the maximum at ~0.3$g_{water}/g_{sorbent}$, which is slightly higher than the critical water uptake, indicating the exceeded condensation in zeolite until all the pores are fully filled [63]. Such porous materials are often used as physical absorbents.

The key indicators of those materials are the specific surface area and specific pore volumes, which determines the sorption capacity and sorption rate.

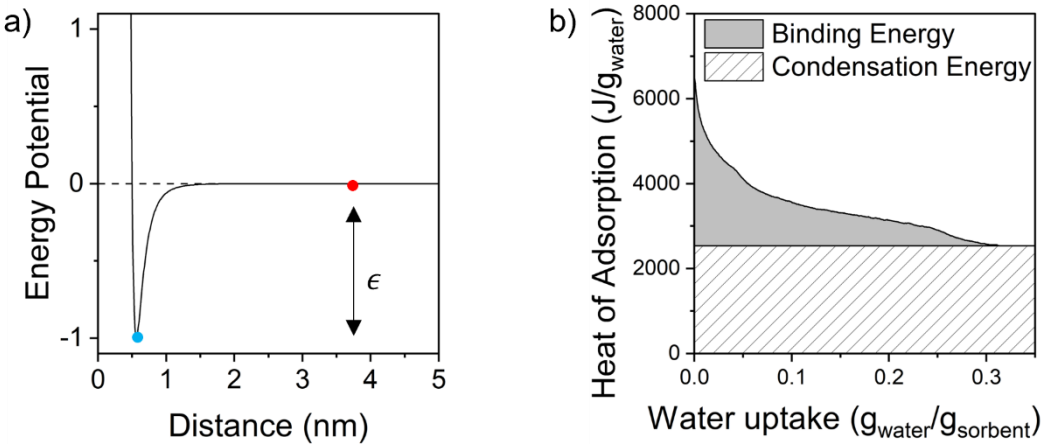


Figure 2-3 Energy potential change and heat of adsorption during physical adsorption, a) Lennard-Jones (L-J) potential and b) Total heat of physisorption according to the water uptake in Zeolite 13X.

On the other hand, chemisorption is a complex process, which has a major difference in the bonding force between sorbent and adsorbate/absorbate. For the formation of chemical bonds in chemisorption, the activation energy E_a is essential for trigging the reactions [64], as illustrated in Figure 2-4. Chemisorption is typically an absorption, which takes part in monomolecular rather than in multi-layers on the surface like physisorption. This is accomplished by the chemisorbed atom jumping in the subsurface layer and finally diffusing on the interstitial sites through the sorbent lattice [65], see the fluctuated red curve in the sorbent part of Figure 2-4. When the chemisorbed molecular has a lower energy potential than the gaseous molecular, the sorption is thus exothermic and has a reaction enthalpy at ΔH_r. Benefited from

the high formation energy of chemical bonds and all the molecular participate in the reaction, chemisorption has a large amount of heat generated/stored and high sorption capacity, which is superior to physical sorbents [61]. However, the chemical absorption is usually limited in sorption rate as well as heat generate rate, due to slow penetration of absorbate deep into the sorbent [66].

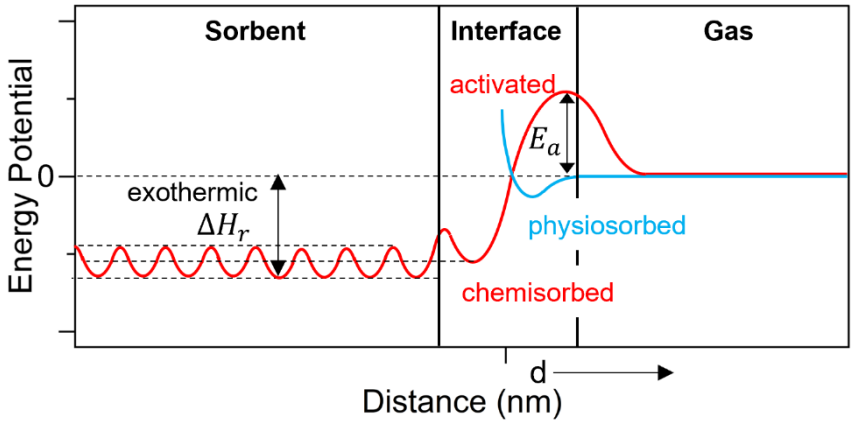


Figure 2-4 One-dimensional energy potential of chemisorption (chemical absorption).

In summary, generally suggested by many authors, both physisorption and chemisorption are belonging to thermochemical heat storage [67]–[69]. But strictly, only chemical reactions involved in heat storage are defined as thermochemical heat storage [58], [70], [71]. In this study, the latter is suggested, and attention is given to a specific thermochemical heat storage technology, which employs the solid hydratable salt as a chemical absorbent and operates in hydration/dehydration reactions.

2.2.2 Inorganic salts as the chemisorption materials

Among the candidate materials in chemisorption energy storage, the inorganic salt hydrates have a low operating temperature, which is promising for solar energy storage and supply for domestic demand [72]. Ideally, a salt-based sorption thermochemical heat storage is based on a pair of reversible gas-solid reactions, in which the forward reaction involves crystallized salt in a solid state reacting with water vapour and then transforming into a hydrated salt crystal, as given in the equation below:

$$Salt(s) + xH_2O(g) \xleftrightarrow{\substack{Temperature,\\ Pressure}} Salt \cdot x(H_2O)(s) + \Delta H_r \qquad \text{Equation 2-4}$$

The reaction enthalpy ΔH_r is independent of the reaction pathway, only related to the change in potential energies of two lattices, the anhydrous and the hydrated. Taking $CaCl_2$ as an example, Figure 2-5 presents the crystallographic structures of those crystals. One can see the intensive difference, not only the crystal system changed from orthorhombic (anhydrous) to monoclinic (hydrated), but also the lattice constant increased. Those changes induce considerable lattice volume expansion and the corresponding reduction in lattice energy potential. The potential change is the basis of the chemical energy stored in the crystals.

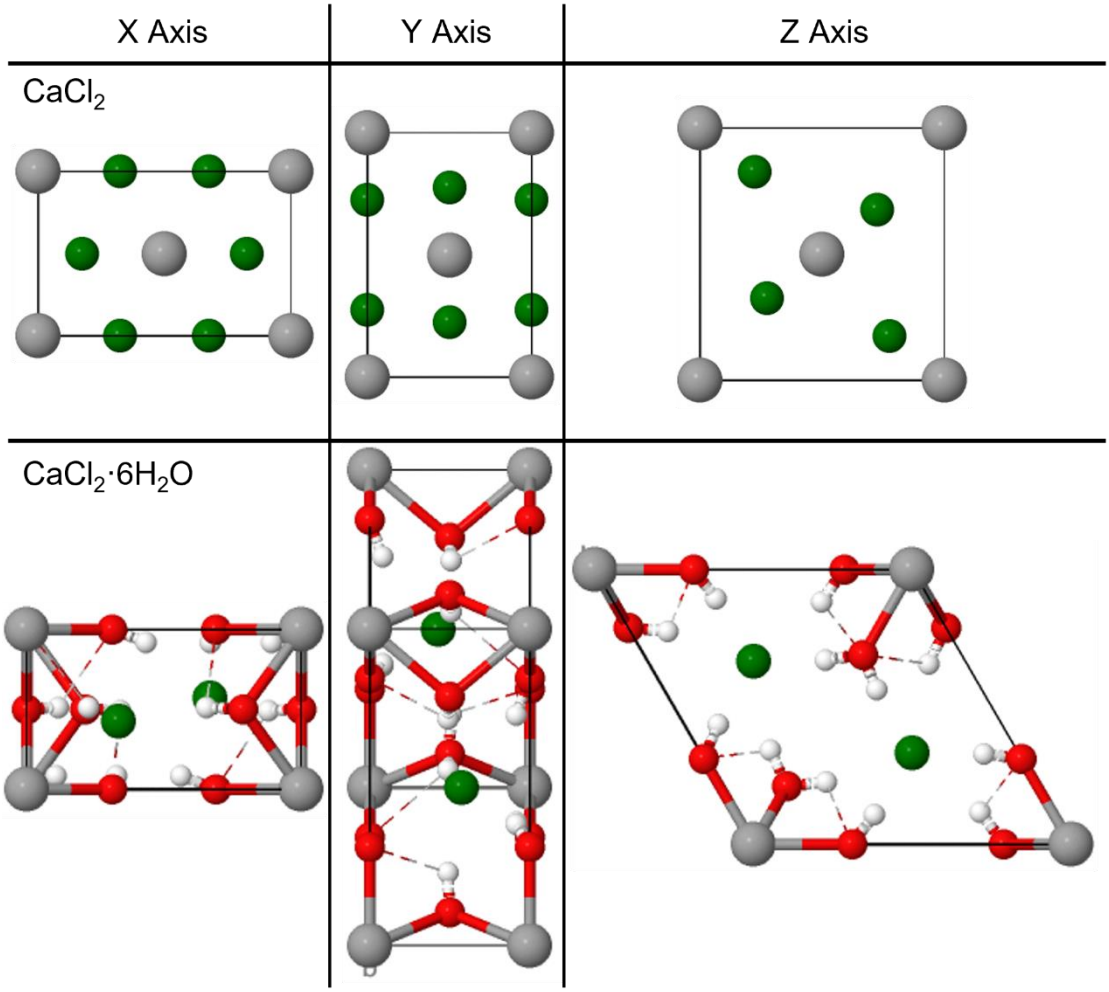


Figure 2-5 Crystallographic structures changed from $CaCl_2$ [73] to $CaCl_2 \cdot 6H_2O$ [74]; dark grey-Ca, green-Cl, red-O, white-H; The dash lines in $CaC_2 \cdot 6H_2O$ represent hydrogen bonds.

Unfortunately, the lattice potential energy is hard to be measured directly, the most conventional estimation method is to follow the Born-Haber cycle [75], as illustrated in Figure 2-6.

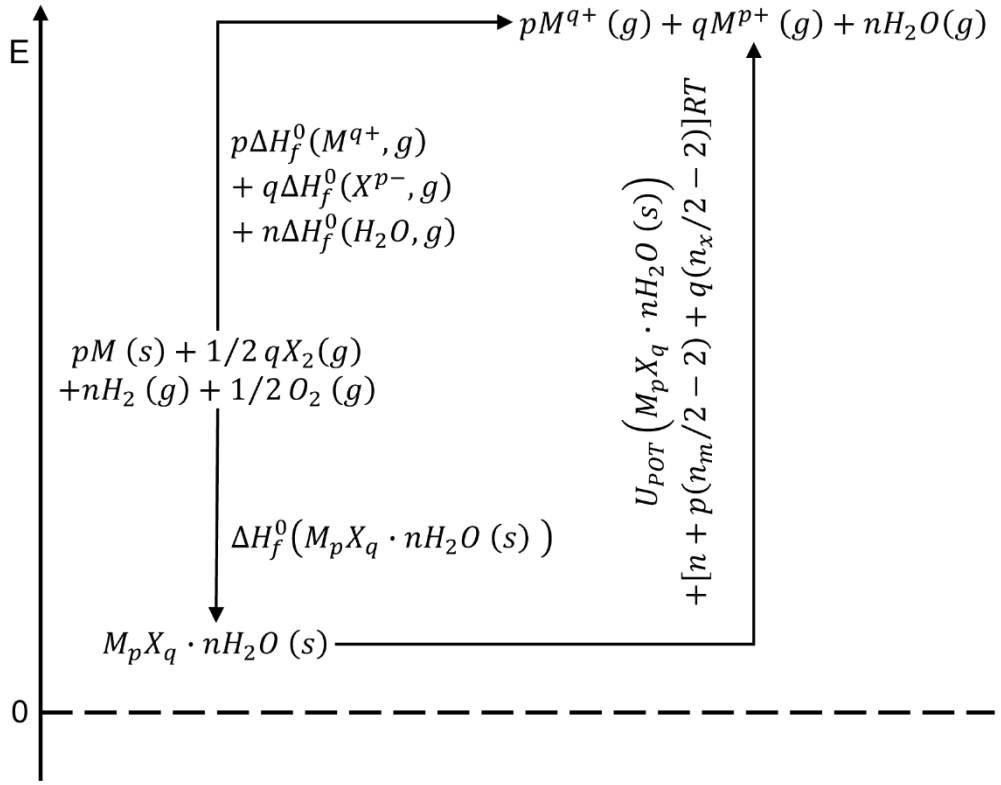


Figure 2-6 estimates the lattice enthalpy U_{POT} of anhydrous $(n = 0)$ and hydrated salt based on Born-Haber cycle.

In the Born-Haber cycle, the values of each thermodynamic term must be determined in advance and the calculation is different in case by case. It is difficult to employ this approach in a high-volume screening for candidate hydratable salts for thermochemical heat storage. To avoid elaborate computation, Jenkins et al., developed a series of methods to estimate the lattice energy of salts, including the full-lattice evaluation of the electrostatic energy [76] and method of estimation from crystals data [77], [78]. The latter estimation was performed by solving the linear generalized equation with the minimum crystal structure data, which contains cell constants and thermochemical radii of ions [77]. For estimating the lattice energy potential of

hydrated salt from a known anhydrous, an alternative method was produced by fitting the thermodynamic data of 342 hydrate salts [79]. The fitted model predicts the energy potential change by $n\theta_U(H_2O)$. Where n is the number of water molecules in hydrated state and the corresponding reaction energy $\theta_U(H_2O) = 54.3\ kJ/mol$. The table below lists the results from the different methods mentioned above.

Table 2-3 Estimated lattice enthalpy of $CaCl_2$ by the different models, values in brackets is the enthalpy change from anhydrous salt.

Lattice enthalpy U_{POT} in kJ/mol				
	$CaCl_2$	$CaCl_2 \cdot 2H_2O$	$CaCl_2 \cdot 4H_2O$	$CaCl_2 \cdot 6H_2O$
Born-Haber cycle	2232	2352 (120)	2470 (238)	2575 (343)
Full-scale computational[76]	2159	2320 (161)	2396 (237)	2481 (322)
Crystal data-based model[78]	2202	2312 (110)	2420 (218)	2529 (327)
Fitted model[79]	2232	2341 (109)	2449 (217)	2558 (326)

The estimations of the fitted model are in good agreement with the result from the Born-Haber cycle, the difference is within 4%. For a pure $CaCl_2$ operates between anhydrous and hexahydrate at room temperature, the theoretical energy potential is averaged at 329.5 kJ/mol, referring to a GSD at 2968 $J/g_{anhydrous}$ (1504 $J/g_{hydrated}$) and a volumetric storage density (VSD) at 6.38 GJ/m^3 (2.57 GJ/m^3 for hydrated salt). Furthermore, an extensive thermodynamic table of hydrated salt was produced by Glaser [80]. As sorted by the energy density from the largest to the smallest, $Ce(SO_4)_2$, Na_2CO_3, Na_2HPO_4, $MgCl_2$, Na_3PO_4, $AlCl_3$, Na_2SiO_3, Na_2SO_4, $MgSO_4$, and $CaCl_2$ have

listed ahead of others and all have the GSD above 3000J/$g_{anhydrous}$. In another study, the state-of-art theoretical framework for salts screening is conducted from a high-throughput first-principles computations [81]. A total of 163 hydrates and 40 hydroxides with known crystal structures were examined in this study. The result of this screening is shown in Figure 2-7. For hydration/dehydration pairs working below 200°C, most of the high energy density materials were sorted out, namely $KF{\cdot}4H_2O$ (2.1MJ/kg, 3.0 GJ/m^3), $AlF_3{\cdot}9H_2O$ (2.0 MJ/kg, 3.1 GJ/m^3), $MgCl_2{\cdot}6H_2O$ (2.0 MJ/kg, 3.1 GJ/m^3), $CaCl_2{\cdot}6H_2O$ (1.6 MJ/kg, 2.9 GJ/m^3), and $CaBr_2{\cdot}9H_2O$ (1.6 MJ/kg, 3.1 GJ/m^3). However, in this study, one shortcoming is the sulfates and nitrates were not included.

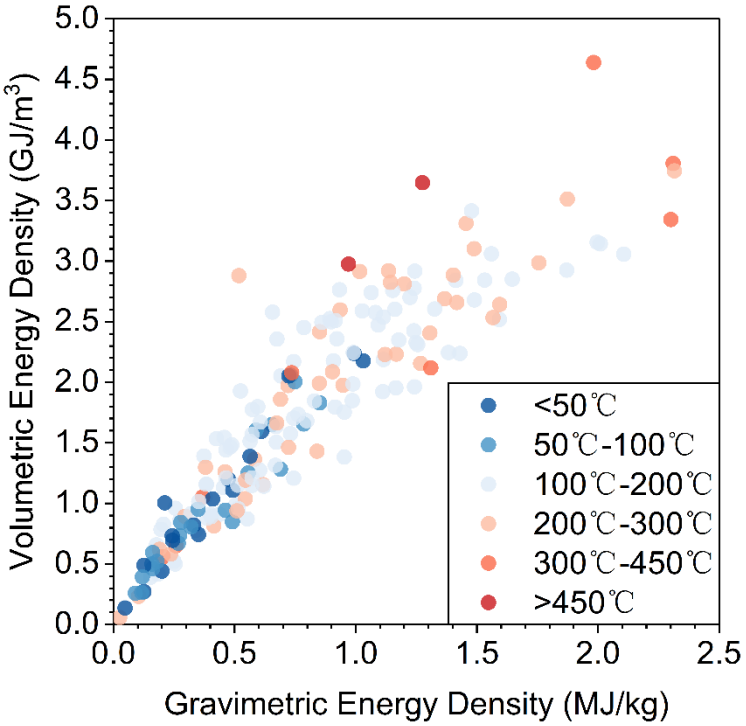


Figure 2-7 Screening the hydrated substrates for TCS, reproduced from [81].

Although energy density is a crucial performance of the TCM, it is not the only

criterion, especially in practice. Considering the safety issue, thermodynamic measurements, and suitability for the application, N'Tsoukpoe et al., designed a multi-step framework for screening low-temperature thermochemical heat storage [72]. Two salts hydrated, namely $SrBr_2 \cdot 6H_2O$ and $LaCl_3 \cdot 7H_2O$, were selected as the most promising salts for the working condition of charging around 110°C and discharging at 60°C. Moreover, Donkers [82] reported a comprehensive evaluation of salt hydrates for seasonal heat storage. Among all the candidates, K_2CO_3 has the less point of concern but is unfavourable in energy density. Unfortunately, under the various conditions (cost, safety, stability, kinetic) that have been considered, it was concluded that no pure salt can satisfy the realistic application of domestic heating. In a recent screening study, salts were sorted for the determined operating conditions [83]. The initial shortlist, which contains five salts, was produced by matching the application weather conditions with the phase diagrams of salts and psychrometric charts. Then, thermogravimetric analysis was carried out to examine the reaction reversibility and kinetic of each salt. As a result, in addition to common TCS salts (such as $MgSO_4 \cdot 7H_2O$, $MgCl_2 \cdot 6H_2O$, $SrBr_2 \cdot 6H_2O$), it suggests the $Na_3PO_4 \cdot 12H_2O$ and $SrCl_2 \cdot 6H_2O$ are also promising materials, which both have the high energy densities. But Na_3PO_4 is possibly to be unstable during the thermal cycles and $SrCl_2$ is pricey.

A summary is given in the table below, listing the candidate pure salts for thermochemical heat storage. The benefits and concerns are also outlined.

Table 2-4 Summary of the candidate salts for thermochemical energy storage

Salts hydrated pair	Properties (By lower hydrated)	Benefits	Concerns
Na_3PO_4 / $Na_3PO_4 \cdot 12H_2O$	ρ=1.62 g/cm^3 ΔH_r=4033 J/g [80]	High energy density, low cost [83]	cycling unstable [83]
$Na_2S \cdot 0.5H2O$ / $Na_2S \cdot 5H2O$	ρ=1.43 g/cm^3 ΔH_r=3408 J/g [84]	High energy density, low cost [85]	Corrosive [86], safety [87], degradation in air [85]
$MgSO_4$ / $MgSO_4 \cdot 7H_2O$	ρ=2.66 g/cm^3 ΔH_r=3607 J/g [80]	High energy density [71], [83]	High full dehydration temperature (~275°C) [88], slow kinetic [89]–[91]
$CaCl_2$ / $CaCl_2 \cdot 6H_2O$	ρ=2.15 g/cm^3 ΔH_r=3413 J/g [80]	Low charging temperature [92], chemically robust [93]	Deliquesces [94], corrosive [92], slow kinetic [92]
$MgCl_2 \cdot 2H_2O$ / $MgCl_2 \cdot 6H_2O$	ρ=1.90 g/cm^3 ΔH_r=2646 J/g [80]	High energy density, low cost [95]	Thermally unstable (hydrolysis >120° C) [85]
$SrCl_2$ / $SrCl_2 \cdot 6H_2O$	ρ=3.05 g/cm^3 ΔH_r=2137 J/g [80]	High energy density[83], chemically robust [96]	High full dehydration temperature, high cost [83]
$LaCl_3$ / $LaCl_3 \cdot 7H_2O$	ρ=3.84 g/cm^3 ΔH_r=1635 J/g [80]	High energy density [81], suitable discharge temperature [72]	High cost [72]
$SrBr_2$ / $SrBr_2 \cdot 6H_2O$	ρ=4.22 g/cm^3 ΔH_r=1464 J/g [80]	High energy density [72], [83]	cycling unstable [83], Caking [97], high cost [83]
K_2CO_3 / $K2CO3 \cdot 1.5H2O$	ρ=2.43 g/cm^3 ΔH_r=714 J/g [80]	Chemically robust [85], [98]	Low energy density and specific output power [85]

2.2.3 Material issues limiting the thermal performances

Although the sorted pure salts show attractive theoretical performance, a considerable gap is existing between lab measurements and practical.

Regardless of the consideration of economical and operation conditions, in the level of the material, the major challenges of the salts remain on the slow mass transfer, and cycling instabilities, resulting in a considerable degradation in reaction kinetic and a reduction in energy storage capacity.

In hydrations, as well as discharging the TCM, water vapour must diffuse into the deep of salt grains. The corresponding mass transfer routine on a different scale is illustrated in Figure 2-8. The absorbate vapour starts convectively flowing through the surface of the grain with an eventual skin resistance [99], followed by diffuses in the macropores between the primary particles. The adsorbate reaches the surface of the primary particles and diffuses in the micropores before the adsorption at the surface. The diffusion in such micropores is in the Knudsen regime. Then, the absorbate molecular is captured by a specific surface group or active ions on the solid surface, regarding selective adsorption, as presented by the blue dot in Figure 2-8. Moreover, for chemical absorption, the absorbate must diffuse in the solid phase and move to the final position, as represented by the dash lines.

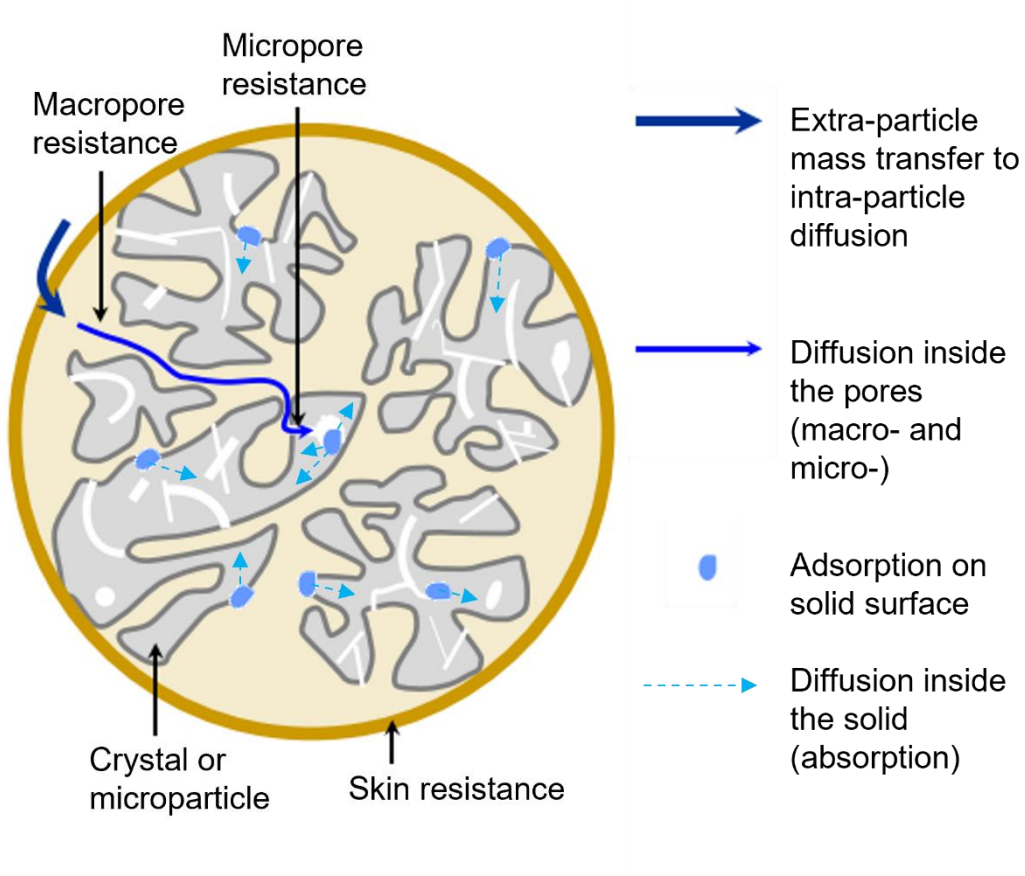


Figure 2-8 Illustration of mass transfer routines in solid absorption, reproduced from [99].

Ostrovskii [100] analysed the diffusion limiting step in adsorption and concluded that diffusion in deliquesced salt solution layer, which forms near the external surface of a granule, is the major limitation before absorbate molecular approach the inner surface of the sorbent. For the following absorption, the mass transfer in solid crystals was studied by Molecular Dynamic (MD) simulation [101], [102]. The estimated mass diffusivity of H_2O in a perfect $MgCl_2$ lattice [103] was far smaller than in solution and in air, as shown in Figure 2-9. In addition, the simulations indicated that the diffusivity is increased by one time in the presence of vacancy defects or element dopants [104]. By the combined

experimental [105] and theoretical [106] studies, it was confirmed that the cracks on the grain surface, and pores or voids inside the grains, which are all induced by the cycle, have an strong improvement in mass transfer. However, it is very difficult to improve the intrinsic diffusivity of pure salt by many orders of magnitude.

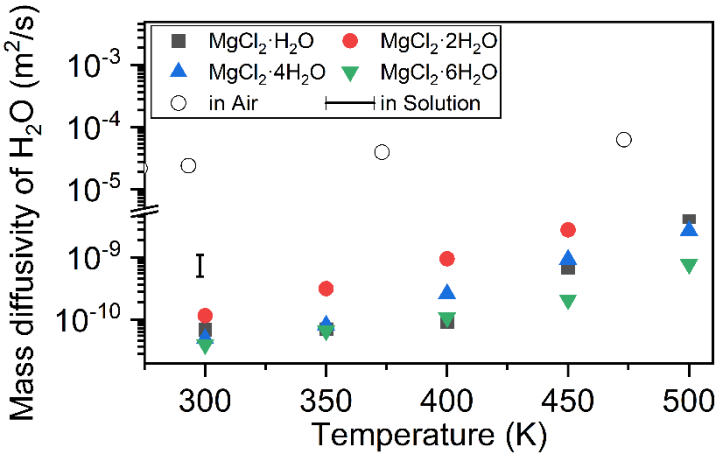


Figure 2-9 Intrinsic mass diffusivity of H2O in air, in $MgCl_2$ solution[107] and in perfect $MgCl_2$ crystal [103].

Accompanying the absorbate adsorbed and diffusion in the solid, the hydration reaction takes place at the transfer quench [108], where the hydrated crystal forms. The crystal transformation is suggested to be achieved via two possible routines [109], as illustrated in Figure 2-10. The first routine is via solid-to-solid transforming, which is happened in the specific conditions zone of vapour pressure and temperature near the phase transition curve. This is so-called a metastable zone, which has a width of about 10°C at a constant vapour pressure. In this zone, the reaction rate is according to classical homogeneous nucleation, which is slow and kinetic is possibly hindered in the worst case [110].

Such a condition can be avoided by increasing the vapour pressure and thus leading to solution-mediated recrystallization (routine II), which has fast diffusion and reaction kinetics [111].

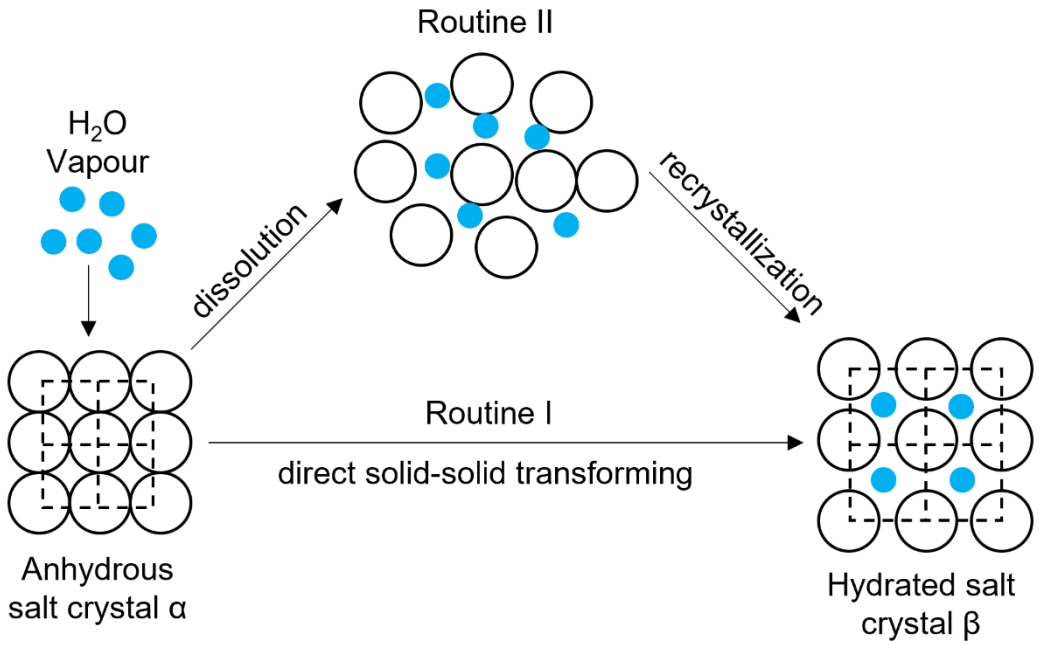


Figure 2-10 Two possible pathways of hydration: (I) a direct solid−solid transition; (II) a solution-mediated transition, reproduced from [109].

When the vapour pressure increased beyond a critical value, the deliquescence happens in inorganic salt [112], especially in salts containing high hygroscopic cation, such as Ca^{2+}, Zn^{2+}, Li^{+}, and Mg^{2+}. The photo images in Figure 2-11 clearly show the salts deliquesce after being exposed to a humid environment and became a solution.

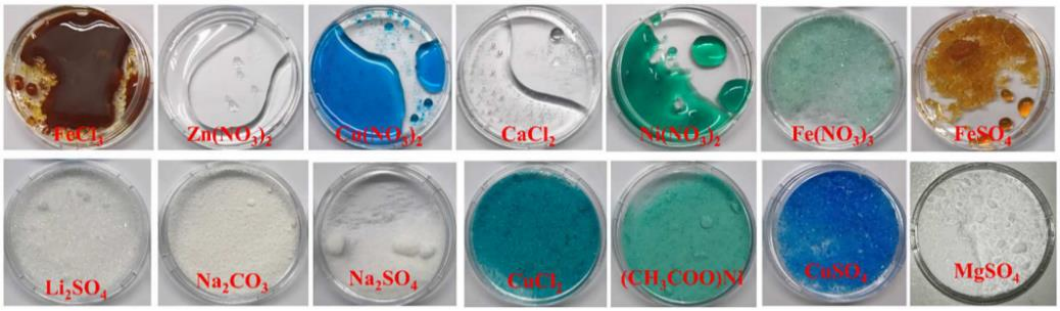


Figure 2-11 Photos of salt after hydration for 24 hours in an atmosphere of 22°C and 60%RH [113].

The deliquesced salt solution has a very high concentration of free ions, which is corrosive to the metals. Commonly heat exchanger materials, such as carbon steel [114], stainless steel [115], copper, and aluminium [86], all show poor tolerance against salt corrosion.

In the following dehydration, referring to the energy charging process, the reaction is conducted in three possible ways as illustrated in Figure 2-12 [116]: A) when the melting point of hydrated salt is higher than the charging reaction temperature, the solid-to-solid transformation takes place; B) when it has a lower melting temperature, the crystal firstly melts into solution follow by a solution-mediate dry out; and C) When charging the salt from deliquesced solution, the solution will be boiling, and the new phase is crystallised from solution. The latter two processes B and C are commonly in practical conditions, however, they showed a slowly kinetic due to a crystalized layer formed firstly at the solid-gas interface, as shown in case B of Figure 2-12. Such a layer is dense and lacks porosity, which dramatically hinders water penetration and slows the charging process.

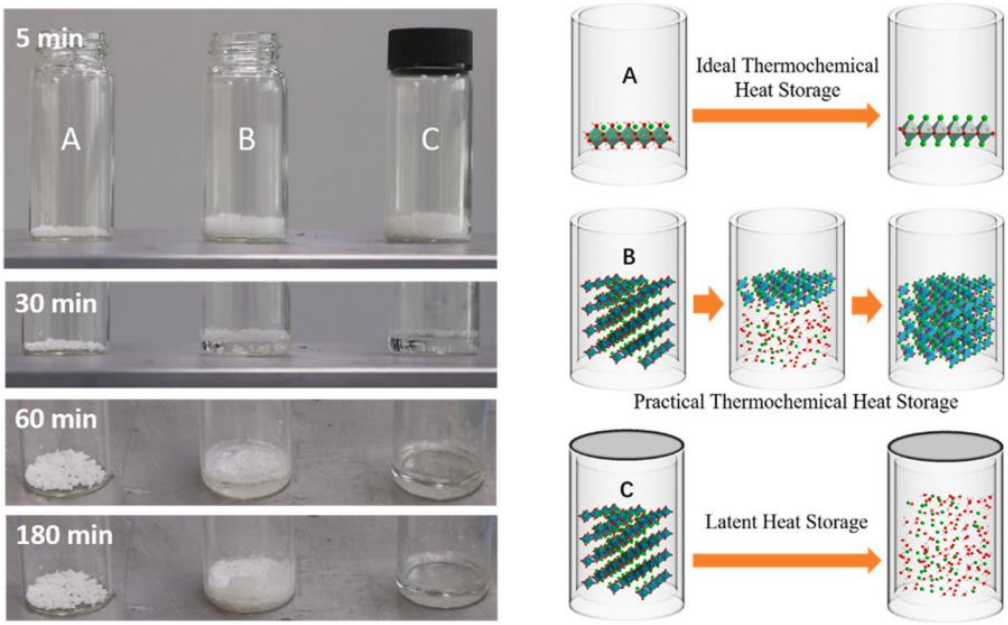


Figure 2-12 The photo images and schemes show the dehydration of $MgCl_2 \cdot 6H_2O$ on a heating plate [116].

In a summary, pure salts as solid thermochemical heat storage materials are facing many drawbacks and are very challenging to be used directly. It is very necessary to develop composite materials, which have not only improved mass and heat transfer but also better stability.

2.3 Composite materials for enhancing the thermal performance

2.3.1 Overview

For enhancing the performance of pure salt, the most promising technology is making a composite. So far, there are two kinds of composites have been developed, namely “salt-in-matrix” and “encapsulated salt”. The former was proposed earlier, so a large number of studies have been published. A comprehensive review is given in the following for both of these technologies.

2.3.2 Salt-in-matrix

The salt-in-matrix is a composite material in that hygroscopic salts were filled and confined in the voids of a porous host matrix. The matrix plays a role to provide a pathway for mass diffusion and the salt plays another role as the absorber to capture the sorbate. The operation principle of the salt-in-matrix working cycle is illustrated in Figure 2-13a [117]. A typical composite operates in 3 steps. Step 1 is the charging as same as the desorption process whereby the thermal energy is used to regenerate, form salt crystallization, and induce the chemical structure change. Step 2 is the storing process through which the anhydrous salt in step 1 is stored away from humidity air. Step 3 is the discharging that recovers the energy through physisorption, chemisorption, and absorption in salt. The corresponding theoretical thermodynamic cycle is presented in Figure 2-13b [118], including a heat up and isobaric process from ① to ③ regarding the charging step 1, followed by a cool down (③ to ④) for recovery sensible heat, the storage is maintaining at point ④, until the discharging takes place and follow the processes from ④ to ① via ⑤.

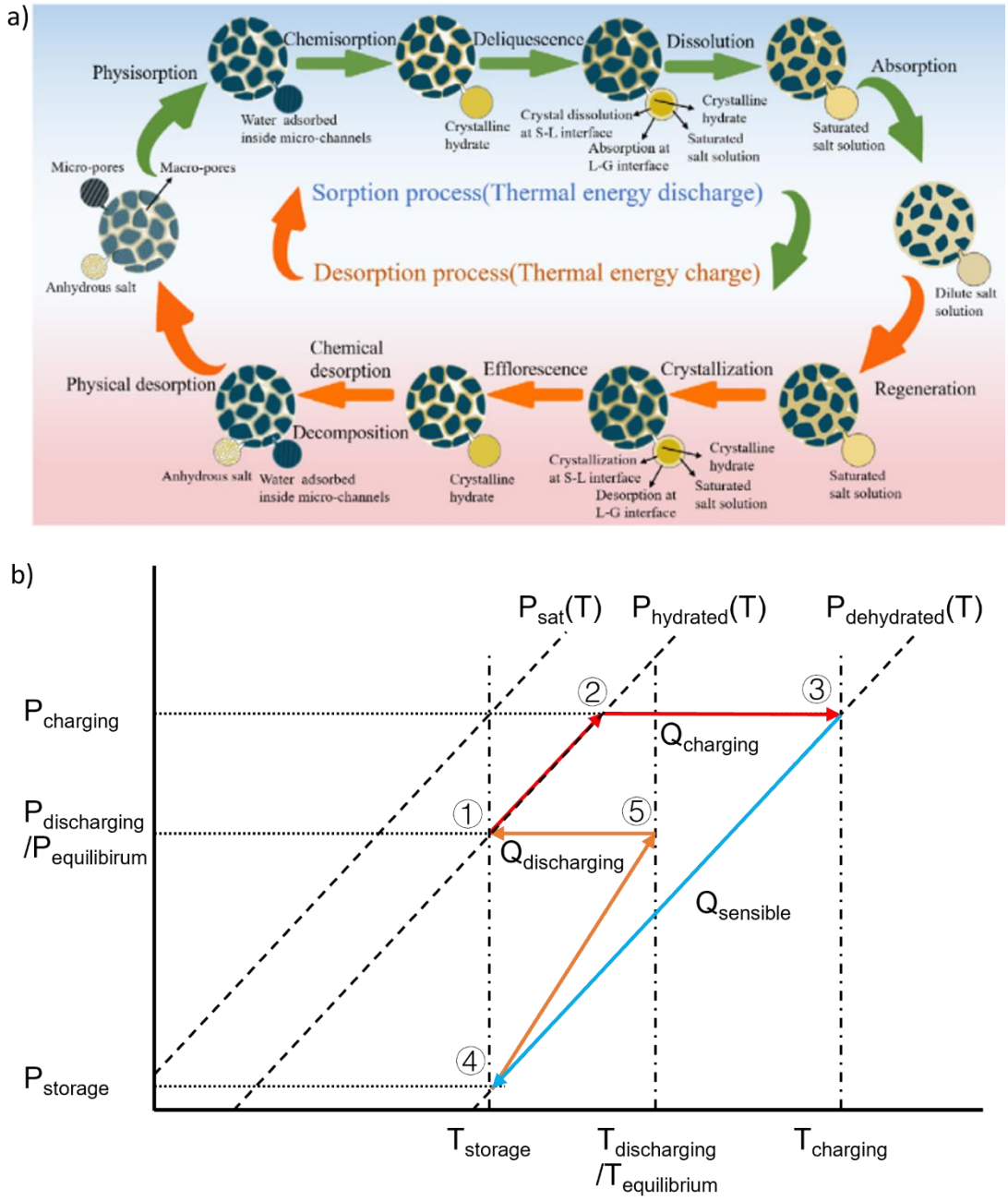


Figure 2-13 The principle of salt-in-matrix materials: a) Illustration of the charging-discharging cycle; b) Theoretical thermodynamic cycle presented in P-T diagram.

The prototype of salt-in-matrix materials was first proposed by Levitskij [57], who filled the porous host matrix (silica gel) with hygroscopic salt ($CaCl_2$). The composite structure was confirmed by the X-ray powder diffraction, which

indicated an average salt crystal size of 15nm [119]. The predicted energy density of the composite was up to 2000J/$g_{dry\ composite}$ at the maximum salt mass fraction of 63%. However, in the best experimental result, the mass fraction of $CaCl_2$ was about 33%. In a further kinetic study [120], an improved mass transfer, as well as a fast conversion rate in composite, was measured by a 10-fold greater rate than in bulk salt. To optimise the composite, the effects of pore structures and salt content were studied and found they can significantly change the mass transfer behaviour in a packed bed [121]. In the case of the large void between matrix grains and the small size of grains, the sorption equilibrium inside grains is immediately reached. The sharp sorption front was formed in bed and appears in an “S-shape” water content distribution along the penetration depth. In the opposite case, it is shown a uniform water content distribution in bed, which the rate is limited by intragrain Knudsen diffusion in the meso- and micro-pores [100]. The salt confined in the intragrain pores play an important role in water absorption capacity as well as the amount of heat generated. When the salt content is high, a dense layer is formed in the intragrain pores, the water transport in the salt layer becomes the major resistance nevertheless the pore structures.

Another drawback of these composites is kinetic reduction during discharging in high vapour pressure conditions. Once the salt begins to be deliquesced in pores, the water transportation becomes slower through the formed solution, this was supported by both experimental and theoretical evidence [100].

Moreover, the leakage might occur in high humidity conditions, resulting in salt loss after cycles.

Great numbers of salt-in-matrix materials were developed by combining TCM salts with the different matrixes. The tables below list these composites, which are sorted by matrix materials.

Table 2-5 The composites of “salt-in-matrix”

Matrix	Salts	References
Silica gel	$CaCl_2$	[122] [123] [124] [125] [126] [127] [128] [129] [130] [131] [132] [133] [134] [135] [136] [137]
	$MgSO_4$	[138] [138] [135]
	LiBr	[135] [137]
	LiCl	[139] [140] [137]
Active carbon	$CaCl_2$	[123] [125] [135]
	LiBr	[135]
Zeolite	$CaCl_2$	[141] [142] [143] [135]
	$MgSO_4$	[144] [145] [118] [146] [143] [135]
	LiBr	[135]
Vermiculite	$CaCl_2$	[147] [135]
	$MgCl_2$	[148]
	$MgSO_4$	[135]
	LiBr	[135]
	$SrBr_2$	[149]
	LiCl	[139]
	K2CO3	[150] [148]
Porous alumina	$CaCl_2$	[121] [132] [151] [152] [153]
	LiCl	[154] [140]
Expanded graphite	$CaCl_2$	[155] [156] [157]
	K_2CO_3	[158]
Aerogel/hydrogel	$MgSO_4$	[159]
	$CaCl_2$	[160] [161]

In a summary, the salt-in-matrix is an efficient design for improving mass transfer as well as reaction kinetics. The method used to prepare the composites is facile and using low-cost porous materials as the matrix will be further helped in scale-up. However, those composites have some drawbacks, such as kinetic hindrance by salt deliquescing-induced clogging in pores, slow mass transfer when the salt mass fraction increased, and cycle degradation by possible salt leakage.

2.3.3 Encapsulated salt

An alternative structure beyond the salt-in-matrix is the encapsulation of salt particles into the capsules, which provide a permanent shell for an individual salt particle. Differing from the salt-in-matrix, the capsule can prevent the salt particle from leaking to the outside and merging with another particle. A well-designed encapsulated salt should have a thermally stable and chemical inertness shell, which should be mechanically stable and semi-permeability to vapour reactant [162]. The idealised encapsulation should have an inner void for hydration-induced grain expansion and avoid stress damage [163]. However, there is a very limited study focusing on encapsulated salt for TCS.

One of the smallest structures of encapsulated salts that have ever been reported is confining the salts in metal-organic frameworks (MOFs), which offer void space with diameters from 5Å up to 3.4nm [164], as shown in Figure 2-14a. By vacuum or infiltration impregnation, the thermochemical salt, such as $CaCl_2$

and LiCl, were successfully encapsulated in UiO-66(Zr), MIL-100 serials and MIL-101 serials [165]. The salt loading has reached at highest of 62%wt with MIL-101(Cr), leading to an experimental energy storage density of 1746±72J/g [164]. However, the shell in these encapsulations is highly mesoporous, which means the salt is possible to leak out of the frameworks. So, be strict, it is not a completed encapsulation.

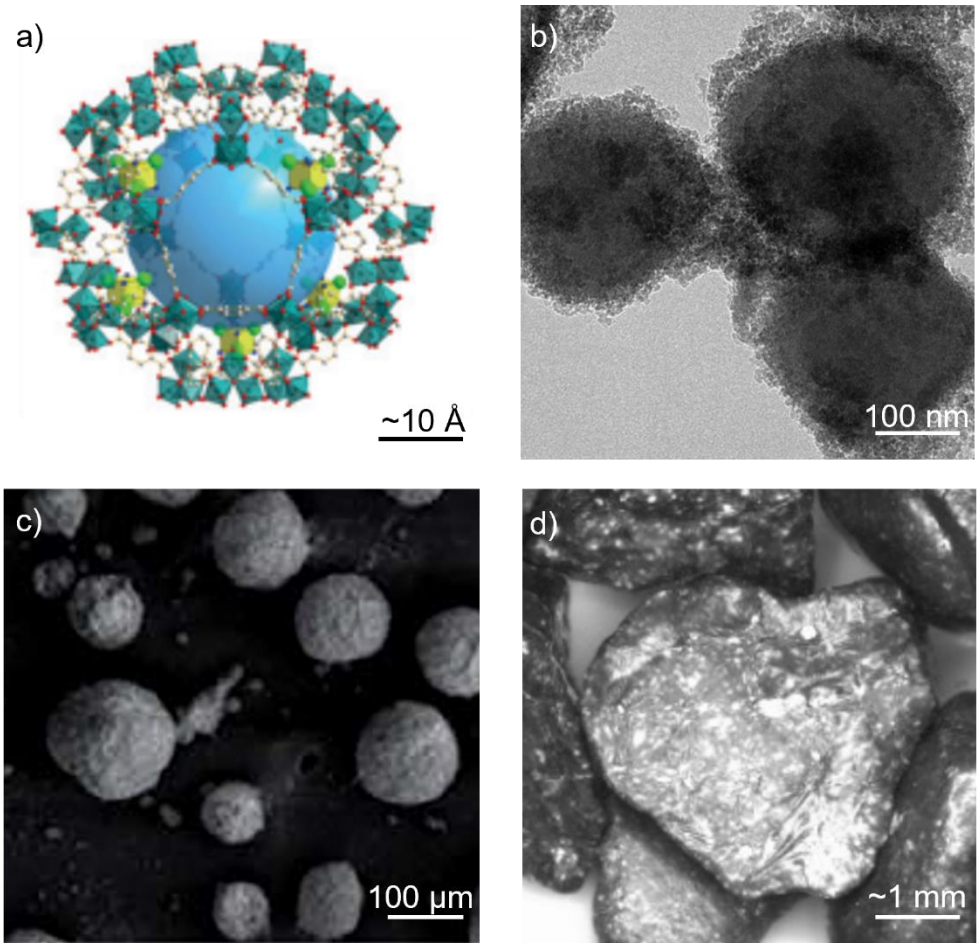


Figure 2-14 Reported encapsulated salt capsules material at the different size scales.

For the encapsulation in the nanoscale, Li et al., [166] and Shkatulov [167] developed their protocol to fill the salt into prefabricated hollow spheres. In both

cases, the hard template was used to build an empty hollow sphere at first, followed by filling the salt from solution soaking. The result of Shkatulov's LiCl@HS is given in the TEM image in Figure 2-14b, which shows the capsules have a diameter of ~365nm and wall thickness at 50nm. The energy storage density is 750J/g (45% of pure LiCl) in this case, which is limited by the unfavourable salt loading ratio caused by the low solubility of salt in water.

For a larger encapsulation in the microns level, for example in Figure 2-14c, Yang et al., designed a method to fabricate the hollow silica spheres from the soft emulsion template [168]. Solid silica shell was derived from binding the amphiphilic polyethylene glycol modified hyper-branched polyethoxysiloxane, which was initially distributed at the water/oil interface and played the role of emulsifier. Then, the salt was filled into the hollow sphere by vacuum impregnation. The composite successfully showed a form-stable ability after exposure to the humidity atmosphere. But the thermal performance was not measured in this study.

An encapsulated composite with a very high salt mass fraction is fabricated by enlarging the ratio between the diameter and shell thickness. As demonstrated by van Ravensteijn [169], the millimetres-sized K_2CO_3 particle was coated by a ~10μm thick polymer shell (as shown in Figure 2-14d) in a fluidised bed coater, which has the advantage to produce kg-level materials per batch. The result shows an extremely high salt loading rate at 97% in total mass and good mechanical strength when using moderately cross-linked and high-molecular-

weight cellulose-based polymers. However, the permeability of coating was measured at ~10^{-11}g/(Pa·s·m), which is under the expectation to provide enough power for heating tap water (must be greater than ~10^{-10}g/(Pa·s·m)). A similar large-size encapsulation case was given by encapsulating $CaCl_2$ by ethyl cellulose via spray dry [170]. Although the encapsulation showed good stability in long-term exposure to a high-humidity environment, the salt content was as low as 29% in the total mass, resulting in a low energy density [147].

Another group of unique encapsulated salt-in-matrix composites employing $CaCl_2$ as TCM was designed and fabricated by Wei et al., [171], [172] The $CaCl_2$ salt was filled in the expanded perlite matrix or coal tar matrix, then the salt-in-matrix were encapsulated by pyrolyzed carbon. The final composites were the black powder in a few millimetres, which has a desorption enthalpy at 1698J/$g_{dry\ sorbent}$ and 1295J/$g_{dry\ sorbent}$, for expanded perlite and coal tar, respectively. With the help of the porous matrix with decades of micron-size pores, vapour mass transfer and heat generation rate inside encapsulation were significantly improved. But the heat transfer between encapsulation and airflow is insufficient due to the powder size being large.

The salt encapsulation can also learn from the encapsulations for other purposes. As a referrable case, Afflerbach et al., [162] developed an oxidic ceramic-based shell for encapsulating the 1-4mm $CaO/Ca(OH)_2$ particles, which are involved in high-temperature hydration TCS. This encapsulation has a ~150μm sintered shell, which is semi-permeable to water vapour due to the

presence of pores. An enhanced mechanical strength was also designed by introducing particle additives to the shell [173]. As a result, an energy density of 576J/g (~40% of pure CaO) and good thermomechanical performance has been reached.

In the recent decade, there are many techniques for encapsulating hydrated salt as phase change material (for LHS) were developed and reviewed [174]–[178]. Differing from the techniques for TCS, the encapsulations are designed to permanently preserve the substrate inside, which the shell is always impermeable. Among all the fabrication protocols, emulsion-templated encapsulation is one of the most usually used methods in this catalogue. As the schematic illustration shown in Figure 2-15, the process involves a template of the PCM solution (melted salt hydrates) droplet dispersed in another immiscible continuous liquid phase. The droplets are stabled by the emulsifiers, which could be molecules [179]–[181] or nanoparticles [182], [183]. Then, the shell is formed at the interface between two phases, typically via interfacial polymerization [184]–[186] or directly-assembly [187] in some other cases. Finally, the product is collected from the dispersions containing salt capsules, by drying the solvent or filtering.

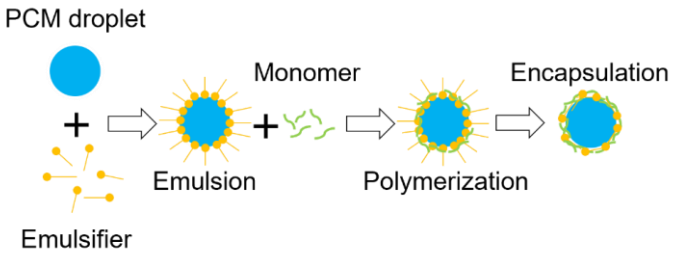


Figure 2-15 Schematic illustration of emulsion-templated in-situ polymerization for encapsulating the PCMs.

2.4 Thermochemical storage system for solar heat

2.4.1 System and reactors design

As an illustration in Figure 2-16, a reactor is necessary for the hydration and dehydration of TCM salt to take place. There are two types of reactors: storage integrated reactor (a, b) or a separate reactor from reactant/sorbent storage tank (c, d) [188]. The integrated reactor is often used for solid TCM, which saves the transportation of materials. But the disadvantage of such a reactor is it has a larger sensible thermal mass, which requires the whole reactor content to be heated up before dehydration (charging) occurs. In contrast, for a separate reactor, it is possible to heat only the required amount of TCM, thereby making the discharging process much more efficient.

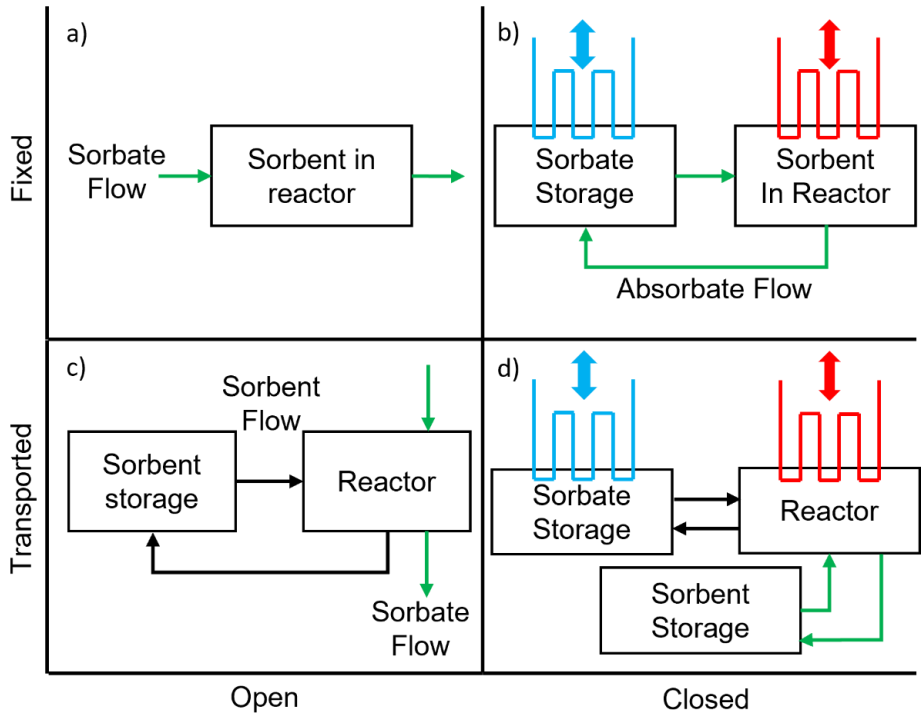


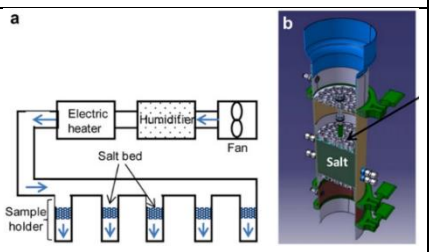
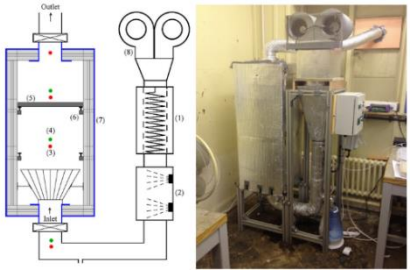
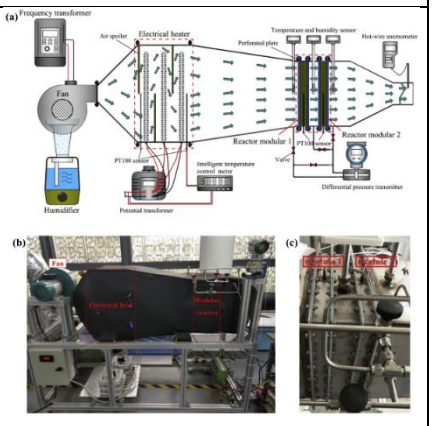
Figure 2-16 Configurations of the thermochemical heat storage systems, reproduced from [189].

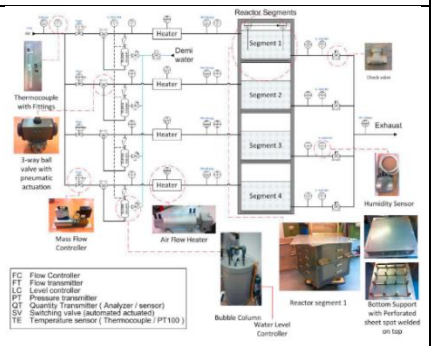
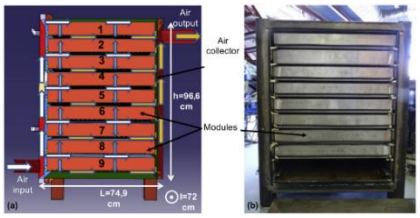
The systems configurations are categorized into the open cycle (a, c) and closed cycle (b, d) [189], [190]. The former refers to a system consisting of a sorbate flow that plays the role of heat transfer fluid [191], [192]. In the latter system, a heat thermal fluid separated from the working pair is used for heat transfer [193]–[195]. Typically, with equivalent geometries and conditions, open systems show higher specific power than closed systems [196] and higher energy efficiency [190]. But, a unique feature of the closed system is it works as a temperature booster, which outputs a higher temperature than charging by increasing the reactant vapour pressure [195], [197].

When the focus is on low-temperature salt sorption heat storage for domestic space heating, the open system is recommended [198], [199]. The open

systems benefit from easy management and have the feasibility to be integrated into the existing HVAC (Heating Ventilation and Air Conditioning) system. The table below lists many experimental works of open sorption heat storage.

Table 2-6 open system for sorption heat storage

Materials	Facility Features	Layout
$SrBr_2$ and H_2O, $SrBr_2$-in-Vermiculite and H_2O [200]	Porous fixed bed Mass: 450-600 g (in 5 modules, parallel connected) Energy density: 430-460 kWh m^{-3} Operating temperature: 20-80°C Power:0.002-0.007 W g^{-1} Discharging duration: ~100 hrs	
$CaCl_2$-in-Vermiculite and H_2O, Zeolite and H_2O, Silica gel and H_2O [201]	Porous fixed bed ($CaCl_2$ composite) Mass: 531 g Energy density: 160 kWh m^{-3} Temperature: 20-120°C Power: 0.09(avg.) 0.18 (peak) W g^{-1} Discharging duration: 5 hrs	
Activated alumina and H2O [199]	Porous fixed bed Mass: 6,521g (in 2 modules, series connected) Energy density: 191 kWh m^{-3} Operating temperature: 20-110°C (Discharging-Charging) Power: 0.04 (peak) W g^{-1} Discharge duration: 13 hrs	

Zeolite and H_2O [202]	Porous fixed bed Mass: 80,000 g (in 2 modules, parallel or series connected) Energy density: 100-200 kWh m^{-3} Operating temperature: 20-180°C Power: 0.0275 W g^{-1} Duration: 6 hrs	
Zeolite and H_2O [203]	Porous fixed bed Mass: 170,000 g (in 4 modules, parallel connected) Energy density: 198 kWh m^{-3} (based on material) Operating temperature: 10-190°C Power: 0.005 (avg.) W g^{-1} Discharge duration: 10 hrs	
$SrBr_2$ and H_2O [204]	Porous fixed bed Mass: 400,000 g (in 9 modules, parallel connected) Thermal storage energy density: 388 (based on materials) kWh m^{-3} Temperature: 25-82°C Power: 0.002 (peak) W g^{-1} Discharge duration: 70 hrs	

It is found that the specific power in most of the results is very low, which is much lower than other thermal storage technologies (typically 0.05 to 0.2W g^{-1} in SHS and LHS [205]). It was suggested that the power is limited by the poor moisture mass transfer in the porous fixed bed. One possible way to improve the mass transfer is using a moisture distributor inside the reactor, such as the design by Casey and Aydin [206], [207], which is shown in Figure 2-17.

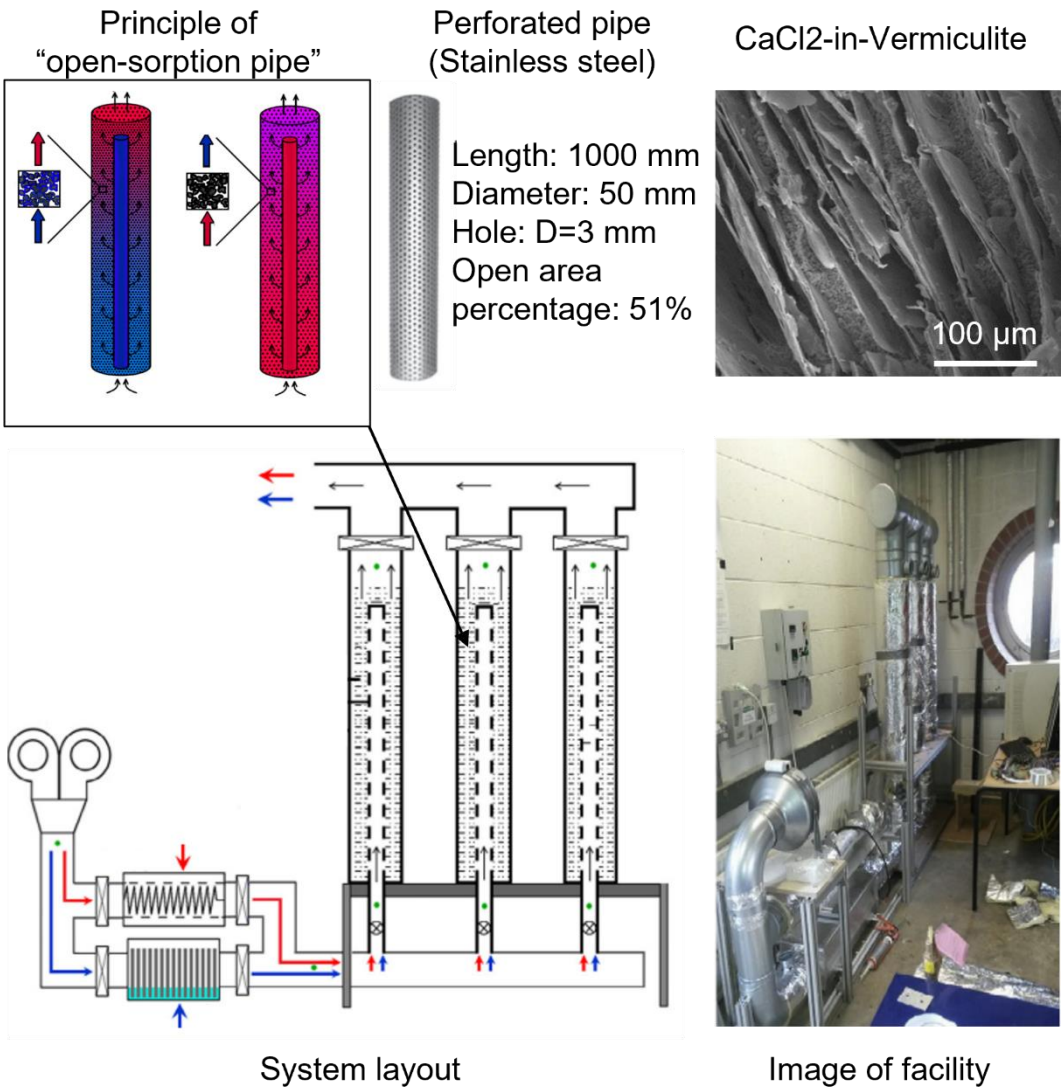


Figure 2-17 The experiments of “open-sorption pipe”.

In this device and system, the use of $CaCl_2$-in-Vermiculite and H_2O (in moist air) as working pair allows the operation temperatures between 20 and 80°C. By introducing a perforated pipe as a gas distributor in the middle of the reactor [206], the average specific discharge power increased from 0.09W/g [201] to 0.11W/g. Notably, the output temperature was increased by 10°C to the benchmark case [207], leading to warm air up to 50°C in the outlet.

Besides the reported open fixed bed reactor, there are a few studies gave

examples of moving bed devices [97], [208], [209]. Compared to the fixed bed, the moving bed has less TCM content staying in the reactor during charging/discharge, thus it has a faster temperature response and smaller pressure drop [210]. However, the materials issues were highlighted in the experimental study [97], mainly linked to the unstable solid flowing containing a large amount of caked pure salt and voids under the moist air. The moving bed employing composite as energy storage materials has not been reported yet.

As the vapour content fed to the TCM is often limited by the saturated vapour pressure of moist air, it is also possible to increase the system discharge power by increasing the mass flow rate. Accordingly, the pressure drops across the bed increases, which is undesired from the view of the practice. To further improve system performance, a fluidised bed reactor was proposed in many studies [188], [211]–[213]. The fluidised bed features a lower pressure drop than the fixed bed under the same flow rate, as shown in Figure 2-18a. It also features enhanced heat and mass transfer due to the strong mixing of particles.

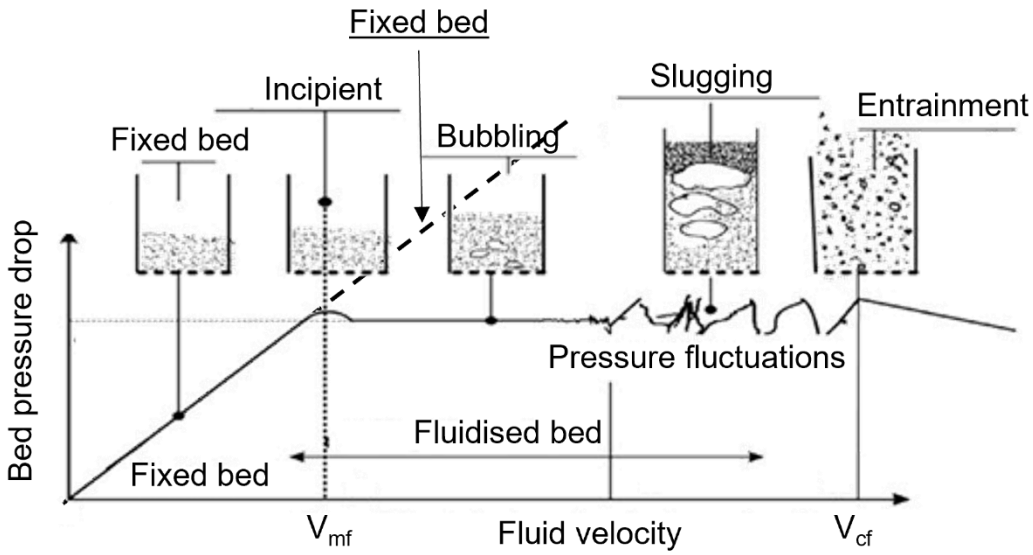


Figure 2-18 Basic of fluidised bed, the pressure drops according to flow regimes [214].

There is a rare case that studied the fluidised sorption thermochemical energy storage experimentally. A prototype fluidised bed containing at most 245g salt-in-silica gel as TCM was carried out by Skrylnyk et al., [215], as shown in Figure 2-19. The reactor consists of a cylinder of 4.5 litres in volume and 0.05m^2 in flow area. The maximum specific power reached at 0.4W/g (0.3 W/g on avg.) when using $CaCl_2$-in-Silica gel and moist air (30°C, vapour pressure at 16.1 mbar) flows at 215L/min (~0.07m/s). This study predicted the result of the up-scaled reactor. It is shown that the feasible energy storage densities are ranging from 50 to 90kWh/m^3, which was predicted to have a discharge thermal power at 1kW.

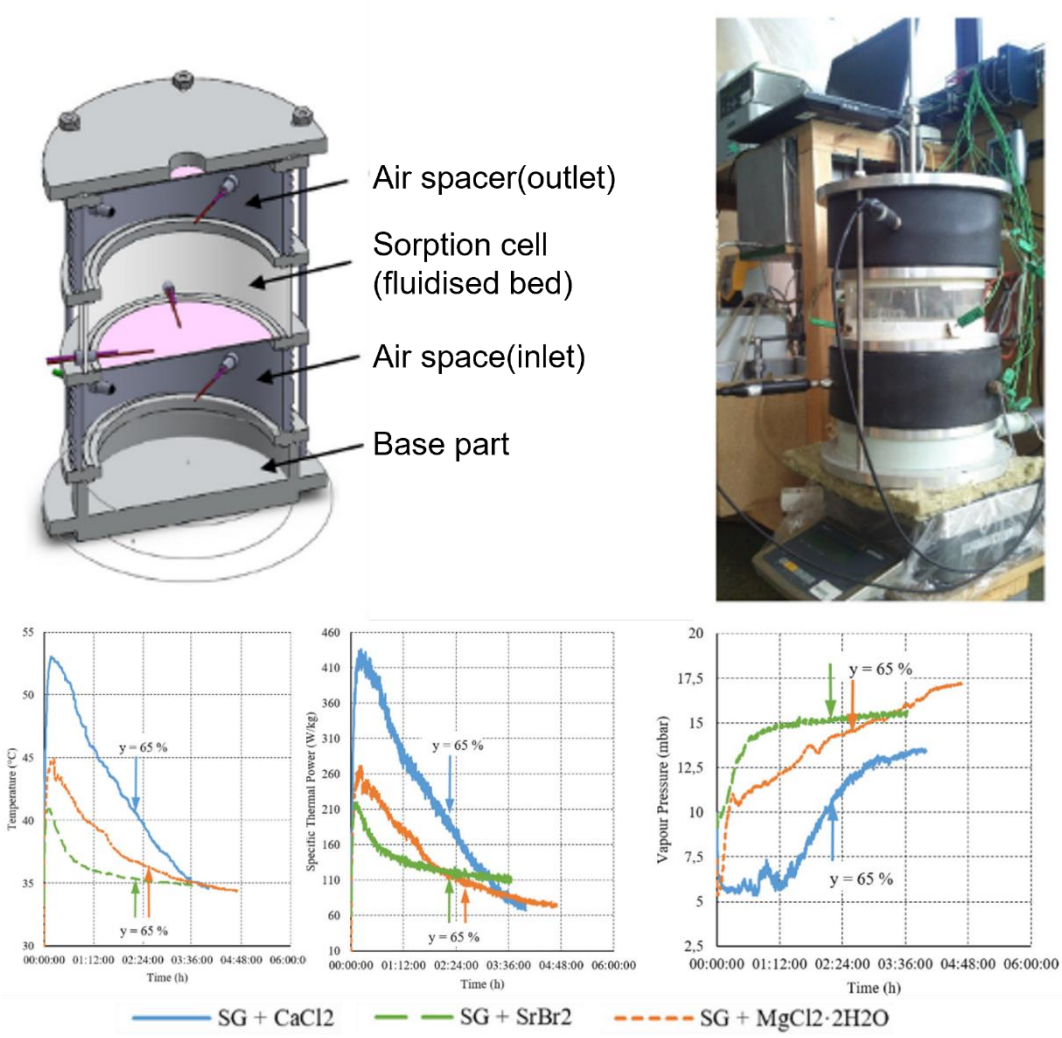


Figure 2-19 The TCS fluidised bed reactor prototype.

2.4.2 Coupled sorption heat storage with solar heat harvesting

There is a large volume of published literature studying the thermochemical energy storage of medium- and high-temperature solar heat [15], [216], especially focusing on particle-like materials handled by the fluidised bed reactors [211], [212], [217]–[220] and solar directly received by TCM [221]–[224]. However, for the low-temperature solar heat below 150°C, there is less attention is given. As mentioned before, the sorption heat storage by salts is suitable for storing low-temperature solar heat, due to the charging temperature

matching solar heat harvested by a non- or low-concentration system. Moreover, a theoretical study shows it is feasible to store solar heat by sorption technologies for a domestic dwelling in the UK[27]. It is also possible for inter-seasonal storage. The existing research on this aspect is mainly related to concept design [67], [225], [226] and experiments for decoupled TCS without solar input [200], [227]–[229]. So far, however, there has been little discussion about coupled TCS and solar harvesting.

2.5 Summary of the literature review

In this chapter, literature on the topics of thermochemical energy storage, sorption heat storage, and the materials and systems for sorption heat storage have been comprehensively reviewed. The focus is on identifying the challenges in using solid salt as the sorbent to store thermal energy harvested from solar via absorption processing and gas-solid reaction. The drawbacks at both the materials level and devices/systems level have been sorted out and discussed. The following observations are drawn:

1) Among all the three types of thermal energy storage technologies, thermochemical heat storage has the highest energy storage density, is energy loss-free during storage, and has the flexibility to discharge energy on demand. Thermochemical energy storage with absorption in solid salt is the lately developed and most promising technology in this catalogue.
2) The performance of salt-based thermochemical energy storage is typically

limited by the poor mass and heat transfer in solids. A possible way to enhance the performance is to form composites.

3) The composites of thermochemical salt are catalogued as “salt-in-matrix” and “encapsulated salt”. The existing studies mostly talked about the former. There has been little quantitative analysis of the latter.

4) The low- and non-concentrated solar system provides solar heat below 150°C, matching the charging temperature of TCS with sorption in salt hydrates. The existing study is mainly focusing on the TCS system individually. Very little is known about the coupled solar harvesting and TCS system in those conditions.

3. Formation of the W/O Pickering emulsion for encapsulating thermochemical salt

This chapter develops a Pickering emulsion template for encapsulating thermochemical salt and discusses the factors that affect the formation of the emulsions. Section 3.1 introduces the background and basics of Pickering emulsion. Section 3.2 describes the materials and experimental method. Section 3.3 discusses the result of experimental findings, focusing on how the nanoparticle assembled on the W/O interface. Section 3.4 concludes the findings in this chapter.

3.1. Introduction

Encapsulated salt is an emerging material for low-temperature thermochemical energy storage with sorption. Such materials combine conventional inorganic salt with chemical absorption in a highly tailored geometry to improve kinetic and stability. However, there are significant challenges in the fabrication of materials, particularly in terms of facile, low cost, and scalable. This chapter concerns a technology for fabricating the encapsulated salt from a Pickering emulsion template. A short review of the most relevant concepts and works is given in the following.

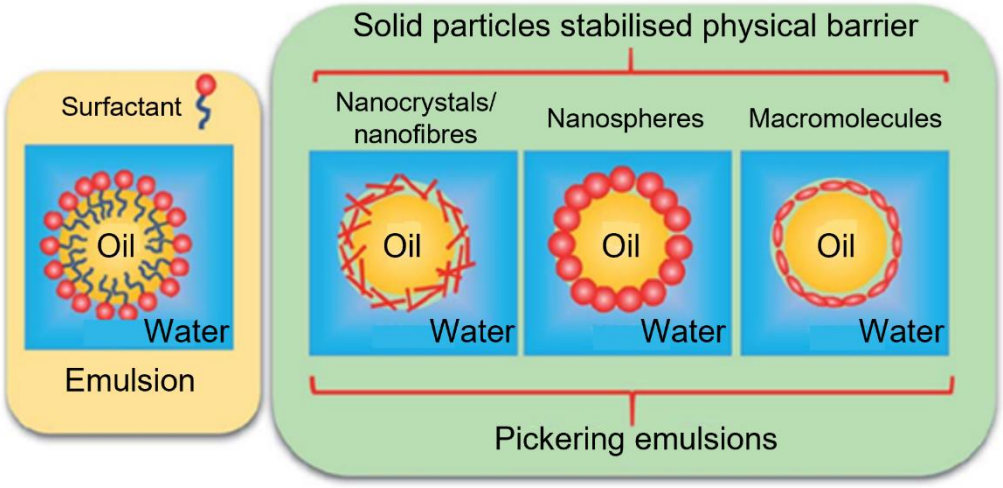


Figure 3-1 Schematic representation of surfactant stabilised emulsion and solid nanoparticle stabilised Pickering emulsions [230].

The “Pickering Emulsion” is a particle-stabilised emulsion consisting of one liquid dispersed in another immiscible liquid, as represented in Figure 3-1. The solid particle packed on the interface forms a physical barrier and prevents the

droplet from coalescence with another [230]. This point helps the Pickering emulsion overcome the thermodynamically unstable behaviour, which is unfavourable and be hardly avoided in the traditional molecular-stabilised emulsion [231]. Typically, the Pickering emulsion has superior stability to maintain the geometry [232]. Hence, such emulsions have drawn considerable attention in templated growth of functional materials [233]–[235].

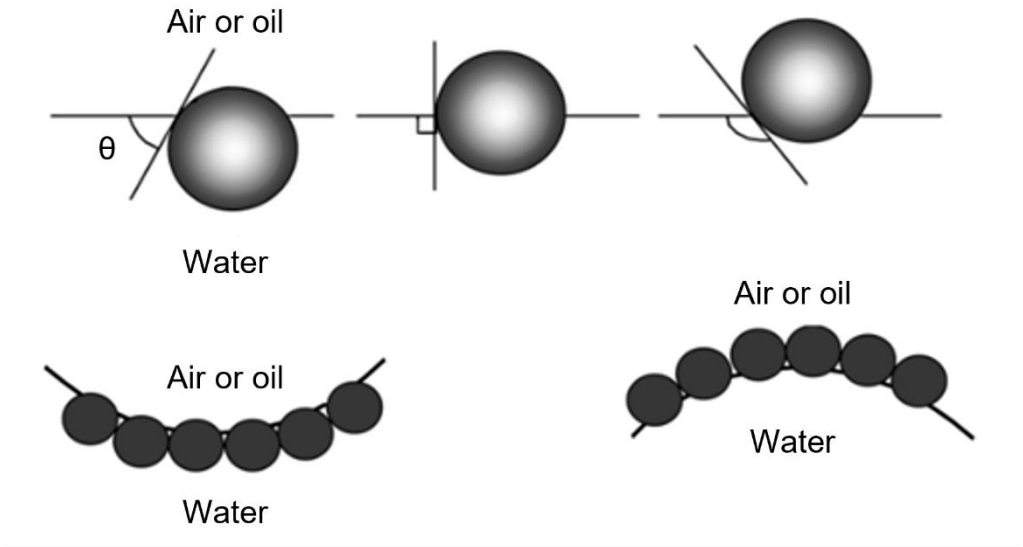


Figure 3-2 Position of the particle at a fluid-water interface for different contact angles θ and the corresponding positioning of the particle at a curved fluid-water interface [236].

Likely to the conventional molecular-stabilised emulsion, the Pickering emulsions are generally classified into two types: Water-in-Oil as known as W/O, and Oil-in-Water (O/W). Emulsion types are believed to be determined in some way by the bond position of the particle at the fluid-fluid interface [237]. As shown in Figure 3-2, when it has a three-phase contact angle θ <90°, the particle is hydrophilic and stabilizes O/W emulsions, whereas is hydrophobic

with a θ >90° for stabilising W/O emulsions. Those nanoparticles are closely or loosely packed in the interface and there are crevices or gaps between them. The chemical reaction can take place at the fluid-fluid interface in such crevices to grow solid substrate at a controlled rate and structure. Those features make the Pickering emulsions feasible to play a role as a template for encapsulation [238], [239].

There were many reports of encapsulation from Pickering emulsions. Radulova et al. reported a core-in-shell structure encapsulation of oils and fragrances from hydrophilic silica particles-stabilised O/W Pickering emulsion [240]. By thermally fusing the poly(glycidyl methacrylate) (PGMA) or polystyrene (PS)-stabilised O/W Pickering emulsion, microencapsulation containing organic phase change materials was demonstrated by Yin et al. [241]. Schoth et al. [182] presented a method to prepare nanocapsules from W/O Pickering emulsion, and demonstrated the encapsulation of inorganic salt as cargo. In the same way, Graham et al. [183] developed an all-silica encapsulation of inorganic salt-based phase change material, which was used for latent heat storage. Therefore, for encapsulating thermochemical salt, it is possible to design an appreciable W/O Pickering emulsion system and then develop a reaction to grow a continuous shell and bind the particle at the interfaces.

In this chapter, the target is to design water-in-oil (W/O) Pickering emulsions stabilised by low-cost nanoparticles as a novel encapsulation system. Firstly, the screening of nanoparticles and emulsification protocol was conducted. Then,

the chemical reaction conditions for encapsulation were experimentally studied. Meanwhile, it was found that a geometry and pH-based behaviour of particle adsorption. Furthermore, in-depth, the interfacial experimental and theoretical study explained the adsorption behaviour of nanoparticles in the fluid-fluid interface, which was also linked to the structure of Pickering emulsions.

3.2. Experimental section

3.2.1. Materials

Two kinds of silica nanoparticles were used in this study, both kindly provided by EVONIK. One of the nanoparticles was the hydrophilic fumed silica Aerosil A200, which has a primary particle diameter of 12nm, a specific area of 175-225m^2/g (BET), and density of Si-OH is around 1.8/nm^2 on its surface [242]. The other one was Aerosil R972 Pharma (R972), which is a hydrophobic fumed silica post-treated with dimethyldichlorosilane. As illustrated in Figure 3-3, the treatment results in most of the original Si-OH groups being replaced by Si-CH_3 groups, and thus the total Si-OH density on the surface of only ~0.5/nm^2 [243], [244]. This nanoparticle has a specific surface of 90-130m^2/g (BET) and a larger primary particle diameter of 16nm [245].

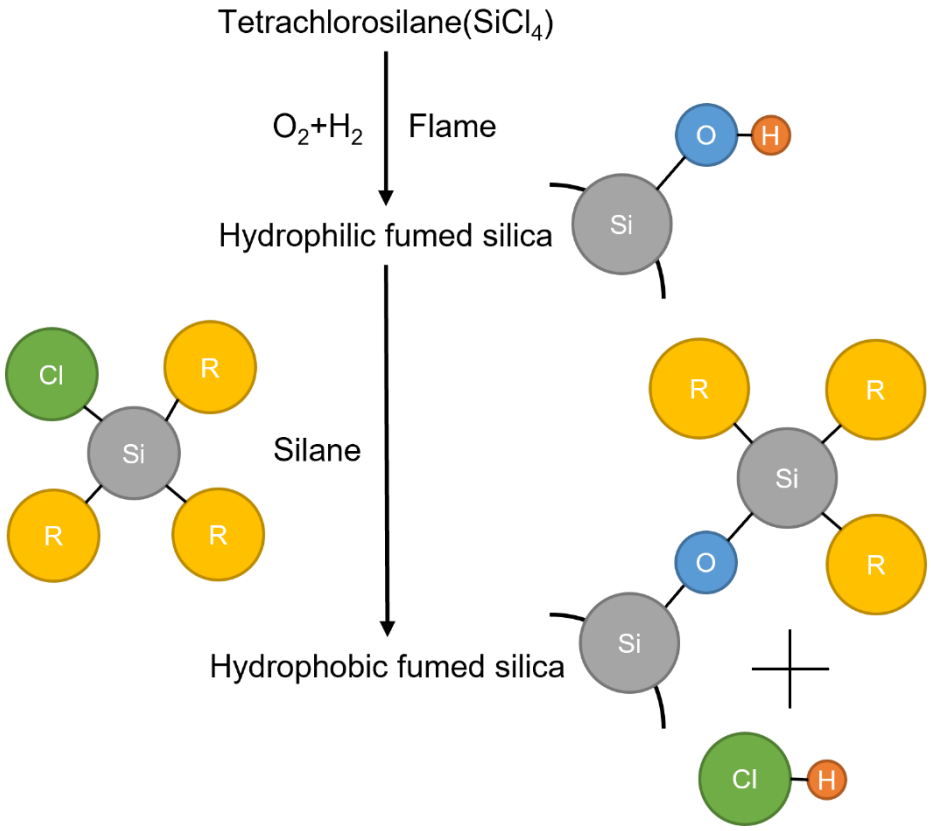


Figure 3-3 Synthetic silica nanoparticle with the different functional groups on the surface via flame pyrolysis [243], [244].

Cyclohexane (C_6H_{12}, 99%) was purchased from GREAGENT. Hydrogen chloride (HCl, 36%w/w in H_2O), Sodium hydroxide (NaOH, 99%) were purchased from ALADDIN. Tetraethyl orthosilicate (TEOS, $SiC_8H_{20}O_4$, 98%) was purchased from ENERGY CHEMICAL. Gellan gum (CAS:71010-52-1,99%) powder was purchased from MACKLIN. Water was obtained from a lab purification system, which has an electrical resistivity above 18 MΩ/cm.

3.2.2. Preparation and characterizations of the nanoparticle and suspensions

The nanoparticle suspensions were prepared by sonication dispersion [246]–

[248]. Typically, 160mg nanoparticle was added into 20ml cyclohexane, then processed in a sonication device (SCIENTZ IID, 20kHz, full power 600W, 6 mm diameter tip, China) for 2 hours (500W power used, 2s/8s on/off duty cycle) in an ice bath.

The size of the nanoparticle was measured by Dynamics Light Scattering (DLS) technique (BROOKHAVEN Instruments BI-ZetaPALS, United States). For each sample, the measurements were repeated 3 times.

The raw nanoparticle and suspension were spread on a silicon wafer and then coated by a ~2nm platinum in a sputter. The sample was then observed with a scanning electron microscope (TESCAN Mira3, operating at 15kV, image mixed by in-beam SE and SE signal).

The surface groups on the nanoparticles, Aerosil A200 and Aerosil R972 Pharma, were examined by using Fourier-transform infrared spectroscopy (FT-IR). The measurements were performed on a spectrometer (BRUKER Vertex 70v, Germany) equipped with an attenuated total reflectance (ATR) module. The nanoparticle powder was dried in an oven at 200°C and pelleted to a size of approximately (Diameter)8*(Height)2mm. The measurement was carried out under either atmospheric or vacuum (~100 Pa) conditions to avoid the influence of moisture in optical path and to enhance the signal of possible -OH group.

The rheological properties of the suspensions were measured by a rheometer (NETZSCH Kinexus lab+, United Kingdoms) with a rotator-cup geometry (DG 26.7) at 25°C. A viscosity test with a linear shear rate table was firstly conducted,

with the shear rates running from 0.1/s to 1000/s. An oscillation test was performed in the following, with the sweep amplitude varied from 0.1% to 100% at a constant frequency of 1Hz.

3.2.3. Study for the formation of a Pickering emulsion

The most conventional way of producing Pickering emulsion is to simultaneously emulsify a suspension of nanoparticles and another immiscible liquid, as illustrated by the route 1 in Figure 3-4. In the emulsification, the strong mechanical pressure forces the nanoparticles flowing towards the established W/O interfaces, which is also generated by mechanics. This results in the nanoparticles being adsorbed at the interface.

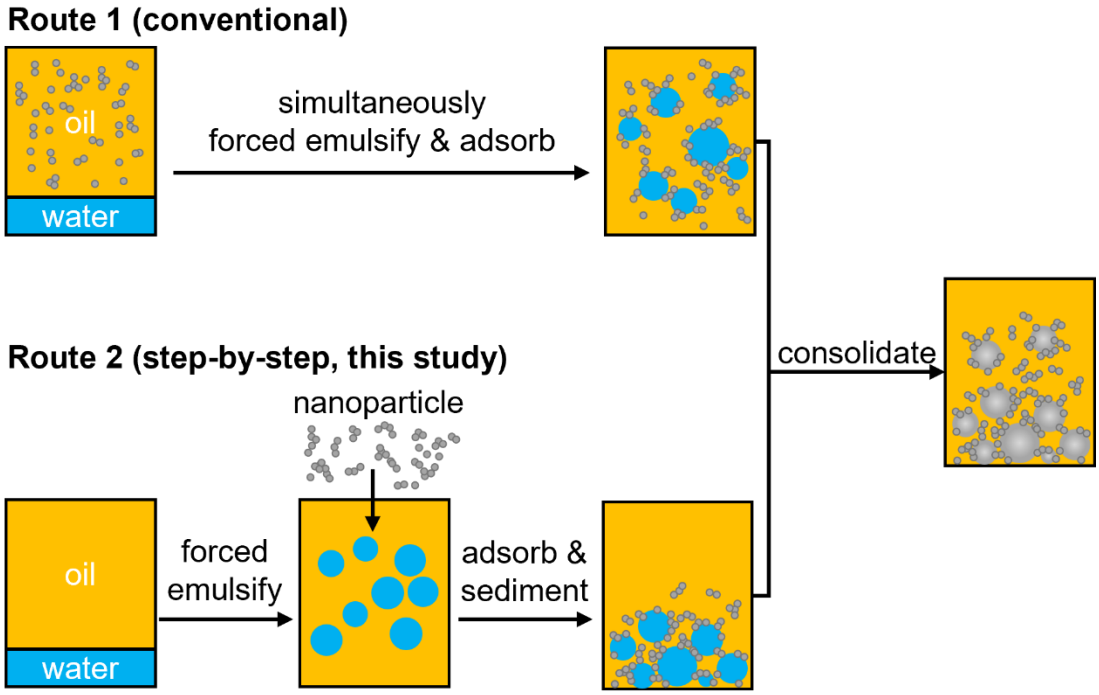


Figure 3-4 Two kinds of emulsification route to create micro-emulsions.

However, to produce a micro-emulsion, it is essential to apply a stronger

mechanical stirring, for example using sonication, to create the drops below microns. Such strong mechanical forces makes it difficult to determine the other weaker interactions, like electrostatic and van der Waals between the nanoparticles and the drops. Therefore, we intend to use another route with a step-by-step emulsification to study the behaviour of nanoparticles dominated by the weak forces. This route is modified from the original proposal by Larson-Smith [249] and is illustrated as the route 2 in Figure 3-4. The bare water/cyclohexane emulsion was prepared by sonication processing the mixture of 100μL water and 10mL cyclohexane (1% by volume) for 5 mins (500W power used, 10s/10s on/off duty cycle). The droplet size of as-prepared emulsion was measured by DLS immediately. After a standing of 30 mins, the emulsion was observed under a Confocal Laser Scanning Microscope (CLSM, LEICA sp8, 485nm laser, Germany) with use of a dye (Rhodamine B, 5μg/mL water). As the dye may influence the interface, the Pickering emulsion was prepared on the base of the bare water/cyclohexane emulsion without the use of dye. The nanoparticle suspension was immediately added to these bare emulsions with different preparation conditions, followed by a slight hand swing to mix them well.

3.2.4. Fabrication of the empty silica encapsulation from emulsion

The direct observation of micro- and nano-emulsions is challenged by the spatial resolution limitations of the optical microscope, and without the dye

which is necessarily used for fluorescence imaging and super-resolution microscopy. Therefore, we proposed a new technique to observe the fine emulsion by reaction-consolidating a dilute emulsion, and then observing the consolidated structures under a SEM. This method is also illustrated in Figure 3-4. The consolidated emulsions were formed by slowly growing a continuous silica layer on the surface of aqueous droplets in W/O emulsions [183], [250]–[252], involving the TEOS hydrolysis, condensation, and fix the nanoparticles. The pH of the aqueous phase was adjusted by 1M HCl or 1M NaOH to pH=2 or pH=12, to catalyse the hydrolysis.

3.2.5. Study for the Interactions between nanoparticle and W/O interface

Several nanoparticle-interface studies at different scales have been carried out to provide further evidence for this self-assembly behaviour of nanoparticles at the W/O interface.

The sessile drop technique was used to measure the contact angles of water (with different pH) on the nanoparticle aggregates in macroscale. The measurements were taken place on a thick film of nanoparticle spread on a silica wafer or a pressed pellet of nanoparticle.

For determining the dynamic of nanoparticle interacted with the bare W/O interface, pendant drop experiment was carried out by hanging a 30μL water drop in cyclohexane with/without dispersed nanoparticle. The Worthington number in experiment is approximately at 0.55, which is sufficient for a good

result [253]. The dynamic interfacial tension was analysed by solving the Laplace-Young equation with the geometry from the continually captured optical images (Biolin Scientific Theta Flex, stainless steel needle with inner diameter at 0.8mm, United States). All measurements were carried out in a gas-tight glass cuvette of dimensions 10 mm x 10 mm x 30 mm. As a result, the volume change of drop was less than ±5% during the measurement. Besides, the static interfacial tension of water/cyclohexane was measured by using Wilhelmy plate method in a force tensiometer (KRÜSS K100, platinum plate, Germany).

Contact angles of individual nanoparticle at the interface was determined by using Gel Trapping Technique (GTT) [254]–[256]. As illustrated by Figure 3-5, the technique relies on gelling the aqueous phase with a non-adsorbing gelling agent, which allows the liquid interface with the adsorbed particles to be replicated with curable polydimethylsiloxane (PDMS). The PDMS replica consists of the liquid interface with the partially embedded particles. The particles position and orientation at the original interface is measured by observation at a very high resolution with a SEM.

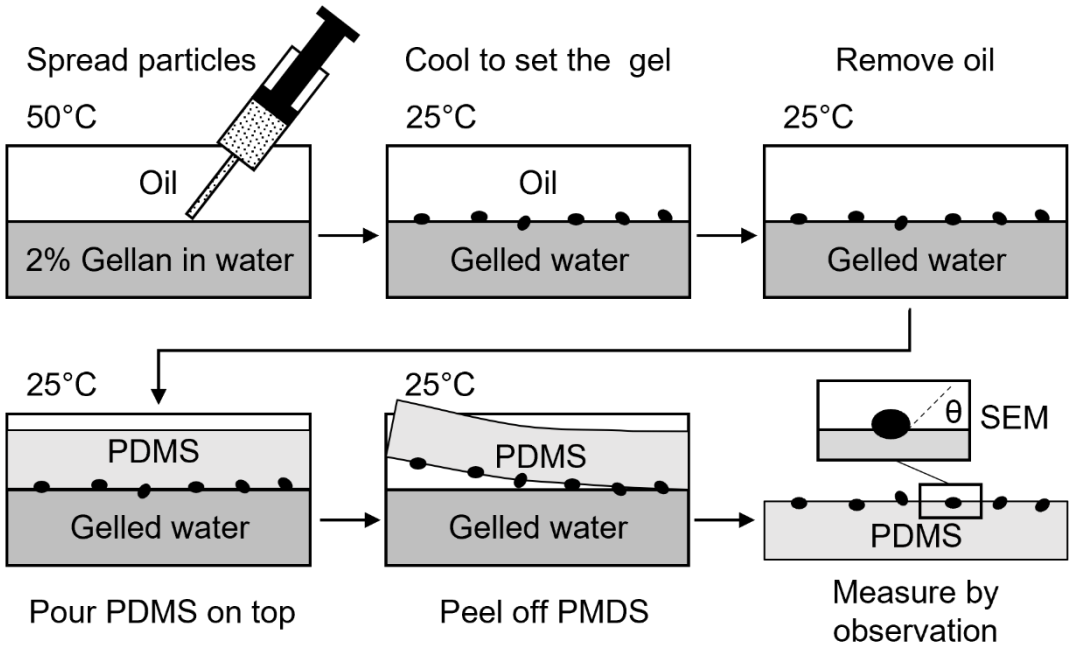


Figure 3-5 Schematic diagram of the gel trapping technique “GTT” for measuring contact angles of a nanoparticle at an oil-water interface.

For measuring the surface electrical charge of nanoparticles, the Phase Analysis Light Scattering (PALS) technique[257] was employed, which is eligible for determining the electrophoretic mobilities of a weakly charged colloid in nonpolar media. The R972 nanoparticle was dispersed in ethanol or cyclohexane at a concentration of 8mg/ml. The suspensions were measured by a zeta potential analyser (BROOKHAVEN Instruments BI-ZetaPALS, United States) equipped with a palladium electrode at 25°C. In the ethanol case, the standard voltage of 4.0V (1100V/m) with a frequency at 10 Hz was applied to the electrode. In another case, the applied voltage increased up to 12V (3300V/m) and 2Hz was used for obtaining reproducible results. The measurements were repeated nine times in each case.

3.3. Result and discussion

In this part, the results and discussions are structured in the five parts: a) the basic characterization of the nanoparticle and the suspension; b) a screening for the protocol of preparing emulsion; c) the detailed results of nanoparticle interacting with the bare emulsion interface; d) a size-selective self-assembly behaviour of nanoparticle is presented; e) the interaction between hydrophobic nanoparticles and bare water droplets is analysed in DLVO framework.

3.3.1. Nanoparticle and suspensions

In Figure 3-6a and b, the high-resolution SEM images clearly show the morphology of nanoparticles. The size of the nanoparticle is in consistency with the data provided by the manufacturer and the value in the references. One can see the primary particle is an irregular sphere and intensively aggregated. The large aggregates are unfavourable for forming the Pickering emulsions. Thus, it is necessary to be broken, e.g., by sonication dispensing. Furthermore, the major difference between the studied nanoparticle is in the wettability, which is differing from the functional group on the surface. The A200 silica nanoparticle is hydrophilic due to the existence of Si-OH, as evidenced by the FT-IR peak around 970cm^{-1} (Figure 3-6c), regarding its stretch vibration. These results also match those observed in earlier studies [258]. In another case of R972, the Si-OH peak nearly vanishes. Unfortunately, the hydrophobic group Si-$(CH_3)_n$, which was supposed to be presented at around 800cm^{-1} and 1260cm^{-1} in the

infrared absorption spectrum [259], is hard to be recognized from the overlapped Si-O vibration peaks.

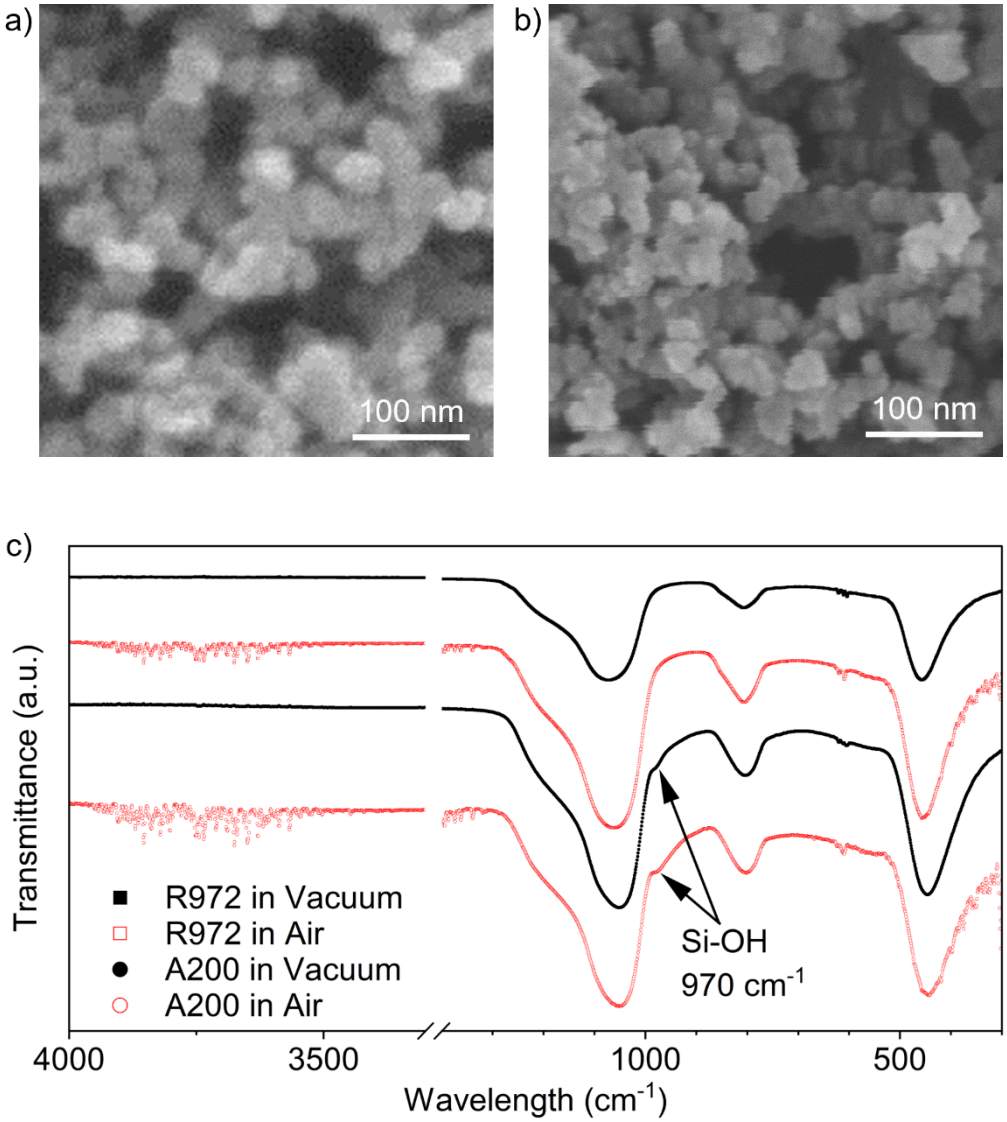


Figure 3-6 The SEM images of the nanoparticles a) R972 and b) A200. c) The FT-IR spectrum of the nanoparticles.

The effect of sonication dispensing was quantitatively examined by the DLS, as the result is shown in Figure 3-7. Due to the de-aggregated of large agglomerate, the median size of the nanoparticle decreased from ~5μm to ~1μm.

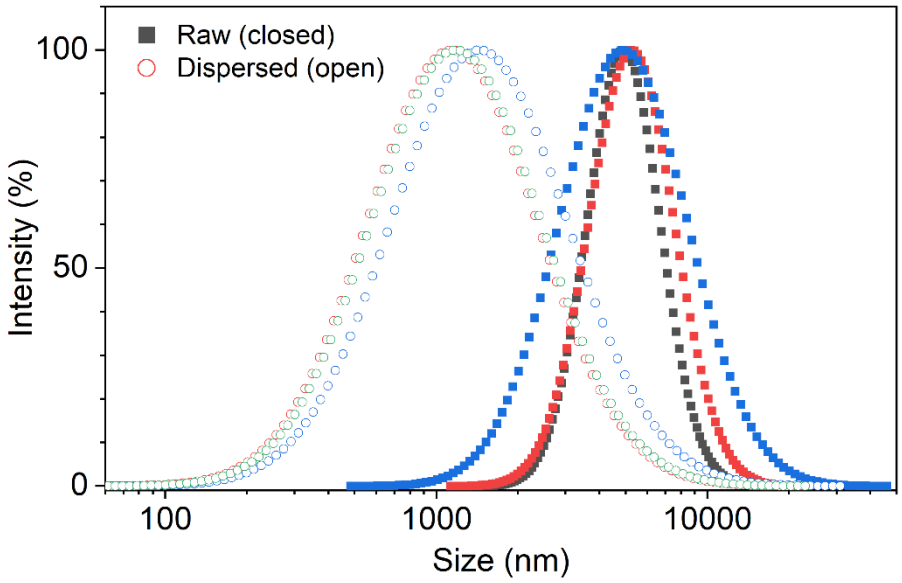


Figure 3-7 Size of raw and sonication dispersed R972 nanoparticle measured by DLS.

Moreover, the morphology of raw and dispersed nanoparticles is compared in Figure 3-8. One can see most of the large clusters in the raw materials (Figure 3-8a) were broken into aggregates (Figure 3-8b). The aggregates (insertion of Figure 3-8b) are the minimal unbroken unit of silica nanoparticles. It consists of decades of primary nanoparticles and has a branched rod-like shape with a diameter of around 50nm and a length of 200-300nm. Those values are consistent with those reported in the references [260], [261].

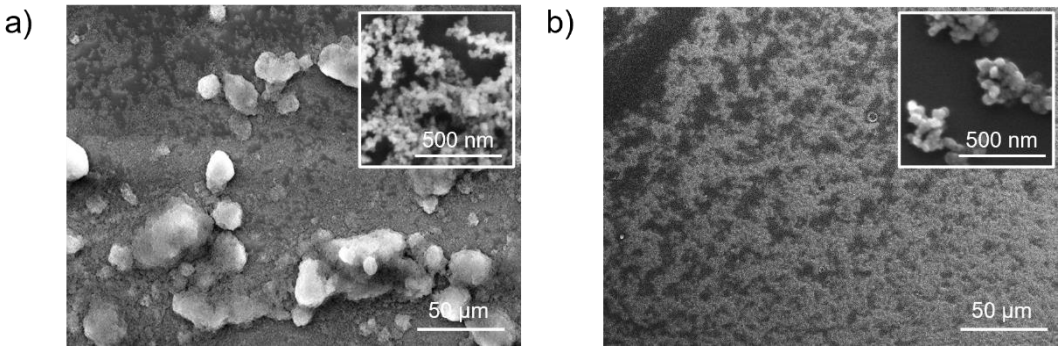


Figure 3-8 SEM images of raw and dispersed R972 nanoparticle.

In Figure 3-9, the suspension containing 10mg/ml raw and dispersed nanoparticles is compared in rheological behaviour. In the linear test result (Figure 3-9a), both suspensions show the shear thinning behaviour, which is explained by the particle re-orientation according to shear force and the breakup of the large agglomerates. The viscosity of suspensions is also in agreement with those reported in reference [262]. In the oscillation result (Figure 3-9b), a linear viscoelastic area from deformation rate γ =0.1% to 3% was determined, suggesting a gel-like behaviour in this condition, attributed to the 3-D network structure of the silica aggregates. With increased the γ, both suspensions show a transition of G' (storage modulus) dropping below G'' (loss modulus), referring to the destruction of the network. One can see a larger G' and a delayed transition in raw nanoparticle suspension, as the result of the stronger network made of silica agglomerates.

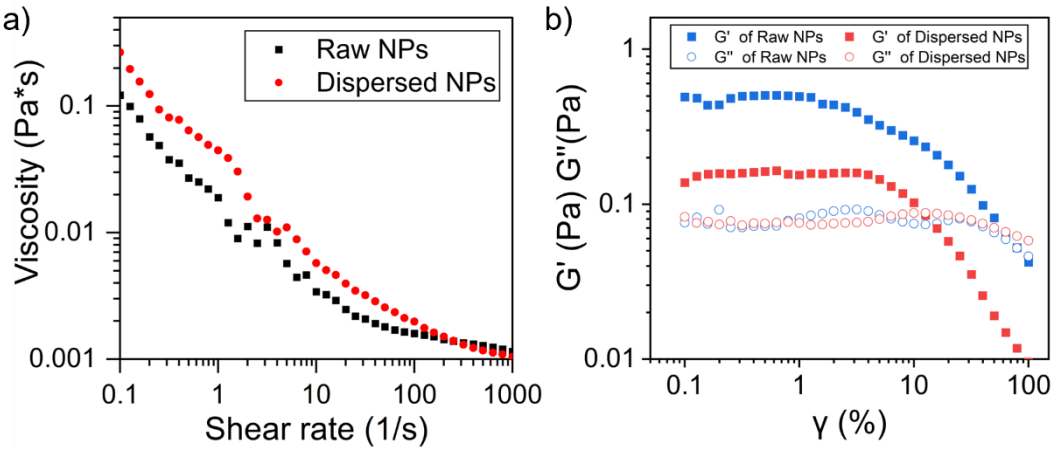


Figure 3-9 Rheological study of suspensions, a) linear test and b) oscillation test.

3.3.2. Screening the protocol of encapsulating from emulsion

The encapsulation protocol was considered as two parts: the formation of W/O emulsion, and the growth of shell on the interface. For the former, there were two factors were further studied: the effect of particles wettability, and the orientation of the particles adsorbing to the interface (particle approaching the interface from the water side or oil side). The experimental conditions and results are listed below.

Table 3-1 The conditions and results of emulsions preparation protocol

Sample	Aqua phase	Oily phase	Result
1	A200 in Water	Cyclohexane	No emulsion
2	Water	A200 in Cyclohexane	O/W Emulsion
3	Water	R972 in Cyclohexane	W/O Emulsion
4	R972 in Water	Cyclohexane	Unable to be dispersed in water

The prepared emulsions are presented in Figure 3-10. For the successfully emulsified samples 2 and 3, it clearly showed that the emulsion type (W/O or O/W) is strongly related to particle wettability. These results corroborate the findings in the previous studies [237], [263], [264]. However, while dispersed in the aqua phase, the hydrophilic nanoparticle is unable to be adsorbed on the interface to form a stable emulsion. As the lack of further detailed experimental results, the reason for this is not clear but a possible explanation is due to electrical repulsion between nanoparticle and interface [265], [266]. As a result,

for encapsulating the thermochemical salt, the W/O emulsion (sample 3) is the only candidate as the template.

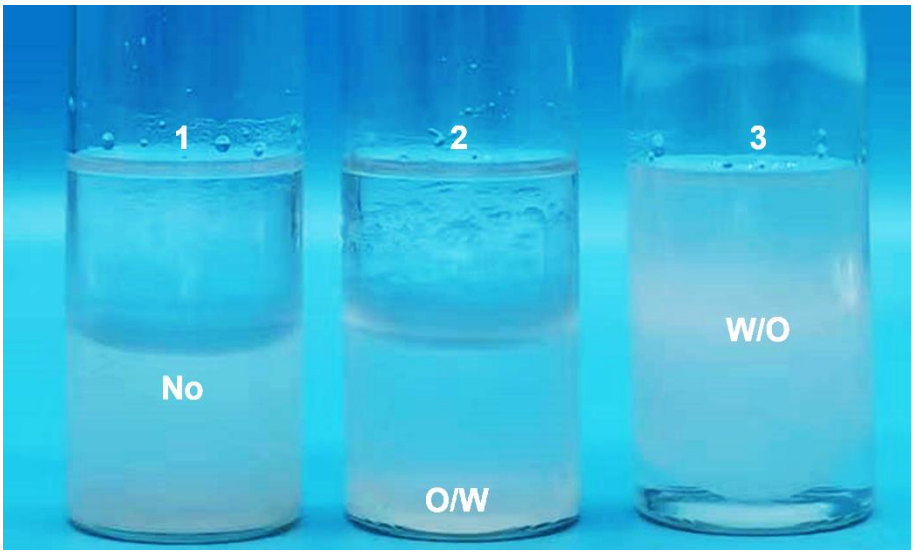


Figure 3-10 Photo images of prepared emulsions.

Returning to the topic of shell growth, a well-known sol-gel reaction of siloxane hydrolysis [267]–[271] was proposed in this study. The silica encapsulation from bare W/O emulsion was studied, as the result is shown in Figure 3-11. The fresh emulsion prepared via sonication had a mean diameter of 258nm, which is close to the reported value [272]. In the following, the droplet was coalescing after 30mins, until the merged droplet sedimented on the bottom of the glass vial and stopped moving. This is evidenced by the large droplet observed with CLSM, see Figure 3-11b. After the TEOS was introduced, the continuous silica (SiO_2) shell formed at the position of the interface, and the encapsulation inherited the sphere geometry from the droplet (Figure 3-11c). The composition of the SiO_2 was further confirmed by the EDX result (Figure 3-11d).

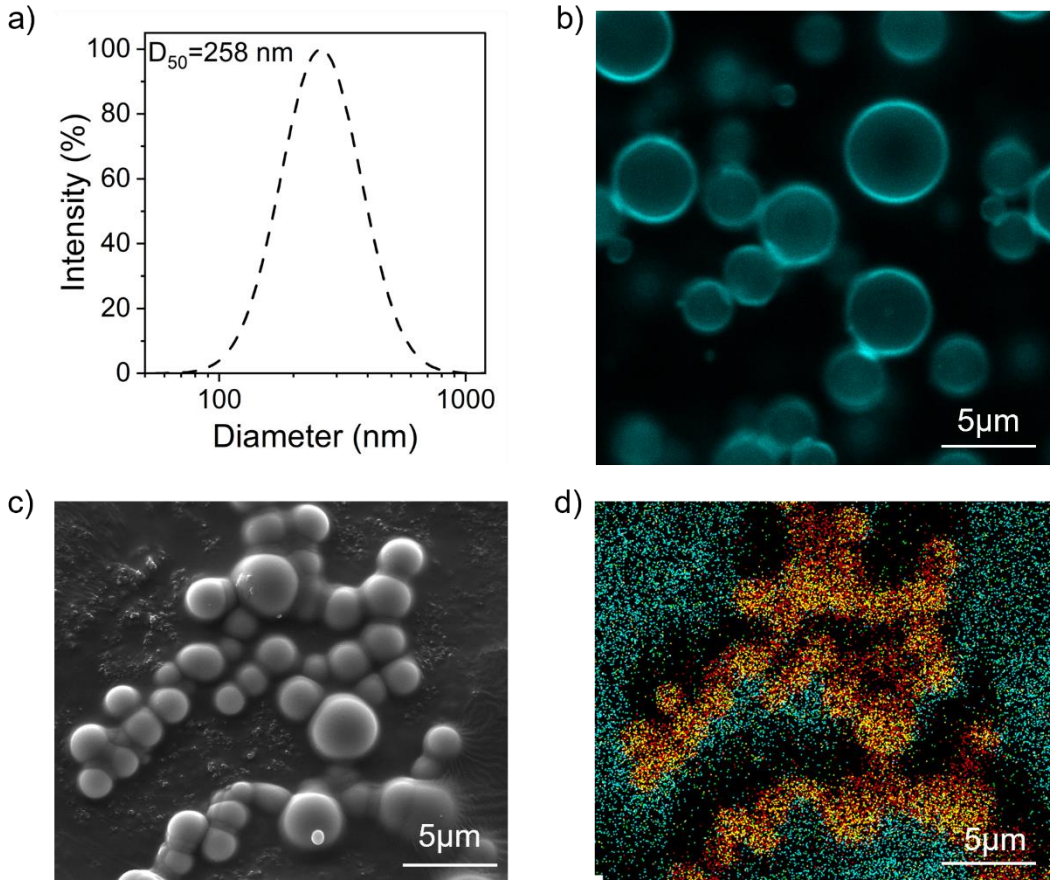


Figure 3-11 Result of silica encapsulation from bare W/O emulsion, a) the size distribution of fresh emulsion, b) the CLSM image of the emulsion after settling for 30 mins, c) the SEM image of silica encapsulation, d) the Energy-dispersive X-ray spectroscopy (EDX) colour mixed elements mapping of silica encapsulation, blue for carbon (substrate was carbon tape), yellow for silicon and red for oxygen.

The encapsulation from the Pickering emulsion was prepared by introducing the same amount of TEOS to the selected W/O Pickering emulsion in the same water and oil volume. For comparing the encapsulation with those from bare emulsions, vigorous shaking was employed to generate a droplet with a similar size in Pickering emulsion. The encapsulation from the Pickering emulsion containing the aqueous phase with different pH is presented in Figure 3-12. In

the condition of pH=2, the desired encapsulation was formed with the nanoparticle-stabilised interface. In other results, it is surprising that the nanoparticle was outside the droplet, and formed “honeycomb-like” aggregates, which trapped the drops only.

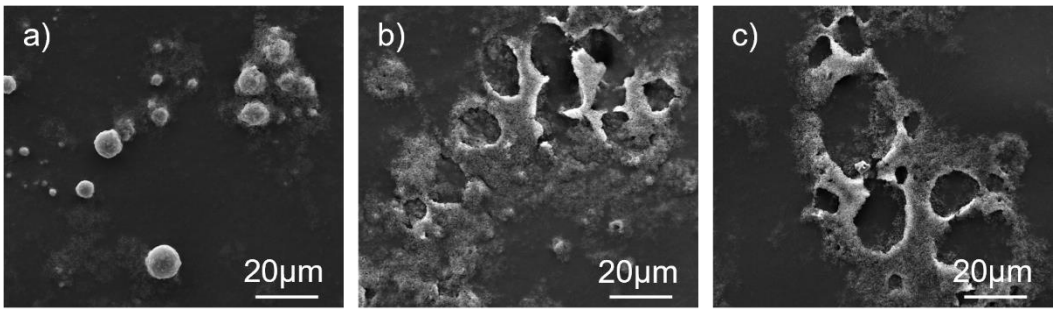


Figure 3-12 The SEM images of encapsulation from the aqueous phase with different pH, a) pH=2, b) pH=7, c) pH=12.

3.3.3. Assembly behaviour of hydrophobic nanoparticle to W/O interface

Figure 3-13 shows a full picture of the encapsulations. A drop-size-related nanoparticle absorption is observed in the SEM images. One can see a little nanoparticle attached to the small encapsulation (Figure 3-13b). In contrast, for the drops larger than 2μm (Figure 3-13c), intensive nanoparticles were found on the surface of the drops. Those nanoparticles were partially embedded in the silica layer (see the insertion in Figure 3-13c), indicating that the absorption of nanoparticles in the W/O interface was originally existing in the emulsion.

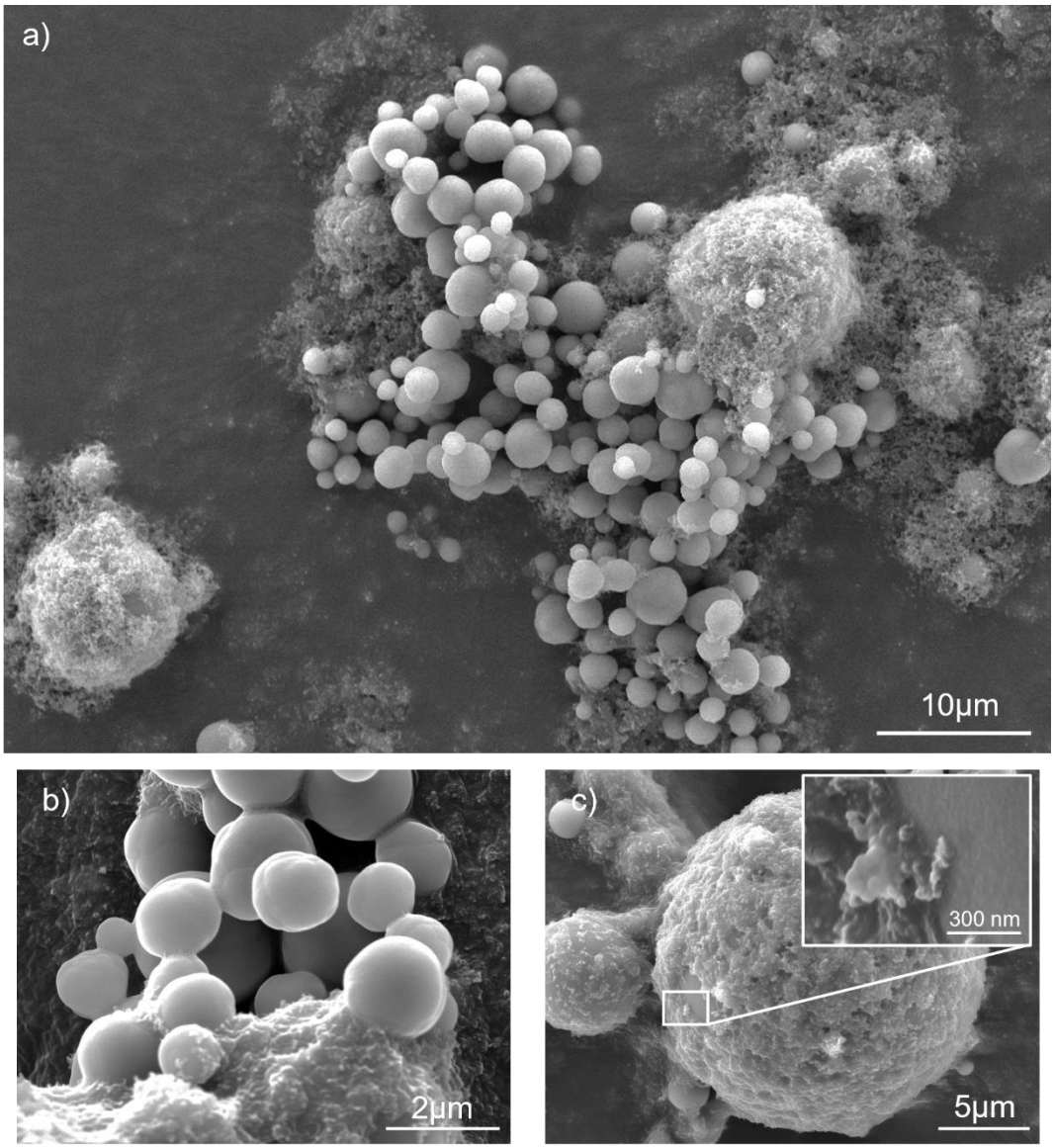


Figure 3-13 a) The SEM image of encapsulations from Pickering emulsion containing aqua phase with pH=2, 10mg nanoparticle in 10mL oil for 100uL water, b) zoomed-in image of the small droplet, c) the large droplet.

This point is also confirmed by the high-resolution CLSM image of the emulsion (Figure 3-14). The shape and position of the W/O interface were identified from the bright field image. Furthermore, as labelled by Rhodamine B, the absorption of nanoparticles in the W/O interface is observed in the laser-induced fluorescence (LIF) image (Figure 3-14b).

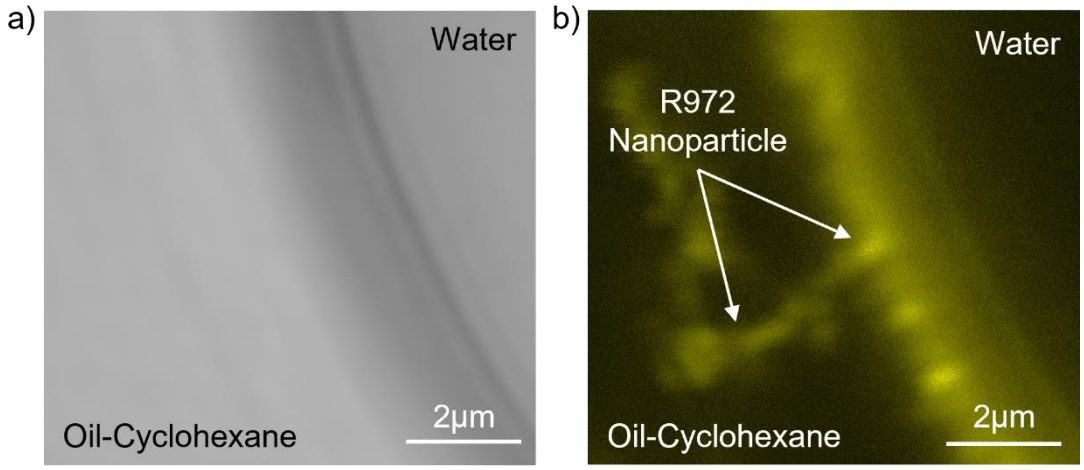


Figure 3-14 Images captured with CLSM, a) the bright field image b) laser-induced fluorescence (LIF) imaging, the nanoparticle and interface were labelled by Rhodamine B.

The drop-size-related nanoparticle absorption was also observed in the emulsions with the increased number of nanoparticles (see Figure 3-15). This suggests that the attractive force between nanoparticles and water drops is geometry related, while the concentration of nanoparticles may contribute a little.

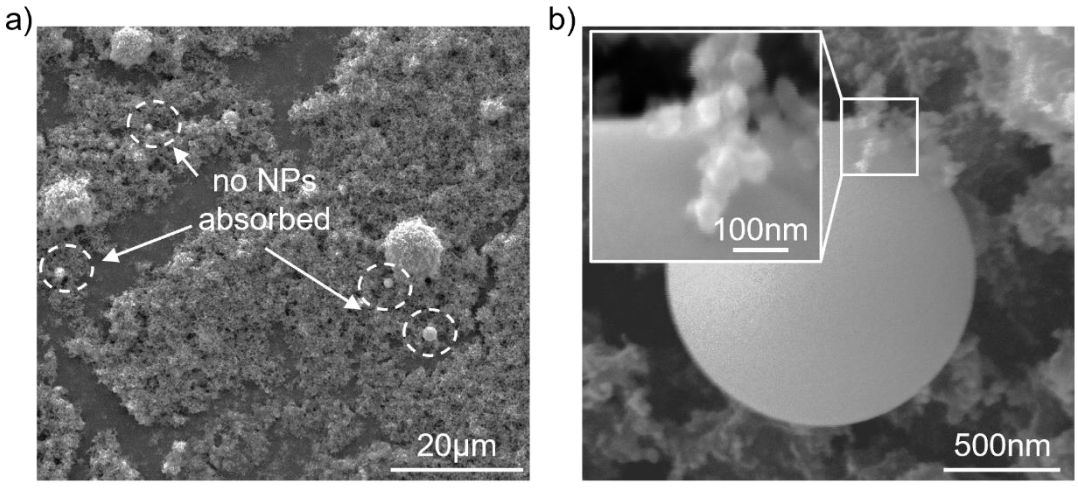


Figure 3-15 encapsulations from Pickering emulsion with high nanoparticle

concentration, 100mg nanoparticle in 10mL oil for 100μL water, a) Low-magnification, b) High-magnification SEM image.

3.3.4. Interactions between nanoparticles and droplets

Multi-scale studies have been carried out to determine the interaction of nanoparticles with water droplets, with the aim of understanding the underlying mechanisms of the above phenomena.

In Figure 3-16, the results of the sessile drop measurement confirmed the hydrophobic wettability of the nanoparticle, in which the contact angle was 130-140°. Besides, it was supposed that the pH may take a major effect on the attachment of nanoparticles to the interface, leading to the different structures of encapsulation as mentioned in Figure 3-12. Consequently, it was expected to be detected a monotonous increase in contact angle according to the pH grow up. Unfortunately, such a trend was not recognized in the measurement results. It is probably due to the surface roughness-induced uncertainty being considerable.

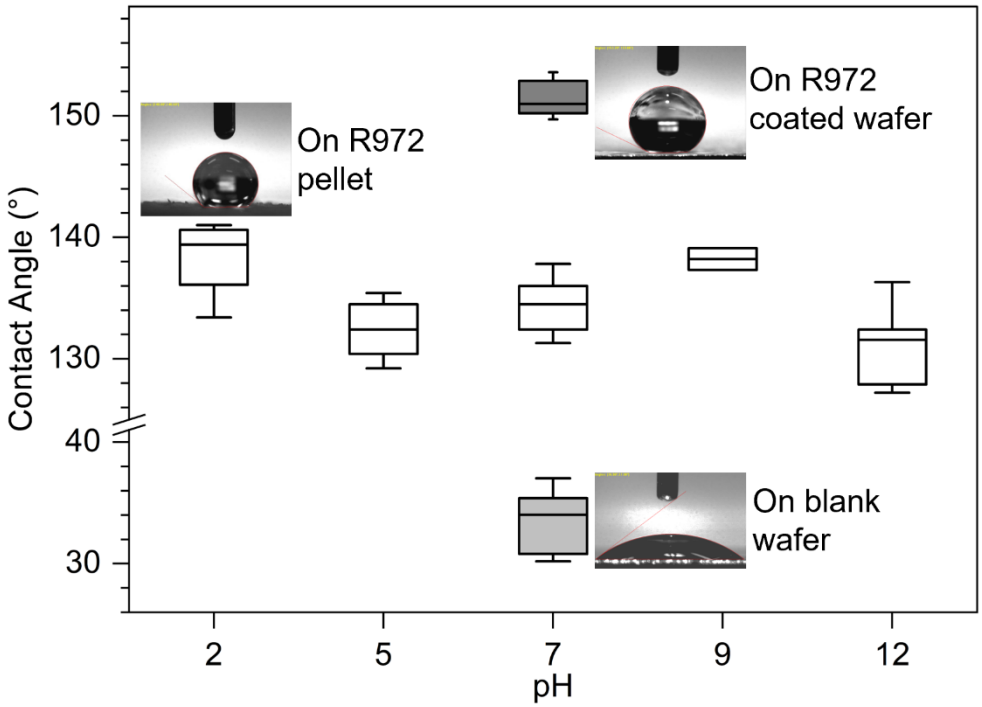


Figure 3-16 Sessile drop measurement for determining the contact angle of nanoparticle aggregates.

Therefore, for obtaining a more convincing result, the three-phase contact angle of the induvial nanoparticle was further measured by “GTT” with SEM, as shown in Figure 3-17.

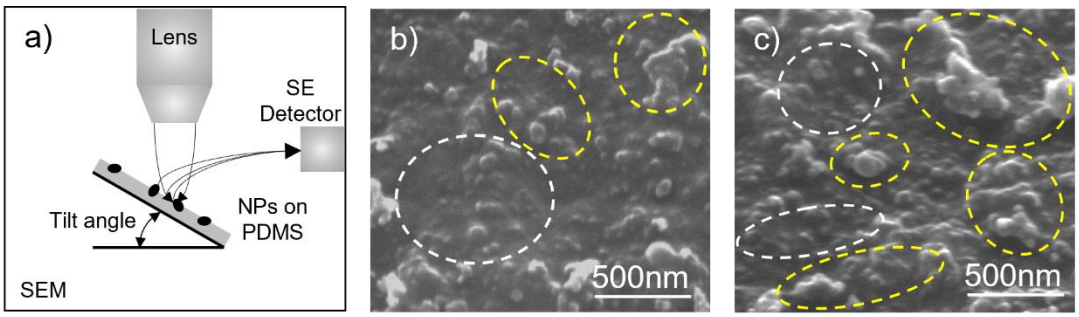


Figure 3-17 “GTT” measurement for the three-phase contact angle of individual nanoparticle, a) observation configuration, b) SEM image with tilt angle at 15°, C) SEM image with tilt angle at 30°.

Generally, the SEM images show two types of absorbed particles: the small nanoparticle (in white circle) have a typical contact angle above 120°, and the large agglomerates (see particles in yellow circle) have most of their body immersed in the water side (contact angle less than 90°).

Alternatively, by monitoring the interfacial tension, pendant drop is a useful technique to study the dynamic of the spontaneous adhesion of nanoparticles to the W/O interface. As the result shown in Figure 3-18a, compared to the initial image, the shape of the water drop was elongated at the end of the measurement, due to the interfacial tension change.

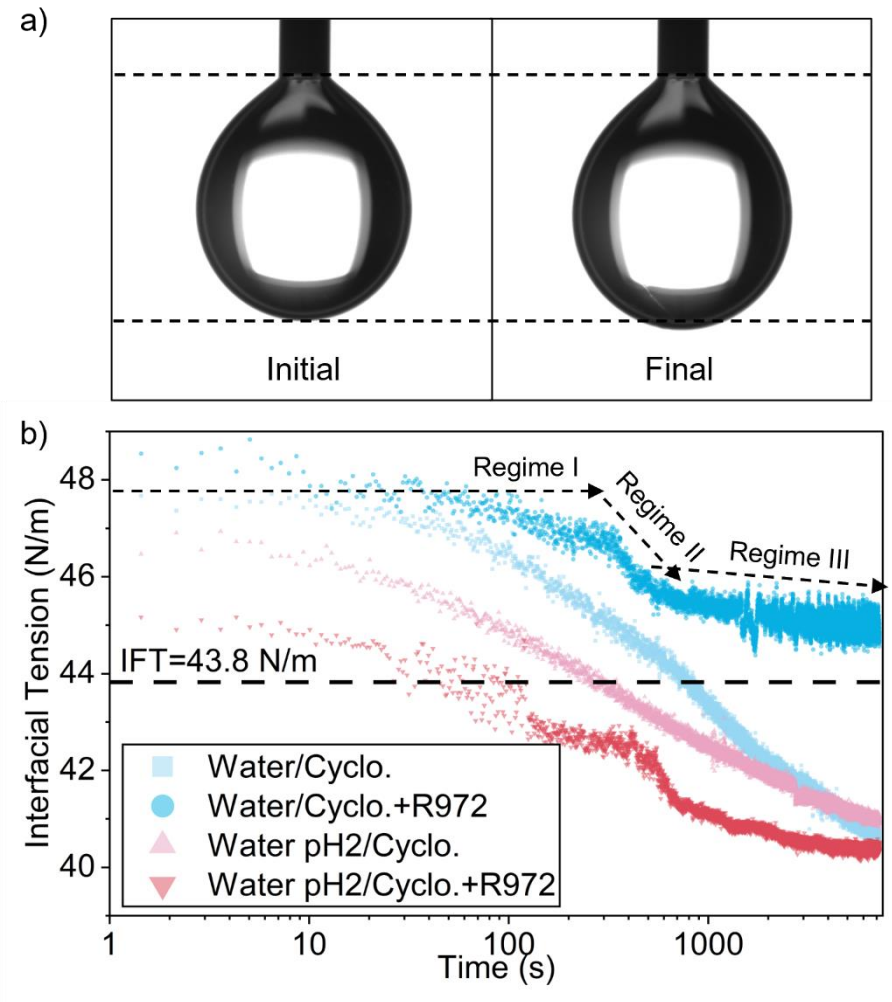


Figure 3-18 Pendant drop measurement for dynamic absorption of nanoparticle to the W/O interface

In Figure 3-18b of the logarithmic profiles of dynamic interfacial tension, all the cases show that there has been a continuous reduction in interfacial tension, possibly due to residual impurities [253] or mutual dissolving of cyclohexane and wate [273], [274]. Particularly, in the nanoparticle-involved cases (dark blue and dark red curves), there was an additional sharp reduction starting at ~300s to ~400s, whereas the curves are smoothing in the no nanoparticle cases (light blue and light red). It is suggesting that the nanoparticle was rapidly absorbed in the W/O interface during this period. This dynamic agrees with typical three-regime absorption progress reported in the literature [275], as labelled in Figure 3-18b. In regime I, the interfacial tension was not appreciably reduced, because it was dominated by the bare W/O interfacial behaviour and initial condition. In regime II, the nanoparticle starts to be absorbed in the interface, and causes an accelerated decrease in tension at a rate of $-(E_d/A)\,dN_p/dt$, where the (E_d/A) is the absorbed energy of nanoparticle in a specific area and dN_p/dt is the absorption rate of nanoparticles [276]. This regime ended with the nanoparticle monolayer saturation in the interface, as illustrated in Figure 3-19a. In the last regime III, the nanoparticle was gelation or aggregated in and near the interface, resulting in a slower reduction in interfacial tension. Surprisingly, the interfacial tension is found to gradually reach a plateau in the case of pH=7 water with the nanoparticle, and the final value was higher than the bare W/O

interfacial tension of 43.8N/m (measured by tensiometer). It is probably because the nanoparticle may finally aggregate near the interface without contacting with the absorbed nanoparticle or interface, rather than keep absorbing in the interface. These aggregates were positioned where the subjected forces were balanced, and blocked the absorption of nanoparticles to the interface, as illustrated in Figure 3-19b. This structure can be also proved by the consolidated morphologies as mentioned above (Figure 3-12b and c), in which the water drop was separated from the surrounding nanoparticle aggregates. Moreover, the present findings are consistent with other research which identified a similar network structure in O/W emulsion [277].

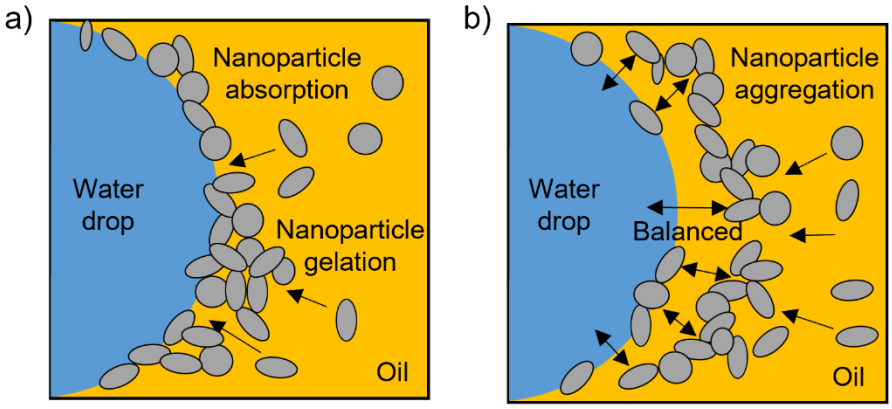


Figure 3-19 The illustration of nanoparticle-interface interactions: a) the typical progress with water (pH=2), b) the proposed progress with water (pH=7 or 12)

3.3.5. Determining the DLVO contributions to assembling

In this section, a semi-quantitative investigation employing the Derjaguin–Landau–Verwey–Overbeek (DLVO) theory [278], [279] was conducted to gain insight into the experimentally observed phenomena. This is achieved by

evaluating the energy potential of a single primary nanoparticle, as illustrated in Figure 3-20.

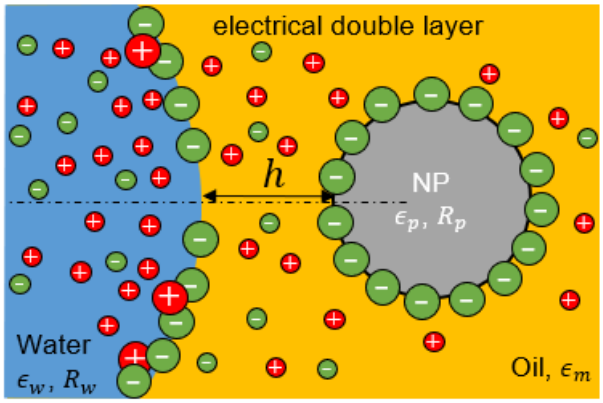


Figure 3-20 The physical model for the DLVO framework.

We consider a simple model including a spheric water droplet with a radius R_w surrounded by the continuous oil phase, and a spheric nanoparticle with a radius R_p located in oil phase. The gapped distance between the nanoparticle and water drop is given by $h = z - R_w - R_p$, where z is the centre-to-centre distance. Two interactions are considered in this framework, namely van der Waals force (F_{vdW}) and electrostatic force (F_{ES}). We hypothesised the particle is ion-impenetrable, while the water droplet is ion-penetrable. Both water/oil interface and nanoparticle/oil interface can possess the electric charge. It is thus proposed that the electrostatic force arises from the accumulation of the electrical double layer force (coulomb force) between water droplet and nanoparticle, and the image force [280]. The image force is an electrostatic interaction that occurs between an excess charge in a dielectric discontinuity field and the induced "image charge". This image charge refers to the induced

surface charge caused by polarization [281]. Be specific, an electric charge in a dielectric medium induces polarization in its surrounding environment. This polarization results in a surface charge density at the interface between dielectric media with varying dielectric properties. The electric field resulting from the surface charge density is commonly referred to as the reaction field. In our case, the reaction field in a medium can be understood as originating from nonreal “image charges” within a fictive homogeneous system. However, the image effect is typically ignored and has only been considered in a limited number of studies [282]. But in this study, due to a huge dielectric difference between water and oil, we believe this effect should be important. Therefore, the total DLVO potential is written in [266]:

$$W_{DLVO}(h) = W_{vdW}(h) + (W_{coulomb}(h) + W_{image}(h)) \qquad \text{Equation 3-1}$$

Which includes the van der Waals energy W_{vdW} and the electrostatic energy in the bracket.

In the first, the van der Waals interaction was evaluated by using the Hamaker approximation of the sphere-sphere geometry [283], in which the energy potential at centre-to-centre distance z is given in:

$$W_{vdW}(z; R_w, R_p) = -\frac{A_{1m/2m}}{3}\left[\frac{R_w R_p}{z^2-(R_w+R_p)^2} + \frac{R_w R_p}{z^2-(R_w-R_p)^2} + \frac{1}{2}\ln\frac{z^2-(R_w+R_p)^2}{z^2-(R_w-R_p)^2}\right] \qquad \text{Equation 3-2}$$

And the corresponding van der Waals force is:

$$F_{vdW}(z; R_w, R_p) = \frac{dW_{vdW}(z;R_w,R_p)}{dh} \qquad \text{Equation 3-3}$$

The nonretarded Hamaker constant $A_{1m/2m}$ was estimated based on the classical Lifshitz theory [284], including the contributions from static dielectric frequency and the UV-visible frequency.

$$A_{1m/2m} \approx \frac{3k_BT}{4}\left(\frac{\epsilon_p-\epsilon_m}{\epsilon_p+\epsilon_m}\right)\left(\frac{\epsilon_w-\epsilon_m}{\epsilon_w+\epsilon_m}\right)+\frac{3h\nu_e}{8\sqrt{2}}\frac{(n_p^2-n_m^2)(n_w^2-n_m^2)}{\sqrt{n_p^2+n_m^2}\sqrt{n_w^2+n_m^2}\left(\sqrt{n_p^2+n_m^2}+\sqrt{n_w^2+n_m^2}\right)}$$

Equation 3-4

In the condition of static dielectric constants $\epsilon_w = 78.5 > \epsilon_p = 3.8 > \epsilon_o = 2.03$, the first static term was estimated at $0.89 \times 10^{-21}\,J$. Moreover, for the latter term, there were $n_p = 1.448 > n_o = 1.426 > n_w = 1.333$. By roughly assuming they have the same absorption frequency ν_e at $3 \times 10^{15}\,s^{-1}$, the total Hamaker constant was thus $A_{1m/2m} = 0.35 \times 10^{-21}$J, which leads to a weak attractive van der Waals force.

Alternatively, the Hamaker constant can be estimated by the combining law [285], [286], which is

$$A_{1m/2m} \approx \left(\sqrt{A_{11}}-\sqrt{A_{mm}}\right)\left(\sqrt{A_{22}}-\sqrt{A_{mm}}\right) \qquad \text{Equation 3-5}$$

This simple method gives a negative result of Hamaker constant $A_{1m/2m}$ at -0.81×10^{-21}J, suggesting a repulsive van der Waals force, which is opposite from that of Lifshitz's theory.

We then proceeded to quantify the electrostatic forces by firstly determining the surface charge density on a nanoparticle. The result of the PALS measurement in Figure 3-21 shows the presence of a negative charge on the nanoparticle

when dispersed in oil. It is shown that there is a zeta potential ζ_p of -30mV in ethanol and a larger value of -100mV in cyclohexane. This result is consisting of a previous measurement of 650 nm silica microspheres in ethanol [287], which gave the ζ_p at -44 mV corresponding with surface charge density at approximate -1.4×10^{-4} C/m^2.

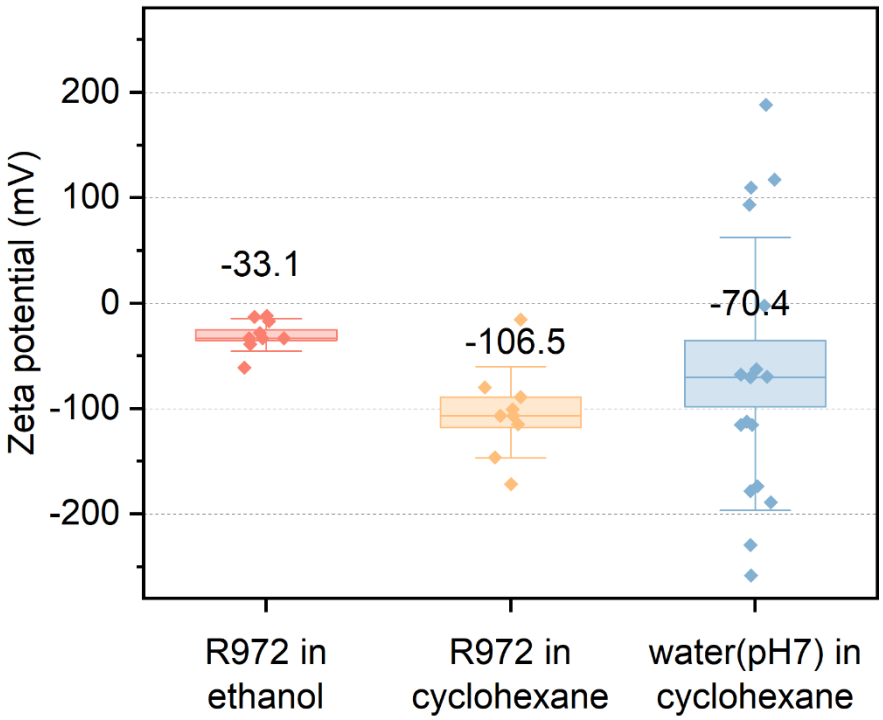


Figure 3-21 Zeta potentials of R972 nanoparticles in ethanol and cyclohexane (both with a concentration at 8mg/ml), also the result of the water drops in cyclohexane as a reference.

To estimate the charge density on the surface of nanoparticle, we employed the semi-empirical equation proposed by Loeb, Overbeek, and Wiersema [288] and using the reference of charge density on the shear plane (where the potential is Zeta potential ζ) [289]. Such the relationship is given as:

$$\sigma_\zeta = \epsilon_m \epsilon_0 \frac{k_B T}{Ze} k \left[2 \sinh\left(\frac{Z}{2}\tilde{\zeta}\right) + \frac{4}{ka} \tanh\left(\frac{Z}{4}\tilde{\zeta}\right) \right] \qquad \text{Equation 3-6}$$

Where a is the particle radius, $\tilde{\zeta} = e\zeta / k_B T$ is the dimensionless zeta potential, Z is the valency of the counterions in media, here assume to be 1, and k^{-1} is the Debye screening length in media, which is defined as:

$$k_o^{-1} = \frac{1}{\sqrt{8\pi\lambda_B N_A c_s}} \qquad \text{Equation 3-7}$$

Where the N_A is Avogadro constant, c_s is the electrolyte concentration in mol/L, and λ_B is Bjerrum length of the media, which is given as:

$$\lambda_B = \frac{e^2}{4\pi\epsilon_r \epsilon_0 k_B T} \qquad \text{Equation 3-8}$$

For cyclohexane at 25°C, the λ_B is 27nm. The concentration of electrolytes was estimated following the method used by Royall [290] and Linden [291]. The concentration of the free ions in the solvent is related to the conductivity through:

$$c_s = \frac{D}{\Lambda^0} \qquad \text{Equation 3-9}$$

where c_s is the concentration in mol/m^3 of fully dissolved electrolytes, Λ^0 (in $m^2 S/mol$) is the limiting molar conductance of electrolyte in a particular solvent, and D is the electrical conductivity of solvent, which was $3 \times 10^{-7}\ S/m$ for cyclohexane measured by PALS. There should be noticed that the electrical conductivity for pure cyclohexane is $7 \times 10^{-16}\ S/m$ [292]. The rise of conductivity should be contributed by the soluble impurity contained in the commercial reagent. Then, Walden's rule [293] was used to estimate the Λ^0 in

proportion to the viscosity η of the solvent to another known solvent, as follows:

$$\Lambda_1^0 \eta_1 = \Lambda_2^0 \eta_2 \qquad \text{Equation 3-10}$$

Here, ethanol ($\eta = 1.08\, mPa \cdot S$ and $\Lambda^0 = 88.9\, cm^2 S/mol$) was used as the reference solvent [291]. By taking the viscosity of cyclohexane at $0.89\, mPa \cdot S$, it conducted $\Lambda^0 = 107.9\, cm^2 S/mol$ for cyclohexane used in this study. By taking this into Equation 3-9, it leads to an ion strength of $c_s = 2.8 \times 10^{-8}\, mol/L$. Thus, the Debye screening length is ~297nm for the cyclohexane in this study. Taking this result back to $\sigma_\zeta = \epsilon_m \epsilon_0 \frac{k_B T}{Ze} k \left[2 \sinh\left(\frac{Z}{2}\tilde{\zeta}\right) + \frac{4}{ka} \tanh\left(\frac{Z}{4}\tilde{\zeta}\right)\right]$ Equation 3-6Equation 3-6 and assuming the dissolved ion is monovalent, therefore, the surface charge density of a single silica nanoparticle is $\sigma_p = -1.8 \times 10^{-4}\, C/m^2$, regarding to the nanoparticle diameter of 16nm and zeta potential of -100mV in cyclohexane.

With these basic, we can estimate the electrostatic energy potential. Since the nanoparticles were assembled from the oil, which is lower in dielectric, the image effect is always attractive, regardless of the sign of the surface charge on the nanoparticles [265], but is repulsive when the particles are initially dispersed in the water phase [265], [266]. As modelled by Danov [265], this image energy between a sphere nanoparticle with a diameter R_p and a planer interface was estimated analytically by following equation:

$$W_{image} = \int_h^\infty F ds = \frac{Q^2 \beta_{23}}{4\varepsilon_m (R_p + h)} w \qquad \text{Equation 3-11}$$

Where the accumulated charge Q carried by a nanoparticle is assumed to be

constant at $4\pi\sigma R_p^2$ (charges on the surface), and f, w are the dimensionless functions accounting for the geometry effect. We determine these functions (f, w) by interpolating the table of numerical result derived by Danov [265].

The last interaction considered in the DLVO theory is Coulomb force within the overlapping electrical double layers of a nanoparticle and a water drop. Two well-known quantitative models had been considered but are not suitable. The first is the Hogg-Healy-Fuerstenau (HHF) model [294], [295], which is appropriate for all kh, large $kR > 5$, but low surface potential (<25mV) [296]. The another model is linear superposition approximation (LSA) method [297], which is accurate for $kh \gg 1$ and $kR \geq 10$. However, the nanoparticle in this case has a very small $k^{-1}{\sim}297$ nm and high surface potential (~100mV). Particularly, when considering the range of $h \to 0$ and without the charge regulation, both model lead to an always attractive (or repulsive) result regardless the signs of surface potential [284]. These points were by Israelachvili as the results of “dangerous assumption” [284]. Therefore, we believe that neither the HHF model nor the LSA method is appropriate for this case. Alternatively, due to a very low electrolyte concentration, it is possible to neglect the effect of the electrical double layer. Consequently, an assumption was made to neglect the effects of the electrical double layer [298]. The nanoparticle was considered as a point charge with $Q = 4\pi R_p^2 \sigma_p$ and was moving in the electrostatic field induced by the surface potential of water droplet, as the energy potential of this nanoparticle is:

$$W_{coulomb}\,(h) = Q\psi(h) = 4\pi R_p^2 \sigma_p \frac{\psi_w R_w}{(R_w+h)} \qquad \text{Equation 3-12}$$

Where the ψ_w is the potential on the surface of water drop. As recently modelled by Uematsu and Ohshima [299], ψ_w is determined by the net charge and surface charge carried by a water droplet. The net charge depends on how these droplet was created [300], as in the previous cases of the droplet being injected from the plastic pipette, it typically carries a positive net charge [301]–[303]. However, this case differs from those, the droplets were created under sonication, which was generated from a vibrating metal horn. To best of our knowledge, there are no relevant evidence determining that the sign or amount of the net charge in such conditions. Moreover, our zeta-potential measurement on neutral water droplet (see Figure 3-21) exhibits that it probably carried the negative net charges, but, with a considerable uncertainty. Therefore, we supposed that the water drop with a neutral pH is slightly negatively charged to a ψ_w of -70.4mV.

Furthermore, we analysed the DLVO effects on a single primary particle (R_p is 8nm) when approaching to a water droplet with a relatively large size of $R_w = 500$nm. The results are shown by the solid lines and dash green line of Figure 3-22.

The van der Waals interactions are short-range, which is responsible for the behaviour of the gapped distance within a few nanometres and are in the range between $-1.1k_BT$ (attractive, estimated from Lifshitz theory, see as solid blue line) to $2.6k_BT$ (repulsive, from combined law, see as solid red line). As a result

of the weak screening effect (long Debye length) in oil with such a low dielectric, the electrostatic forces show a long-range influence up to several hundred nanometres. Conversely, the image force contributes to an attractive short-range potential of up to $-8.6k_BT$ near the interface, but its strength rapidly diminishes as the gap distance increases.

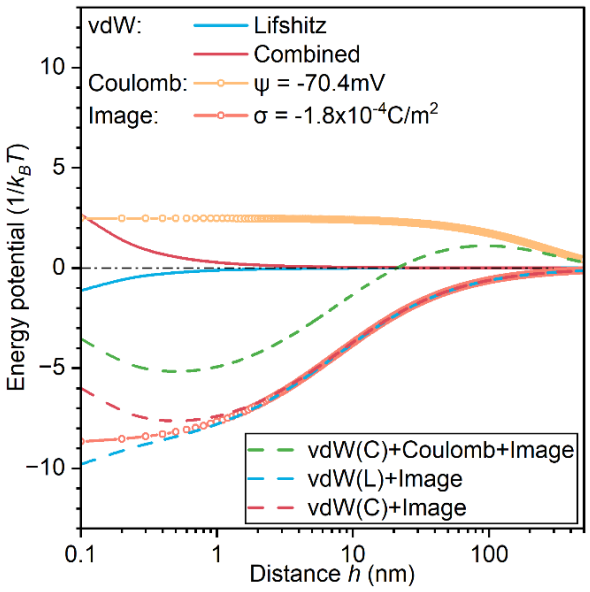


Figure 3-22 The estimated DLVO contributions of a nanoparticle with a diameter at 16nm approaching to a spheric water drops with a diameter of 1000nm.

The total energy potential (represented by the green dashed line) exhibits a repulsive energy barrier of $1.1k_BT$ at a gapped distance of approximately 95nm, primarily due to the significant repulsive Coulomb force. As a result, the nanoparticles remain at a distance from the water drop. However, the amplitude of the barrier is only slightly higher than the thermal energy (k_BT). Consequently, there is a possibility that minor flow-induced fluctuations (or gravity) could overcome this barrier, allowing a small number of nanoparticles to cross it and

reach the interface. This scenario is depicted in Figure 3-23a. Alternatively, when the surface charges of the water drop are neutralised by lowering the pH, the influence of the Coulomb force can be eliminated. Consequently, in the case of the attractive van der Waals force, as depicted by the red dashed line in Figure 3-22 and illustrated by Figure 3-23b, a majority of nanoparticles can approach the water drop closely and potentially be absorbed by the W/O interface. This point can explain the experimental finding in Figure 3-12a, also the self-assemble behaviour of nanoparticle shown in Figure 3-18.

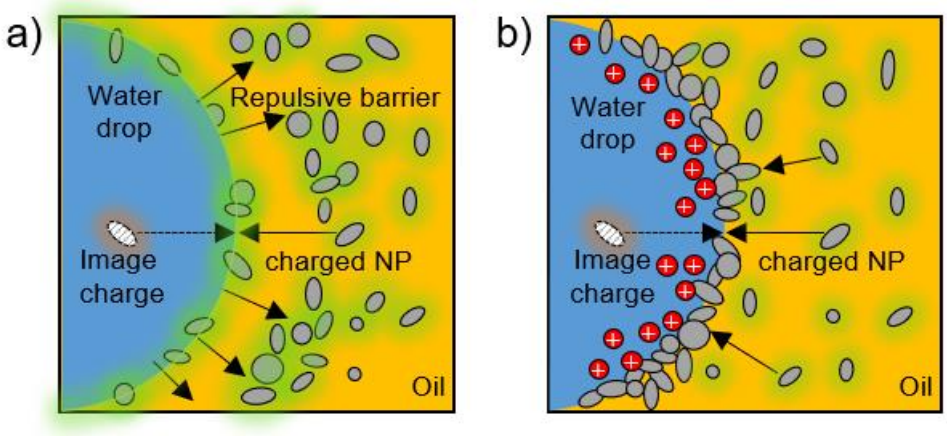


Figure 3-23 Behaviour of nanoparticles near a water drop with the different charged surfaces.

3.4. Conclusion

For screening the protocol for encapsulating salt using W/O Pickering emulsion as a template, experimental and theoretical work has been carried out. The findings include:

1) An appreciable W/O Pickering emulsion is developed when using hydrophobic fumed silica nanoparticles dispersed in oil and then mixed with

water. On other hand, an O/W Pickering emulsion can be made from hydrophobic nanoparticles dispersed in oil and mixed with water.

2) By introducing a Sol-Gel reaction, the encapsulation is successfully prepared from the water phase with low pH (pH=2). In the other conditions (pH=7 and pH=12), a highly aggregated nanoparticles network was found, indicating that the nanoparticle was not adsorbed in the W/O interface.
3) In low pH conditions, nanoparticles prefer to be adsorbed on the large water droplet (>~2μm).
4) The interfacial study confirmed the existence of different behaviour of hydrophobic nanoparticles adsorbed on the water droplet. For the water droplet with pH=2, the nanoparticle show a spontaneous absorption and is finally absorbed in the interface. For the water with normal pH, the nanoparticle is attracted by the water droplet but finally stays at positions close to the water droplet, which does not change the W/O interfacial tension.
5) Those phenomena can be explained by the DLVO theory, which considers van der Waals force, Coulomb force, and image force. The nanoparticle is electrical charged, which is experimentally confirmed. The image force is attractive, leading to the nanoparticle self-assembled to a water drop. The Coulomb force can be repulsive, and thus push the nanoparticle away from the drop.

4 Tailored Pickering emulsions for encapsulating salt

This chapter develops the Pickering emulsions for encapsulating thermochemical salt, the focus is on how to tailor the geometry and structure of Pickering emulsions. Section 4.1 introduces the background and demand for encapsulated thermochemical salt with a tailored structure. Section 4.2 describes the materials and experimental method. Section 4.3 discusses the measures for tailoring the geometry of Pickering emulsions. Section 4.4 concludes the findings in this chapter.

4.1 Introduction

As one of three kinds of thermal energy storage technologies, thermochemical heat storage (TCS) is the least developed but the most promising one to provide a high energy density and a loss-free way for heat storage over a long duration. For a TCS working at low temperatures (typically <150°C), salt hydrates exhibit great advantages, including high theoretical energy density [19], [72], [81], affordable [304]–[306], and feasibility for scale-up to kW/MWh level [203].

The principle of such a TCS is employing a pair of reversible chemical sorption reactions between water vapour and absorbent salt. In a thermal discharging/salt hydration reaction, the absorption of water by an anhydrous salt (or lower hydrate) is accompanied by the release of heat and the formation of a higher hydrated salt, while the reversed process for thermal charging/salt dehydration is endothermic. However, such a reaction in the solid salt grains owns many drawbacks, e.g. a slow kinetic due to poor mass transfer of water molecules from the gains surface into the core [90], and the performance degradation after cycles due to geometry instability of pure compounds [197], [307]. The most popular approach so far is to fill the salt hydrate in the pores of a matrix material [61], [308], e.g. mesoporous materials [148], [150], aerogel [161], MOF [164], that serves as a successful scaffold for stabilizing the geometry. However, the vapour transport pathways are still limited in those structures [309] and are fundamentally difficult to be increased or expanded. To

improve water transportation and maintain the geometry at the same time, an alternative way is making an encapsulated salt, so-called a “salt capsule”, where the salt particles are permanently confined in a predefined space inside a compartment individually from each other. The benefits associated with such an encapsulation include preventing the merging of the salt particles and providing high porosity pathways for vapour diffusion. The moisture diffusion onto the salt particles will be efficient from the convective flow around the capsules, and reaction kinetic benefits from the decreased penetration length in confined solid grains. These capsules should be present in a free-flow powder macroscopic. Potential usage of such a powder material is processed in the fluidized-bed reactors [212], [219], [220], [226], [310]–[312]. In this case. the mass transfer, as well as reaction kinetics, will be further enhanced by intensive powder mixing, leading to output magnitudes higher thermal power than the salt-in-matrix materials packed in a fixed-bed reactor.

However, there are challenges in designing such an encapsulated salt, not only in the fabrication method but also in engineering the performance. To date, there is very limited research working on encapsulated salt for thermochemical energy storage. One successful case is given in filling the salt into the hollow silica capsules derived from a polymer aggregates template [167], which fabricated the capsules with 365nm diameter and realized an energy density of 1100J/g (96MJ/m^3). But, this protocol lacks size-adjustable ability [313]. Another case was presented in a similar way that filling the salt into the 100 μm diameter

hollow capsules made of PEG–PEOS assembled in an emulsion template [168]. However, the inefficient filling of salt is a shortage in this protocol.

As the thermochemical performance is strongly dependent on geometry [99], [130], [314], it is necessary to develop an encapsulation method with the capability of geometry tailoring. Here, we presented a facile method to fabricate the salt capsule, employing a Pickering emulsion template covering a very wide range of geometry and encapsulating salt in one pot. This chapter is aimed to bring a compensative study of the Pickering template and gives a practical guideline to create an encapsulated salt with tailored geometry from microscale to nanoscale. That result draws a full picture of the design-guided fabrication of encapsulated salt-based TCS materials.

4.2 Experimental section

4.2.1 Materials

Calcium chloride dihydrate ($CaCl_2 \cdot 2H_2O$, 99%), sodium chloride (NaCl, 99%), sodium hydroxide (NaOH,99%), and tetraethyl orthosilicate (TEOS, 99%) were purchased from Energy Chemical (www.energy-chemical.com, China). Cyclohexane (C_6H_{12}, 99%) was purchased from Greagent. Hydrogen chloride (HCl, 36%w/w in H_2O), and rhodamine B (AR) were purchased from Aladdin (www.aladdin-e.com, China). Ultrapure Water was obtained from a lab purification system, which has a >18MΩ/cm resistivity. Hydrophobic fumed silica nanoparticle Aerosil R972 Pharma was kindly donated by Evonik.

4.2.2 Emulsions preparation

Fumed silica nanoparticle was dispersed in cyclohexane by sonication (Scientz, IID 20kHz, 200W, 6mm standard horn). Then, the salt and rhodamine B (5μg/ml) were dissolved in water. The pH of the aqueous solution was adjusted by 1M HCl or 1M NaOH and was examined by the pH tester. The aqueous solution was added to the oil suspension, followed by emulsification. Two kinds of emulsification devices were employed in this study, a rotor-stator mixer providing shear-force mixing (Figure 4-1a), and a piezoelectric generator providing the sonication implosion (Figure 4-1b). The former device consists of a rotor with 6.9mm in outside diameter and a stator with 7.3mm in internal diameter. The sonication device has a 6mm outside diameter amplitude transformer, which can deliver a maximum of 600W power for emulsification. For all samples, the volume of nanoparticle suspension and water solution was fixed at 20mL and 1mL, respectively. The emulsification processing time was constant at 3 mins for all cases. All the samples were placed in the ice bath during the emulsification.

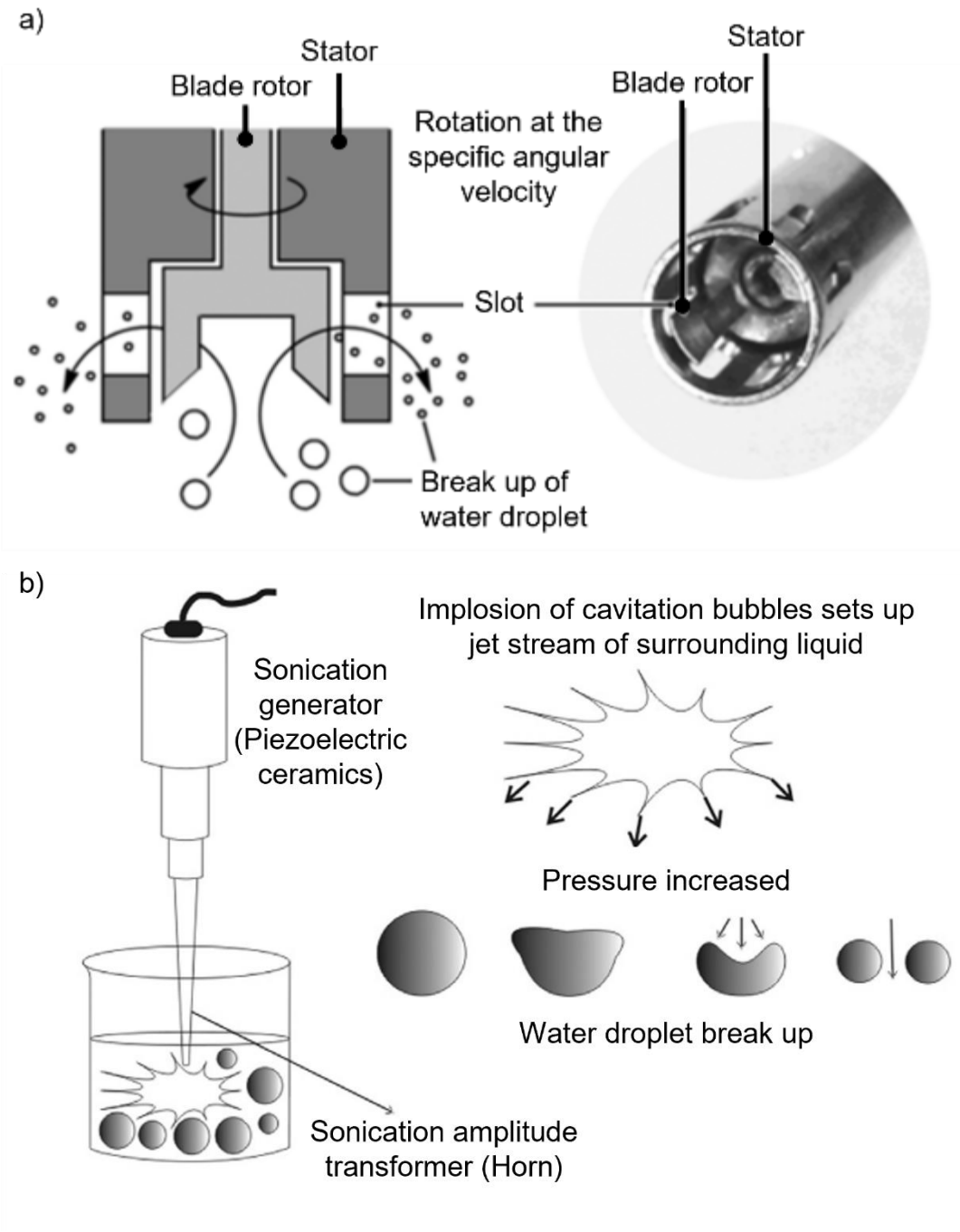


Figure 4-1 Illustration of emulsification devices and principles: a) rotor-stator mixer [315]; b) sonication [316].

4.2.3 Encapsulations from Pickering emulsions

The encapsulation was obtained by adding TEOS(1mL) to the emulsions. As the TEOS has no solubility in water, the reaction will take place in the interface.

There are four steps in the reaction, as illustrated in Figure 4-2. The reaction was lasting for 24 hours. The production was collected by slowly drying the wet gel in a fumed cabinet.

[Hydrolysis]

$$\equiv Si-OR + H_2O \Leftrightarrow \equiv Si-OH + ROH. \quad (1)$$

[Alcohol condensation]

$$\equiv Si-OR + \equiv Si-OH \Leftrightarrow \equiv Si-O-Si \equiv + ROH. \quad (2)$$

[Water condensation]

$$\equiv Si-OH + \equiv Si-OH \Leftrightarrow \equiv Si-O-Si \equiv + H_2O. \quad (3)$$

[Overall reaction]

$$Si(OR)_4 + 2H_2O \xrightarrow{OH^-} SiO_2 \downarrow + 4ROH. \quad (4)$$

where R is C_2H_5.

Figure 4-2 Hydrolysis-Condensation reaction of TEOS for encapsulation [269].

4.2.4 Morphology characterizations

A confocal scanning laser microscope (LEICA DMi8, with 20X and 40X objective lens, 532nm laser) was used to observe the samples of emulsion. The emulsion was dyed by adding Rhodamine B into the water phase (5μg/mL water) before emulsification. The fluorescence signal was induced by the laser with a wavelength of 532nm and was collected at wavelengths between 580nm-620nm. For consolidated samples, images were taken under SEM (TESCAN MIRA3) operated at 10kV. The samples were coated by Pt for 10mA and 90s

before measurements.

4.3 Result and discussion

4.3.1 Effect of particle dosage and emulsification energy on emulsions

The samples made from different NP dosages and different shear energies of emulsification were observed under Confocal Laser Scanning Microscope (CLSM), the results are shown in Figure 4-3. In all the cases, water droplets were identified clearly, and the intensive fluorescent signal near the W/O interface was detected. The images in the first row present the samples prepared under a constant low shear rate at 2800rpm. By increasing the NP dosage from 10mg to 100mg with the same water volume of 1mL, the droplet size in different emulsions remained in a similar range of 10μm to 50μm with a mean value of about 30μm. Exceed silica NP outside the droplets was observed in the samples with 50mg NP and 100mg NP. Those NPs formed the aggregated network and provided an extra spatial barrier to avoid aqueous droplets merging. When the applied emulsification energy increased, smaller droplets were created, as shown according to the images in each column. Comparing all the samples prepared at different energy with the same 10mg NP, the droplet sizes have the closed mean value, but a border range was shown in the sample prepared from the high shear force. It indicates the created W/O interfacial area matches the number of particles, and that all the particles are adsorbed in the interface in the same density. In other cases of 50mg NP

and 100mg NP, increased emulsification energy resulted in a decrease in drop size and less dissociated nanoparticles.

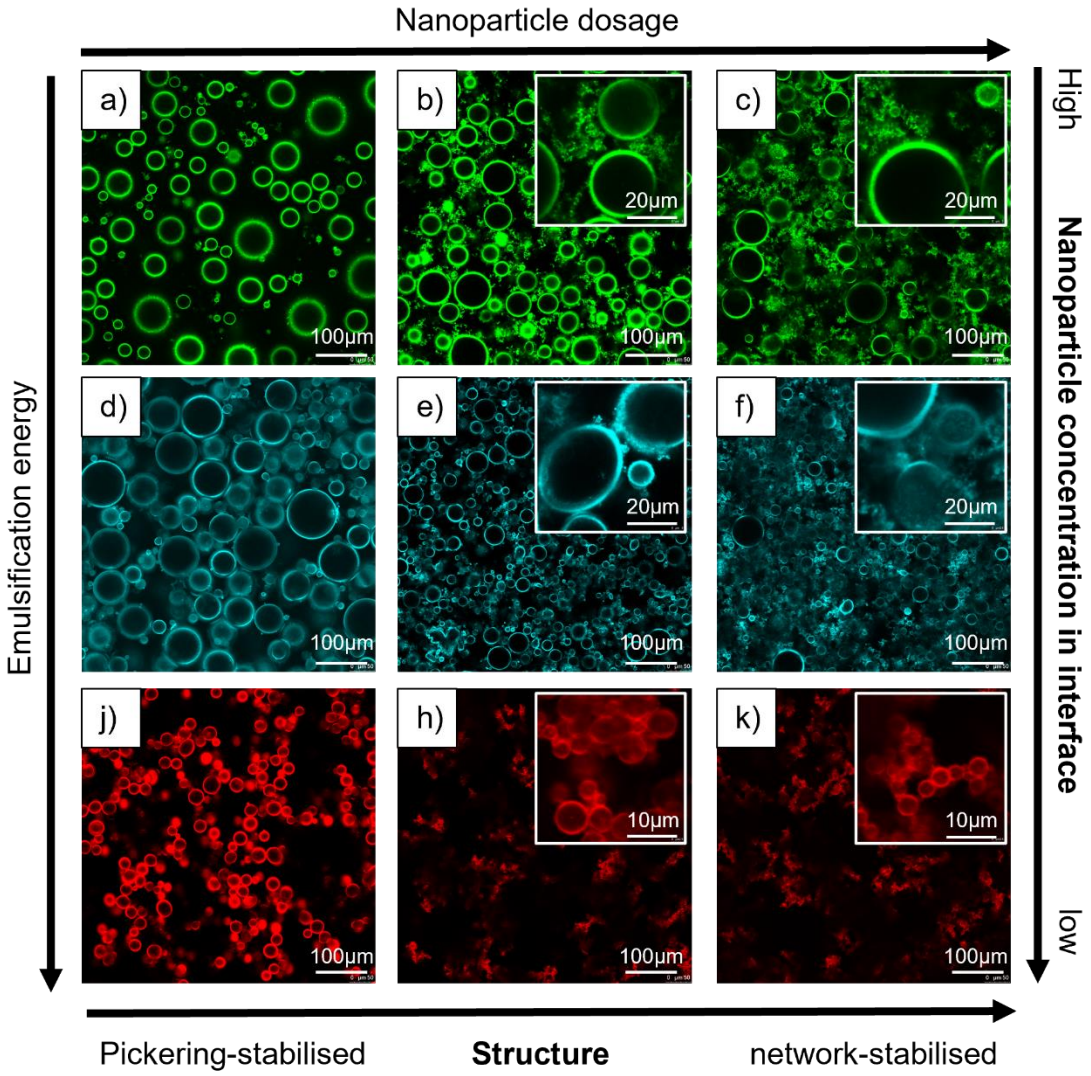


Figure 4-3 CSLM images of W/O emulsions prepared with different conditions. From the first to the third row are the emulsions of 1ml water in 20mL Cyclohexane with 10mg R972 NP, 50mg NP, and 100mg NP, respectively. Different colours represent the different emulsification: green is for emulsified by rotor-stator at 2800 rpm (linear velocity at ~1.0m/s), blue is 8000 rpm (~2.8m/s) and red is sonicated at 500W, respectively.

Besides, some stable ellipsoidal droplets were observed in moderate shear rate

and high particle concentration cases, see the zoomed insertion of the image in Figure 4-3e. The droplet deformation was caused by the large number of particles intensively jamming in the W/O interface [317], [318] and stabilising the interface. Meanwhile, the shear flow was insufficient to further break up this droplet [319]. In contrast, a typical surfactant-stabilised droplet will restore to the sphere after a short relaxation period [320].

As shown in Figure 4-4, the minimum size of the droplets was in sonicated samples, which was 9.5μm, 1.6μm and 1.4μm, for 10mg/ml, 50mg/ml and 100mg/ml samples, respectively. By fitting in the lognormal distributions, the mean size of those emulsions was 19.2μm, 3.6μm, and 2.6μm, for the corresponding 10mg/ml to 100mg/ml samples.

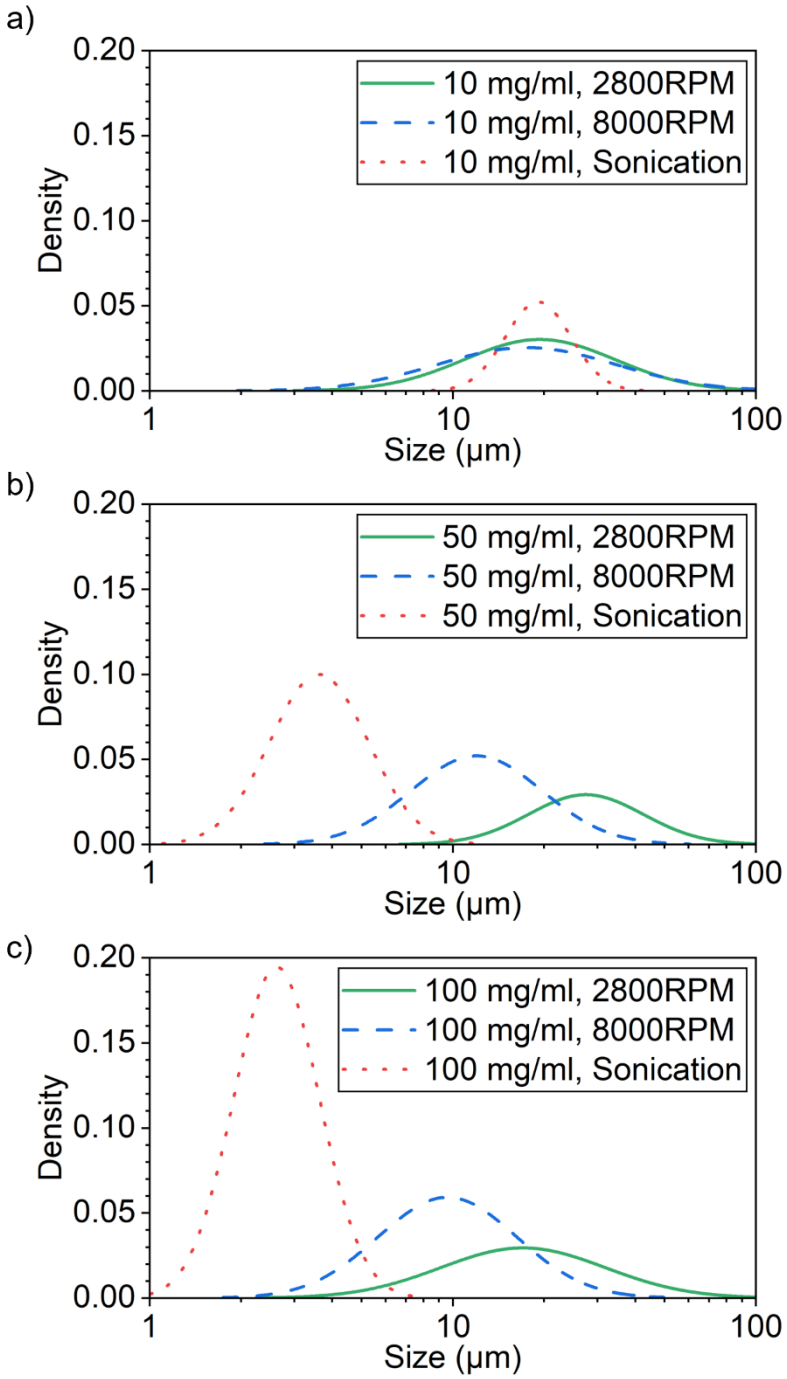


Figure 4-4 Size distributions of droplets in emulsions, fitted in lognormal distributions.

In addition, the inter-droplet spacing was larger in the emulsions with smaller droplets. This was evidenced by the obvious expansion in the volume of the emulsion after a long duration of settling (see Figure 4-5). It may be linked to

the droplet size distribution becoming narrow [321]. Moreover, it is possible to be associated with different microscopic structures. It was observed that the branched clusters containing dozens of droplets formed in sonicated samples (see Figure 4-3h and k). The droplets were assembled by sharing a monolayer of the particles at interfaces between a pair of neighboured droplets [322], [323]. This cluster has a gel-like ability [324], leading to a free-standing structure and decreased packing density, which results in a larger volume of the emulsion (sonicated sample in Figure 4-5).

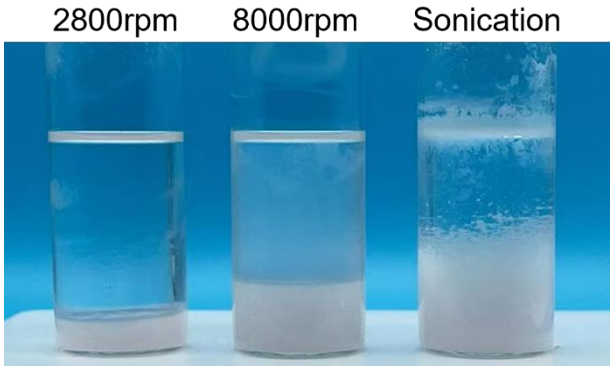


Figure 4-5 Photo Images of emulsions prepared by different emulsification conditions. From left to right is processed at 2800rpm in the rotor-stator mixer, at 8000rpm in the same mixer, and sonication with 500W. The NP dosage was constant at 50mg/ml and the water volume was also the same.

4.3.2 Stability of Pickering emulsions

Moreover, the stability of the Pickering emulsion template was examined by comparing the CLSM images of the pristine emulsions and the emulsions stored for a week, see Figure 4-6. A minor change was found in morphology and size distribution. The above behaviours highlight the ability of wide

geometric manipulation and long-term stability of the Pickering emulsion, which benefits it playing the role of the template.

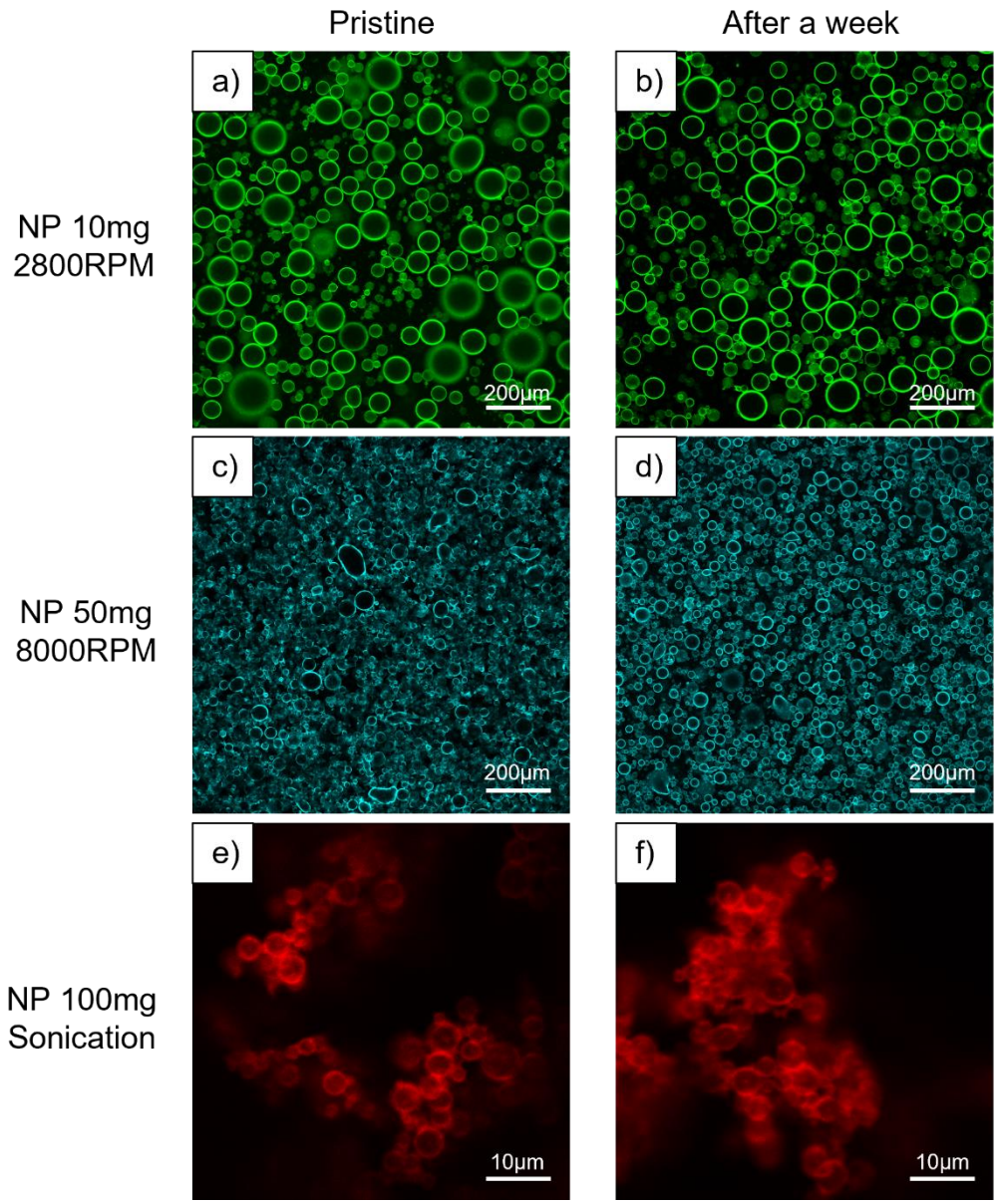


Figure 4-6 CLSM images of pristine emulsions and aged after a week.

4.3.3 Influence of Rhodamine B

The emulsion structures were possibly influenced by RhB. As the structure is shown in Figure 4-7, the RhB has both excellent solubilities in water due to

hydrophilic groups (marked in the blue circle) and highly lipophilic (functional groups in the red circle) [325]. It is suggested that the RhB should play a role as a surfactant [326], which co-stabilises the emulsion structure accompanying the nanoparticle. We also found that some of the RhB can diffuse into the oily phase, adsorbing on silica nanoparticle and labelling it. Despite the influence of RhB, to the best of our knowledge, the use of dye is the only feasible method to observe living emulsion on the microscale.

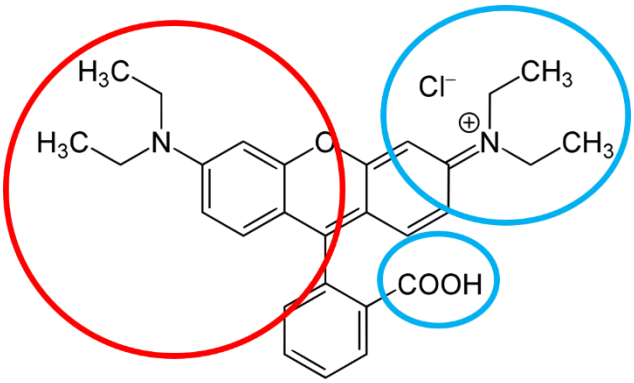


Figure 4-7 The chemical structure of Rhodamine B.

4.3.4 Encapsulation from the emulsions

With the stable emulsion templates, the hollow capsules were derived from interfacial polymerization, which consolidates the interface stabilised by the Pickering particles. Firstly, the emulsions and encapsulation prepared with RhB are shown in Figure 4-8. In all the cases, water droplets were identified from the LSCM images, appear in clusters and have similar droplet sizes. In the SEM images, one can see that continuous layers were successfully formed to consolidate the emulsion in all cases. However, there are differences in detailed

structure. In cases of pH=2 and pH=12, the consolidated structure inherited the original geometry of the emulsions, either in round droplet morphology or size. However, the case of pH at 2 shows the maximum coverage of silica nanoparticles attached to the interface, nearly fully covered, indicating the capsules were derived from a classical Pickering-stabilised emulsion. Another sample with a pH of 12 shows a weakly covered surface on the droplets. The nanoparticles may be failed to be absorbed in the W/O interface due to the repulsive electrostatic interaction [327] between the negatively charged droplet in -OH rich condition [328] and a likely charged particle. In the neutral pH case, it is seeming that the major part of silica NP was agglomerated in the continuous phase that trapped water droplets and only a few of NP were adsorbed in the interface, which was a typical network-stabilised emulsion reported in previous studies [277], [329], [330].

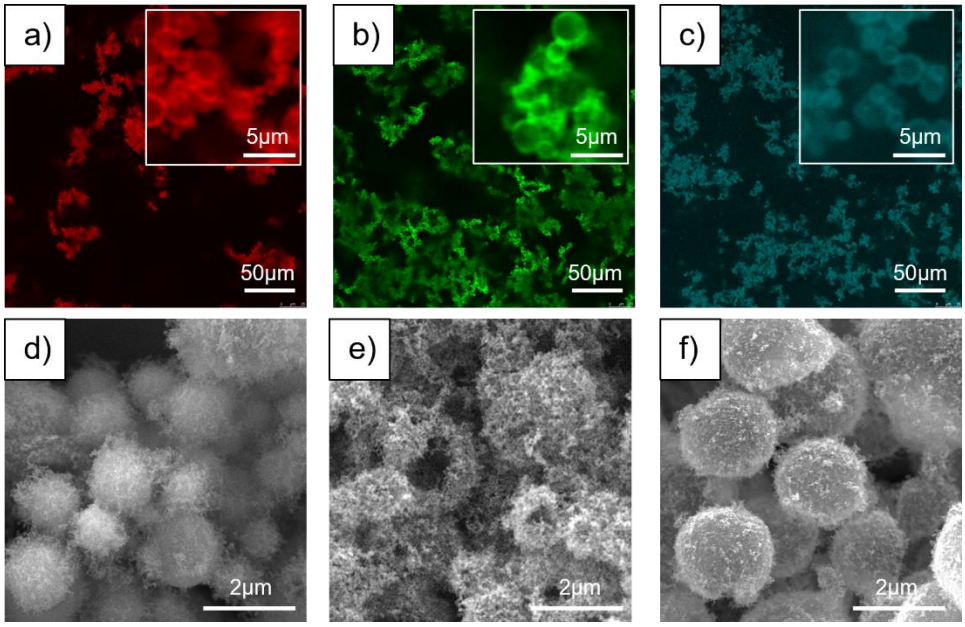


Figure 4-8 CLSM images of the Pickering emulsion template and corresponding SEM images of the consolidated encapsulations. The NP dosage was

200mg/ml (mass of NP to the volume of water), and the water-to-oil volumetric ratio is 1:20, from left to right column is the sample prepared from water with pH=2, 7, 12, respectively.

The morphologies of consolidated capsules prepared without RhB are presented in Figure 4-9. The larger droplets were obtained from the emulsions of nanoparticles solely involved (without RhB). In the condition of the pH at 2, the round capsule structure was obtained with massive silica nanoparticle aggregates attached to the surface, consisting of the RhB-involved case. The mean diameter is 2.17μm by directly measured from the SEM image. In the pH=12 case, the cluster of capsules was also identified, but most of them were broken. This was different from those without RhB. It was a result of the different chemical structures of O-Si-O polymer, which was catalysed by different pH. Stiffness three-dimensional O-Si-O polymer tended to be derived from TEOS hydrolysed in alkalinity conditions [268], leading to the capsule collapse and breaking during drying from the wet gel. In contrast, the fine network of long-chain O-Si-O polymer derived from the acidic catalysed reaction has a better strength to keep the complete capsules. In addition, comparing the RhB-involved case of pH at 12, it should be informed that RhB was conserved inside the shell and strengthened the shell.

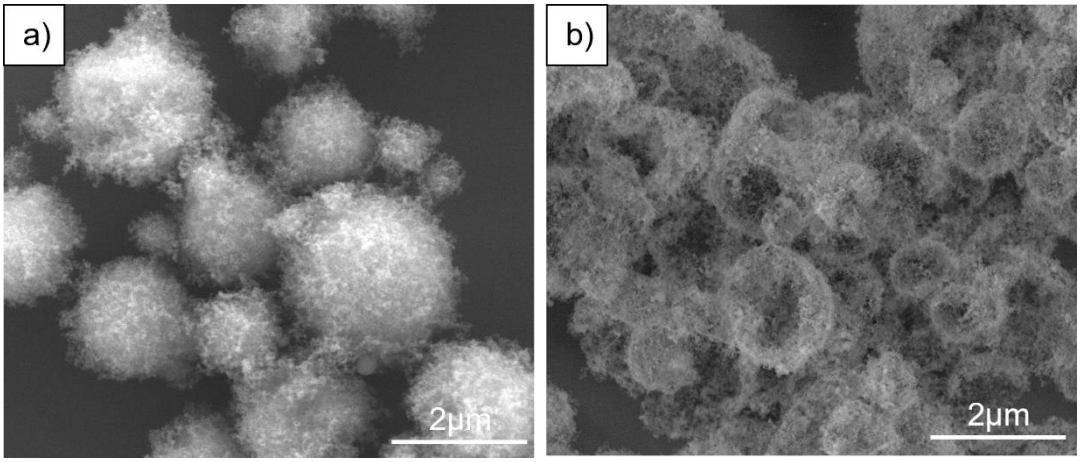


Figure 4-9 SEM images of capsules prepared from emulsions without RhB, a) water phase was adjusted to pH=2, and b) pH=12. The NP dosage is consisting of 200mg/ml (mass of NP to the volume of water).

However, among the cases of pH=4, 7, and 10 (Figure 4-10), it is hard to distinguish any characteristic structure. They are all irregular agglomerates of NP. It is possibly related to the insufficient catalyst and network structures formed in the emulsions.

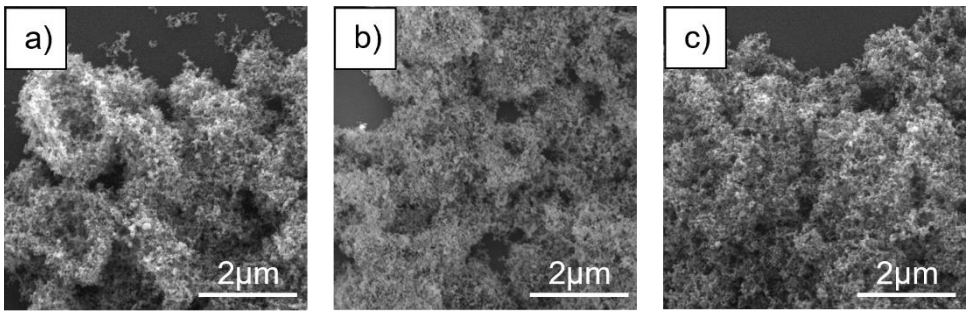


Figure 4-10 SEM images of encapsulations from emulsions containing water at pH=4, 7, and 10 (without RhB).

4.3.5 Pickering and network structures of the emulsions

The above results suggested there were two kinds of structure in the emulsions, namely Pickering and network. Those structures can be also distinguished by

the macroscopic observations (see Figure 4-11). It was found that the sample at pH=7 had the lowest volume in both emulsion and packed capsules. The reduction in the volume of pH=7 emulsion is preferred to be caused by the close packing of unabsorbed NP in the continuous phase.

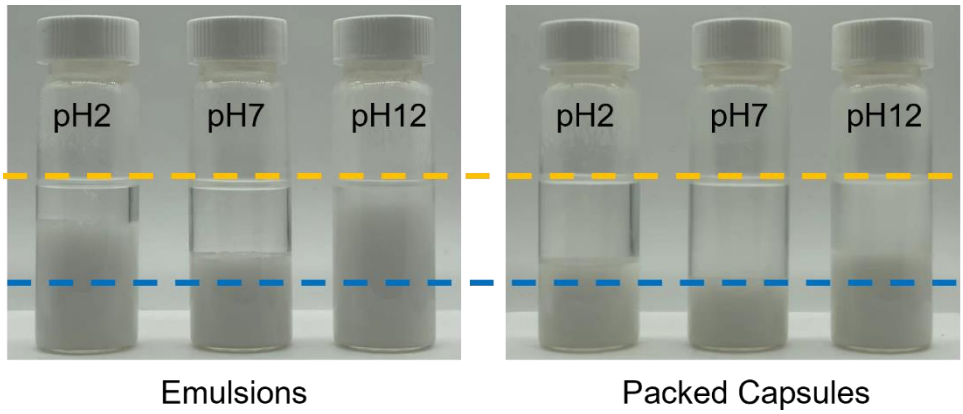


Figure 4-11 Photo images of emulsions containing water phase with different pH (left to right 2,7,12. The NP dosage was constant at 200mg/ml and the water-to-oil ratio is 1:25 in volume.

4.3.6 Nanoparticle dosage effect on the size of the droplet

Assuming all the NP is absorbed in the interface with a constant concentration, the total mass of NP determines the total interface area. This accumulated surface area of the spheric droplets with the size in a log-normal size distribution is given in [331]:

$$S = \frac{6V}{\mu e^{3(ln\sigma)^2}} \qquad \text{Equation 4-1}$$

Where S and V are the total surface area and volume of droplets, μ is the number-median diameter and σ is the geometric standard deviation. We

assumed all the particles, that have a total mass m, are adsorbed in the interface with the concentration in the interface is $C_{NP@interface} = m/S$ (in unit $mg/\mu m^2$). Then a relationship between nanoparticle dosage and number-median diameter can be derived as below

$$\mu = \frac{V}{m}\frac{6C_{NP@interface}}{e^{3(ln\sigma)^2}} \qquad \text{Equation 4-2}$$

In conditions of emulsification by sonication, the size of samples with different NP dosages (to the same volume of water phase) have a similar standard deviation σ~0.35.

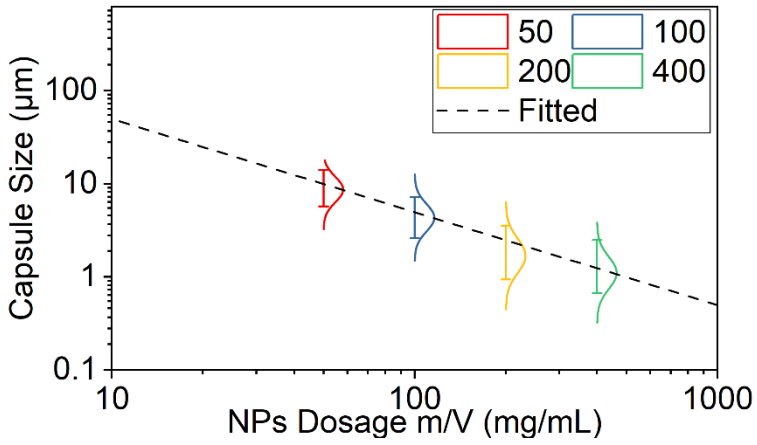


Figure 4-12 Fitting for capsule sizes prepared from pH=2 emulsions. The value in the legend represents the NP dosage (mg/mL water volume)

The statistics for the size of droplets prepared from different NP dosages as shown in Figure 4-12. By fitting the data using Equation 4-2, the concentration of NP in the interface was estimated at $C_{NP@interface}$~$8.8 \times 10^{-11}\ mg/\mu m^2$. By taking the values back to the Equation 4-2, it conducted a simple linear relationship between the mean diameter of droplets and nanoparticle dosage

as $\mu = 498.6\,V/m$.

4.3.7 Salt effect on structure of encapsulation

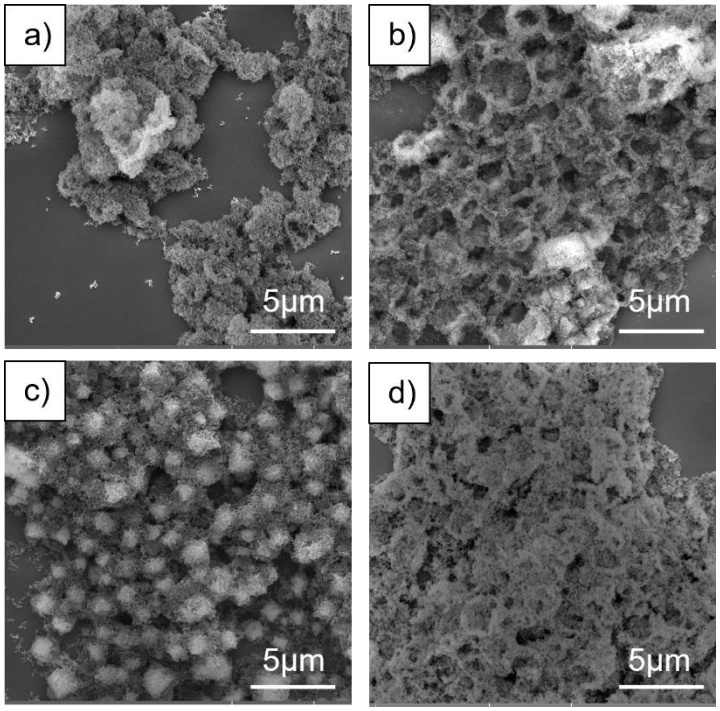


Figure 4-13 SEM images of consolidated structure from emulsions containing different salt solutions as water phase: a) 1mM NaCl, b) 1M NaCl, c) 4M NaCl, and d) 1M $CaCl_2$. The NP dosage was constant at 200mg/ml and the pH was constant at 7.

The salt effect on encapsulation was studied. By solely adding different salt to the aqueous phase without changing the pH and adding a surfactant, we found that the consolidated structures (Figure 4-13) were not encapsulation, regardless of the salt valences and concentration. It is likely to be the result of the previous case of pH at 7 without RhB, that the drops were embedded in an NP aggregated network. It is suggested that the NP were aggregated outside the water droplet rather than absorbed in the W/O interface as illustrated by

Figure 4-14a.

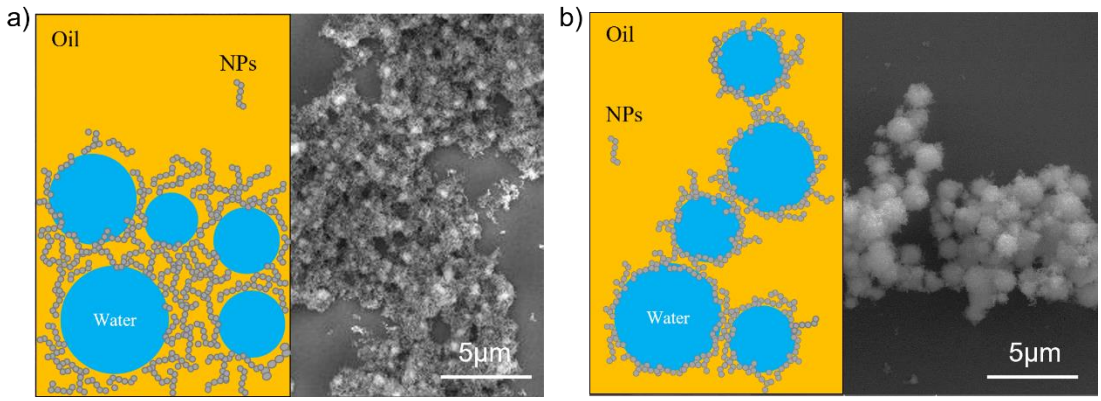


Figure 4-14 Illustration of a) Network (pH=7) and b) Pickering (pH=2) type emulsions, and SEM images of capsules derived from the corresponding emulsion template, the NP dosage is 400mg/ml, and the water phase contains 1M NaCl.

Surprisingly, when the pH of the salty solution was adjusted to 2, both the structures of emulsion and consolidated changed to expected encapsulation, as shown in Figure 4-14b. The emulsion structure is the Pickering type, in which the NP is strongly absorbed in the interface. It is probably due to the NP surface conditions being changed by the H^+, which came from the aqueous solution during the strong mixing. Consequently, the NP was easily attracted by and bonded at the W/O interface.

4.3.8 Salt effect on the encapsulation sizes

In addition, we found there was a considerable reduction in the diameter of capsules prepared from brine water. As shown in Figure 4-15, there is a ~29% diameter reduction for 1M NaCl as water phase and a ~48% reduction for

saturated 9M $CaCl_2$ solution. The most explanation for this was preferred to the build-up of osmotic pressure to suppress the Ostwald ripening [332], [333]. However, in Pickering emulsion, due to the existence of a particle barrier on the droplet, there is no chance for two droplets to get in touch and exchange the water phase. Thus, Ostwald ripening may contribute a little to the droplet size change.

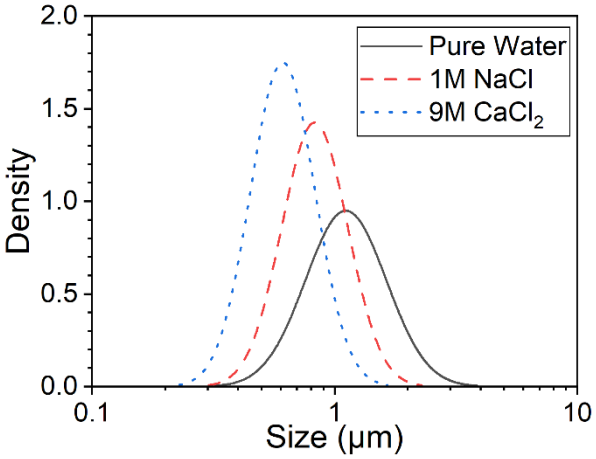


Figure 4-15 Size distribution of capsules prepared from different water phases with a constant 400mg/ml NP dosage

To explain this, we proposed another mechanism that a slight change of particle wettability in the brine/oil interface may be dominated the droplet size reduction. It was concluded from the calculation below.

From the thermodynamic point of view, we wrote the surface Gibbs free energy ΔG of formation of a W/O Pickering emulsion while neglecting the entropy as [334]:

$$\Delta G = n_d\left(A_{wo}\gamma_{wo} - N_p\pi R_p^2\gamma_{wo}(1+\cos\theta)^2\right) \qquad \text{Equation 4-3}$$

Where, N_d is the total number of droplets in the system, A_{wo} is the surface area of a droplet, γ_{wo} is the interfacial tension of two fluids, N_p is the number of NPs attached in the interface of an individual droplet, R_p is the radius of an NP, and θ is the three-phase contact angle. In a system containing a constant volume of liquid, that $V = 4/3\, N_d \pi R_d^3$ and a total number of NP $C = N_d N_p$ are all in constant. We assumed the NP covered the interface by a constant concentration η. Thus, in an individual droplet, by the geometric relationship, there is an expression for the number of NP:

$$N_p \approx \frac{\eta A_{wo}}{\pi R_p^2} = \frac{4\eta R_d^2}{R_p^2} \qquad \text{Equation 4-4}$$

And the number of droplets is conducted from the conservation of volume:

$$N_d = \frac{3V_d}{4\pi R_d^3} \qquad \text{Equation 4-5}$$

By combining the above equations, it becomes:

$$C = N_d N_p = \frac{3V_d \eta}{\pi R_d R_p^2} \qquad \text{Equation 4-6}$$

On other hand, the surface area of a droplet is:

$$A_{wo} = 4\pi R_d^2 = 4\pi \left(\frac{3V}{4\pi n_d}\right)^{2/3} \qquad \text{Equation 4-7}$$

Taking Equation 4-6 and Equation 4-7 into Equation 4-3, it transformed into an equation based on droplet radius and particle three-phase contact angle:

$$\Delta G = \frac{3V}{R_d}\gamma_{wo} - C\pi R_p^2 \gamma_{wo}(1 + \cos\theta)^2 \qquad \text{Equation 4-8}$$

Finally, it became:

$$R_d = \frac{3V\gamma_{wo}}{\Delta G + C\pi R_p^2 \gamma_{wo}(1+\cos\theta)^2} \qquad \text{Equation 4-9}$$

Due to the change in Gibbs free energy being dependent on the energy input during the emulsifying, we assume there is the same ΔG under the same treatment conditions (time and treatment power) for all the emulsions in this study. The target remains on finding how other parameters effect on R_d. Therefore, we performed a parametric study for all the combinations of the possible ΔG, θ and C.

As the size of the droplet is in a narrow distribution, we can assume they have the same size with a radius at R_d, which neglects the distribution profile. The nanoparticle used in this emulsion existed in the smallest unit of an aggregate, which is not able to be further crushed. Each aggregate is highly branched and contains dozens of primary particles, which are connected by the sintered neck [261]. This picture of particle aggregates absorbed in the interface is illustrated by Figure 4-16. For the total number of absorbed particles C, we only account the primary particles absorbed in the interface rather than the number of aggregates, also see Figure 4-16.

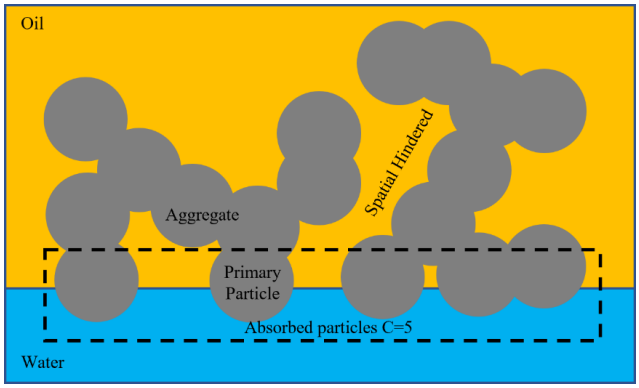


Figure 4-16 The illustration of the nanoparticle absorbed in the W/O interface.

The particle size is therefore corresponding to the size of the primary particle, which has a radius of $R_p = 8nm$. Other values of the parameters in our system are listed below.

Table 4-1 parameters used in calculation.

Parameter	Range	Comments
V	1 ml	0.055 mol of water
R_d	200 to 1000 nm	
R_p	8 nm	For the primary particle of a silica aggregate
η	0.01 to 0.7	The ratio is from weakly covered to dense covered, due to the spital steric of the packed hard sphere, the largest value is assumed to be 0.7 as in the very close pack condition. However, the coverage is far low than 0.7 in a realistic case.
γ_{wo}	50.2 mN/m	This Is the bare Water/Cyclohexane interfacial tension. For Brine/Cyclohexane, there should be a lift of less than 1.5 mN/m for 1M NaCl [335], which contributes a little to the result.
θ	90° to 180°	For hydrophobic particles used in this study

Firstly, for all the possible combinations of η and R_d, the total number of nanoparticles C was estimated by Equation 4-6, as the result shown in Figure 4-17.

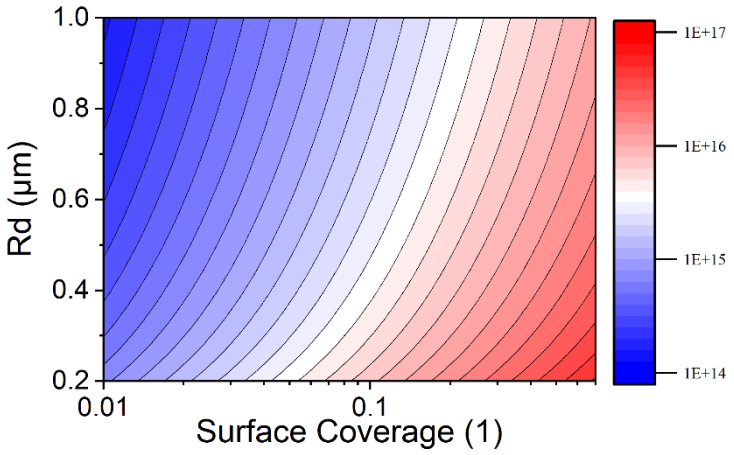


Figure 4-17 NP concentration C on interface estimated from all the possible conditions.

The result shows the total number of absorbed nanoparticles was possibly in the range of 1.4×10^{14} to 5.2×10^{16}. By fixing the number of absorbed nanoparticles, then based on Equation 4-8, we can estimate the Gibbs free energy according to contact angle and droplet size.

For the case of minimum particles absorbed in the interface Figure 4-18a, the change in contact angle affects a little of the droplet radius. In the particle maximum absorbed case, the graph shows that there has been a gradual fall in the droplet radius due to decreases in contact angle when the Gibbs free energy ranged from 0.1J to 0.4J.

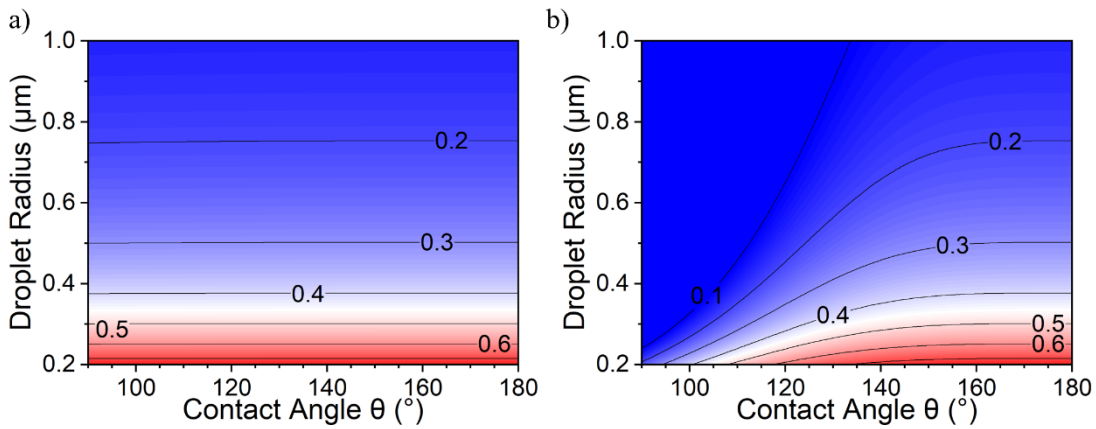


Figure 4-18 The relationship between droplet radius and particle wettability with the number of absorbed particles is fixed, the Gibbs free energy is labelled on the lines, unit in J/ml for water. a) the number of absorbed fixed at the lowest $C = 1.4 \times 10^{14}$, and b) fixed at the highest $C = 5.2 \times 10^{16}$.

In the same way, the Gibbs free energy was also estimated when the particle contact angle was fixed. The droplet radius in the emulsions with different energy and the number of absorbed particles are shown in Figure 4-19. In the case of a contact angle at 120°, it is possible for the droplet radius to decrease from 0.5μm to 0.3μm by following the lines of ΔG around 0.3J. However, the corresponding increases in the number of absorbed particles should be greater than two orders of magnitude. In another case of a contact angle at 135°, it does not found that any contour lines covering the desired decreases in droplet radius.

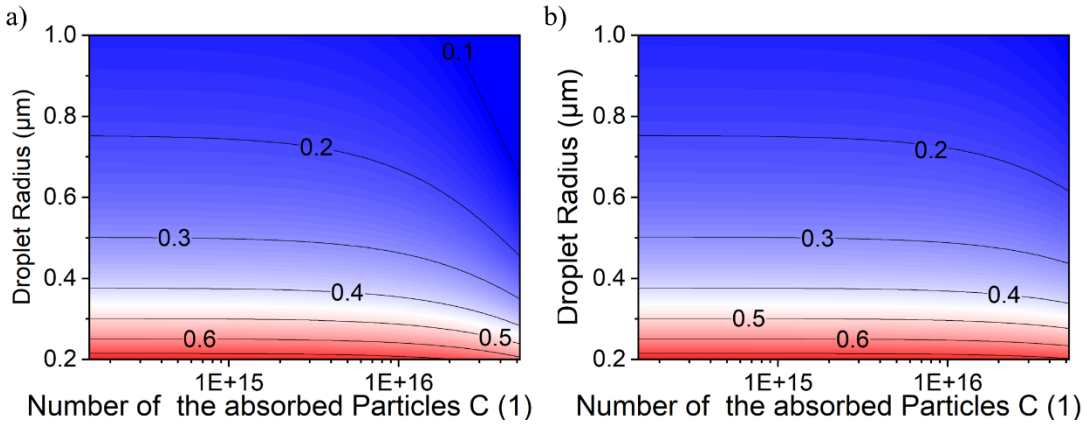


Figure 4-19 The relationship between droplet radius and the number of absorbed particles with particle contact angle is fixed, the Gibbs free energy is labelled on the lines, unit in J/ml for water. a) the particle contact angle is 120°, and b) the particle contact angle is 135°.

The effect of any individual factor, either of contact angle or number of absorbed nanoparticles, is not significant for reducing the size of the droplets by half. The decreases in contact angle and increases in the number of absorbed particles are more likely to take effect together. As an illustration in Figure 4-20, the introduction of salt to the water may change the wettability of the nanoparticle (primary particle), and the particle is likely to be rotated to the orientation of more particles that can be absorbed during the absorption. Consequently, a slight decrease in contact angle and not much additional particle absorption is able to produce enough reduction in droplet size.

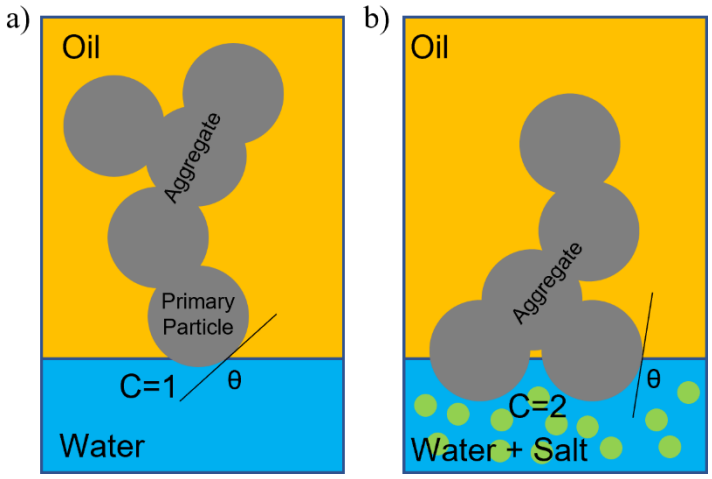


Figure 4-20 The illustration of NP absorbed in a bare Water/Oil interface and Brine/Oil interface, both the number of absorbed particles and contact angle changed.

4.4 Conclusion

In this study, we discussed how to tailor the geometry of W/O Pickering emulsions. There are four measurements to reduce the size of droplets in

emulsions, including increasing emulsification energy, increasing the dosage of nanoparticles, adding salt to the water phase, and using a surfactant. In this way, the size of droplets in the emulsion is precisely and continually adjusted on the nanoscale and microscale. Based on those findings, the encapsulated salt can be fabricated by introducing a continuous shell derived from TEOS, which is hydrolysed under an acid condition. The pH also shows a great influence, not only acting as a catalyst for hydrolysis but also changing the emulsion structure. A low pH condition is preferred to conduct the desired capsules, due to the possible change in the wettability of the nanoparticle.

It can be concluded that, with both experimental and theoretical analysis, this work proposed a facile method to make the encapsulated salt for TCS. Furthermore, it gives a practical guideline to tailor the structure and geometry of the Pickering emulsions.

5 Thermal performance and optimization of encapsulated salt

This chapter fabricates the encapsulated $CaCl_2$ with various sizes and shell thicknesses, discusses the thermal performance links to those parameters, with a special focus on single particle. Section 5.1 introduces the background of encapsulated thermochemical salt. Section 5.2 describes the materials and experimental method. Section 5.3 presents and discusses the relationship between thermal performance and size of encapsulation. Section 5.4 concludes the findings in this chapter. These findings can be used to guide and select the best-suitable encapsulated salt for the specific applications.

5.1 Introduction

Salt sorption-based thermochemical heat storage (TCS) is an emerging technology for long-duration thermal storage [67]. This technology relies on reversible dehydration/hydration reactions, regarding thermally charging and discharging for heat. For charging as well as dehydration of salt hydrates, the water molecules is being released through chemical bonds breaking and transported to the ambient through the crystal lattice [90], [336]. For the discharging/hydration, the vapour water condenses on the surface of the solid sorbent and diffuses into the lattice accompanying the reaction [106], [108]. Those reactions are the solid-gas reaction [337], which involves the coupled mass and heat transfer and thus has the diversity kinetic. It is suggested that the reaction rate are always limited by the slow mass transfer in the solid [130], [307]. The mass transfer can be improved by an optimised geometry of solid sorbent [314]. In practice, sorbent is used in the form of powder, pellets, granules, or bricks. These various sizes and shapes strongly influence the performances, including energy storage density, specific power and thermal efficiency [99]. For salt as a sorbent, it is promising that confining salt grains sizes by encapsulation. Based on the previous studies, the salt was successfully encapsulated from the well-designed Pickering emulsions. In this chapter, the aim is to optimise the geometry of encapsulated salt for better thermal performance. Both the effect of shell thickness and encapsulation size

on thermal performance is studied. A framework to evaluate the performance of encapsulated salt is proposed in the following.

5.2 Experimental section

5.2.1 Materials

Calcium chloride dihydrate ($CaCl_2 \cdot 2H_2O$, 99%), and tetraethyl orthosilicate (TEOS, 99%) were purchased from Energy Chemical (www.energy-chemical.com, China). Cyclohexane (C_6H_{12}, 99%) was purchased from Greagent. Hydrogen chloride (HCl, 36%w/w in H_2O) was purchased from Aladdin (www.aladdin-e.com, China). Ultrapure Water was obtained from a lab purification system, which has a >18MΩ/cm resistivity. Hydrophobic fumed silica nanoparticle Aerosil R972 Pharma was kindly donated by Evonik.

5.2.2 Fabrication of encapsulated $CaCl_2$

Fumed silica nanoparticle was dispersed in 20mL cyclohexane by sonication (Scientz, IID 20kHz, 200W, 6mm standard tip) in a concentration. The $CaCl_2$ was dissolved in water at a mass fraction of ~40%wt, followed by adjusting the pH to 2 by 1M HCl. The aqueous solution was added to the oil suspension, followed by emulsification taking place in an ice bath. For all samples, the amount of cyclohexane and the aqueous solution was fixed at 20mL and 1 mL, respectively. For emulsification, sonication (6mm, 600W) was used, and the emulsification time was constant at 3 mins for all cases. The diameter of

encapsulation was tailored by changing the amount of fumed silica nanoparticles. The shell thickness was increased by adding more TEOS. The list of encapsulated $CaCl_2$ is presented below.

Table 5-1 Studied encapsulated $CaCl_2$.

Samples (Diameter-shell thickness)	Preparation conditions			
	$CaCl_2$ aqueous solution (mL)	Fumed silica (mg)	Cyclohexane (mL)	TEOS (mL)
800nm-25nm	0.5	250	20	0.5
800nm-50nm	0.5	250	20	1.0
800nm-100nm	0.5	250	20	2.0
8000nm-250nm	1.0	50	20	1.2

5.2.3 Morphology characterization

SEM images were taken under SEM (TESCAN MIRA3) operated at 10kV. The samples were coated by Pt for 10mA and 90s before measurements. STEM images were taken under a transmission electron microscope (FEI, Talos F200X G2) in Scanning-TEM (STEM) mode with HAADF (High-angle annular dark field) detector. Energy-dispersive X-ray spectroscopy (EDX) mappings were also acquired in STEM mode.

5.2.4 Thermal performance characterized by STA

Simultaneous Thermal Analysis (STA) was performed in a Netzsch STA 449 F1 Jupiter equipped with an S-Type thermocouple. As the profile shown in Figure 5-1, the sample was initially standing under moist air until saturation, followed

by the STA switch to dry air flow and heat up for dehydration. The dehydration was until 140°C and lasted for 30mins on the elevated temperature before the sample cooled down. The hydration took place by switching to moist air when the sample was stable at 30°C. The dry or moist air flow was purged as a reactive gas, which flowed at 80SCCM. The protective gas was Ar_2, which flowed at 100SCCM. The humidity of moist air was measured by an in-pipe humidity sensor, which was maintained at 85±3% and 29.5±0.5°C, corresponding to a vapour pressure of around 1800Pa. The samples were exposed in a fume cabinet condition (~25°C, 80%RH) for a week to reach the same hydrated state. The samples were carefully weighted at 5.15±0.05mg for each measurement, to avoid the influence of the mass [338].

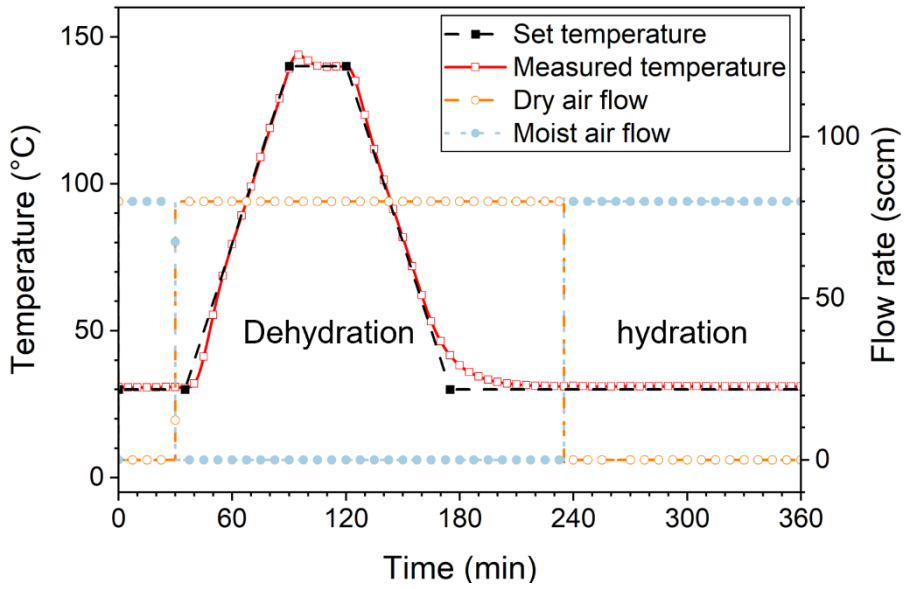


Figure 5-1 temperature and airflow profile used in STA.

5.2.5 Dynamic vapour sorption

The dynamic vapour sorption measurement (DVS) was taken place in a mass-

based vapour sorption analyzer (Beishide, BSD-DVS) at 30°C. The isotherm vapour pressure-jump schemes were used for measurement, as shown in Figure 5-2. The samples were absorbing water at a constant vapour pressure stage until saturation, and then the vapour pressure increased to the next stage. The stages were set to P/P_0=0.1, 0.2, 0.3, 0.5, 0.7 of the saturation vapour pressure (P_0) of 4243Pa at 30°C. The samples were carefully weighted at 10±1mg to avoid the influence of the mass.

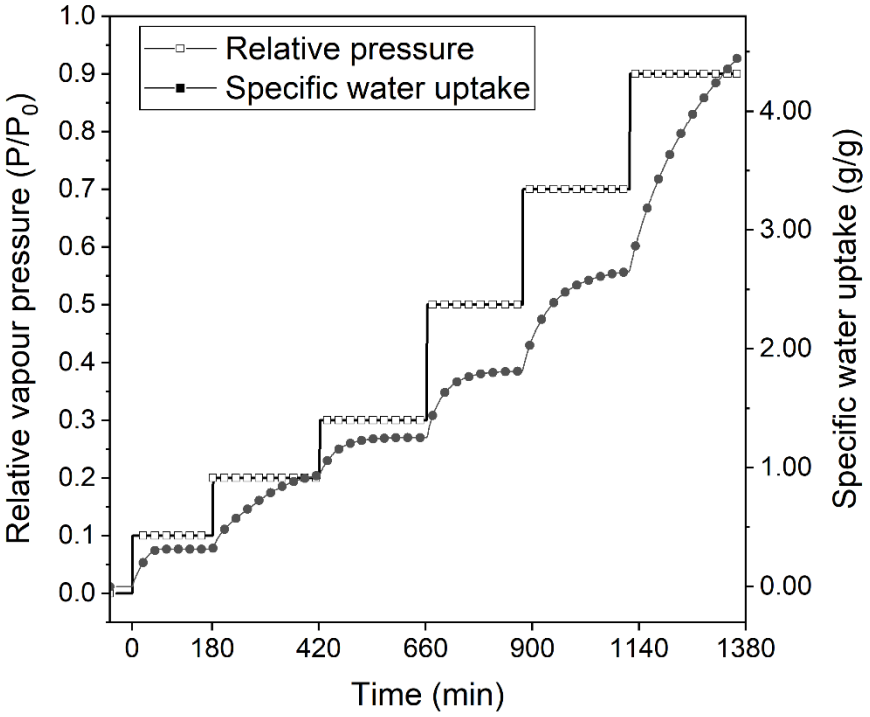


Figure 5-2 The profile of pressure-jumping DVS measurement and the result of pure $CaCl_2$ (solid symbol).

5.3 Result and discussion

5.3.1 Effect of shell thickness on thermal performance

The fabricated encapsulated $CaCl_2$ with a diameter of ~800nm are shown in

Figure 5-3. The capsules were uniform spheres and has the same size distribution among each sample. There was no salt grain was identified outside the capsules, suggesting the encapsulation was successful.

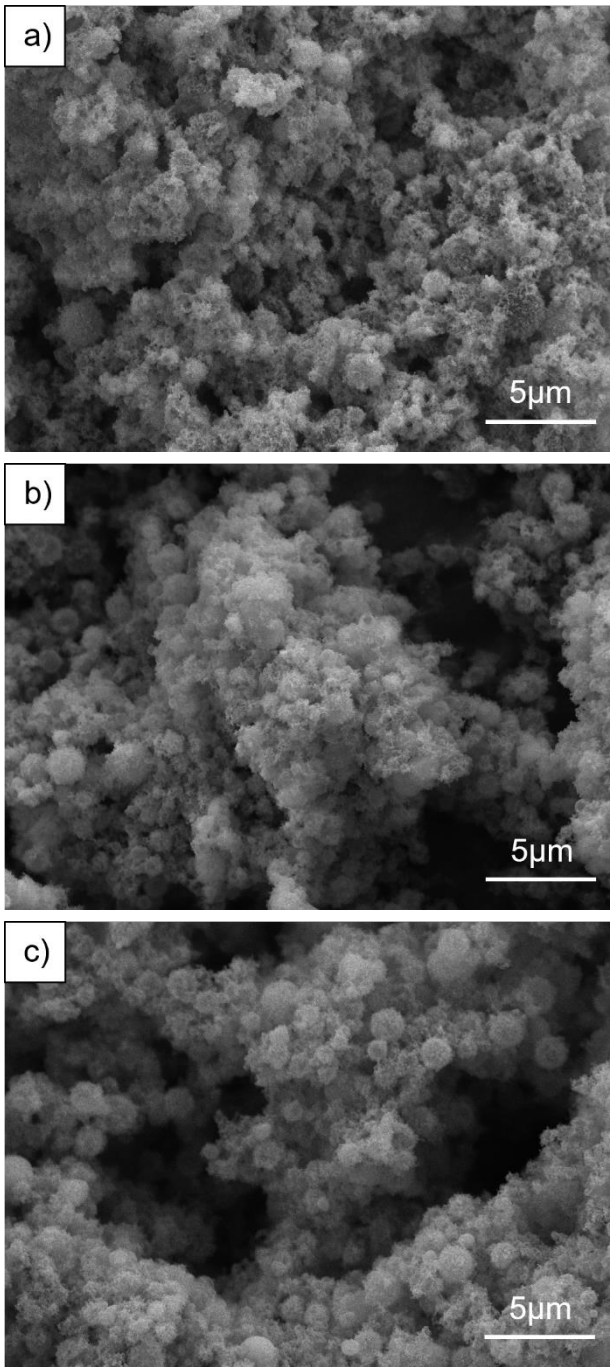


Figure 5-3 SEM images of encapsulated $CaCl_2$ with ~800nm diameter and shell thickness of (a) 25nm, (b) 50nm, (c) 100nm.

The encapsulation structure was further confirmed by STEM-HAADF images in Figure 5-4. There was a significant void inside the encapsulation, due to the volume shrink of salt grain crystallised from the precursor salty solution. The shell thickness was directly measured from the STEM-EDX mapping (see insertions of Figure 5-4a, c, e). The result confirmed the shell thickness was consistent with the designed value of ~25nm, ~50nm and ~100nm.

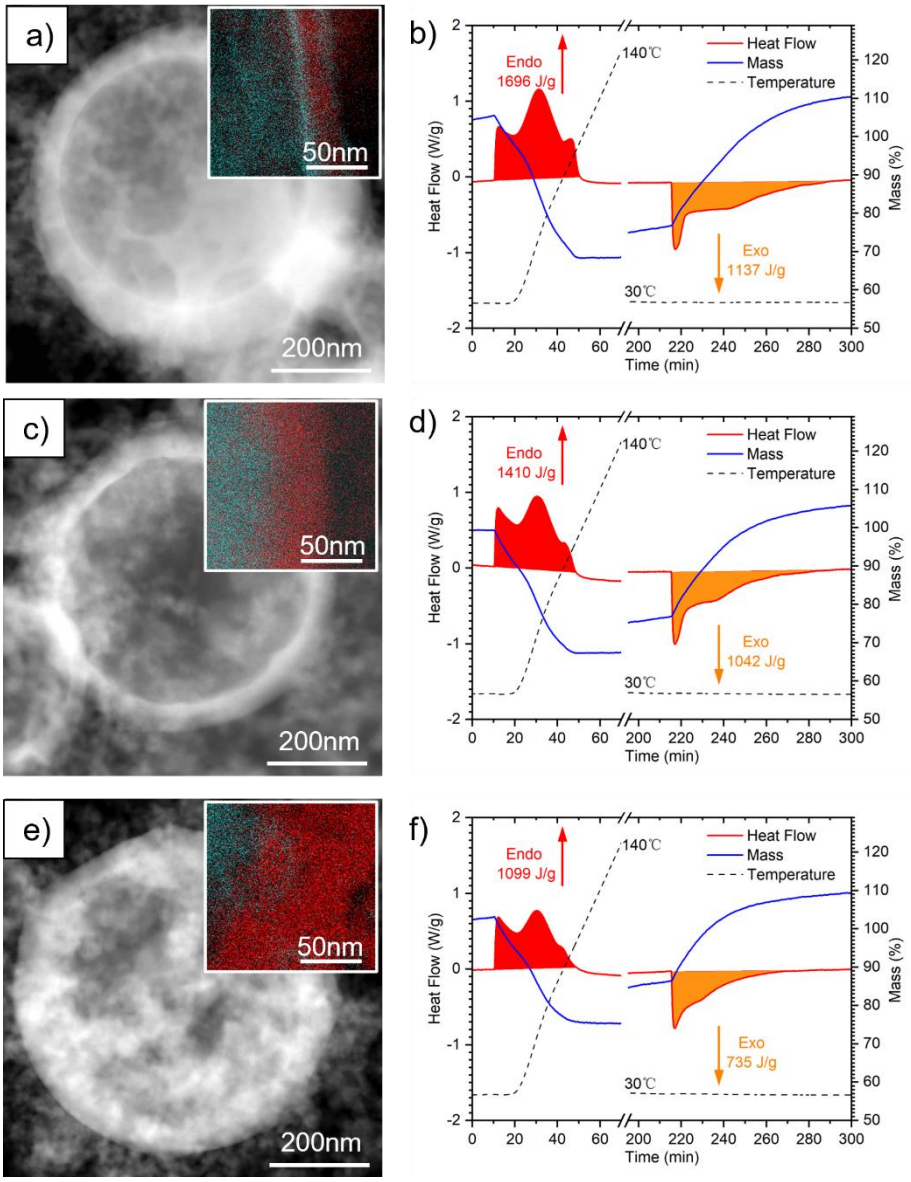


Figure 5-4 STEM-HAADF images and STA of the encapsulated $CaCl_2$ with ~800nm diameter and shell thickness at (a, b) 25nm, (c, d) 50nm, (e, f) 100nm.

The insertion in a, c, and e is the EDX colour-mixed mapping of the local shell, blue represents the elements of Ca and Cl, and red is for Si and O.

In the STA result (Figure 5-4b, d, and f), thermal charging, as well as dehydration, was taking place accompanied by water dried out from the hydrated salt, giving the peaks of endothermic (red). The peaks are composed of three overlayed parts, referring to the transition from the initial deliquesced state to $CaCl_2 \cdot 6H_2O$, followed by $CaCl_2 \cdot 6H_2O$ to $CaCl_2 \cdot 2H_2O$, ends with $CaCl_2 \cdot 2H_2O$ to anhydrous $CaCl_2$. Then the temperature was coming back to 30°C to store energy for a short duration. The following discharging, enabled by purging moisture, gave the exothermic peaks (orange) with a lower enthalpy (compared to the charging), at 1137J/g, 1042J/g, and 735J/g for the 25nm, 50nm, and 100nm samples, respectively. The mass fraction of anhydrous $CaCl_2$ in each dried encapsulation was estimated at 38%, 31% and 22%, corresponding to the enthalpy of 1238J/g, 1009J/g, and 737J/g, for 25nm, 50nm, 100nm samples, respectively. The degradation of measured specific enthalpy according to the shell thickness increases agreed with those estimations. Moreover, the enthalpy differences between endothermic and exothermic were contributed by the evaporation of exceeded liquid water in the initial discharged stage.

The dehydration and hydration kinetics were evaluated by the first-order derivation of mass gain curves (also called difference thermal analysis DTA), see Figure 5-5. In dehydration (Figure 5-5a), it shows similar characteristics in

all the samples, including the peak shapes, and the dry-out temperature/time. In the period of 15 to 45 mins, the dehydration rate shows a higher peak value in the thinner shell samples, but the onset and peak position was the same. It suggests that increases in water loss rate were the result of the high mass fraction of salt rather than the lower diffusivity resistance in thicker shells. The hydration curves show a similar trend. Therefore, it was indicated that the shell thickness effect is minor on the nanoscale.

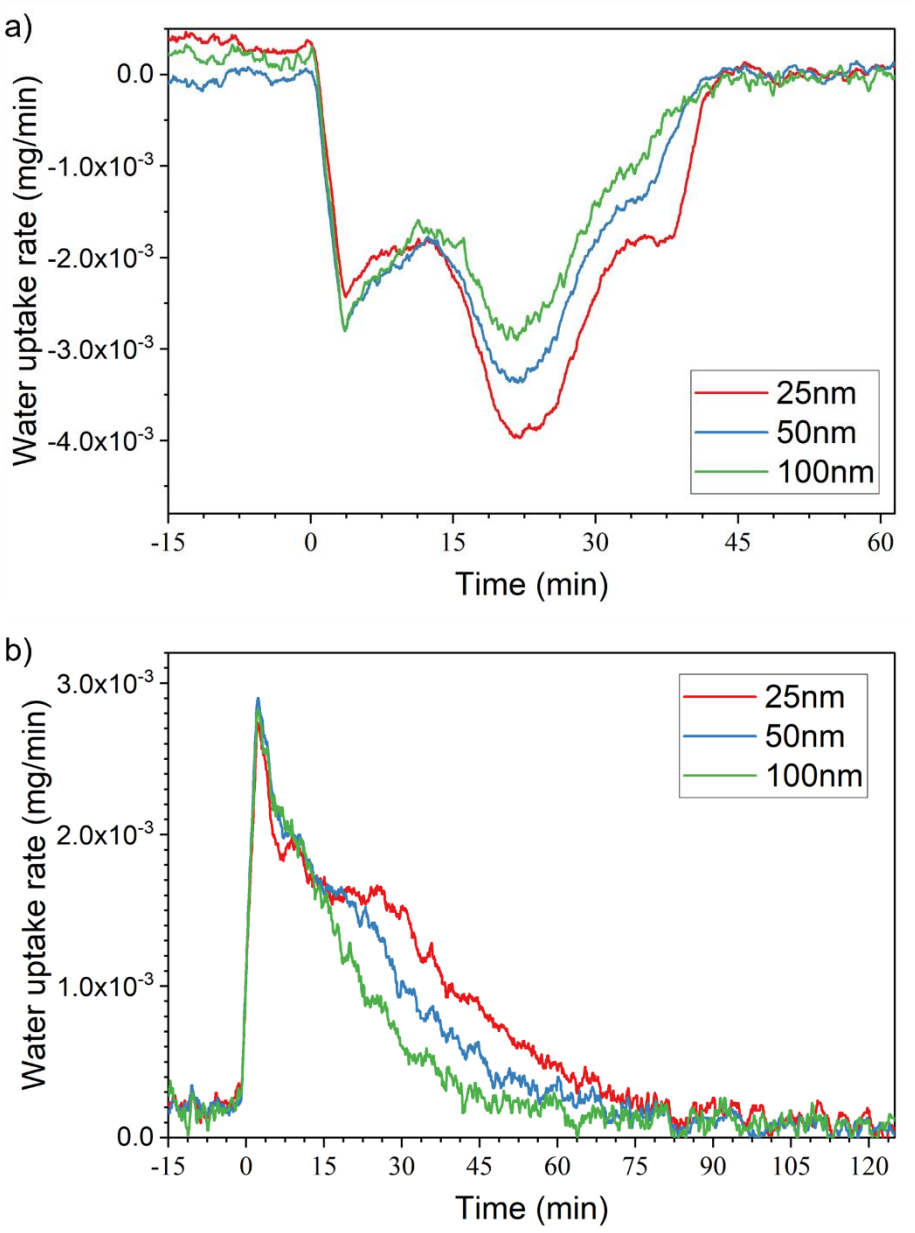


Figure 5-5 Water uptake kinetic of 800nm capsules with different shell thicknesses, a) dehydration, b) hydration.

5.3.2 Effect of encapsulation size on thermal performance

The capsules with different diameters were studied in the same way, as the results are shown in Figure 5-6. By increasing the size of the encapsulation, we found there were a considerable number of buckling capsules in the 8μm sample. Fortunately, the shell was completed. For unconfined pure $CaCl_2$, the grains merged into a bulk, and numerous pores were observed on the surface. The thermal performance and kinetic were evaluated by STA. Compared to the nanoscale encapsulations, the mass change profiles show a delayed dry-out temperature of 5.8°C (consumed an additional ~3mins, 7% of baseline) for 8um capsules and 31.0°C (consumed an additional ~15.5mins, 35% of baseline) for the unconfined salt sample. In the hydrations, the encapsulated salt and raw salt show the same peak values but a few differences in trends. It is suggested that vapour diffusion in the air was the rate-limiting process during the initial period [147]. For the latter long-lasting part, the hydration rate was limited by the water vapour diffusion of the intra-particle. Surprisingly, we found the exothermic energy of pure salt was 2464J/g (based on dry mass), which was only 75% of the 3252J/g enthalpy for fully hydrated to the $CaCl_2{\cdot}6H_2O$ from the anhydrous $CaCl_2$ [339]. It is indicated that a part of the salt was not hydrated and released heat. However, the accumulated gained mass during hydration was already higher than the mass difference between the hydrated and

anhydrous states, suggesting water distribution inside the salt grain was inhomogeneous. As the result, the diffusion of water molecules was somehow hindered through the production layer [148], which formed on the outside of the unreacted grain.

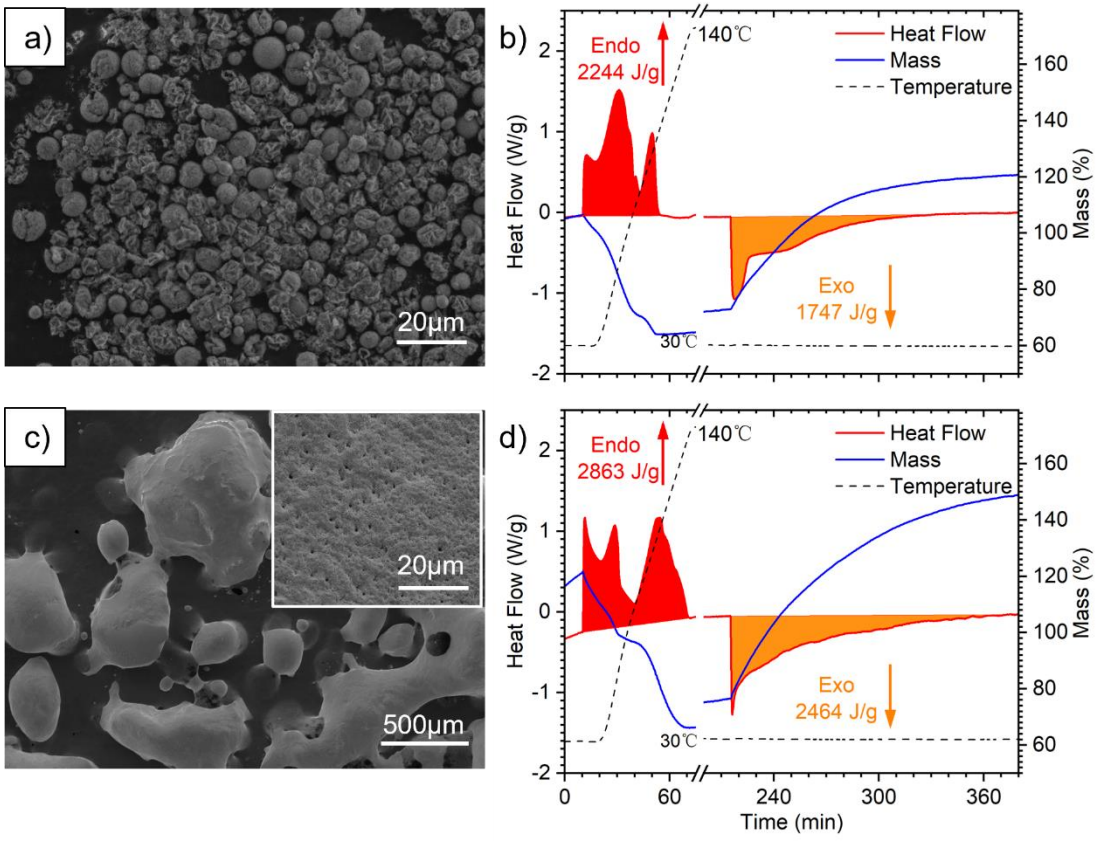


Figure 5-6 SEM and STA results of $CaCl_2$ capsules with different diameters: a, b) capsules of 8μm mean diameter with ~300nm thick shell, 5.12mg for STA measurement, and c, d) unconfined pure $CaCl_2$, 5.2mg for STA measurement.

The kinetic was studied by the pressure-jumping DVS measurements. As shown in Figure 5-7, the breakthrough curve of each pressure stage was compared between different encapsulation sizes.

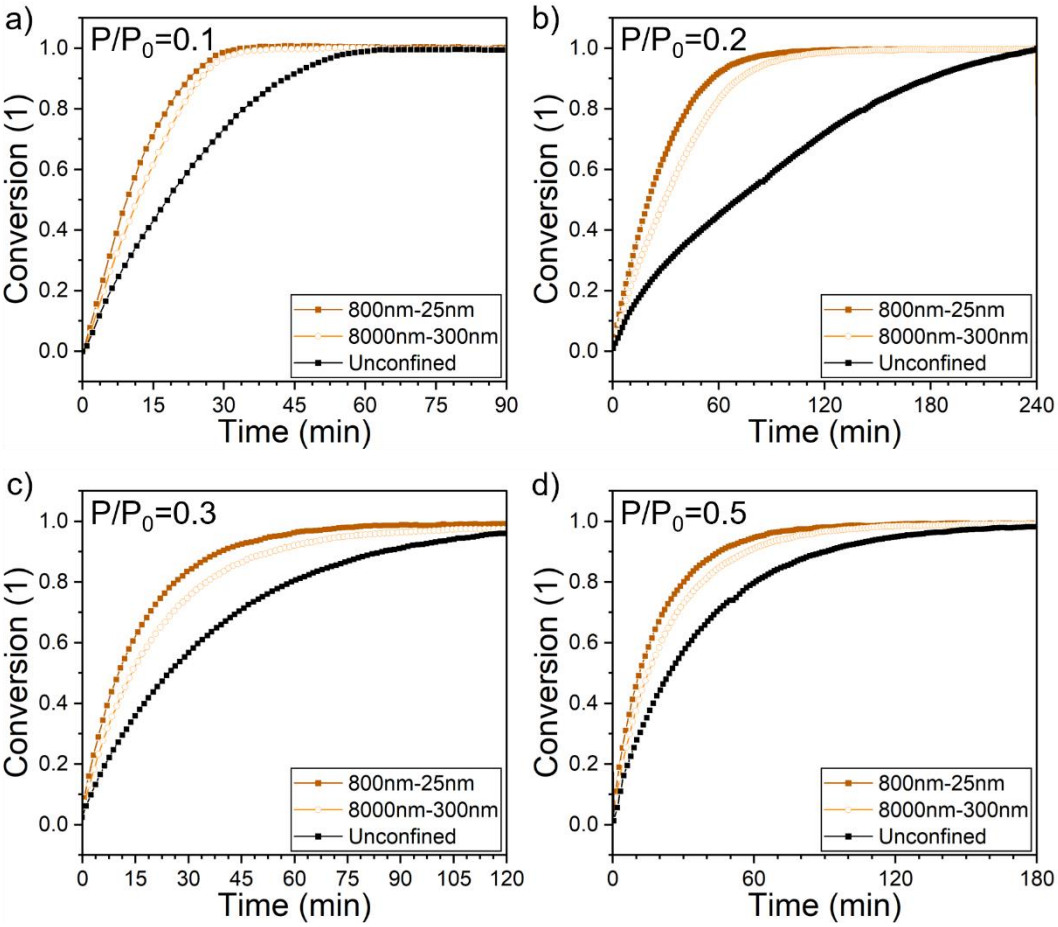


Figure 5-7 Breakthrough curves of encapsulated salt and unconfined pure salt at each P/P_0 stage in DVS measurement.

In all the pressure stages, the conversion rate degraded according to the encapsulation size increases. In the high vapour pressure conditions, it took a long time to equilibria, which links to the increases in specific water uptake. For an in-depth understanding of the hydration mechanism, the breakthrough curves were redrawn to the conversion-conversion rate curves, as shown in Figure 5-8.

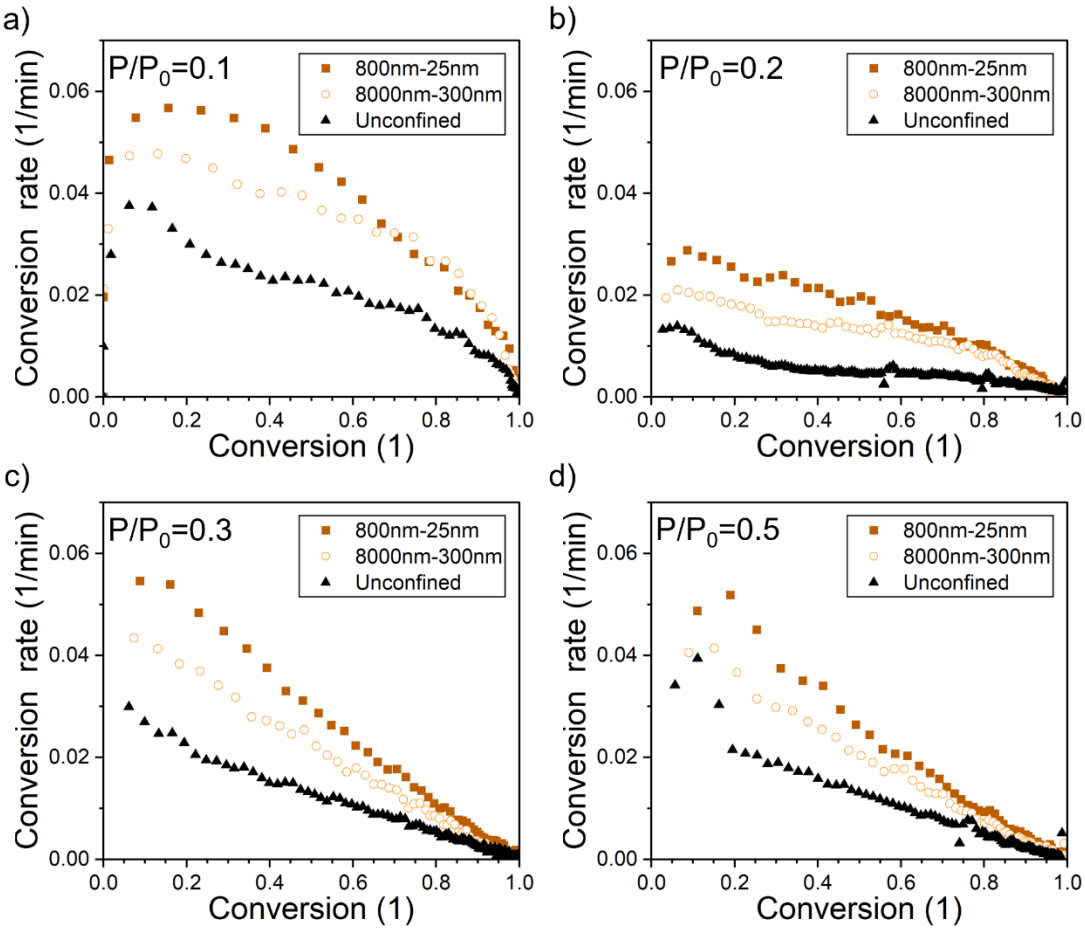


Figure 5-8 the conversion-conversion rate curves of hydration at different vapour pressure

In Figure 5-8a of P/P_0=0.1, the graph shows that there has been a slight increase in the conversion rate when the conversion was between 0 to 0.2. There were followed by a gradual fall in the rest range of conversion. This increase was possible due to the slow nucleation under the low vapour pressure [108], which was described by the Avrami-Erofeyev model [340]. After the nuclei formed, the growth of nuclei become fast as well as the conversion rate increased. The conversion rate reached a peak when the crystals begin to congest the neighbourhood. Then, the degradation in rate was observed, which

was controlled by the shrinking of the reaction interface progress toward the centre of the crystal. In other vapour pressure stages (P/P_0=0.2, 0.3 and 0.5), the figures reveal that there have been steady declines in conversion rate associated with conversion increases. It indicates a first-order reaction mechanism, which was described by the Mampel model [341]. This model is a special case of the Avrami-Erofeyev model, which describes the random nucleation at the surface of crystals and the isotropic growth of the nuclei from the surface to the centre. The rate-limiting step takes place at the internal interface, which is between the unreacted phase and the growing new phase. In all the conditions, the small encapsulated $CaCl_2$ has the highest conversion rate. It highlights the effect of confinement on grain size.

5.3.3 Effects of encapsulation on energy storage efficiency

The above findings conclude the effect of encapsulation on thermal performance. The introduction of a shell reduces the specific reaction enthalpy of pure salt. However, the confinement effect leads to the improvement of reaction kinetic both in hydration (discharging) and dehydration (charging). By simple geometry, it is obvious that a large encapsulation with a thin shell will have a high reaction enthalpy and high energy storage density. But it has a drawback of slow dehydration, which require more energy during thermal charging to maintain the material at elevated temperature. Therefore, it is necessary to consider how to evaluate the effect of encapsulation from the view

of thermal energy storage. For the charging process, we suggest a simple thermal balance relationship to evaluate the efficiency [190]:

$$\eta_{charging} = \frac{stored\ energy}{input\ energy} = \frac{mH_{thermochemical}}{mC_p\Delta T + mH_{thermochemical} + m\phi_{free\ water}H_{free\ water} + qt}$$

Equation 5-1

The numerator represents the thermochemical energy stored in a dry mass m of encapsulated or pure salt. The denominator is the accumulation of them for parts. The first part is the sensible heat cost to bring the material to an elevated temperature ΔT. The second item is the thermochemical energy as well as the enthalpy change during losing the bonded water. The following part includes the energy cost of evaporation ($H_{free\ water}$ is ~2256J/g) of free water in a mass $m\phi_{free\ water}$, regarding the excess water in the STA results. And the last part is the energy cost to maintain the system temperature against the heat dissipation, which is the product of power q (a constant related to the system configuration) and consumed time t. The consumed time depends on dehydration kinetic, in other words, the conversion rate. We consider an idealized scenario, that the sensible heat is fully recovered ($mC_p\Delta T = 0$) and there is no exceeding free water ($\phi_{free\ water} = 0$). Thus, it can be simplified into:

$$\eta_{charging} = \frac{1}{1 + \frac{q}{m\Delta H_{thermochemical}}t}$$

Equation 5-2

In this equation, the dehydration conversion time t for a salt particle with a radius r_p is estimated by integrating the conversion rate $f(\alpha)d\alpha$, as $t = \int_0^1 f(\alpha)d\alpha$. The conversion rate of dehydration is approximately described in

the Linear Driving Force (LDF) model [147], [342]:

$$\frac{d\alpha}{dt} = k_{dehydration}(1-\alpha) \qquad \text{Equation 5-3}$$

Therefore, the full conversion time is:

$$t = \frac{-\ln(1-a)}{k_{dehydration}} \qquad \text{Equation 5-4}$$

To link it to the geometry, the kinetic rate was suggested by the references [343], [344] as:

$$k_{dehydration} = k_m \frac{D_{so}}{{r_p}^2} \qquad \text{Equation 5-5}$$

Where the $k_m = C_{geom}\exp(-E_a/RT)$ considers the geometry effect C_{geom} and the reaction condition effect. Finally, the efficiency of thermal charging is simplified into:

$$\eta_{charging} = \frac{1}{1+C_{dehydration}\frac{{r_p}^2}{\Delta H_{thermochemical}}} \qquad \text{Equation 5-6}$$

Where the $C_{dehydration} = -\ln(1-a)q/mk_mD_{so}$ is a constant.

For discharging, the reaction is possible to be kinetically hindered in low vapour pressure conditions [111], [163], [345], and result in degradation in stored energy. Unfortunately, we found it difficult to be evaluated this effect either in theoretically or experimentally. Therefore, we assumed the discharging occurs in a high vapour pressure condition, in which the salt can be fully reacted, and all stored energy is released ($\eta_{discharging} = 1$).

Besides, the thermochemical energy storage density $\Delta H_{thermochemical}$ is monotonously increased through the encapsulation size increased, we define $\eta_{energy\ density} = H_{encapsulated}/H_{pure\ salt}$ as the efficiency of encapsulation. The total efficiency is proposed as $\eta = \eta_{charging}\eta_{discharging}\eta_{energy\ density}$. The physical meaning of this expression is the full-cycle efficiency of encapsulated salt compared to pure salt. As the result, we predict the total efficiency with different $C_{dehydration}$, as shown in Figure 5-9.

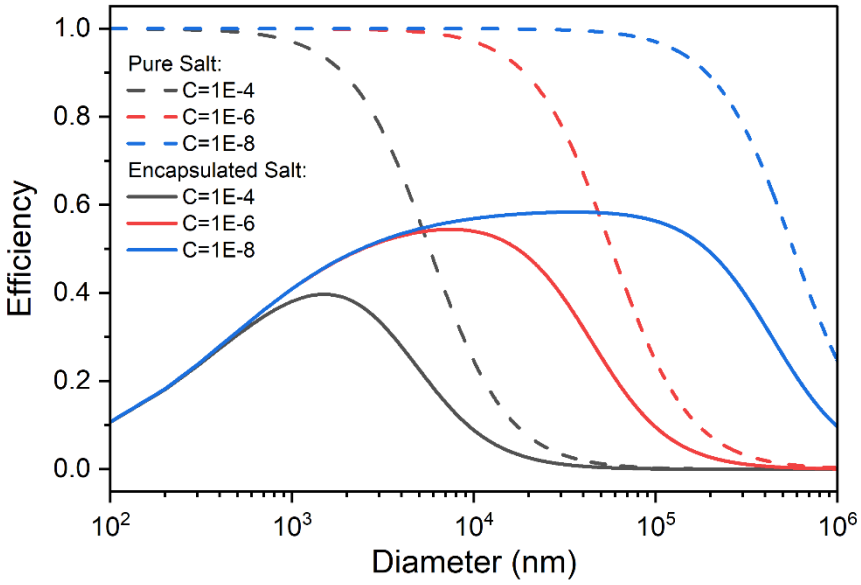


Figure 5-9 The efficiency of encapsulated salt compared to pure salt

For the different conditions represented by different $C_{dehydration}$, the efficiency reaches the maximum value at 39.7%, 54.4%, and 58.3% in encapsulated salt with an optimised diameter at ~1.5μm, ~7μm, and ~35μm, respectively. The major degradation of the efficiency is the energy storage density loss due to the participated mass of the shell in the encapsulation structure. Therefore, the areas for further research should be focused on developing a better material

for shells.

5.4 Conclusion

In this study, we discussed the thermal performances of different encapsulated salt. By increasing the thickness of the shell, we found the influences on reaction kinetic are negligible, and the rate-limiting process has been and remains on the moisture diffusion outside the encapsulation. On the other hand, the encapsulation with increased diameter presented a considerable degradation in dehydration kinetic. Determined by STA, an additional 7% time consumed was found in the encapsulated salt with a diameter of 8μm, compared to the 800nm encapsulation as the baseline. For unconfined pure salt, there was an extra increase in dry-out temperature and time. The kinetic of those salts are studied by DVS in the following. In the hydration process, the smaller encapsulated salt always has a higher conversion rate. It highlights the effect of encapsulation on the improvement of the reaction kinetics. In large unconfined pure salt particles, the hydration kinetic was hindered in low vapour pressure conditions, leading to uncompleted heat discharging.

To evaluate the performance of the encapsulated salt, we suggested a total efficiency, by combining the encapsulation efficiency, charging efficiency, and discharging efficiency. The result gives in a monotonous descent for pure salt according to the 2^{nd} power of particle radius. For encapsulated salt, considering the encapsulation efficiency is in the opposite trend, we concluded the

maximum efficiency of encapsulated $CaCl_2$ should be reached at a diameter range of ~1.5-35μm. It is suggesting that the efficiency can be further improved by alternating to a stronger shell material and concentrated salt solution. The corresponding optimised size should be changed in those conditions. In conclusion, with both experimental and theoretical analysis, this study gives an in-depth understanding of how to use encapsulated salt from the view of engineering and application.

6 Encapsulated salt for thermochemical energy storage with fluidised bed reactor

This chapter examines the utilization of encapsulated salt in a high-performance thermochemical energy storage through the use of a fluidized bed reactor. Section 6.1 introduces the background of sorption-based thermochemical energy storage. Section 6.2 describes the experimental method for fabricating and characterising the Micro$CaCl_2$, Nano$CaCl_2$. Section 6.3 discusses the performance of Nano$CaCl_2$, compared to the Micro$CaCl_2$ and pure salt. Section 6.4 concludes the finding in this chapter.

6.1 Introduction

Thermal energy currently accounts for over 50% of the world's final energy consumption, predominantly met by fossil fuels. The decarbonisation of thermal energy, therefore, represents one of the biggest challenges for achieving the net-zero target around 2050 [1], [2]. The preliminary results of a recent study by the Royal Society suggest the need for short-, medium-, and long-term energy storage technologies. For the UK alone, a future renewable-energy dominant energy system requires ~100-120GW/100-200GWh, ~100-130GW/2-6TWh and ~70-80GW/~35-40TWh for short-, medium- and long-term storage, respectively [4]. A significant amount of work addresses short-term energy storage e.g., lithium-ion & sodium-ion batteries, supercapacitors, and flywheels [5]; a much smaller amount of effort has been made on the medium- and long-term energy storage [7], [8]. The current global energy storage installations are around 200GW, which is insufficient for meeting the needs of even a relatively small country such as the UK. Thermal energy storage (TES) has the potential to meet the medium- and long-term energy storage requirements, particularly thermochemical storage (TCS), one of three TES technologies. The TCS technology is based on reversible reactions and/or sorption processes. Taking solid-gas based TCS as an example, it can be illustrated by:

$$A_{solid} + HEAT \leftrightarrow B_{solid} + C_{gas}$$

The advantages of TCS-based technology include zero energy loss during storage, making it particularly suitable for long-term applications [67], [84], [225], [346]; the use of inorganic compounds as the storage material, ensuring cost-effectiveness [95]; and the provision of high energy density [81], leading to a compacted system.

This work focuses on sorption-based TCS using hydratable salts as the storage material aimed for low- and medium-temperature applications (<150°C) [72], [82]. TCS based on such materials store the heat in chemical bonds of anhydrous inorganic salts and generates heat by reacting with water vapour. Several experimental studies have shown the feasibility of the TCS using pure salts at various scales [204], [206]. However, pure salts present poor structural stability problems due to deliquescence [112] and caking [347], leading to significant degradation in the reaction kinetics and energy storage density after a very small number of thermal cycles [200], [348]. Pure salts are also unfavourable due to the slow diffusion of water molecules through large solid grains, which limits the reaction rate and power output [99]. To address the above challenges associated with pure salts, TCS composites, particularly the so-called salt-in-matrix, have been proposed. This facilitates small-sized salt grains dispersed within a matrix, providing an enhanced mass transfer pathway for water vapour, and improved heat transfer in the reacting bed. Aristov and Levitskij are among the first to pioneer salt-based composites [57], [349]. Work in this area has continued since then and the 'salt-in-matrix' remains an area of

the TCS research community [350]. The overall performance of such composites depends on the porous structure of the host matrix [131] and the amount of salt-occupied volume in the pores [121]. For the former (pore structure), a recent development has demonstrated the successful use of a porous host with aligned pores [351]; whereas for the latter, increased content of salt in the pores makes it possible for deliquesced salt to leak out [117], [142], [143], [352]. Recent studies [118], [138], [148], [149], [353] have also shown that high salt content composites experience kinetically hindered hydration due to stagnant water vapour in the matrix. This results in a mass transfer barrier which is subject to the pores being narrowed or clogged by the expanding salt. We propose the use of the salt micro-/nano-encapsulation method to resolve these challenges. Encapsulation is an effective method of preventing salt leakage. This effect has been demonstrated in some recent studies on the use of macro-encapsulation as a skin for bulk salt-in-matrix composites [171], [354], [355]. Our proposed encapsulation is radically different, characterised by a structure with individual micro-/nano- salt particles/agglomerates as the core confined within a water vapour permeable shell, so-called “salt capsules”. In addition, in our approach there are extra gaps between the capsules, providing additional channels for water vapour transport, increasing the rate of reaction, and eliminating the kinetic hindrance. In contrast to salt-in-matrix, our salt capsules are in the form of fine particles, allowing them to be used in a fluidised bed reactor within an open/closed TCS system with a separate storage tank.

[188], [212]. A major advantage of such a system is its high flexibility in scheduling the charging and discharging processes by supplying the amount of energy (material) according to the demand/energy input. This configuration also benefits from a lower pressure drop than a fixed bed reactor at high flow rates [226], a significant improvement in vapour transport and heat transfer [220], the provision of high specific power [215] and a high theoretical thermal efficiency [188]. In addition, storage capacity is scalable and independent of reactor power, providing further flexibility in system sizing.

However, much less effort has been made into the encapsulation of salt. A few studies can be found on, for example, the encapsulation of salts at nano- [166], [167], micro- [128], [168], and macro- [169] scales. These published studies have employed multi-step protocols that are complicated and expensive. Crucially, these methods are incapable of achieving size/geometry manipulation, which is important for optimising the thermal performance of the TCS [99], [314]. Furthermore, the cost-effective and resource-efficient production of salt capsules is also a significant obstacle.

Here, we demonstrate an encapsulation strategy for making salt capsules at the nanoscale and microscale, using low-cost raw materials and a simple process based on Pickering emulsion. Experiments were performed on the thermochemical reactions of the fabricated capsules. A significant extent of enhancement in reaction kinetics was observed. The encapsulated TCS composite had an energy density of over 1700 kJ/kg, which is approximately

an order of magnitude greater than that of latent heat storage under similar temperature conditions. Thermal cycling experiments showed excellent stability of the TCS composite material. Laboratory-scale experiments demonstrated the fluidisation of fine salt capsules for the first time, enabling a long-duration discharge process over 12 hours.

6.2 Experimental section

6.2.1 Materials

Calcium chloride dihydrate ($CaCl_2 \cdot 2H_2O$, 99%), Lithium Chloride (LiCl, 99%), Potassium carbonate (K_2CO_3, 99%), Magnesium sulfate heptahydrate ($MgSO_4 \cdot 7H_2O$, 98%), Tetraethyl orthosilicate (TEOS, 99%) was purchased from Energy Chemical (www.energy-chemical.com, China). Cyclohexane (C_6H_{12}, 99%) was purchased from Greagent. Hydrogen chloride (HCl, 36%w/w in H_2O) and Silica gel were purchased from Aladdin (www.aladdin-e.com, China). Water was obtained from a lab purification system, which has a >18MΩ resistivity. Hydrophobic fumed silica nanoparticle Aerosil R972 Pharma was kindly donated by Evonik.

6.2.2 Emulsion template preparation

Typically, a brine-in-oil Pickering emulsion was prepared by dispersing 5 to 20 mg/ml R972 Pharma nanoparticle in cyclohexane. A sonication device (Scientz, IID 20kHz, 600W) with a 6mm standard horn was used to disperse a batch of

approximate 20ml suspension for 2 hours (80% power, 4s/4s on/off) in an ice bath. Then, 1ml salt aqueous solution with pH=2, adjusted by 1M HCl, was added into the suspension at 30°C. The cloudy microemulsion was obtained by a further sonication treatment without an ice bath for 10mins (80% power, 8s/4s on/off)

6.2.3 Fabrication of the Nano$CaCl_2$ and Micro$CaCl_2$

$CaCl_2 \cdot 2H_2O$ was dissolved in water at 50°C to form a saturated solution with a density of 1.58g/ml (approximately CaCl2 at 0.9g/ml), followed by adding 1M HCl to adjust the pH to 2, then cooled back to 30°C to form a supercooled solution. For Nano$CaCl_2$, the suspension of 15mg/ml R972 Pharma nanoparticle in cyclohexane was prepared according to the above protocol. There was 0.5mg/ml R972 Pharma nanoparticle in cyclohexane for Micro$CaCl_2$. Then, 1ml salt solution was added into the 20ml suspension at 30°C, followed by emulsification. In the next step, 1ml (for Nano$CaCl_2$) or 0.5ml (for Micro$CaCl_2$) TEOS was added into the prepared emulsion drop by drop, followed by mixing via handshaking. The emulsion was then held stationary for 12 hours to form the shell. The product was collected by gently evaporating the oil phase in a fume cabinet and then in the oven at 120°C.

6.2.4 Fabrication of the composite of $CaCl_2$-in-silica gel

The CaCl2-in-silica gel was prepared following the reference [119]. Hydrophilic silica gel was washed with ethanol, followed by DI water. Then, the silica gel

was dried in oven at 200°C for 3 days. The treated silica gel was immersed in $CaCl_2$ aqueous solution and slowly dried in an oven at 60°C. The morphology of obtained CaCl2-in-silica gel is shown in Figure 6-1. The EDX analysis confirmed the mass fraction of anhydrous salt was ~50% in the composite.

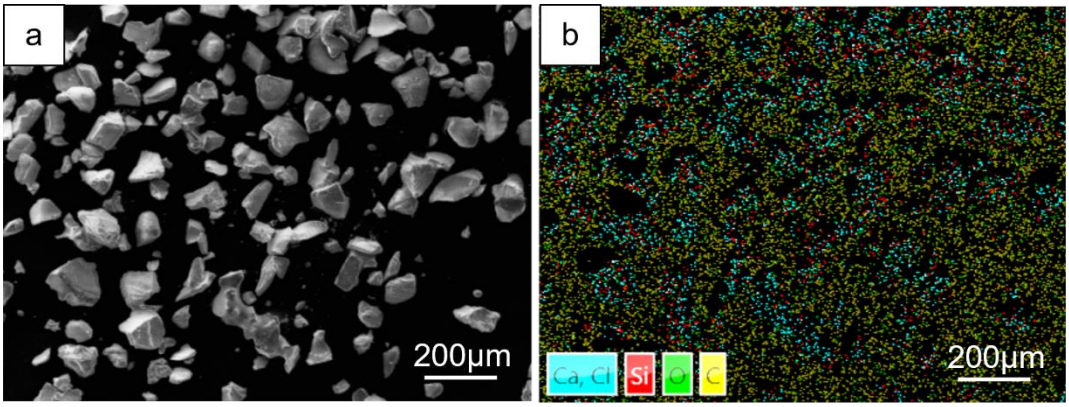


Figure 6-1 The SEM images and corresponding EDX colour mixed mapping of $CaCl_2$-in-silica gel composite.

6.2.5 Morphology of Nano$CaCl_2$ capsules

Approximately 10mg of Nano$CaCl_2$ were re-dispersed in 10ml cyclohexane in a sonication bath for 10mins. A 10µL suspension was then dropped on an SEM stub with carbon tape. The samples were coated with Pt for 10mA and 60s before measurements. An SEM (TESCAN MIRA3) was used for the analyses operated at 20kV and SEM-EDX mappings were captured by an Oxford Instrument EDX.

TEM micrographs were obtained with Thermo Fisher FEI Talos F200X G2 operated at 200kV. The sample preparation protocol was the same as that for the SEM analyses. The STEM-EDX mappings were taken by using a Gatan

EDAX EDX.

6.2.6 XPS study of Nano$CaCl_2$ Capsules

XPS investigation was performed by using a Thermo Fisher ESCALAB Xi+ X-ray Photoelectron Spectrometer. The powder sample was fixed on carbon tape. The original surface signal was first collected for calibration using an adventitious carbon peak at 284.8eV. Then, the sample surface signal was collected after first cleaning with an Ar ion beam for 2s. The depth profile was collected by Ar ion beam etching for the 20s. The strength of the ion beam used was 4.0 keV (about 2.34nm/s for 1mm Ta_2O_5).

6.2.7 In-situ XRD and Raman microscopy study

Temperature-controlled XRD was conducted in the 9kW Rigaku SmartLab with an Anton Paar temperature-controlled stage. The stage was used without a lid and the powder sample is loaded in a steel holder assembled on the heater. The heating/cooling rate is 5°C/min. There is 5 mins equilibrium time before each scan. The test room maintained ~75%RH at 25°C during the experiment. In-situ Raman testing was measured in a Linkman Stage (THMS600) via Horiba microscope (LabRAM HR Evolution), and a 532nm laser was used with a 50X objective lens.

6.2.8 Characterization of kinetic and thermal performance

Simultaneous Thermal Analysis (STA) was performed in a Netzsch STA 449 F1

Jupiter equipped with an S-Type thermocouple. The nitrogen was purged into the furnace with a flow rate constant at 80SCCM. The profile of temperature and gas is shown in Figure 6-2. During the hydration, a homemade humidifier is used to add moisture to dry nitrogen. The purged wet nitrogen was measured by an in-pipe sensor ahead of the furnace inlet, which maintained around ~28°C and ~80%RH during the test.

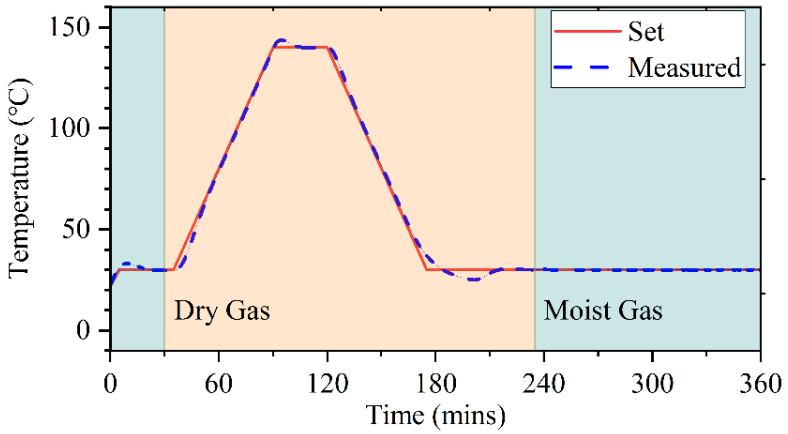


Figure 6-2 Temperature and reactive gas profile in STA

Dynamic Vapour Sorption (DVS) was performed with a 3H-2000PS Dynamic Vapour/Gas Sorption Analyzer (Beishide Instrument Technology (Beijing) Co., Ltd.). Samples of similar mass (15mg) were tested in the quartz crucibles at the same time. The pure salt was ground powder. The samples were first dried at 180°C for 2 hours under a dry nitrogen flow, followed by cooling to 30°C with the same flow. Water uptake (isothermal sorption) was then measured by raising the relativity humidity (vapour pressure) in a controlled step-by-step manner. This is called a "pressure jump test", and the exact procedure has already been described in Figure 5-2. A cycling test was carried out immediately

after the first set of pressure jump tests. The condition used for cycling includes: 2.5 hours of hydration at 30°C 90%RH, followed by 1.5 hours of dehydration around 180°C and 0.5 hours of cooling back to 30°C. The heat rate was 3°C/min and the cooling rate was 5°C/min. A total of 50 cycles were tested. A further set of pressure jump tests was performed for the cycled samples. The samples were not changed during the whole test.

Optical microscopy dynamic observation is carried out on an IKA heating plate under a Mitutoyo measuring microscope, as the setup is shown in Figure 6-3. The scale has been carefully calibrated with a standard ruler at the beginning. The procedure consists of 30 minutes of dehydration at 150°C, and 30 minutes of hydration at ambient temperature. The environment was maintained at ~28°C and ~60%RH, which allow the salt to reach full deliquescence at ambient temperature.

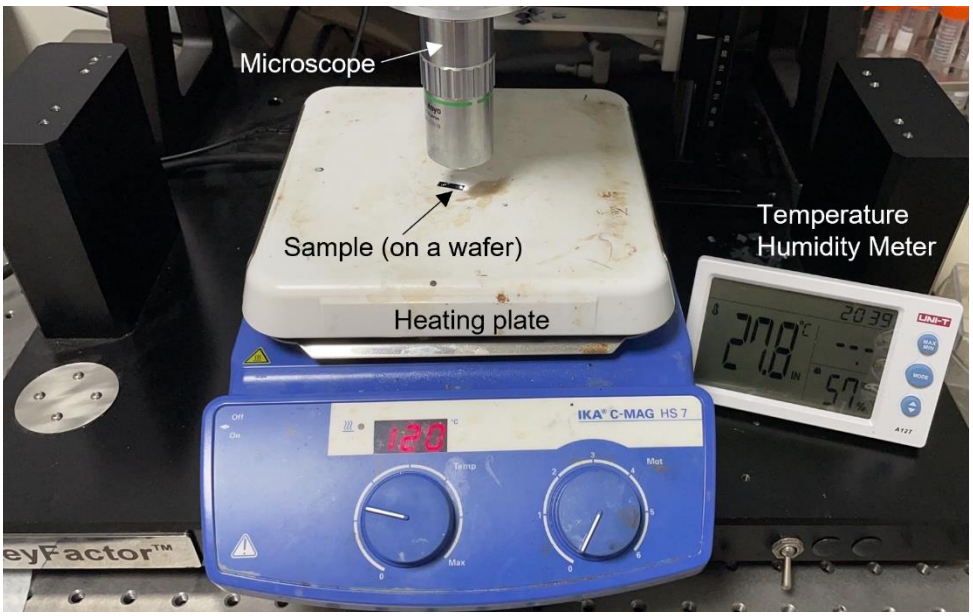


Figure 6-3 Setup of Microscopic dynamic observation.

Thermogravimetric analysis was performed with a Mettler Toledo TGA2. For dehydration kinetics, pure $CaCl_2$ and $NanoCaCl_2$ powders were placed in a fume cabinet for a week to reach a water sorption equilibrium (~22°C, 70-80%RH). Then, different amounts of the samples were weighed and placed in 70μL crucibles made of aluminium oxide. Measurements were taken from 25°C to 200°C with a constant ramp of 2.5°C/min under a dry nitrogen atmosphere.

6.2.9 The conversion profile model fitting for reaction kinetic

Sögütoglu et al. [108] suggested three possible rate-limiting processes of the hydration kinetics: a) nuclei-growth in metastable zone; b) shrinking of advancement reaction interface; and c) diffusion of water through product layer. These factors may occur individually or in parallel, depending on the conditions (e.g., grain size, vapour pressure). These processes can be identified by fitting the conversion profile to an appropriate reaction model from [356]. The conversion (reaction) rate can be parameterized in terms of three major variables: the temperature, T; the extent of conversion, a; the pressure, P as follows:

$$\frac{da}{dt} = K(T)f(a)h(P)$$

In our case, it was isothermal and isobaric thermochemical reaction during the DVS test at each vapour pressure, $K(T)$ and $h(P)$ are constant. Thus, the reaction rate is determined by $f(a)$, which is a predefined model describing a physical mechanism. To simplify the data processing, the integral form equation

was used to estimate the parameter and fit the curve, as written below:

$$g(a) = kt$$

where k is the reaction rate constant and $g(a)$ is the integral of $f(a)$, which should be a given function of a, as listed in Table 6-1. We tried every model in the Table and pick the most appropriate model to fit the data.

Table 6-1 Models used in the profile fitting.

Model (Code)	**Integral form** $g(\alpha) = kt$
1-D diffusion (D1)	α^2
2-D diffusion (D2)	$((1-\alpha)\ln(1-\alpha)) + \alpha$
3-D diffusion-Jander (D3)	$(1-(1-\alpha)^{1/3})^2$
Ginstling-Brounshtein (D4)	$1-(2/3)\alpha-(1-\alpha)^{2/3}$
contracting area (R2)	$1-(1-\alpha)^{1/2}$
contracting volume (R3)	$1-(1-\alpha)^{1/3}$
Avrami-Erofeyev (A2)	$[-\ln(1-\alpha)]^{1/2}$
Avrami-Erofeyev (A3)	$[-\ln(1-\alpha)]^{1/3}$
Avrami-Erofeyev (A4)	$[-\ln(1-\alpha)]^{1/4}$
First-order (F1)	$-\ln(1-\alpha)$
Second-order (F2)	$[1/(1-\alpha)]-1$
Third-order (F3)	$(1/2)[(1-\alpha)^{-2}-1$

6.2.10 Demonstration of a fluidised bed reactor for NanoCaCl$_2$

The fluidised bed test rig is an open system as shown in Figure 6-4. We used compressed air from a compressor. A pressure regulator was used to control the gauge pressure around 50kPa and was connected to a set of dry columns filled with silica gel to dry the airflow. The dried air flow rate was controlled by a

flow controller (FCM, max. 50L/min, CKD, Japan). Two switch valves were used to switch the gas flow between humidify line and bypass. The humidifier consisted of a 20L stainless steel vessel with a jacketed heater. The humidification process was achieved by blowing dry air into the water in the tank and the humidified air flows out of a pipe connected above the water level. A heater was used to keep the temperature slightly above the ambient temperature, so that the water continues to evaporate.

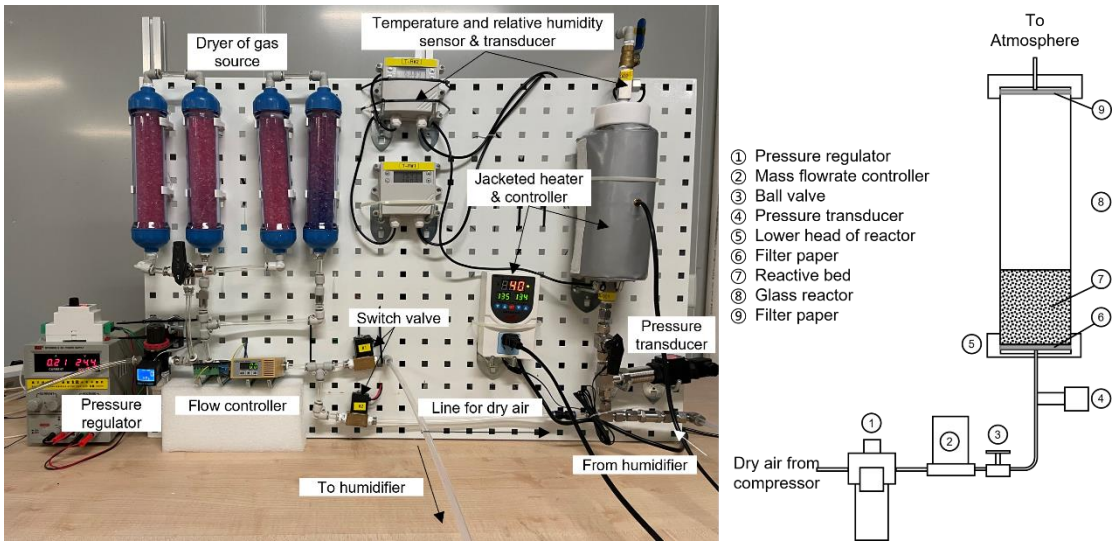


Figure 6-4 Design of fluidised bed thermochemical test rig.

The reactor consists of a PTFE membrane filter and PTFE head (see Figure 6-5) at the inlet and outlet, and a round borosilicate glass tube as the test section with an internal diameter of 50 mm and a length of 140 mm. A jacketed heater is fitted to the outside of the glass tube to provide heat input during the charging process and to act as a thermal insulator. The reactor can be isolated to maintain storage state by closing two isolated valves located in the inlet and outlet of the reactor. The temperature and relative humidity at the inlet and outlet

are directly measured by the in-pipe sensors. The inlet and outlet vapour pressures are converted from these data using the saturation vapour pressure conducted from August-Roche-Magnus equation. A K-type thermocouple is mounted on the outer wall of the reactor at mid-height to measure the bed temperature. Due to the thermal resistance of wall, this measured temperature is slight lower than the bed temperature. The outlet temperature is measured by a thermocouple inserted in the reactor and above the outlet filter.

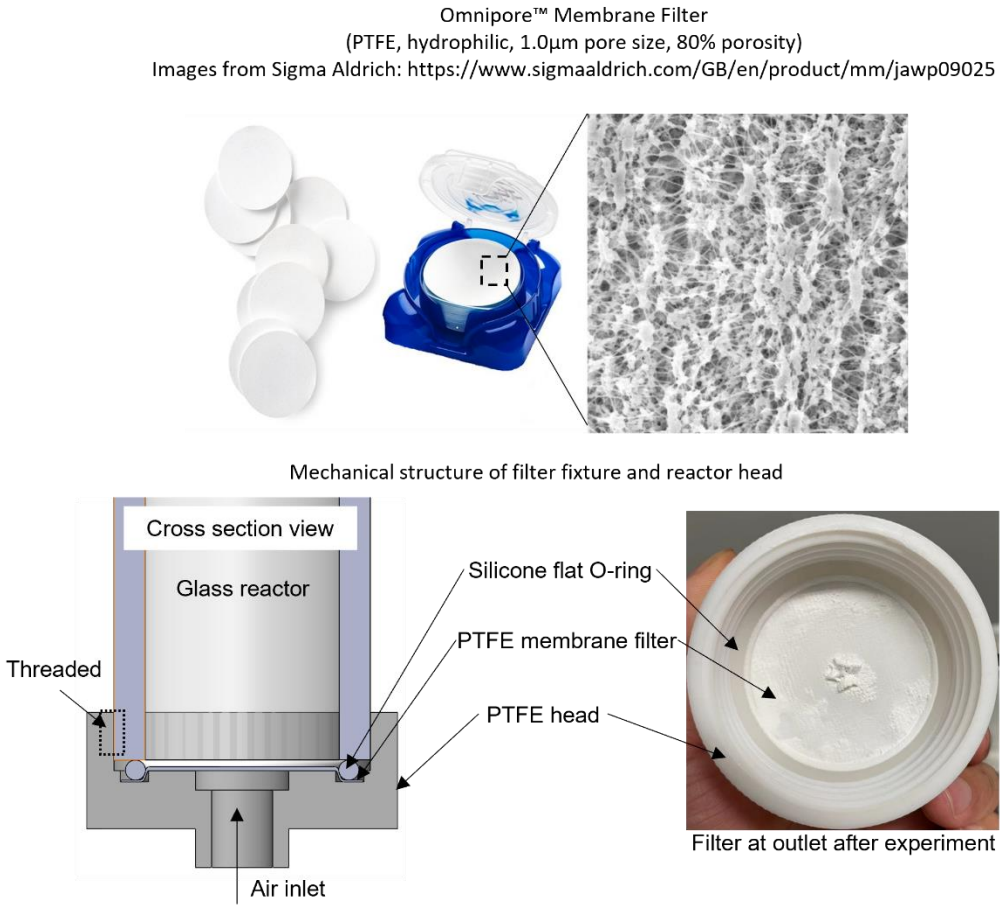


Figure 6-5 Details of reactor and PTFE membrane filter

6.3 Result and discussion

6.3.1 Pickering-emulsion templated yolk-shell silica nanocapsules for thermochemical energy storage

Thermochemical salt capsules were fabricated from the template of size-tailorable Pickering emulsions containing nanoparticle-stabilised droplets dispersed in an immiscible liquid. Figure 6-6 illustrates the process. An aqueous saline droplet covered with hydrophobic nanoparticles (NPs) is suspended in a continuous oil phase to form the water-in-oil (W/O) emulsion. These NPs are strongly bound to the W/O interface and exhibit irreversible adsorption [238], [239], [263]. The NP layer forms a physical barrier between the droplets, making the droplets stable against coalescence and providing a facile and reproducible template for encapsulation [182], [251].

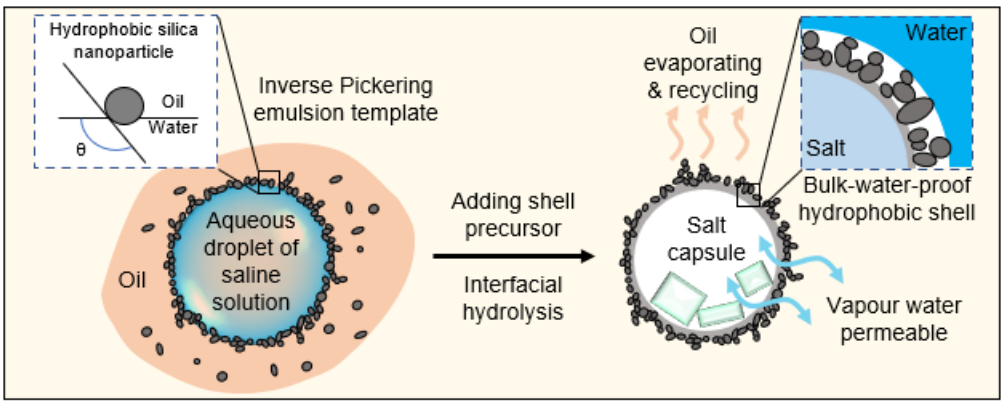


Figure 6-6 Synthesis pathway, and Illustration of Pickering emulsion templated encapsulation and structure of the designed capsules.

The type of Pickering emulsion (W/O or O/W) depends on the wettability of the NPs. For the W/O emulsion, we chose commercial flame pyrogenic

hydrophobic modified silica NPs (with a massive -Si-CH_3 group on the surface) [357] as the Pickering emulsifier. These NPs are aggregates containing many primary particles of about 16nm in size (see Figure 6-7).

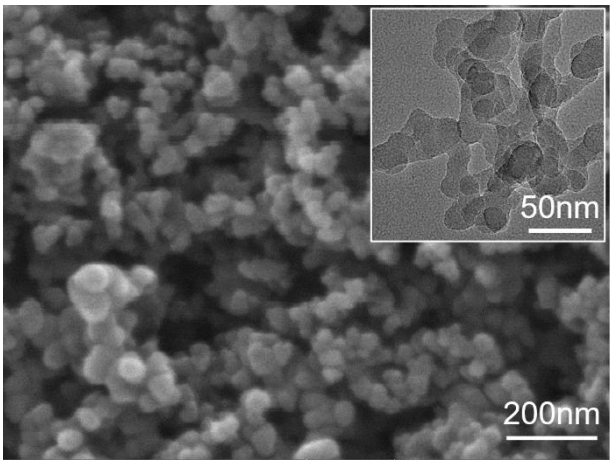


Figure 6-7 SEM and TEM images of R972 Pharma fumed silica nanoparticle.

The wettability of the NPs was confirmed by measuring the contact angles of water and cyclohexane (oil phase) on the surface covered by the NPs, which were 152° and 14°, respectively (Figure 6-8).

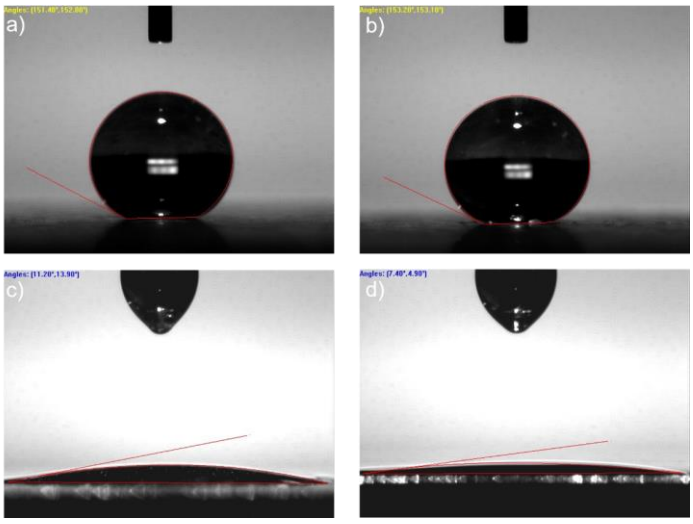


Figure 6-8 Contact Angle of R972 Pharma coated wafer: a) DI Water; b) Solution of 20%wt $CaCl_2$ in Water; c) Cyclohexane; d) Solution of 20%wt $CaCl_2$ in Ethanol.

The type of emulsion is determined by the formation of white sediment at the bottom after a few minutes of standing, with this bottom layer being the W/O emulsion and the clear oil phase on the top (Figure 6-9).

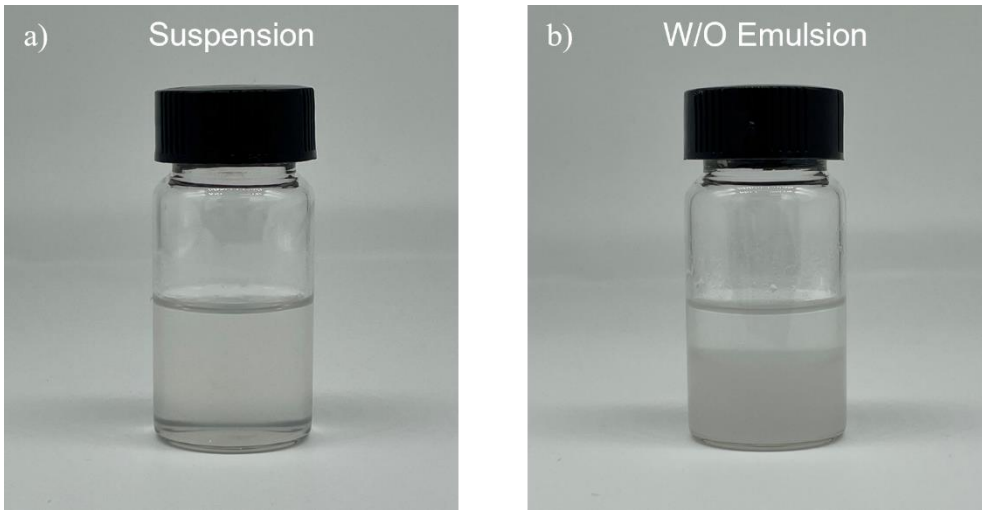


Figure 6-9 Photo images of a) Silica NP suspension (15mg/ml in cyclohexane) and b) inversed emulsion of $CaCl_2$ aqueous solution in cyclohexane (10%v/v)。

Aggregates of NPs adsorb onto the W/O interface and form a nanoscale homogeneous solid film to stabilise the interface [358]. The area of the stabilised interface is linearly proportional to the number of NPs. Thus, the mean diameter of the droplet (D_{mean}) in the emulsion can be adjusted by changing the NPs dosage (m_{NP}) for a given volume of the dispersed phase (V_{water}). We found that there is a simple relationship of $D_{mean} = C \cdot V_{water}/m_{NP}$, where $C = \sim 240$μm·mg/mL when using supersaturated CaCl2 solution as the water phase. In this way, the droplet diameter can be precisely adjusted from the micro- to the nano- scale, as shown in the fitted plot with the measured droplet size in Figure 6-10.

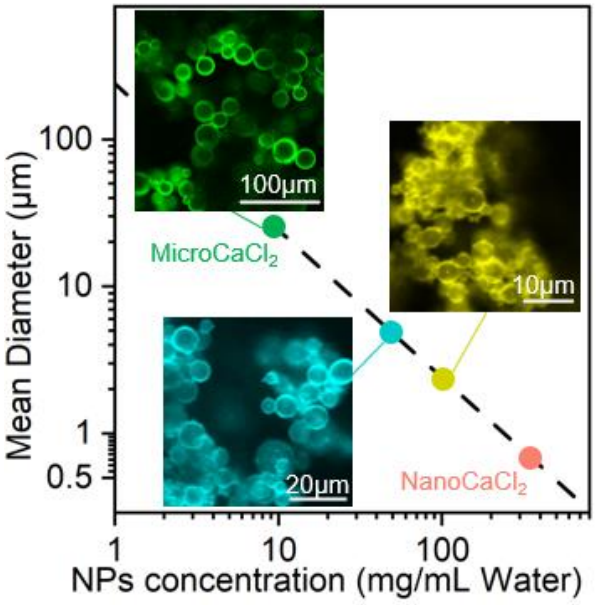


Figure 6-10 The relation between the size of droplets and nanoparticles dosage, with the Laser Scanning Confocal Microscopic (LSCM) images of emulsions.

The vapour-permeable shell is essential to allow the thermochemical reaction to take place within the encapsulation. This shell is formed by the W/O interfacial polymerisation in the emulsion template. Siloxane is chosen as an example material in this study. It was formed by hydrolysis of tetraethyl orthosilicate (TEOS) at the W/O interface in the liquid-occupied interstices between NP aggregates, as shown by the light grey circle around the capsule in Figure 6-6. As the layer can grows continuously outwards from the initial interface, water must diffuse through the formed shell [359], thus leaving very small channels in the shell to provide vapour permeability for the thermochemical reaction. Finally, the process is finished by drying the wet gel suspension, with the organic solvent used in the process recycled for both economic and environmental considerations.

Several thermochemical salts, including $CaCl_2$, LiCl, $MgSO_4$ and K_2CO_3, were studied and the results (Figure 6-11) suggest that the protocol could be general. The salt loading in the capsules depends on their solubility in water, with a high loading being desirable for an increased energy density.

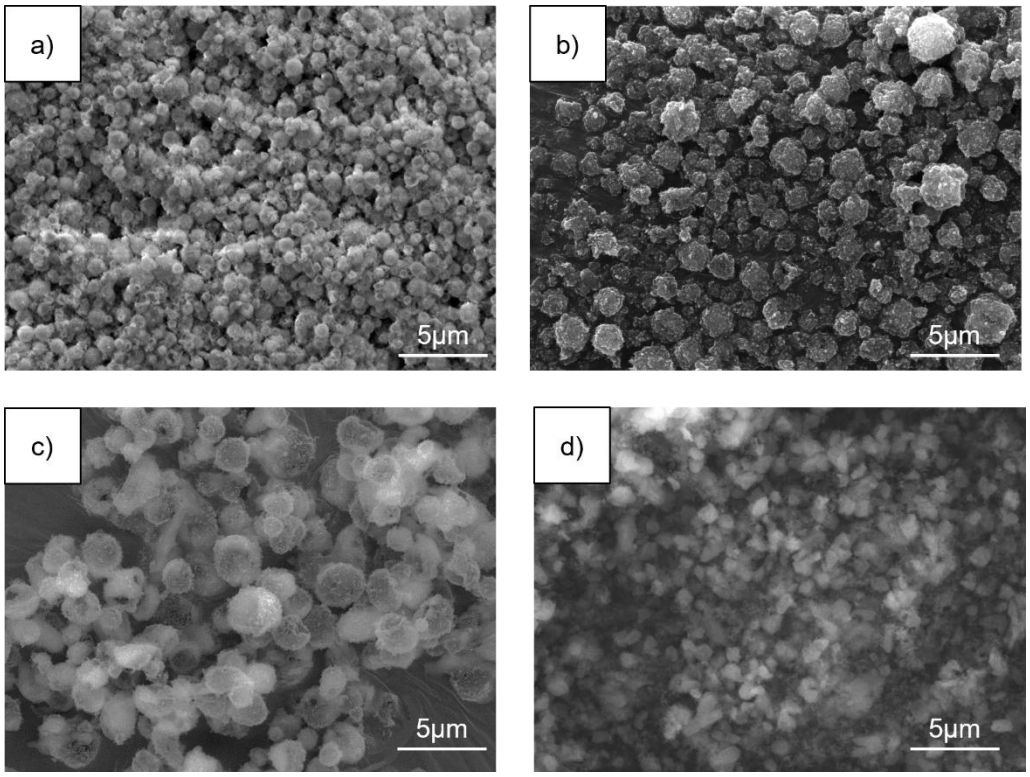


Figure 6-11 SEM images of different thermochemical salt capsules: a) $CaCl_2$; b) LiCl; c) K_2CO_3; d) $MgSO_4$.

By comparing the energy density of each of the salts (Table 6-2), $CaCl_2$ was selected for further comprehensive study, due to its high solubility (0.90 moles of anhydrous per 100 ml water at 30°C) and high reaction enthalpy (total 361 kJ/mol from anhydrous to hexahydrate).

Table 6-2 Estimation of the theoretical energy density of different salt encapsulated from Pickering emulsions.

Salt	Solubility (Anhydrous, in moles, at 30℃)	Thermochemical Reactions	Reaction Enthalpy (kJ/mol)	The estimated energy density of composite (based on anhydrous, in J/g)
K_2CO_3	0.83	$K_2CO_3+1.5H_2O = K_2CO_3\cdot1.5H_2O$	95.5	467.5
$CaCl_2$	0.90	$CaCl_2+2H_2O = CaCl_2\cdot2H_2O$	236.9	722.2
		$CaCl_2\cdot2H_2O+4H_2O = CaCl_2\cdot6H_2O$	124.3	1376.4
$MgSO_4$	0.33	$MgSO_4+7H_2O = MgSO_4\cdot7H2O$	335.3	1100.5
LiCl	2.05	$LiCl+H_2O = LiCl\cdot H_2O$	62.2	903.7
$MgCl_2$	0.59	$MgCl_2+2H_2O= MgCl_2\cdot2H_2O$	153.1	813.4
		$MgCl_2\cdot2H_2O+4H_2O= MgCl_2\cdot6H_2O$	252.7	1342.6

To load the capsules with more salts, a supercooled solution with a supersaturated $CaCl_2$ content was used, the concentration of which was determined to be ~1.19 mol/100mL of water. There were two kinds of $CaCl_2$ capsules prepared for demonstration, with the mean diameters in microscale (~24μm, hereafter referred to as Micro$CaCl_2$) and nanoscale (Nano$CaCl_2$), respectively. The prepared Nano$CaCl_2$ capsules are free-flowing fine powders and appear to be mono-dispersed as shown in Figure 6-12a. The average diameter of the capsules is ~700nm (the size distribution is shown in Figure 6-12b

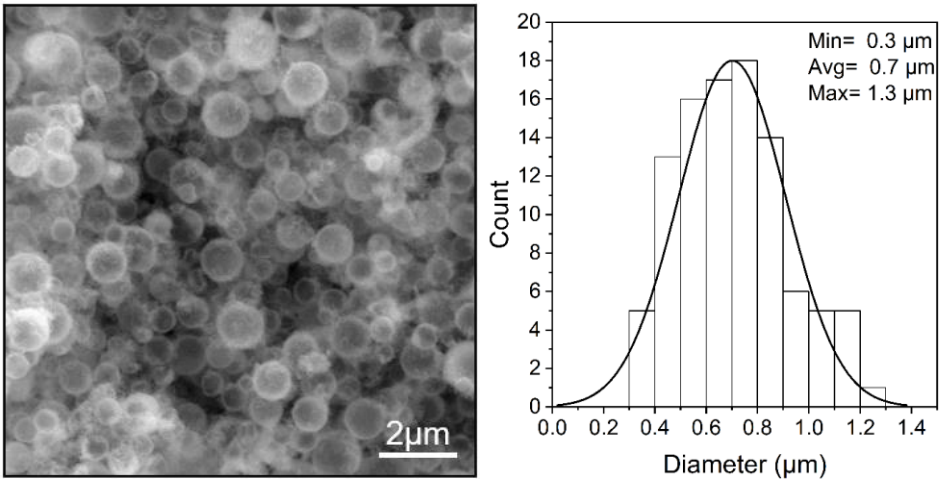


Figure 6-12 a) Scanning Electronic Microscope (SEM) image of Nano$CaCl_2$. b) Size distribution of as-fabricated Nano$CaCl_2$.

The yolk-shell structure in individual nanocapsules was observed under TEM (Figure 6-13), which is shown filled by the $CaCl_2$ grains and void. The void offers space for crystal expansion during hydration (for $CaCl_2$, a 30% volume expansion occurs from anhydrous to hexahydrate), thus reducing possible stress damage on the shell [163]. The deliquesced $CaCl_2$ solutions will absorb moisture until an equilibrium is reached between the water vapour pressure of the solution and that of the air. As the result, there is a further 50% expansion from hexahydrate to the salt solution with a concentration of 19%wt $CaCl_2$ (equilibrium concentration at 25°C, 80% relative humidity, data source from [360]), which is possible to fulfil the void and result in leakage. This case can be avoided by controlling the humidity or immediate removal of the reacted material from the reactor, for example, employ a separate reactor with materials transport [208], [361]. The shell has outer irregular whiskers partially embedded in the inner continuous thin layer as shown in the insertion of Figure 6-13. The

whiskers attached to the shell are composed of the NPs aggregates, providing a nanoscale roughness hydrophobic structure. The orthosilicate hydrolysed continuous layer is measured to be ~25nm in thickness and can become thicker as the TEOS dosage increased.

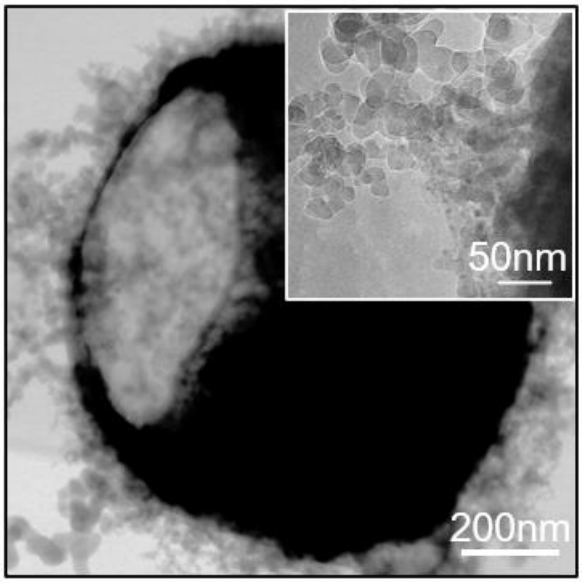


Figure 6-13 Scanning Transmission Electronic Microscope (STEM) bright-field image of a single Nano$CaCl_2$ capsule, the insertion is the zoom-out image of functional silica nanoparticles whisker attached on the shell.

The inherent hydrophobic behaviour can form an air gap to prevent liquid water from wetting the shell surface, as proved by the contact angle of water on Nano$CaCl_2$ in Figure 6-14. Consequently, this unique structure eliminates the contact between the inner salt and the outer water, thus can minimising the possibility of salt leakage through ion transport (as illustrated in the insert of Figure 6-6).

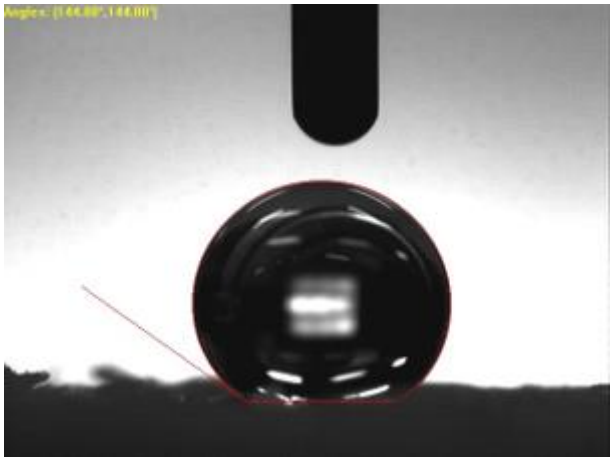


Figure 6-14 Contact angle of water on Nano$CaCl_2$.

To determine the spatial distribution of elements in the nanocapsules, STEM-EDX mapping is employed. The yolk-shell structure of $CaCl_2$-encapsulation is identified by mapping Si and Ca and the corresponding HAADF image (Figure 6-15).

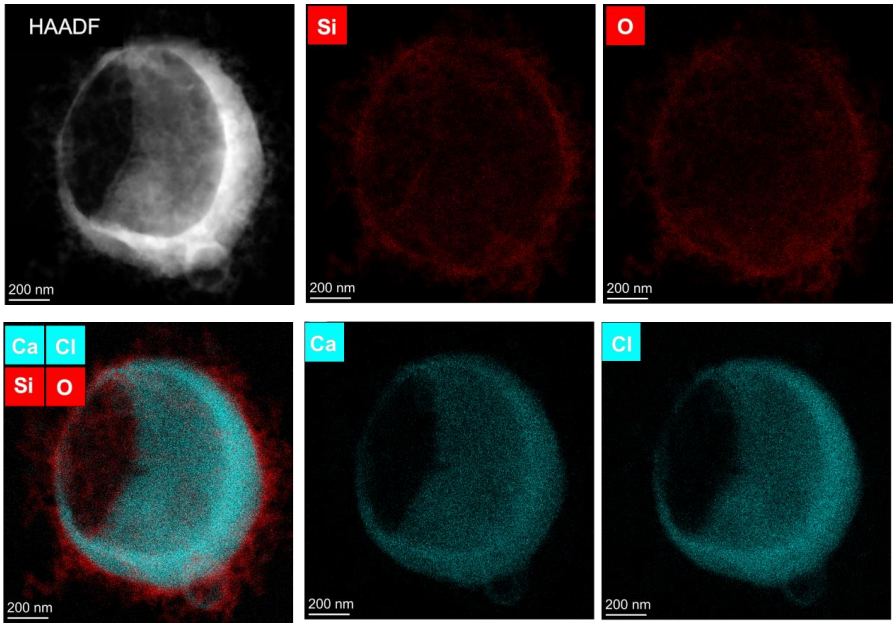


Figure 6-15 High-angle annular dark-field STEM (HAADF-STEM) with overlayed Energy-dispersive X-ray spectroscopy (EDX) elemental distribution mappings (in atom%) for Si and Ca in a single capsule.

The in-depth XPS characterization of Ca further confirms the structure of the nanocapsules. By ion etching in XPS, the Ca peak intensities increase with etching time (Figure 6-16).

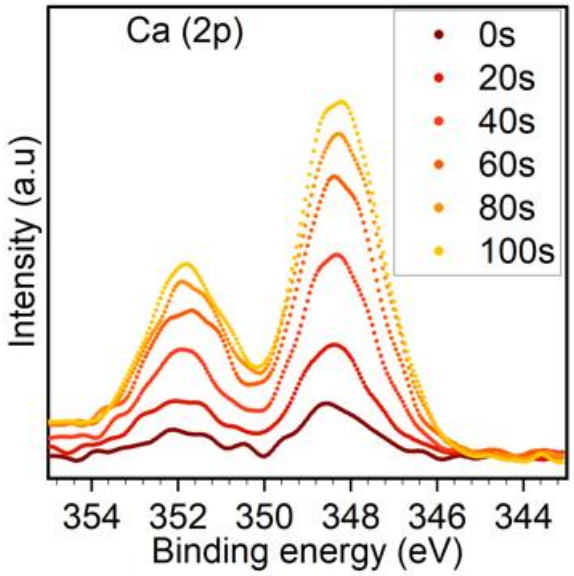


Figure 6-16 X-ray photoelectron spectroscopy (XPS) spectrum of Ca 2p core-level at different depths (deeper with increased ion etch time).

Moreover, the Cl peak intensities increase according to the Ca, while the Si and O intensities decrease (Figure 6-17). The carbon peaks was used to calibrate the bias in binding energy, which is also shown in Figure 6-17.

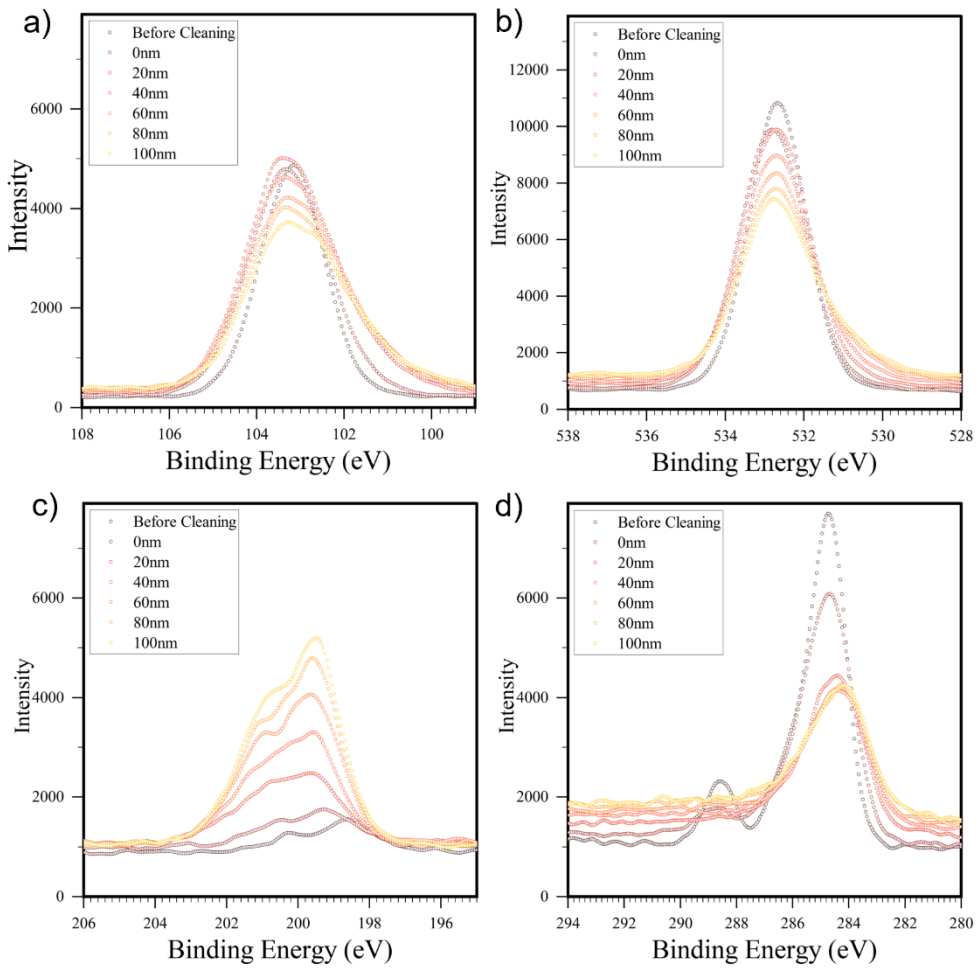


Figure 6-17 XPS depth Investigation of other elements in NanoCaCl$_2$: a) Si2p; b) O1s; c) Cl2p; d) C1s.

As Figure 6-18 shows, the detailed analysis of the Si 2p core-level spectrum describes the chemical structure of the silica on the surface of the shell, including three kinds: O-Si-O at about 103.5eV, Si(CH$_3$)-O$_{1.5}$ at about 102.7eV and Si(CH$_3$)$_2$-O at about 102.0eV [362], [363]. There are 42.9% of the Si atoms on the surface that have a covalently bonded -CH$_3$ group, which gives the shell permanent hydrophobicity.

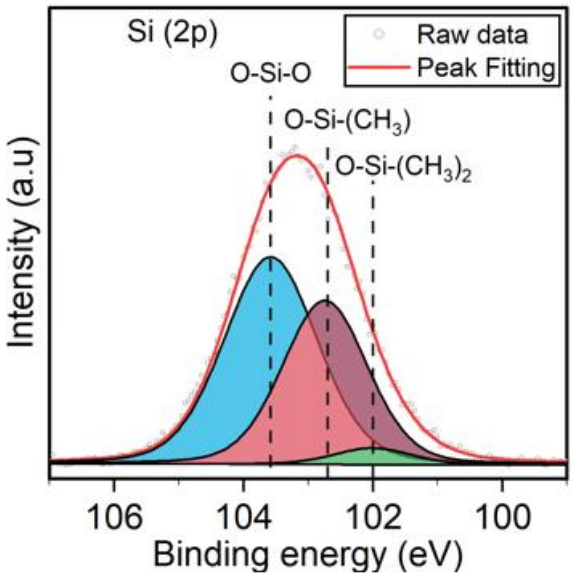


Figure 6-18 XPS spectrum of Si 2p core-level of the capsule shell.

6.3.2 Thermochemical energy storage in the nanocapsules

Figure 6-19a schematically illustrates a complete thermochemical energy storage cycle based on Nano$CaCl_2$, comprising four states (labelled from ① to ④): charged, storage, discharged, and over-discharged. In the charging process, crystals of anhydrous solid salt (charged state) are formed by thermal energy input and held at an elevated temperature, which is accompanied by crystallization of the grains from the solution and the diffusion of water out of the hydrated crystal. Conversely, the discharge step includes two processes: a) for short-term or immediate heat demand, sensible heat is released from hot anhydrous salt, and b) for long-term application, chemisorption of water in the anhydrous salt, triggered by reaction with moisture, gives out a large amount of heat during the transformation to hydrated salt crystal. Between the above two processes, the cold anhydrous salt can be stored in the charged state for cross-

seasonal storage by isolating the salt from moisture. Over-discharging can take place from state ④ to ① when the inner fully hydrated salt crystal deliquescence to a solution. It is not expected to happen during discharging due to no heat generation from taking up excessive moisture, leading to more energy costs in the subsequent charging step. However, in cases where a high discharging power is needed, a high vapour pressure reactive flow would be needed, which makes the deliquescence hard to avoid.

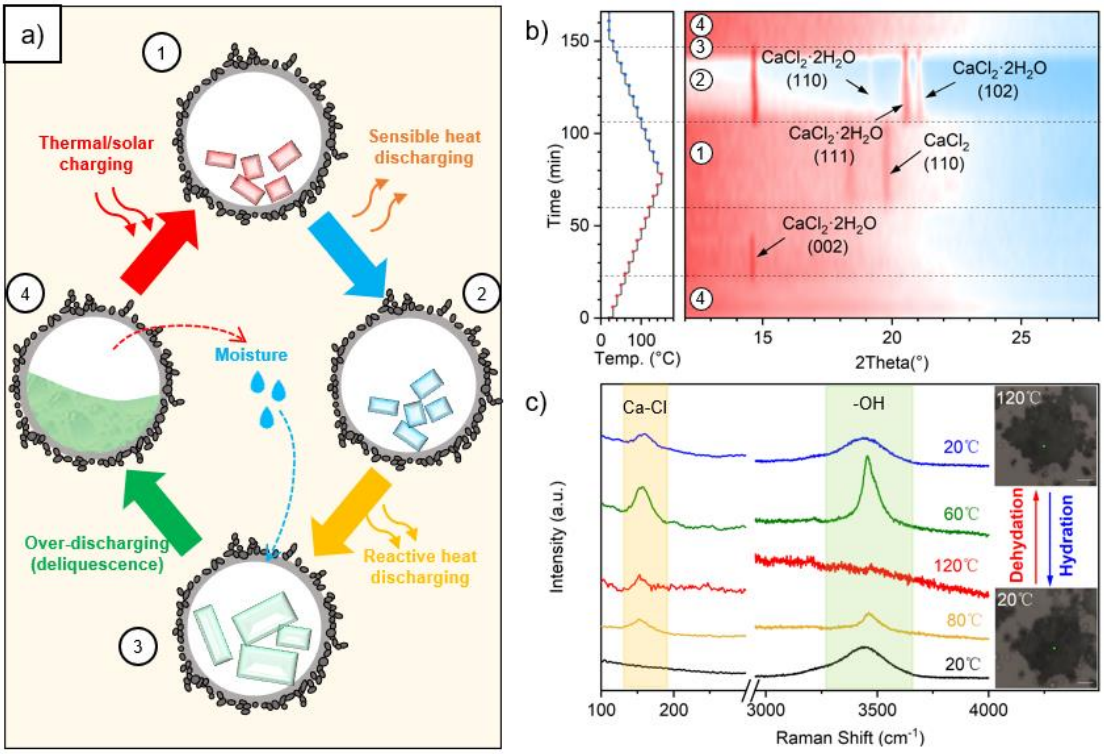


Figure 6-19 Illustration of a thermochemical energy storage cycle and analysis. a) Illustration of a thermochemical cycle consisting of 4 states. b) In-situ X-ray diffraction (XRD) analysis of NanoCaCl$_2$ in a thermochemical cycle. c) In-situ Raman Microscope analysis of NanoCaCl$_2$ in a thermochemical cycle, the scale in insertion is 20μm.

To prove the thermochemical reaction cycle of NanoCaCl$_2$, crystallographic and

Raman spectroscopic analyses were performed to confirm the above states. First, in-situ temperature-varying XRD was carried out, and the result for a dehydration-hydration cycle is presented in Figure 6-19b. The sample was in the over-discharged state ④ initially, referring to the amorphous profile and followed by heat up. The first peak at 14.6° appears when the temperature reaches 60°C, which belongs to the {002} plane of $CaCl_2 \cdot 2H_2O$ [74], indicating crystallization from the solution during charging. A solid-solid phase change is observed at 120°C, which is due to the transformation of the dihydrate crystal to the anhydrous phase, evidenced by the peak at 19.2° for anhydrous $CaCl_2$ {110} [364]. This represents the end of the charging phase. As the characterisation was performed under atmospheric conditions, spontaneous discharge took place during the cooling down process due to the presence of water vapour in the atmosphere. The cycle ends when the salt absorbs water from the injected high-humidity air (25°C and ~75%RH during measurements), completing the discharge process and returning the salt to its original over-discharged state.

Temperature-dependent in-situ Raman microscopic analysis was then used to further examine the changes in the microstructure during the cycle; see Figure 6-19c. The experiment was started from the same over-discharged state ④. The crystallization of $CaCl_2$ from the solution at around 60°C can be identified by the Ca-Cl bond at 157cm^{-1} due to B2g and B3g mode stretching [365]. In the meantime, the -OH bond stretch peak at ~3450cm^{-1} becomes weak, since the

bulk water dries out, leaving only the bonded water. As the temperature rises, the -OH bond vanishes at 120°C, suggesting that the salt is fully charged and transformed to anhydrous $CaCl_2$. This is consistent with the XRD data. The emergence of Ca-Cl and -OH bonds when the salt was cooled down shows that the salt was absorbing water from the atmosphere forming $CaCl_2 \cdot 2H_2O$. This can be a challenge, particularly for longer-term storage, due to the presence of moisture leading to discharge, but can be addressed by controlling the storage environment.

6.3.3 Thermal performance of Nano$CaCl_2$

In an attempt to quantify the energy storage potential of the Nano$CaCl_2$, Simultaneous Thermal Analysis (STA) over a thermochemical cycle was performed (Figure 6-20). The charging process is made up of 3 overlayed peaks with a combined endothermic enthalpy of 1774J/g. The discharge process has an exothermic enthalpy of 1037J/g of hydrated Nano$CaCl_2$ or 1705J/g of anhydrous Nano$CaCl_2$.

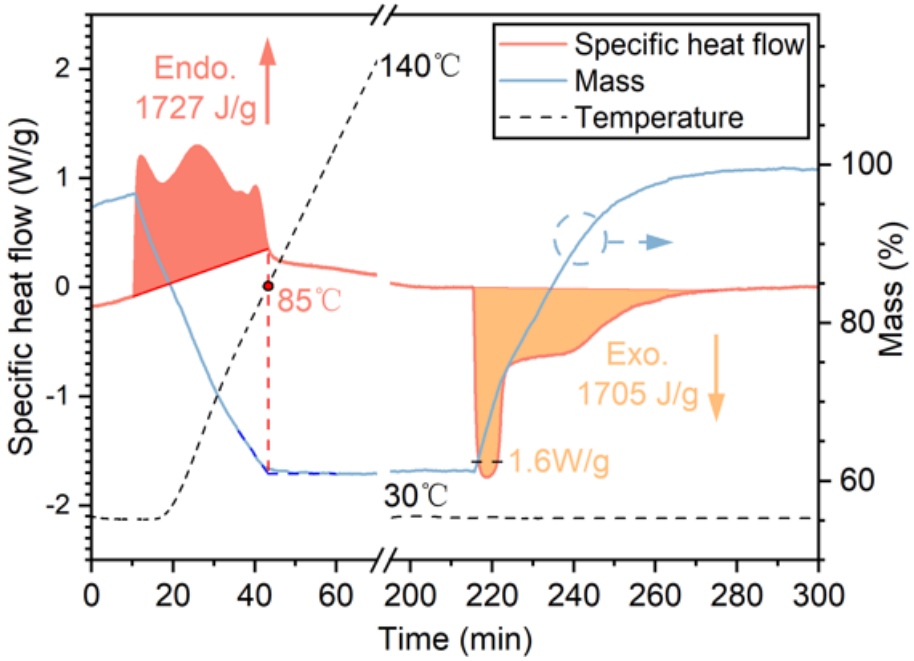


Figure 6-20 Simultaneous Thermal Analysis (STA) of NanoCaCl$_2$

The specific energy storage capacity is proportional to the amount of salt loaded, which is related to the sorption capacity. The water isotherm sorption behaviours of the encapsulated salts were therefore studied in the isotherm DVS experiments, as the results are shown in Figure 6-21. Including reference sorbents, all the CaCl$_2$-based composites exhibit the same trend as the pure CaCl$_2$, starting with the water sorption in solid salt below P/P$_0$=0.22, followed by the absorption in deliquescent liquid. The sorption capacities of encapsulated salt are 52% and 85% of the pure salt, for NanoCaCl$_2$ and MicroCaCl$_2$, respectively. These results agree with predictions based on the reactant usage, also the measured reactive enthalpy of NanoCaCl$_2$ (Figure 6-20). In comparison with the reference sorbents such as CaCl$_2$@GA [161], CaCl$_2$-UiO-66 [366], MIP-200 and MOF-801 [367], the encapsulated salt has a

significant enhancement in the sorption capacity below the vapour pressure of P/P_0<0.22. Additionally, upon the optimised geometry of encapsulation, the salt loading in the capsules has been increased by a considerable extent compared with that of the state-of-the-art salt-in-matrix composites [161], [368], [369].

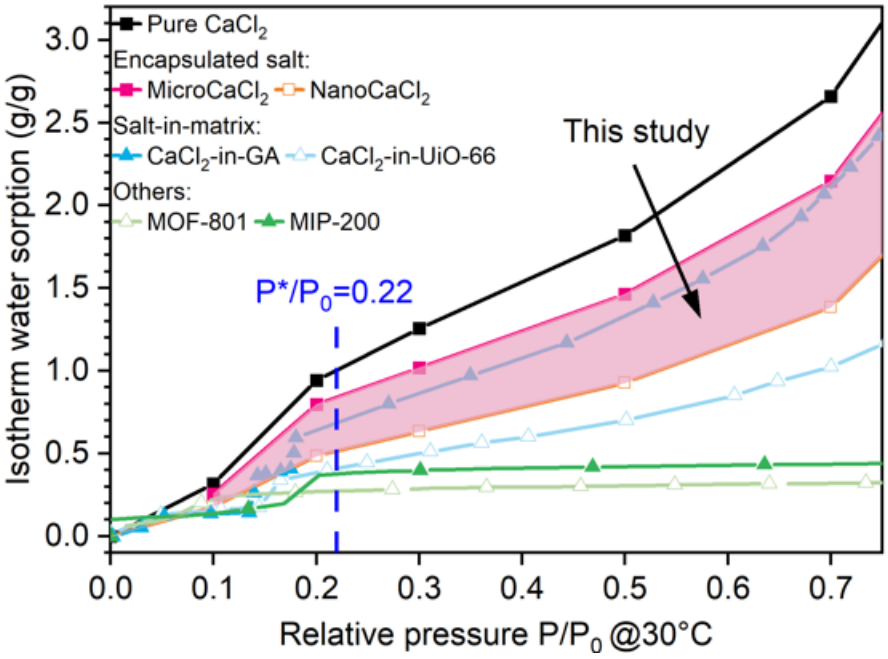


Figure 6-21 Isotherm water sorption capacity of TCS composite materials at 30°C.

To evaluate the reliability of encapsulated $CaCl_2$, 50 cycles of dehydration/hydration were performed in the DVS, as the results are shown in Figure 6-22. The transient specific water uptake of each salt is normalised by using its specific sorption capacity at P/P_0=0.22 (interpolated from the isotherm DVS) as a reference. The normalised values are presented as the State of Charge (SoC). The SoC of 100% represents the fully charged state of anhydrous, 0% represents the fully discharged state of hexahydrates, and the negative SoC represent the over-discharging states. The results show the

conversion rate according to SoC, demonstrating the excellent cyclability of Nano$CaCl_2$ in terms of little degradation in kinetics with SoC between 0% and 100%. The hydration behaviour of Nano$CaCl_2$ conforms to the characteristics of the process including two steps [340], [370], which are dominated by the nuclei-formation/growth and diffusion of water near the solid-gas interface [108], respectively. These steps proceed simultaneously, and the overall rate depends on the slower. Therefore, the rise of conversion rate before the SoC drop to ~50% can be linked to the process being dominated by the nuclei-related mechanisms, while the decrease of rate (in SoC<~50%) is limited by diffusion[148]. A similar profile is observed in the dehydration with the reversed direction of conversion, indicating that the same mechanisms are in control of the dehydration. On the other hand, the cycling performance of pure salt was unstable and degraded over time. This is contributed by the irregular change, particularly merging, in the geometry of grains/particles, due to lack of encapsulation confinement. The conversion rate of pure salt is consistently lower than that of Nano$CaCl_2$, likely due to the slower diffusion in larger particles. Especially, the dehydration profile of pure salt changes to a three-step process. An extra low-lying constant conversion rate is observed between the SoC range of 40% to 20%. This is possibly a result of the limited vapour transport through the crystal crust, which is formed near the skin of particles [371] and has low porosity.

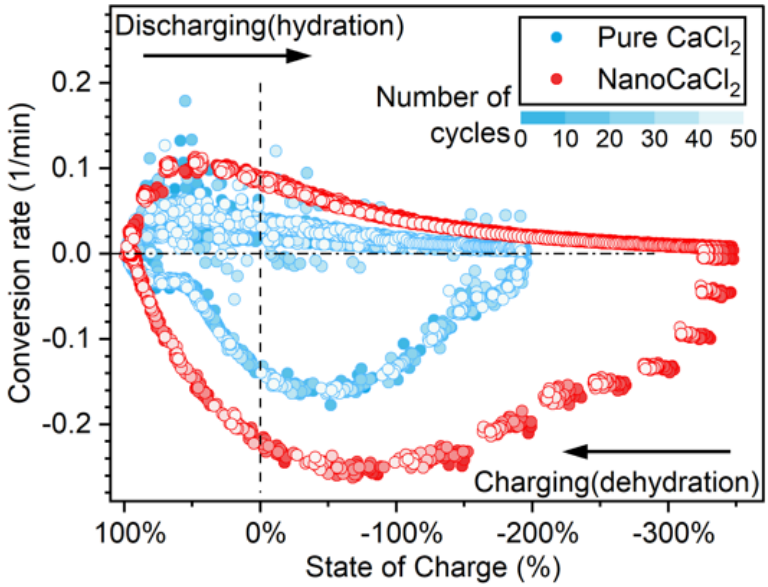


Figure 6-22 Dynamic Vapour Sorption (DVS) stability test with 50 cycles of $NanoCaCl_2$ and ground pure $CaCl_2$.

Further comparisons with $MicroCaCl_2$ are shown in Figure 6-23. $MicroCaCl_2$ show the intermediate conversion rates between $NanoCaCl_2$ and pure salt in both of hydration and dehydration. The cycling stability of $MicroCaCl_2$ is also good and in consistent with that of $NanoCaCl_2$. These results demonstrate the effect of encapsulation to regulate the reaction kinetics and ultimately improve the stability.

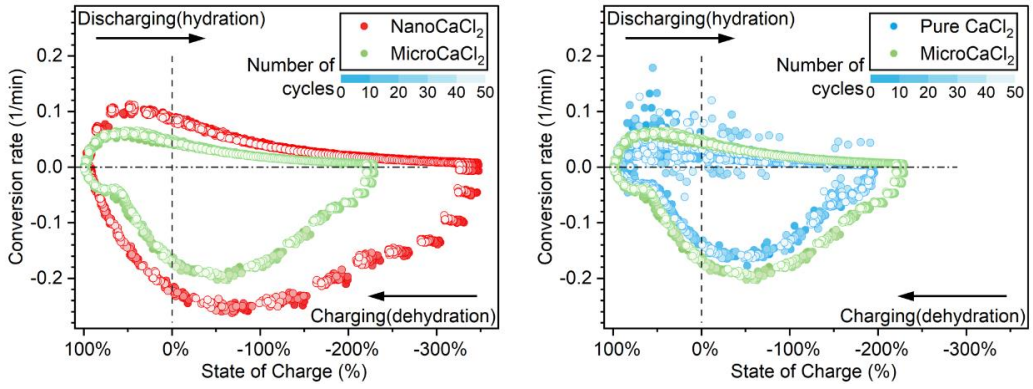


Figure 6-23 Results of MicroCaCl2 in DVS stability test.

Further optical microscopy results in Figure 6-24 show the dynamic deformation of pure $CaCl_2$ microparticles during a cycle. Due to its deliquescent behaviour, the initially dispersed salt particles had been migrated and merged to form larger particles after only one cycle of hydration and dehydration. The below SEM image shows the low porosity surface of the cycled dehydrated particle, confirming the presence of the crystal crust as mentioned above, which negatively impacts the water diffusion and kinetic. These provide microscopic insight into the kinetic degradation of pure $CaCl_2$. In contrast, the morphology and structure of $NanoCaCl_2$ show no difference between the initial state (Figure 6-12a) and cycled state (see Figure 6-24b, and the detailed SEM-EDX info is shown in Figure 6-25).

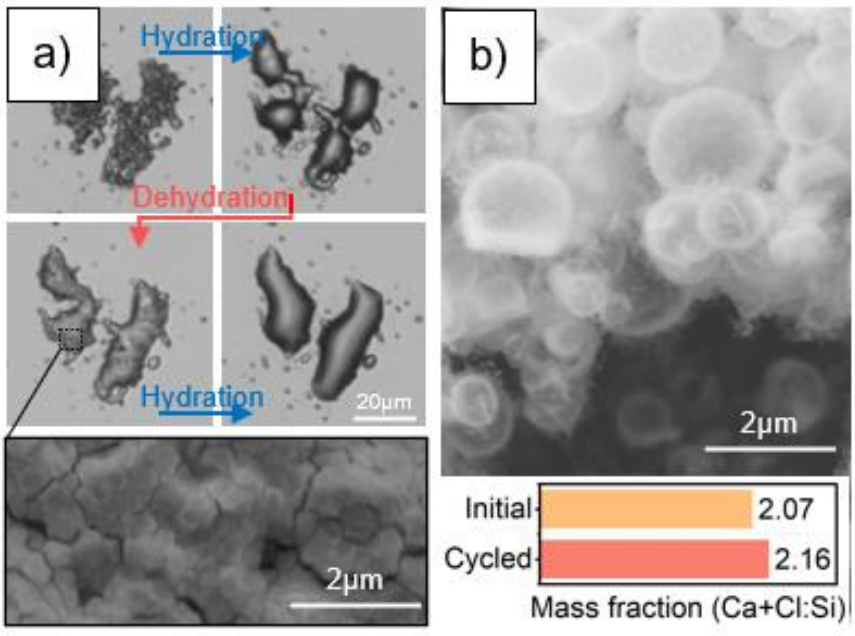


Figure 6-24 a) Dynamic microscopic images of pure $CaCl_2$ during a cycle and SEM Images of cycled pure salt. b) SEM Image of cycle $NanoCaCl_2$ with EDX quantitative evaluation.

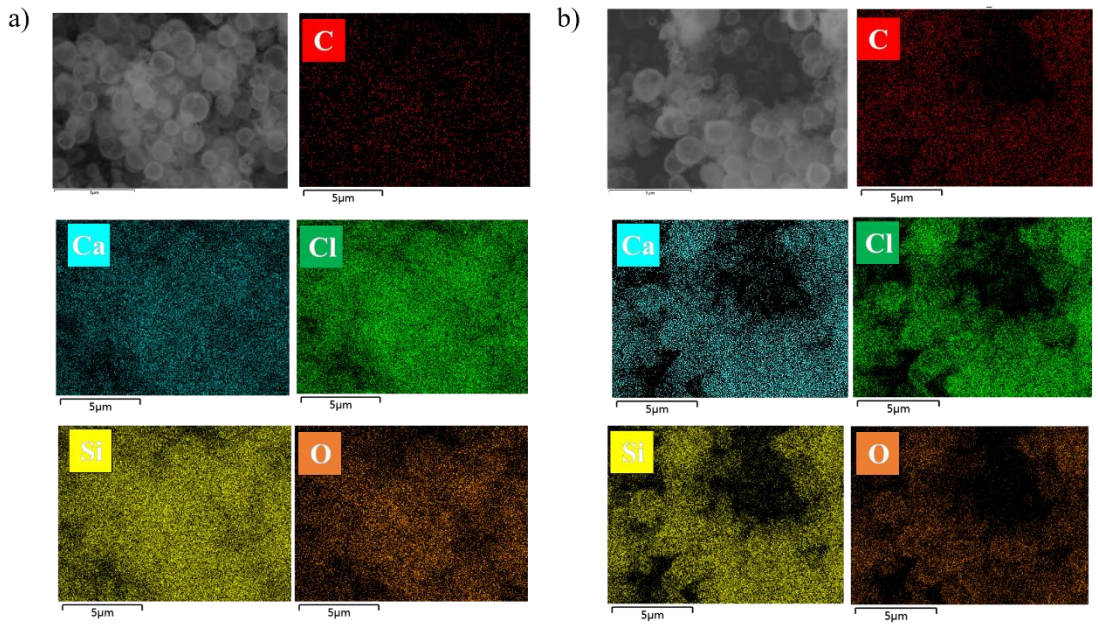


Figure 6-25 SEM and EDX Images of Fresh and Cycled Nano$CaCl_2$.

This is further supported by the dynamic observation on Nano$CaCl_2$ (Figure 6-26), which shows an unchanging morphology throughout a cycle. Note that the image is somewhat blurred due to the limited resolution of the optical microscopes. But the profile of Nano$CaCl_2$ can be still recognised during the cycle.

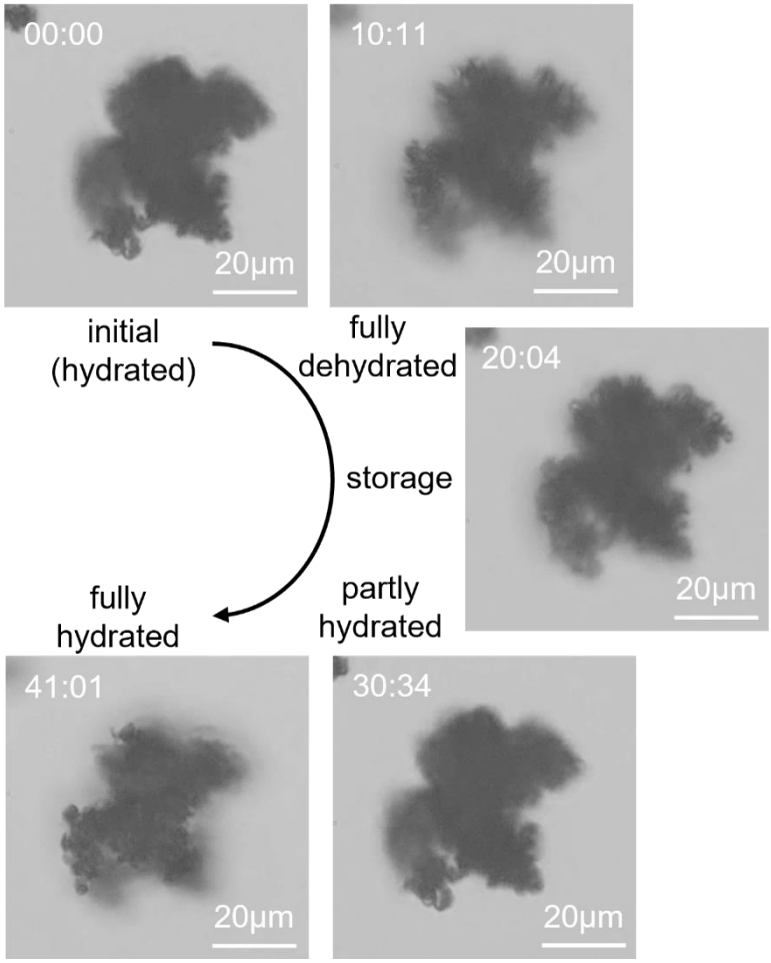


Figure 6-26 Microscopy images during the charging/discharging cycle, a) Nano$CaCl_2$.

However, a slight buckling of Micro$CaCl_2$ was observed during dehydration, but it returned to its spherical shape during hydration (Figure 6-27). It suggests that the shell is flexible and can effectively accommodate the volume expansion of the salt. Crucially, no salt leakage was observed in any of the encapsulated cases, providing strong evidence of the leakproof effect of the encapsulation with a continuous siloxane shell.

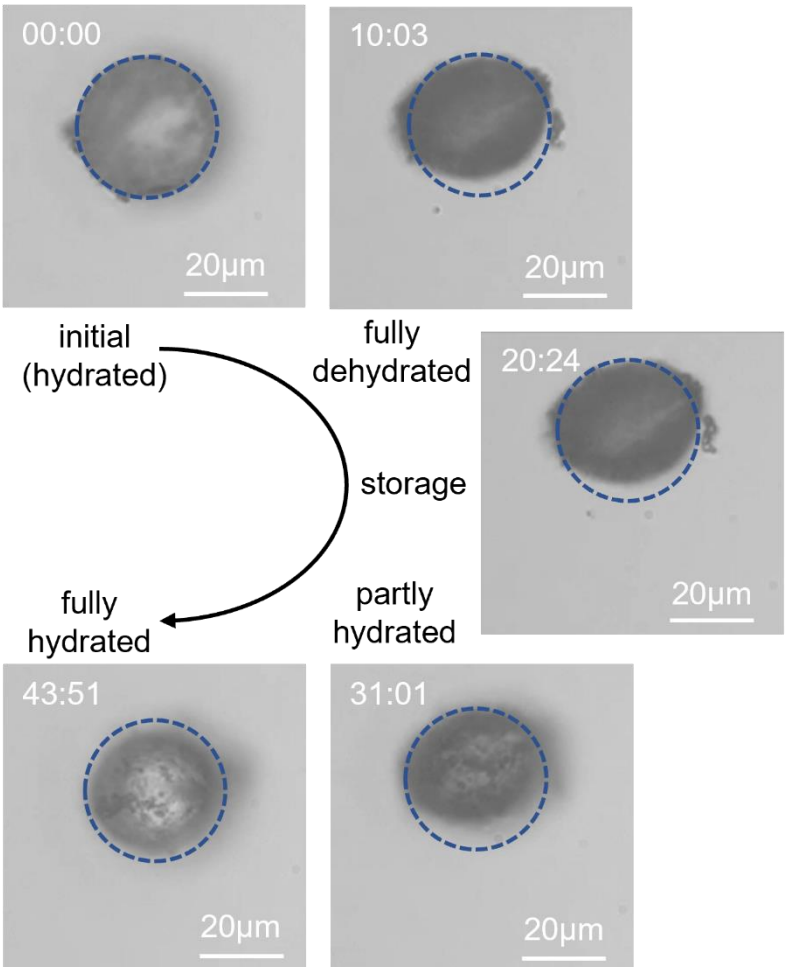


Figure 6-27 Microscopic dynamic of MicroCaCl$_2$.

6.3.4 Reaction kinetic and mass transfer in capsules

To further evaluate the effect of encapsulation on kinetics, we used a “pressure jump” DVS experiment to investigate the hydration behaviour at different vapour pressures. The hydration kinetics focus on the transformation of anhydrous salt to hexahydrate, which generates heat and occurs at vapour pressures of P/P_0<0.22 at 30°C. Figure 6-28 show that the breakthrough curve for the salts with vapour pressure jump from P/P_0=0 to 0.1 and 0.1 to 0.2, respectively.

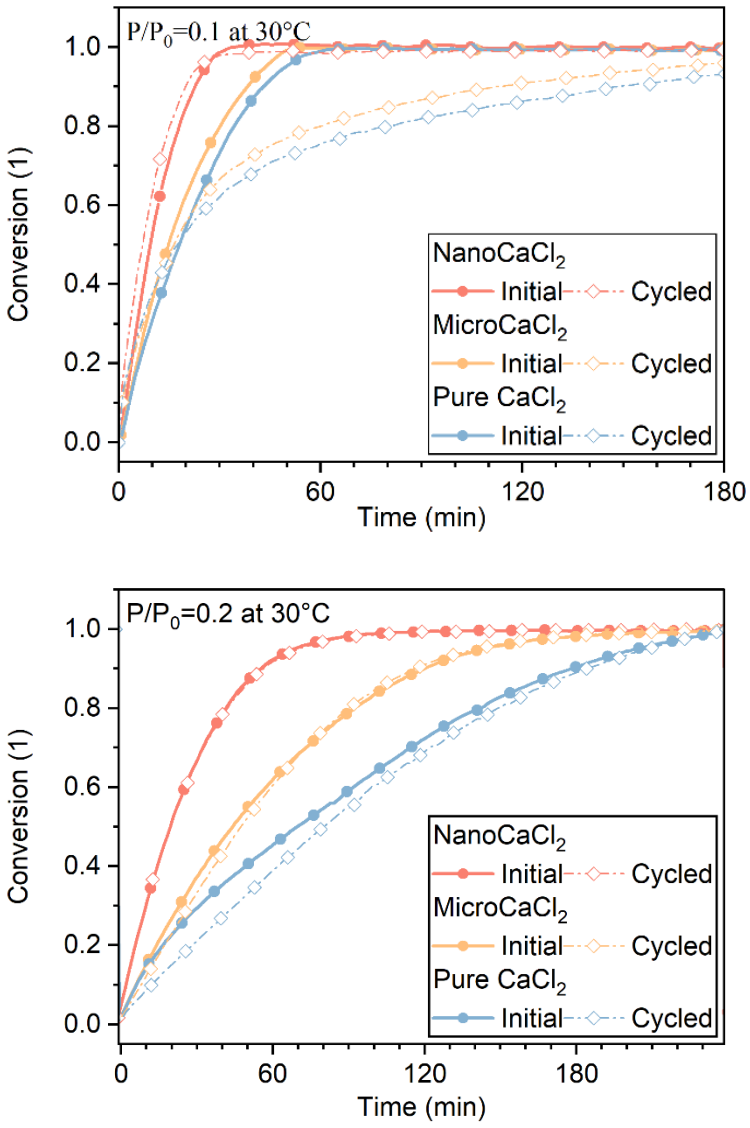


Figure 6-28 Hydration breakthrough curves of encapsulated and pure $CaCl_2$, under P/P_0 jump from 0.0 to 0.1, and 0.1 to 0.2 at 30°C.

In the former (P/P_0 from 0.0 to 0.1), the $NanoCaCl_2$ shows the fastest conversion, and the start of the differential conversion profile is nuclei-dominated, which is agree with the results of the DVS cycle test. The other part of the profile can be fitted with the kinetic model of contracting volume-dominated (R3) [340] and remains an unchanged rate constant (0.026/min) after cycles (Figure 6-29). The $MicroCaCl_2$ and pure salt are fitted with the same

model with the lower rate constants of 0.015/min and 0.013/min, respectively. However, after cycles, both MicroCaCl$_2$ and pure salt demonstrate a significantly slowed conversion (Figure 6-28a) and a change in their conversion profile (Figure 6-29), likely due to the merging and deformation of particles. In the latter condition (Figure 6-28b), the uncycled salts exhibit a decreased conversion rate corresponding to the increased size of confinement and are all fitted with the R3 model. After cycles, the hydration profile of salts, pure and with micro-confinement, changed to the area-contracting model (R2) (Figure 6-29), indicating the change in geometry (sphere/cube to cylinder), which probably contributes to kinetic degradations between initial and cycled (Figure 6-28b). This outcome, which is related to the effect of particle size and geometry, is consistent with the predictions from previous theoretical studies [314], [372].

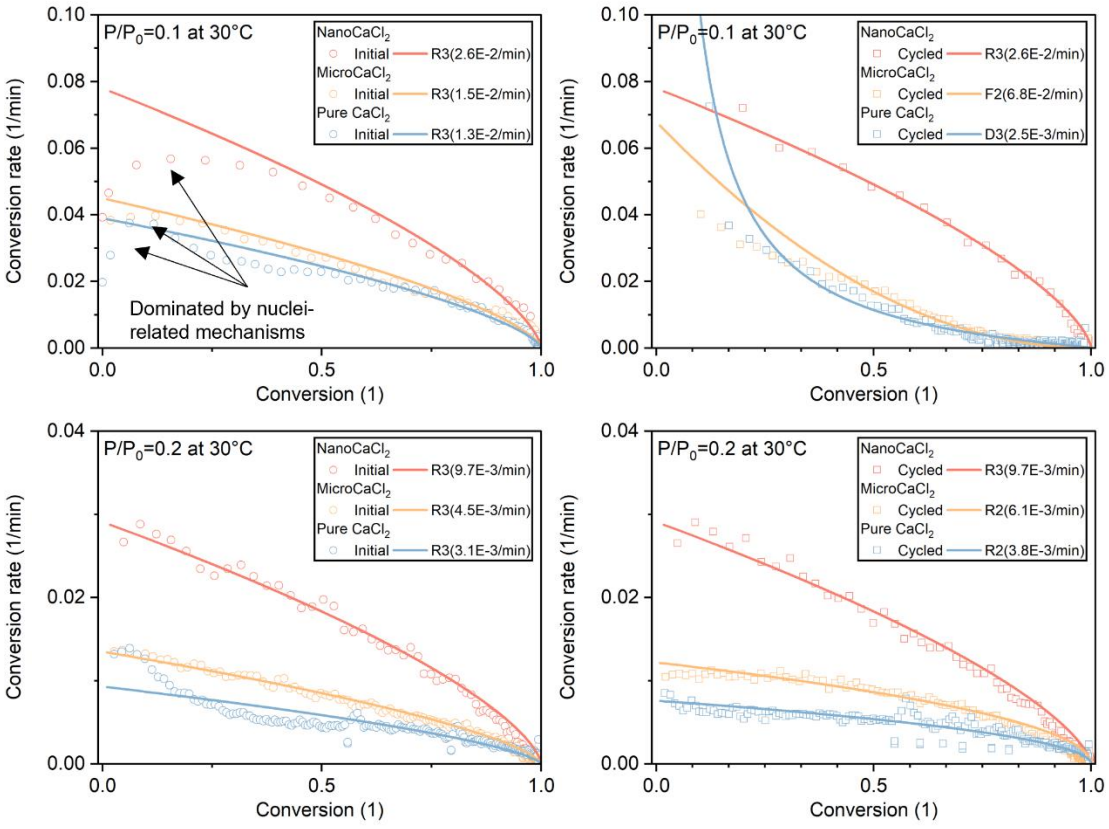


Figure 6-29 Reaction kinetic of hydration, low vapour pressure.

Besides, the sorption kinetics of over-discharging is also presented in Figure 6-30, which shows the conversion profile can be fitted with the order-based models. These models illustrate that the decelerating conversions are associated with the remaining reactant (here is the concentrated saline solution).

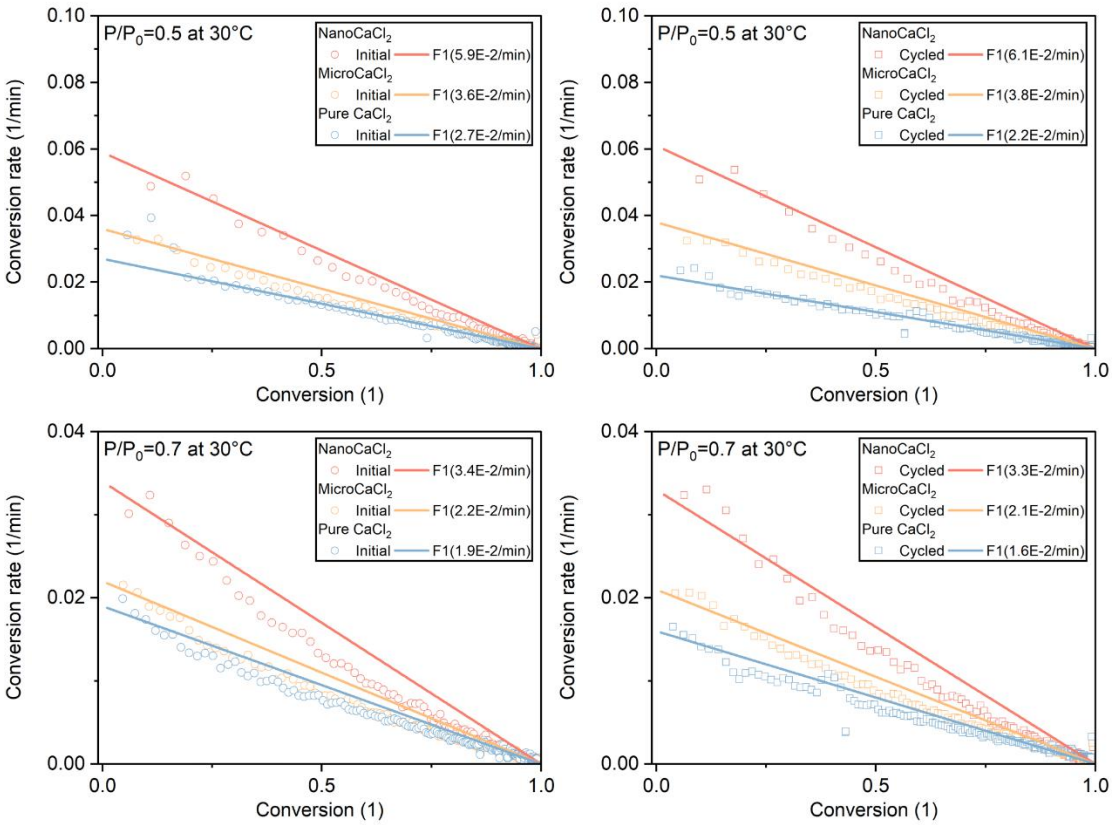


Figure 6-30 Reaction kinetic of hydration, high vapour pressure.

The enhancement of nano- and micro-encapsulation on dehydration can be seen in Figure 6-31. With the same mass of salts and a heating rate of 2.5°C/min, the temperatures required for full dehydration of Nano-, Micro-, and pure CaCl2, is determined to be about 110°C, 140°C, and 170°C respectively.

The lower temperatures indicate a smaller resistance to water diffusion within these structures and can vary with different flow rates, humidity levels, and heat rates.

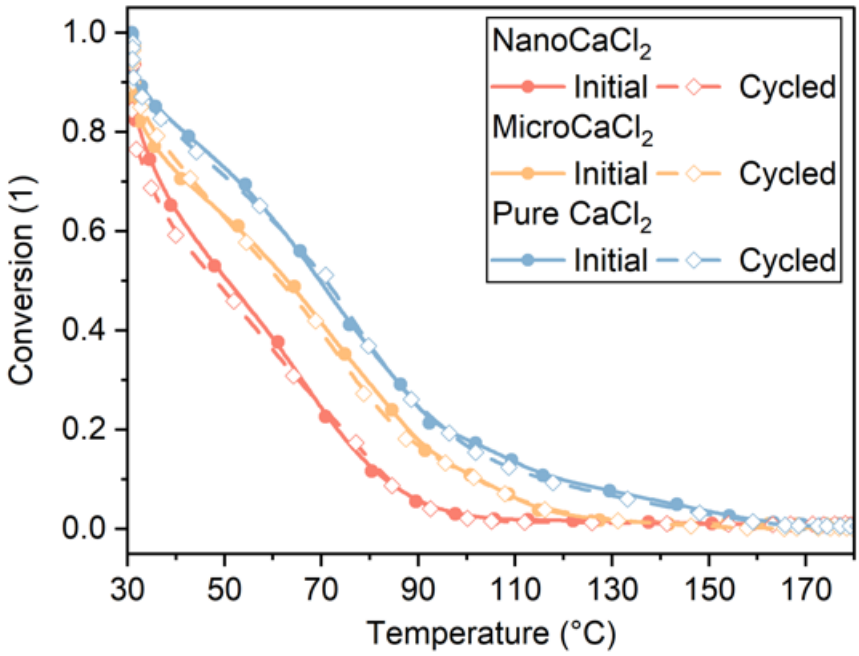


Figure 6-31 Dehydration kinetics of encapsulated and pure $CaCl_2$ with the same mass of the sample.

Thermogravimetric analyses (TGA) using the different masses of each salt are performed to characterise the mass transfer behaviour in packed particle conditions [338]. Compared to the pure salt, the result of reduced temperature differences in NanoCaCl2 confirms the enhanced vapour transport in the high macro-porosity gaps between the capsules (Figure 6-32).

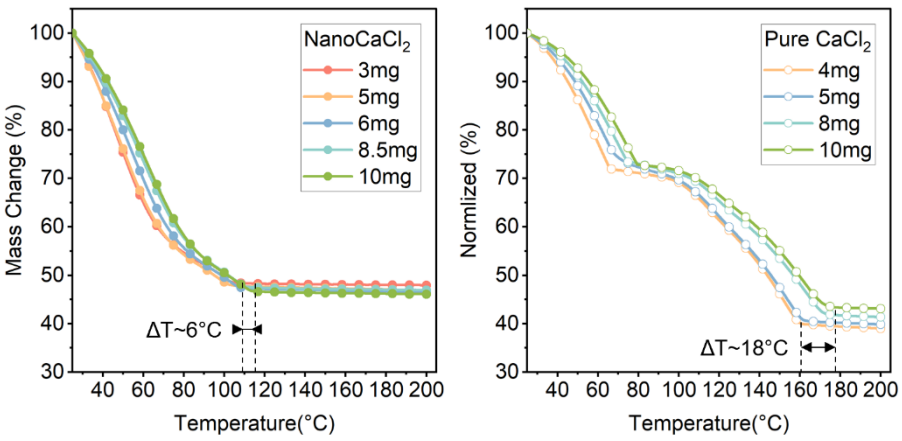


Figure 6-32 TGA with different sample mass.

6.3.5 The fluidisation of encapsulated salt

The proposed system for encapsulated salt fine powders consists of a (separate) reactor and multiple storage tanks for charged or discharged materials. In such a way, the TCS materials can be transported between them; see Figure 6-33a for an example. As the benefits of the separate system have been outlined in the introduction, we will assess their feasibility here. We conducted a series of laboratory-scale proof-of-concept experiments focusing on the in-reactor phenomena, including the flowability and charge/discharge behaviour of the composite materials. A set of highly encouraging results is shown in Figure 6-33b, demonstrating the fluidisation behaviour of NanoCaCl$_2$ in tens of grams. A minimum fluidisation velocity of ~1.6cm/s is observed (this velocity is based on a 50mm diameter vessel and a flow rate of ~2L/min), which is likely to be higher than the results for classical nanoparticles [373], [374]. This suggests that the nano-encapsulated salt be fluidised in the form of large agglomerates, with sizes of a few to tens of microns [375], [376]. Further

experimental results show the presence of multiple fluidisation regimes including bubbling and turbulence with/without light entrainment. These results classify the Nano$CaCl_2$ as an “aeratable particle” (Type A in Geldart diagram [377]), suggesting its suitability for use in most conventional fluidised beds.

Figure 6-33c presents the results of charge/discharge experiments conducted using fluidised NanoCaCl2, with a starting weight of ~50g (partially hydrated), and a static bed height of approximately 80mm. During charging, heat is supplied by a jacketed heater, with the outlet temperature being controlled in the range of 90-100°C. The result shows the charging is finished within 2 hours with a dry air flow of 7.4L/min. The maximum dehydration rate is 0.09g/min and the total amount of dehydrated water is estimated at ~4g. The subsequent discharge experiments show a peak temperature lift of 7°C at the outlet, with the peak hydration rate at 0.06g/min. The water absorbed by the bed is estimated to be ~21g in 12.5 hours of discharging, which reaches 72% of the fully hydrated water sorption capacity of the materials used (the sorption capacity of the 46g dehydrated NanoCaCl2 is 27.5g when it is fully hydrated from anhydrous to hexahydrate).

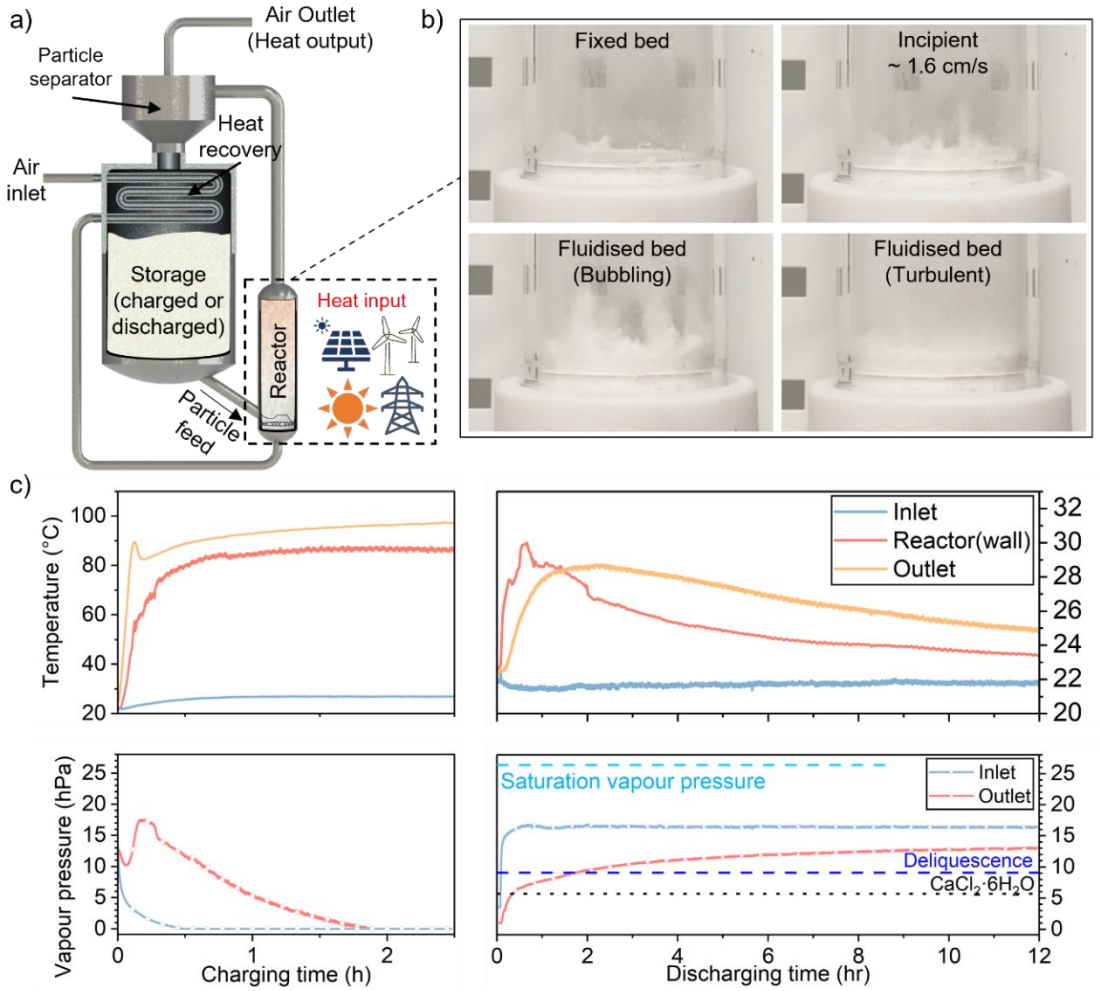


Figure 6-33 Application of NanoCaCl$_2$. a) A proposed open TCS system with a fluidised bed reactor and a separate storage tank. b) Fluidisation behaviour of NanoCaCl2. c) Thermal charging/dehydration and discharging/hydration of NanoCaCl2 with a lab-scale fluidised-bed reactor.

6.3.6 Evaluation on the overall performance of NanoCaCl$_2$

In Figure 6-34, we compare the performance of NanoCaCl$_2$ with other TES materials, including water for sensible heat storage [205], [378], and Phase Change Materials (PCMs) for latent heat storage [205], [379] with Li-ion batteries (LIBs) for electrochemical storage as a reference [380], [381] (which can be further converted to thermal energy via ohmic heating). Our material

gives the highest specific discharge power of >1.6 kW/kg, which is 60% higher than the state-of-art LIBs technology, and the highest gravimetric storage density (GSD) at 0.47kWh/kg, nearly twice of the LIBs. Although the volumetric storage density (VSD) of $NanoCaCl_2$ is slightly lower than the LIBs, it is still an order of magnitude greater than PCMs and water, showing potential for space-limited applications such as air-conditioning in electric vehicles [382].

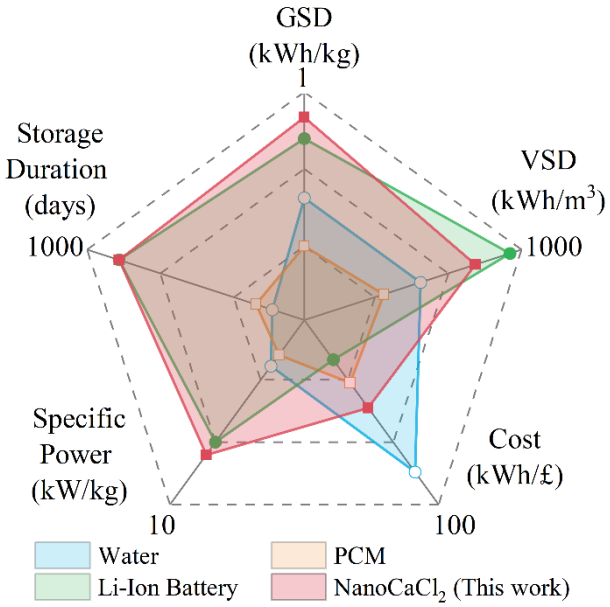


Figure 6-34 Comparison of state-of-art materials for thermal energy storage (scale is in logarithmic)

The cost of $NanoCaCl_2$, estimated (based on Table 6-3) at ~£3.86/kWh, is highly competitive (about $1/5^{th}$ of the PCMs and $1/20^{th}$ of the LIBs) in MWh-scale systems, such as office building space heating [84], [379] and supply domestic hot water [383]. The long-duration storage of $NanoCaCl_2$ is comparable to LIBs, allowing for flexible adaption of the storage operational times [346].

Table 6-3 Cost Estimation on $NanoCaCl_2$

Raw Materials	Price (GBP/ton)	Raw Usage (ton/ton composite)	Cost (GPB/ton composite)
Salt	200	0.63	126
NP	1300	0.33	429
Shell Precursor	2300	0.40	920
Organic Solvent	984.9	0.30	303.4
Material Subtotal (GBP/ton)		1778.4	
Processing Cost (GBP/ton)		50	
Total Cost (GBP/ton composite)		1828.4	

6.4 Conclusion

In summary, we developed a general method for nanoscale encapsulation of abundant and cheap thermochemical salts in one pot using a Pickering emulsion template, which differs from strategies reported previously. The nano-salt capsules show outstanding hydration-dehydration kinetics enabled by a unique bilayer shell composed of an out layer of silica NP whiskers and a continuous organosilane inner layer. The whisker-like nanostructure and intrinsic hydrophobic $–CH_3$ groups of the outer layer could prevent the inner salt from wetting by exterior liquid water through the formation of an air gap, while providing channels for the mass transfer of water vapour during the charging/discharging process. By using calcium chloride as an example, we demonstrate that the $NanoCaCl_2$ possesses several exciting thermal properties, including a superior specific power with a peak value at ~1.6W/g at 30°C and

~2100Pa vapour pressure, and a high gravimetric energy storage density of over 1700J/g based on anhydrous nanocapsules and a low regeneration temperature of around 85°C. Nano$CaCl_2$ also shows an order of magnitude performance enhancement over pure $CaCl_2$ in both water loading and hydration-dehydration kinetics. Moreover, the nanocapsules with the designed bilayer shell show excellent cycling stability with no significant degradation for 50 cycles. Furthermore, the heat release rate can be easily modulated on-demand by tuning flow rate, temperature and pressure.

With the lab-scale fluidised bed device, the fluidisation of encapsulated salt is demonstrated. A clear transition from stationary to fluidisation was proved not only by the observation but also the strong evidence from the trend of pressure drop. It provides support for the feasibility of using the encapsulated salt in a fluidised bed device, which has a potentially higher heat generation rate than a conventional packed bed.

The above salient features, plus cost-effectiveness, and easy-to-scaleup at both materials and device levels, make Nano$CaCl_2$ a highly promising material for providing a cost-effective, easy-to-scaleup, and flexible solution to long-duration thermal energy storage.

7 Encapsulated salt for solar heat storage

This chapter demonstrates the use of encapsulated salt for directly harvesting and storing solar heat. Section 7.1 introduces the background. Section 7.2 describes the design of material for enhancing solar absorption and the device. Section 7.3 presents the result and discusses the experiments. Section 7.4 concludes the findings and suggests future research.

7.1 Introduction

The motivation of this chapter lies on to design a device for a directly solar charging the hydratable salt based TCM, which potentially improves the efficiency of solar harvesting and conversion. The idea of direct solar charging was originally proposed for high-temperature solar heat storage with oxides [212], [224], [384]. The advantages consist of efficient photothermal conversion [385] and rapid heating rates. However, there is a lack of knowledge and related expertise for the low-temperature solar heat system.

In this chapter, the above gaps are addressed a lab-scale device experiment. The composite TCS material was also used in a solar heat system, demonstrating the feasibility of solar charging, long-term storage, and on-demand discharge. The device is designed for demonstrating the thermochemical storage of solar heat, using the developed nano encapsulated salt with enhanced solar absorption.

7.2 Experimental section

7.2.1 Materials

Calcium chloride dihydrate ($CaCl_2 \cdot 2H_2O$, 99%), Tetraethyl orthosilicate (TEOS, 99%) and Titaniumnitride (TiN, 60nm, 99%) nanoparticle were purchased from Energy Chemical (www.energy-chemical.com, China). Cyclohexane (C_6H_{12}, 99%) was purchased from Greagent. Hydrogen chloride (HCl, 36%w/w in H_2O)

and Poly(vinyl alcohol) (PVA, Product No. P139533) were purchased from Aladdin (www.aladdin-e.com, China). Water was obtained from a lab purification system, which has a >18MΩ resistivity. Hydrophobic fumed silica nanoparticle Aerosil R972 Pharma was kindly donated by Evonik.

7.2.1 Preparing the Solar-NanoCaCl$_2$

The Solar-NanoCaCl$_2$ was prepared by the same protocol with a modification of the salt solution. 20mg/ml PVA was dissolved in water by stirring around 95℃ followed by cooling to room temperature. As-received TiN nanoparticle with pre-determined mass was then added to the PVA solution. This was followed by sonication under similar conditions as the process for preparing the silica suspension. The obtained suspension was then filtered by a 0.22um PTFE filter to remove large aggregates. A pre-determined amount of salt was then added to the suspension for dissolution in a shaker. The following encapsulation protocol was as same as the NanoCaCl$_2$ case in Chapter 6. Note that the salt mass in the aqueous phase is lower than in the NanoCaCl$_2$ case.

7.2.2 The solar heat storage device and test rig

The solar heat test rig was an open system, as shown in Figure 7-1. Dry air from the compressor was used as carrier gas. The flow rate was regulated by a mass flow controller (1000SCCM, Sevenstar, China). A manual three-way switch valve was used to switch the gas flow between humidifying line and the bypass. The humidifier was composed of a 1L glass bottle sealed by silicon

rubber and the surrounding thermal insulation. There were two isolated valves, which were positioned at the inlet and outlet of the solar reactor. A solar simulator (SUN 3000, ABET Technologies) with an AM1.5 filter was used to heat and charge the solar reactor. A 100mm*100mm aperture (Laser cut aluminium plate) was installed between the solar simulator and solar reactor to regulate the irradiation area. The solar irradiation was calibrated by an optical power meter (10mm sensor, Thorlab) at one standard sun.

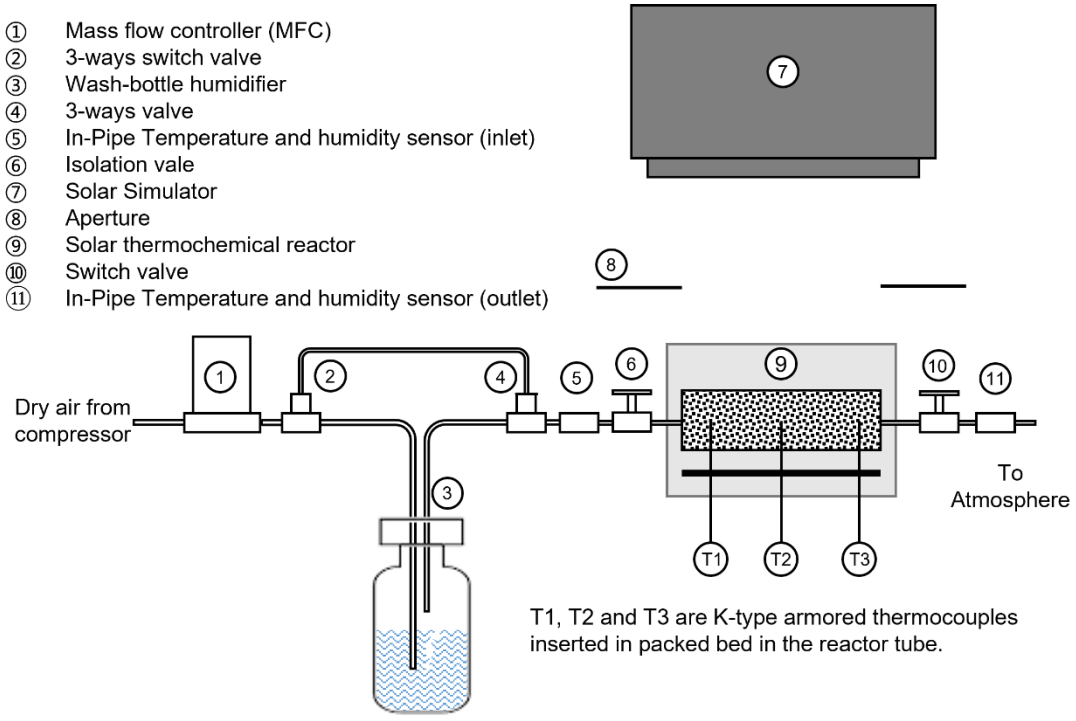


Figure 7-1 Design of solar thermochemical test rig.

The CAD drawing of the solar thermochemical rector (device) is shown in Figure 7-2, consisting of cover glass, reactor tube, and a pair of 3D-printed polylactic acid (PLA) fixtures used to fasten the reflector. The reactor was a 140mm long round quartz tube with an inner diameter of 16mm and a wall thickness of 2mm. A Polypropylene filter paper (pore size 0.44μm) was placed

at the end of the tube to prevent composite materials from blowing off. The reflector was made from an aluminium mirror sheet (Miro-SUN, Alanod) and was bent into a parabolic shape to concentrate the solar irradiation to the reactor. The concentration ratio is designed to 2.5 times for realising an essential charging temperature.

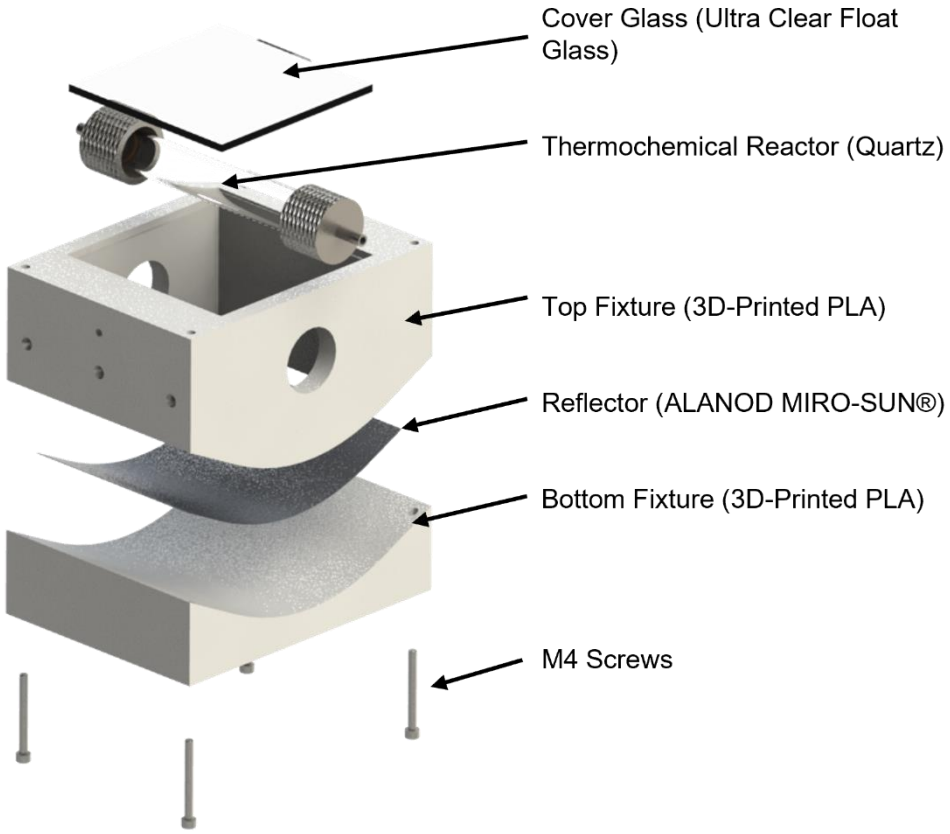


Figure 7-2 CAD drawing of the thermochemical solar reactor.

The indoor solar charging test was conducted with a 500SCCM air flow and a simulated standard sun. The charging was manually stopped once the outlet vapour pressure reached the inlet. Then the solar reactor was isolated by turning off the valve. The device was stored for a week. In discharging, the

same air flow rate was used but switched to flow through the humidifier to generate moist air. The temperature and vapour pressure at the inlet and outlet (indexed as T_Inlet, T_Outlet, VP_Inlet and VP_Outlet) were measured by the humidity sensor, and the temperature of the packed bed (indexed as T_Bed) was measured by an armoured K-type thermocouple inserted in the middle of the bed. All the thermocouples used in the test had been calibrated by a reference K-type couple. The environmental temperature was maintained at ~22°C during the charging and discharging.

7.3 Result and discussion

7.3.1 Encapsulated salt with enhanced solar absorption

The Nano$CaCl_2$ has a charging temperature compatible with the operational temperature of a non- or low-concentrated solar thermal system (<150°C), which can be employed in the domestic solar heating system [82], [198]. However, the Nano$CaCl_2$ highly reflect solar irradiation. For enhanced solar absorption, commercial titanium nitride (TiN) NP was incorporated into the capsules as an additive to the salt solution. The TiN NP had a primary particle size of 20nm and is in cubic phase which is chemically inert and highly thermally stable [386].Their morphology is shown in Figure 7-3a, and size distribution is determined by DLS in Figure 7-3b.

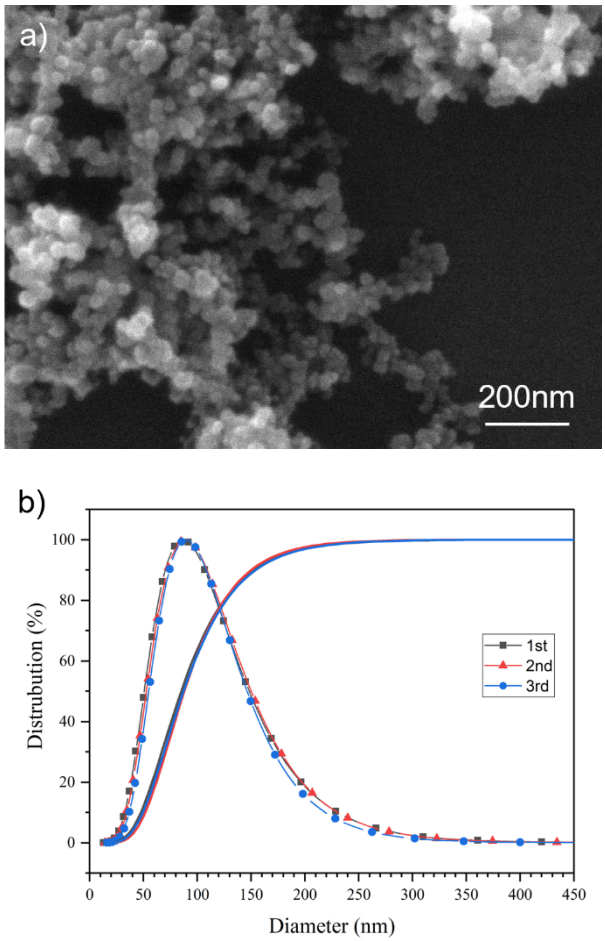


Figure 7-3 Morphology and size distribution of as-received TiN Nanoparticle a) SEM images and b) DLS show the size distribution.

However, the as-received TiN nanoparticle is prone to sediment in the salt solution, a hydrophilic polymer (polyvinyl alcohol) coating was used to modify the surface of the sonication-dispersed nanoparticle, leading to a well-dispersed suspension, see Figure 7-4. This strategy is fully compatible with our protocol of the nano-capsulation method, ensuring that the nanoparticle-based solar absorber and other potential functional additives can be encapsulated by our one-pot method.

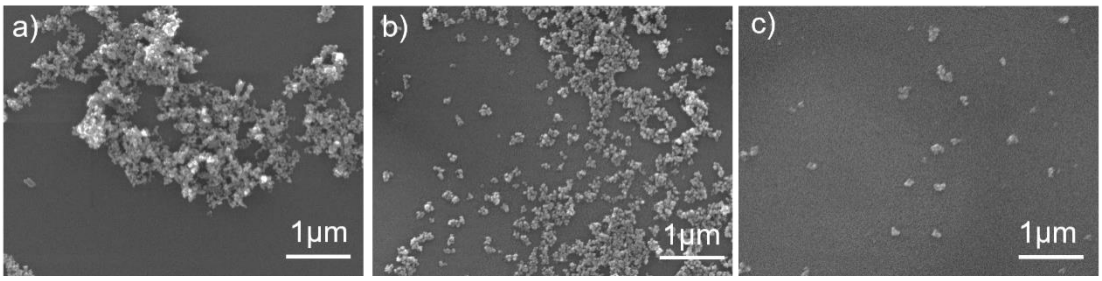


Figure 7-4 SEM images of TiN Nanoparticle dispersed in Water, a) 1mg/ml TiN without PVA; b) 1mg/ml TiN in 30mg/ml PVA; c) 0.1mg/ml TiN in 30mg/ml PVA.

We term the prepared nanocapsules as “Solar-Nano$CaCl_2$”, which has the SEM images of samples with different TiN dosages shown in Figure 7-5.

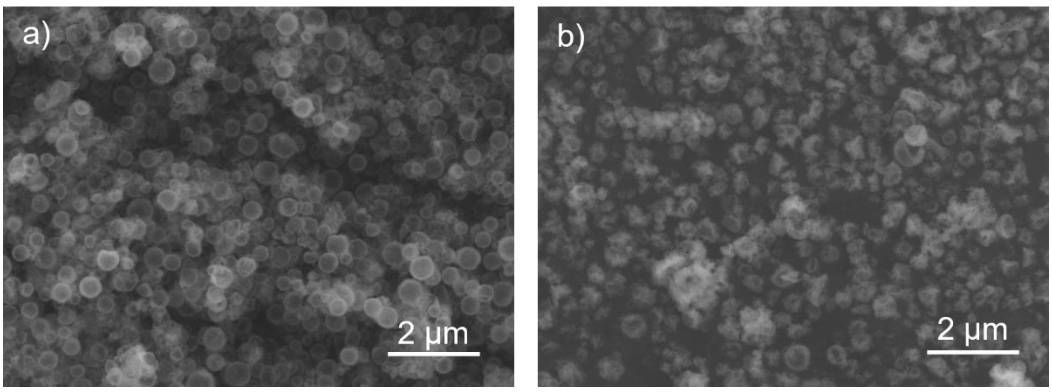


Figure 7-5 SEM Image of Nano$CaCl_2$ with different TiN solar absorber loading, a), 5mg/ml TiN, b), 20mg/ml TiN.

Figure 7-6 shows the TEM image of Solar-Nano$CaCl_2$ and corresponding TEM-EDX mappings of each element. The TiN NP can be seen clearly inside the capsule and the salt is distributed around it. Although the solar harvesting performance could be enhanced by introducing more TiN NP, the addition of excessive TiN NP with PVA thickens the suspension, leading to failed emulsification.

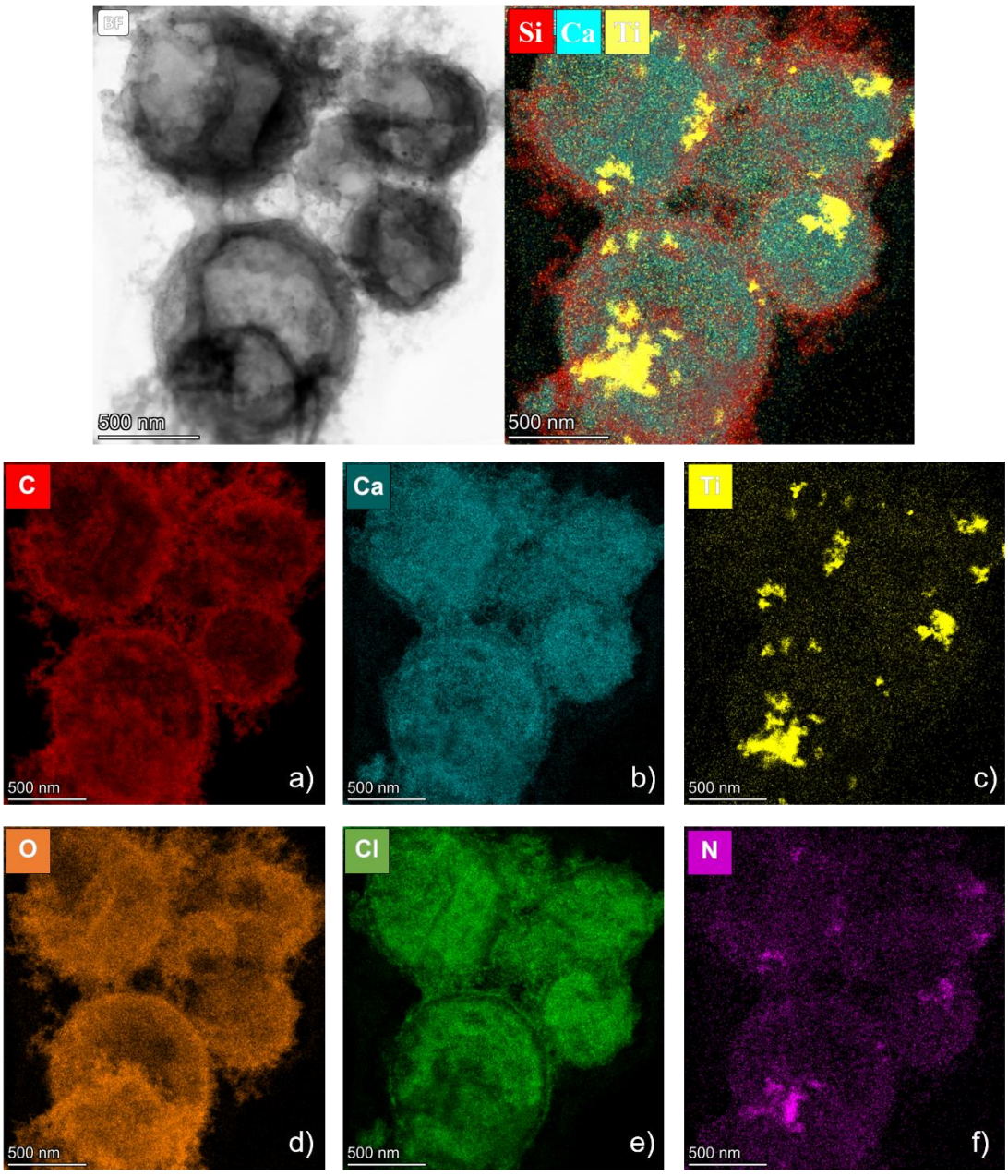


Figure 7-6 TEM bright field of as fabricated capsules with TiN solar absorber (called Solar-NanoCaCl$_2$) and corresponding STEM-EDX mapping.

The optimisation was therefore conducted, which showed that a dosage of 20mg/ml NP was optimal. As shown in Figure 7-7a, the Solar-NanoCaCl$_2$ powder turns darker as the TiN NP dosage increases. The corresponding absorption spectra over the wavelength from 250 nm to 2500 nm confirms the

enhanced absorption by TiN NP (Figure 7-7b). As the blue spectrum in Figure 7-7b shows, the two typical peaks at 1450nm and 1950nm can be ascribed to $CaCl_2$ [387]. The solar spectrum weighted absorptance of Solar-Nano$CaCl_2$ can be enhanced from ca. 3.0% to ca. 51.7% over that span.

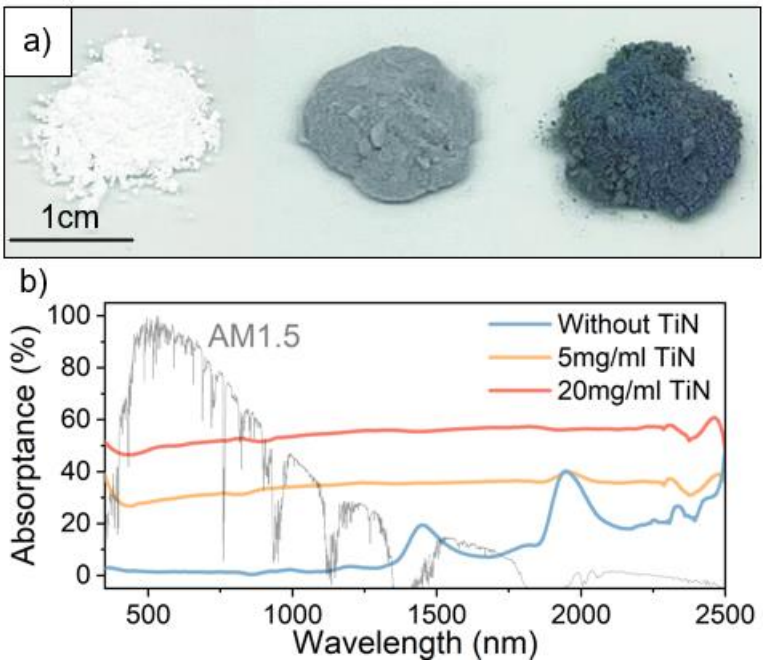


Figure 7-7 Integration of Solar-Charged Thermochemical energy storage. a) Photo image of Nano$CaCl_2$ and Solar-Nano$CaCl_2$ with 5 and 20 mg/ml TiN dosage; b), UV-VIS-IR absorptance spectrum of above powders.

7.3.2 Device test for coupled TCS and solar heat harvesting

In the case of indoor demonstration, the simulated operating conditions are chosen to be realistic. As shown in Figure 7-8, the dehydration temperature of 115°C is required to fully charge a $CaCl_2$ from a starting condition of ~20°C and ~80%RH (vapour pressure at ~2000Pa). This is significantly higher than the 70°C dehydration required for the low vapour pressure case, as we showed in the fluidisation test (Chapter 6).

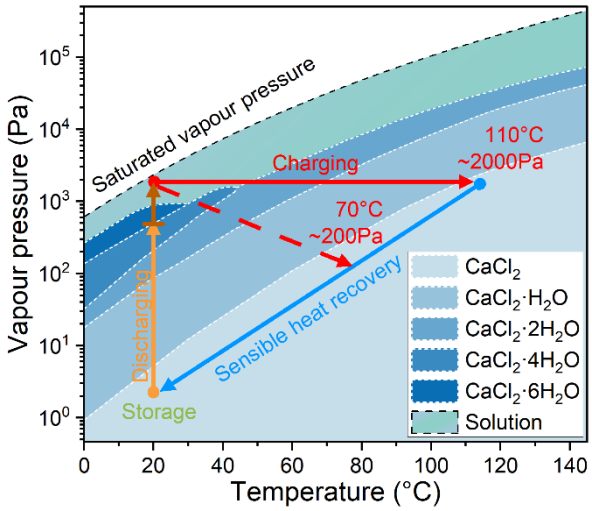


Figure 7-8 Designed conditions for solar-charging thermochemical storage processes with Solar-NanoCaCl$_2$

Therefore, we designed a solar device contains a round quartz tube as the reactor, with a 2.5 times parabolic optical concentrator for achieving such the charging temperature, as the photo image shown in Figure 7-9 (the test rig and conditions are described in method section). Roughly 7g of fully hydrated Solar-NanoCaCl$_2$ (about 4g upon fully dehydrated) was loaded in the reactor and the solar charging was conducted under one sun (100mW/cm^2, a total of 10W) at a 500SCCM air flow.

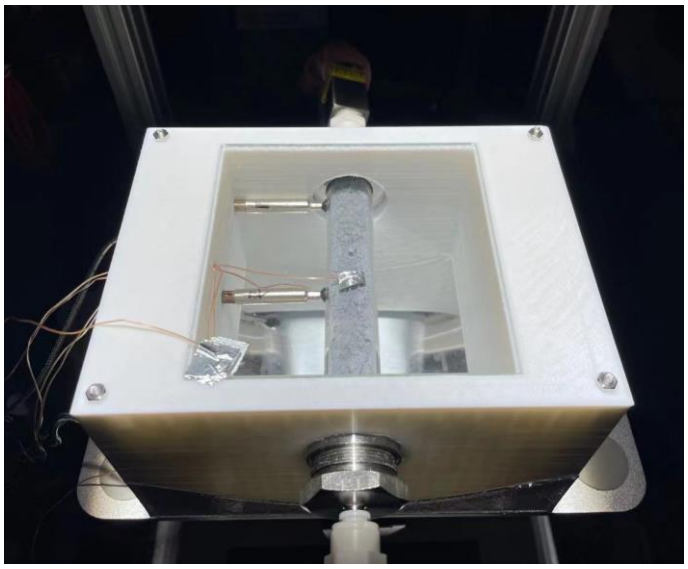


Figure 7-9 a) Photo of the designed thermochemical solar reactor while tested under solar irradiation.

Figure 7-10a shows the results of the solar charging, with temperature and vapour pressure tracked during the experiment. The solar charging (dehydration) process can be confirmed by measuring the vapour pressure change between the outlet and inlet. When the bed temperature raised to 120°C, the vapour pressure at the outlet was higher than the inlet by 4000Pa, indicating that water was being released from Solar-Nano$CaCl_2$. After four hours of solar irradiation, the outlet vapour pressure dropped back to the inlet level, suggesting the Solar-Nano$CaCl_2$ had been fully charged. The reactor was then isolated to prevent undesired thermochemical reactions during storage. The storage term is dependent on real demands, be that hourly or seasonally. In this case, after a week of storage, discharging was performed by the introduction of a humidified air. As Figure 7-10b shows, a 3.5°C temperature lift was observed with the thermochemical reaction lasting half an hour, which

ended with the outlet vapour pressure reached the reactive equilibrium pressure (~500Pa) of $CaCl_2 \cdot 6H_2O$ at the test temperature of ~22°C. The heat release process was rapid, with the heat accumulating in the particle bed and the vessel in sensible heat form. Such heat can be used to provide warm air in a continuous manner for more than 12 hours.

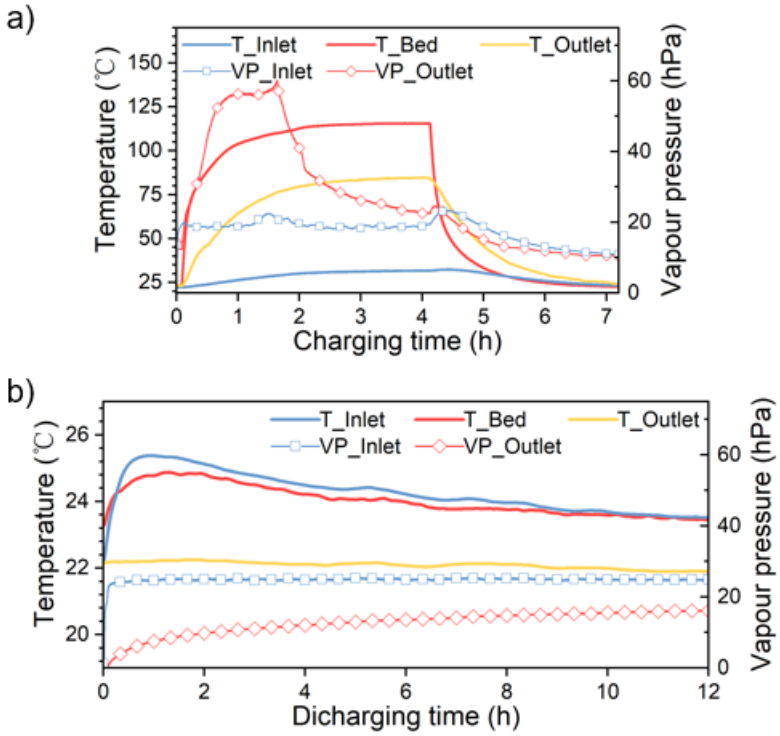


Figure 7-10 a) Temperature and vapour pressure history in solar charging. b) Temperature and vapour pressure history in discharging.

We also observed that the pressure drops across the bed during both the hydration and dehydration increased slightly (see Figure 7-11). This was likely to be due to a slight compact of the particle bed rather than deliquesced solution clogging.

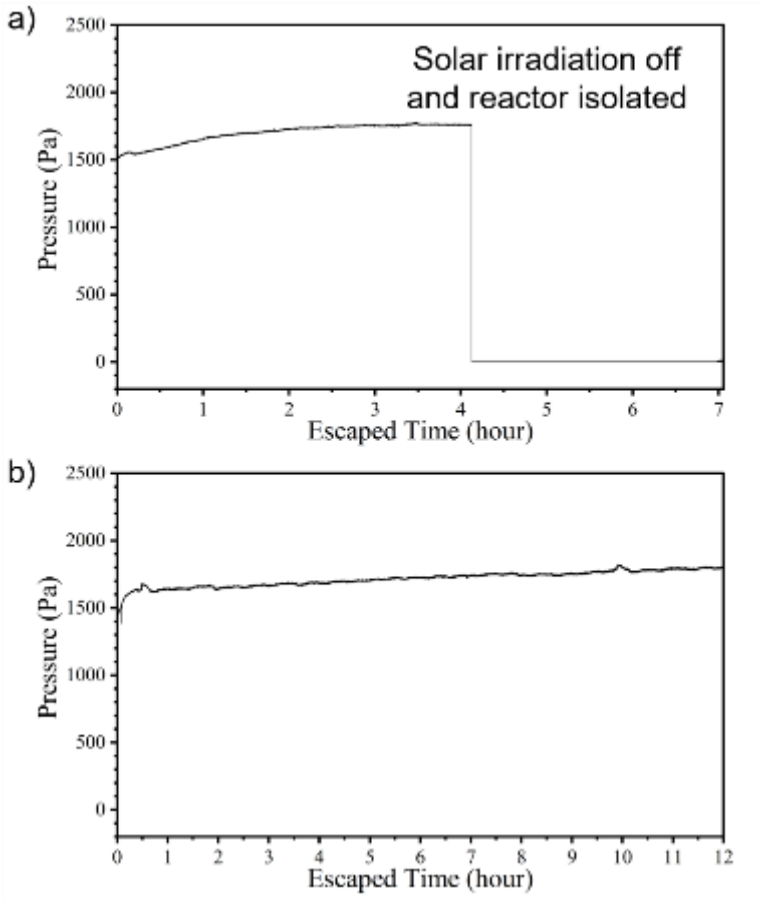


Figure 7-11 Pressure drop across reactive bed during a), dehydration and b), hydration.

7.4 Conclusion

We successfully incorporated TiN NP into the Nano$CaCl_2$ (the product is so called "Solar-Nano$CaCl_2$") for enhancing the harvesting of solar heat. An enhancement of the solar energy absorption by Nano$CaCl_2$ from 3.0% to 51.7% at 250-2500nm spectrum under one standard sun was demonstrated.

In the packed bed solar reactor, a temperature up to 120°C is demonstrated under one-sun irradiation, providing a sufficient condition for dehydration. After a week of storage, a small amount (7g) of hydrated Solar-Nano$CaCl_2$ was

shown to be able to provide a heated air flow with a temperature lift of 3.5°C for over 2 hours without thermal insulation. This result successfully demonstrates the designed workflow, including solar charging, long-term storage and on-demand discharging.

These results demonstrated the feasibility of the solar coupled long-term thermochemical energy storage using the nano encapsulated composite TCS material. However, the thermal efficiency is not high in such a small demonstration device, due to the poor thermal insulation and relatively large thermal mass of mechanical parts compared to materials. In practical applications, the thermal power can be boosted by increasing the inlet vapour pressure and flow rate, and a higher temperature lift can be obtained in a scaled-up reactor with a better thermal insulation, such as a commercial evacuated tube solar collector.

8 Conclusion

This chapter gives a summary of the main conclusions obtained from this work. Recommendations for the future are also given based on this work.

8.1 Summary of the main conclusions

This works focuses on three aspects associated with the thermochemical heat storage technology: i) to fundamentally understand the method of encapsulating thermochemical salt from Pickering emulsion, ii) to develop the method for tailoring and optimising the thermal performance of encapsulated salt, iii) to develop the technique to coupled encapsulated salt with solar energy storage. The following are the main conclusions:

1) The thermochemical heat storage with water vapour sorption in solid salt has a high density of energy storage. Pure salt has many drawbacks, such as poor mass transfer and stability, which is due to deliquesced in high vapour pressure hydration and aggregation in dehydration.
2) The W/O Pickering emulsion is formed by mixing hydrophobic fumed silica nanoparticles in oil suspensions and the aqueous solution. In the conditions of low pH in the aqueous solution, the nanoparticle is self-assembled in the W/O interface from the dispersed in oil. In this system, the major attractive force is identified, which is the electrostatic image force. The van der Waals force presents in a repulsive manner and is possible to be balanced with

the attractive force, resulting in a non-touching adsorbed nanoparticle surrounding the water droplet.

3) There are four measurements to decrease the size of droplets in emulsions, including: increasing emulsification energy, increasing the dosage of nanoparticles, adding salt to the water phase, and using a surfactant. In this way, the size of droplets in the emulsion is precisely and continually adjusted on the nanoscale and microscale. Based on those findings, the encapsulated salt can be fabricated by introducing a continuous shell derived from TEOS, which is hydrolysed under an acid condition. The pH also shows a great influence, not only acting as a catalyst for hydrolysis but also changing the emulsion structure. A low pH condition is preferred to conduct the desired capsules, due to the possible change in the wettability of the nanoparticle.

4) By increasing the thickness of the shell, we found the influences on reaction kinetic are negligible, and the rate-limiting process remains on the moisture diffusion outside the encapsulation. On the other hand, the encapsulation with increased diameter presented a considerable degradation in dehydration kinetic. By STA characterisation, an additional 7% time consumed was found in the encapsulation with a diameter of 8μm, compared to the 800nm encapsulation as the baseline. For unconfined pure salt, there was an extra increase in dry-out temperature and time. For hydration as well as discharging, the conversion rate was always higher in

the smaller encapsulated salt. It highlights the effect of encapsulation on the improvement of the reaction kinetics. In large unconfined pure salt particles, the hydration kinetic was hindered in low vapour pressure conditions, leading to uncompleted heat discharging.

5) A fluidised bed is an optimised design of the device. It is met by the fluidisation of encapsulated salt, which provides strong mixing of powder, low flower resistance and a higher heat generation rate compared to the conventional packed bed. The fluidisation of the fabricated nano-encapsulated salt is demonstrated on the lab scale, evidenced by a clear transition of linear growth-to-plateau in pressure drop according to increased air velocity.

6) A general method for nanoscale encapsulation of abundant and cheap thermochemical salts in one pot using a Pickering emulsion template has been developed, which differs from strategies reported previously. The nano-salt capsules show outstanding hydration-dehydration kinetics enabled by a unique bilayer shell composed of an out layer of silica NP whiskers and a continuous organosilane inner layer. The whisker-like nanostructure and intrinsic hydrophobic $–CH_3$ groups of the outer layer could prevent the inner salt from wetting by exterior liquid water through the formation of an air gap while providing channels for the mass transfer of water vapour during the charging/discharging process. By using calcium chloride as an example, we demonstrate that the Nano$CaCl_2$ possesses

several exciting thermal properties, including a superior specific power with a peak value at ~1.6W/g at 30°C and ~2100Pa vapour pressure, and a high gravimetric energy storage density of over 1700J/g based on anhydrous nanocapsules and a low regeneration temperature of around 85°C. Nano$CaCl_2$ also shows an order of magnitude performance enhancement over pure $CaCl_2$ in both water loading and hydration-dehydration kinetics. Moreover, the nanocapsules with the designed bilayer shell show excellent cycling stability with no significant degradation for 50 cycles. Furthermore, the heat release rate can be easily modulated on-demand by tuning flow rate, temperature and pressure.

7) For the first time, the fluidisation of encapsulated salt is demonstrated with the lab-scale fluidised bed device. A clear transition from stationary to fluidisation was proved by the observed phenomena. The fluidised charging and discharging of encapsulated salt has been demonstrated, which has a potentially higher heat generation rate than a conventional packed bed. It provides strong support for the feasibility of using the encapsulated salt in a large-scale commercial fluidised bed reactor.

8) We further incorporated TiN NP into the Nano$CaCl_2$ (Solar-Nano$CaCl_2$) for harvesting and storing solar heat. By packing the Solar-Nano$CaCl_2$ into a packed bed-based thermochemical reactor, an enhancement of the solar energy absorption by NanoCaCl2 from 3.0% to 51.7% at 250-2500nm spectrum under one standard sun was demonstrated. This led to up to

120°C of charging temperature in the demonstration device. After a week of storage, a small amount (7g) of hydrated Solar-Nano$CaCl_2$ charged for less than 4 hours was shown to be able to provide a heated air flow with a temperature lift of 3.5°C for over 2 hours without thermal insulation.

8.2 Recommendations & future work

Although some interesting and promising results have been concluded in this thesis, there are still many areas worth to be further investigated. The recommendation for future work is as follows:

1) To screen/develop the shell material for encapsulation. The desired shell should be light in density, high in mechanical strength, appreciable vapour permeability and high resistance to liquid water. The silica shell discussed in this thesis meets a few of those requirements. Essentially, a better shell material, which is capable of the Pickering emulsion protocol, should be developed further.
2) Scale up the manufacturing of encapsulated salt: the method of Pickering emulsion has shown the potential to scale up and the materials are all commercially available. It is highly suggested to develop a continuous production facility for encapsulating the salt. The key challenge should be the continuous dispensing and emulsification device.
3) To integrate the encapsulated salt with a direct solar charging fluidised bed reactor: there has been seen the feasibility of using encapsulated salt in a

fluidised bed and the use of encapsulated salt with enhanced solar absorption to store solar heat. It is possible to integrate those two technologies in a system with a separate storage tank and a fluidised reactor.

Appendix: Publications

JOURNAL ARTICLES:

1) **Zheng Du**, Electrostatic effects on formation of submicron water-in-oil Pickering emulsions, in preparation.
2) **Zheng Du**, Tailoring the performance of encapsulated salt for thermochemical energy storage, in preparation.
3) **Zheng Du**, Nanoscale encapsulation of hydratable salts for flexible long-duration thermochemical energy storage, submitted.

Bibliography

[1] G. P. Thiel and A. K. Stark, “To decarbonize industry, we must decarbonize heat,” *Joule*, vol. 5, no. 3, pp. 531–550, 2021, doi: 10.1016/j.joule.2020.12.007.

[2] A. Henry, R. Prasher, and A. Majumdar, “Five thermal energy grand challenges for decarbonization,” *Nat. Energy*, vol. 5, no. 9, pp. 635–637, 2020, doi: 10.1038/s41560-020-0675-9.

[3] International Energy Agency, “World Energy Outlook 2022,” 2022.

[4] C. L. Smith, “The Need for Energy Storage in a Net Zero World,” *Virtual Conference on Medium-Duration Energy Storage in the Net-Zero UK*, 2020. https://www.era.ac.uk/Medium-Duration-Energy-Storage-Event

[5] T. M. Gür, “Review of electrical energy storage technologies, materials and systems: Challenges and prospects for large-scale grid storage,” *Energy Environ. Sci.*, vol. 11, no. 10, pp. 2696–2767, 2018, doi: 10.1039/c8ee01419a.

[6] Z. Dostál and L. Ladányi, “Demands on energy storage for renewable power sources,” *J. Energy Storage*, vol. 18, no. April, pp. 250–255, 2018, doi: 10.1016/j.est.2018.05.003.

[7] J. A. Dowling *et al.*, “Role of Long-Duration Energy Storage in Variable Renewable Electricity Systems,” *Joule*, vol. 4, no. 9, pp. 1907–1928, 2020, doi: 10.1016/j.joule.2020.07.007.

[8] N. A. Sepulveda, J. D. Jenkins, A. Edington, D. S. Mallapragada, and R. K. Lester, “The design space for long-duration energy storage in decarbonized power systems,” *Nat. Energy*, vol. 6, no. May, 2021, doi: 10.1038/s41560-021-00796-8.

[9] R. Shan, J. Reagan, S. Castellanos, S. Kurtz, and N. Kittner, “Evaluating emerging long-duration energy storage technologies,”

Renew. Sustain. Energy Rev., vol. 159, no. January, p. 112240, 2022, doi: 10.1016/j.rser.2022.112240.

[10] U.S. Department Of Energy, “DOE Global Energy Storage Database,” 2021. https://sandia.gov/ess-ssl/gesdb/public/statistics.html (accessed Oct. 25, 2022).

[11] LDES Council, “NET-ZERO HEAT: LONG DURATION ENERGY STORAGE TO ACCELERATE ENERGY SYSTEM DECARBONIZATION,” 2022. [Online]. Available: https://www.ldescouncil.com/assets/pdf/221108_NZH_LDES brochure.pdf

[12] W. Weiss and M. Spörk-Dür, “Solar Heat Worldwide 2022 Edition,” 2022. [Online]. Available: https://www.iea-shc.org/Data/Sites/1/publications/Solar-Heat-Worldwide-2021.pdf

[13] E. Bellos and C. Tzivanidis, “Alternative designs of parabolic trough solar collectors,” *Prog. Energy Combust. Sci.*, vol. 71, pp. 81–117, 2019, doi: 10.1016/j.pecs.2018.11.001.

[14] A. Bonk, S. Sau, N. Uranga, M. Hernaiz, and T. Bauer, “Advanced heat transfer fluids for direct molten salt line-focusing CSP plants,” *Prog. Energy Combust. Sci.*, vol. 67, pp. 1339–1351, 2018, doi: 10.1016/j.pecs.2018.02.002.

[15] S. Kuravi, J. Trahan, D. Y. Goswami, M. M. Rahman, and E. K. Stefanakos, “Thermal energy storage technologies and systems for concentrating solar power plants,” *Prog. Energy Combust. Sci.*, vol. 39, no. 4, pp. 285–319, 2013, doi: 10.1016/j.pecs.2013.02.001.

[16] A. Sharma, V. V. Tyagi, C. R. Chen, and D. Buddhi, “Review on thermal energy storage with phase change materials and applications,” *Renew. Sustain. Energy Rev.*, vol. 13, no. 2, pp. 318–345, 2009, doi: 10.1016/j.rser.2007.10.005.

[17] H. Zhang, J. Baeyens, G. Cáceres, J. Degrève, and Y. Lv, “Thermal energy storage: Recent developments and practical aspects,” *Prog.*

Energy Combust. Sci., vol. 53, pp. 1–40, 2016, doi: 10.1016/j.pecs.2015.10.003.

[18] A. J. Carrillo, J. González-Aguilar, M. Romero, and J. M. Coronado, “Solar Energy on Demand: A Review on High Temperature Thermochemical Heat Storage Systems and Materials,” *Chem. Rev.*, vol. 119, no. 7, pp. 4777–4816, 2019, doi: 10.1021/acs.chemrev.8b00315.

[19] I. Gur, K. Sawyer, and R. Prasher, “Searching for a Better Thermal Battery,” *Science (80-.).*, vol. 335, no. 6075, pp. 1454–1455, Mar. 2012, doi: 10.1126/science.1218761.

[20] A. H. Abedin, “A Critical Review of Thermochemical Energy Storage Systems,” *Open Renew. Energy J.*, vol. 4, no. 1, pp. 42–46, 2011, doi: 10.2174/1876387101004010042.

[21] IRENA, *Innovation Outlook: Thermal Energy Storage*. 2020. [Online]. Available: https://www.irena.org/publications/2020/Nov/Innovation-outlook-Thermal-energy-storage

[22] IEA, “Energy Technology Perspectives 2020,” 2020. doi: 10.1787/ab43a9a5-en.

[23] D. Aydin, S. P. Casey, and S. Riffat, “The latest advancements on thermochemical heat storage systems,” *Renew. Sustain. Energy Rev.*, vol. 41, pp. 356–367, 2015, doi: 10.1016/j.rser.2014.08.054.

[24] P. Pinel, C. A. Cruickshank, I. Beausoleil-Morrison, and A. Wills, “A review of available methods for seasonal storage of solar thermal energy in residential applications,” *Renew. Sustain. Energy Rev.*, vol. 15, no. 7, pp. 3341–3359, 2011, doi: 10.1016/j.rser.2011.04.013.

[25] L. Jiang, R. Z. Wang, L. W. Wang, and A. P. Roskilly, “Investigation on an innovative resorption system for seasonal thermal energy storage,” *Energy Convers. Manag.*, vol. 149, pp. 129–139, 2017, doi: 10.1016/j.enconman.2017.07.018.

[26] Z. Y. Xu and R. Z. Wang, “Absorption seasonal thermal storage cycle

with high energy storage density through multi-stage output," *Energy*, vol. 167, pp. 1086–1096, 2019, doi: 10.1016/j.energy.2018.11.072.

[27] Z. Ma, H. Bao, and A. P. Roskilly, "Seasonal solar thermal energy storage using thermochemical sorption in domestic dwellings in the UK," *Energy*, vol. 166, pp. 213–222, 2019, doi: 10.1016/j.energy.2018.10.066.

[28] M. Mansoor, M. Stadler, M. Zellinger, K. Lichtenegger, H. Auer, and A. Cosic, "Optimal planning of thermal energy systems in a microgrid with seasonal storage and piecewise affine cost functions," *Energy*, vol. 215, p. 119095, 2021, doi: 10.1016/j.energy.2020.119095.

[29] X. Peng, T. W. Root, and C. T. Maravelias, "Storing solar energy with chemistry: The role of thermochemical storage in concentrating solar power," *Green Chem.*, vol. 19, no. 10, pp. 2427–2438, 2017, doi: 10.1039/c7gc00023e.

[30] G. Drake *et al.*, "Development of a small-scale solar thermocchemical energy storage system," *GHTC 2017 - IEEE Glob. Humanit. Technol. Conf. Proc.*, vol. 2017-Janua, pp. 1–8, 2017, doi: 10.1109/GHTC.2017.8239267.

[31] K. Kubiński and Ł. Szabłowski, "Dynamic model of solar heating plant with seasonal thermal energy storage," *Renew. Energy*, vol. 145, pp. 2025–2033, 2020, doi: 10.1016/j.renene.2019.07.120.

[32] A. Crespo, C. Fernández, A. de Gracia, and A. Frazzica, "Solar-Driven Sorption System for Seasonal Heat Storage under Optimal Control: Study for Different Climatic Zones," *Energies*, vol. 15, no. 15, 2022, doi: 10.3390/en15155604.

[33] M. Goldstein, "Some Physical Chemical Aspects of Heat Storage," in *Use of solar energy for heating purposes heat storage*, 1961, vol. 7, no. 2, p. 84.

[34] W. E. Wentworth and E. Chen, "Simple thermal decomposition reactions for storage of solar thermal energy," *Sol. Energy*, vol. 18, no.

3, pp. 205–214, 1976, doi: 10.1016/0038-092X(76)90019-0.

[35] G. Ervin, “Solar heat storage using chemical reactions,” *J. Solid State Chem.*, vol. 22, pp. 51–61, 1977.

[36] R. W. Carling, “Dissociation pressures and enthalpies of reaction in MgCl2 · nH2O and CaCl2 · nNH3,” *J. Chem. Thermodyn.*, vol. 13, no. 6, pp. 503–512, 1981, doi: 10.1016/0021-9614(81)90105-1.

[37] A. Kanzawa and Y. Arai, “Thermal energy storage by the chemical reaction augmentation of heat transfer and thermal decomposition in the CaO Ca(OH)2 powder,” *Sol. Energy*, vol. 27, no. 4, pp. 289–294, 1981, doi: 10.1016/0038-092X(81)90061-X.

[38] A. A. Koutinas, P. Yianoulis, and A. Lycourghiotis, “Industrial scale modelling of the thermochemical energy storage system based on CO2 + 2NH3 ↔ NH2COONH4 equilibrium,” *Energy Convers. Manag.*, vol. 23, no. 1, pp. 55–63, 1983, doi: 10.1016/0196-8904(83)90009-2.

[39] J. H. McCrary, G. E. McCrary, T. A. Chubb, and Y. S. Won, “An experimental study of SO3 dissociation as a mechanism for converting and transporting solar energy,” *Sol. Energy*, vol. 27, no. 5, pp. 433–440, 1981, doi: 10.1016/0038-092X(81)90008-6.

[40] G. De Maria, L. D’Alessio, E. Coffari, M. Paolucci, and C. A. Tiberio, “Thermochemical storage of solar energy with high-temperature chemical reactions,” *Sol. Energy*, vol. 35, no. 5, pp. 409–416, 1985, doi: 10.1016/0038-092X(85)90129-X.

[41] I. Fujii, K. Tsuchiya, M. Higano, and J. Yamada, “Studies of an energy storage system by use of the reversible chemical reaction: CaO + H2O ⇌ Ca(OH)2,” *Sol. Energy*, vol. 34, no. 4–5, pp. 367–377, 1985, doi: 10.1016/0038-092X(85)90049-0.

[42] D. J. Close and T. L. Pryor, “The behaviour of adsorbent energy storage beds,” *Sol. Energy*, vol. 18, no. 4, pp. 287–292, 1976, doi: 10.1016/0038-092X(76)90055-4.

[43] D. J. Close and R. V. Dunkle, “Use of adsorbent beds for energy

storage in drying of heating systems," *Sol. Energy*, vol. 19, no. 3, pp. 233–238, 1977, doi: 10.1016/0038-092X(77)90066-4.

[44] T. L. Pryor and D. J. Close, "Measurements of the behaviour of adsorbent energy storage beds," *Sol. Energy*, vol. 20, no. 2, pp. 151–155, 1978, doi: 10.1016/0038-092X(78)90188-3.

[45] R. A. Shigeishi, C. H. Langford, and B. R. Hollebone, "Solar energy storage using chemical potential changes associated with drying of zeolites," *Sol. Energy*, vol. 23, no. 6, pp. 489–495, 1979, doi: 10.1016/0038-092X(79)90072-0.

[46] R. Scarmozzino, R. Aiello, and A. Santucci, "Chabazitic tuff for thermal storage," *Sol. Energy*, vol. 24, no. 4, pp. 415–416, 1980, doi: 10.1016/0038-092X(80)90307-2.

[47] R. Aiello, A. Nastro, and C. Colella, "Solar energy storage through water adsorption-desorption cycles in zeolitic tuffs," *Thermochim. Acta*, vol. 79, no. C, pp. 271–278, 1984, doi: 10.1016/0040-6031(84)87112-9.

[48] G. Restuccia, V. Recupero, G. Cacciola, and M. Rothmeyer, "Zeolite heat pump for domestic heating," *Energy*, vol. 13, no. 4, pp. 333–342, 1988, doi: 10.1016/0360-5442(88)90028-X.

[49] W. M. Miller, "Energy storage via desiccants for food/agricultural applications," *Energy Agric.*, vol. 2, no. C, pp. 341–354, 1983, doi: 10.1016/0167-5826(83)90029-3.

[50] C. J. Swet, "New Directions in High Temperature Solar Thermal Storage," *Phys. Technol. Sol. Energy*, vol. 2, pp. 389–411, 1987, doi: 10.1007/978-94-009-3941-7_14.

[51] W. Raldow, "Thermal efficiencies of chemical heat pump configurations," *Sol. Energy*, vol. 27, no. 4, pp. 307–311, 1981, doi: 10.1016/0038-092X(81)90064-5.

[52] H. Bjurström and W. Raldow, "the Absorption Process for Heating, Cooling and Energy Storage—an Historical Survey," *Int. J. Energy Res.*, vol. 5, no. 1, pp. 43–59, 1981, doi: 10.1002/er.4440050105.

[53] C. ‐S Cheng and Y. ‐S Shih, “Exergy and energy analyses of absorption heat pumps,” *Int. J. Energy Res.*, vol. 12, no. 2, pp. 189–203, 1988, doi: 10.1002/er.4440120202.

[54] S. B. Riffat, J. R. Knight, and J. R. Skelton, “A vapour re-compression heat pump using liquidised CaCl2/H2O/NH3 and CaCl2/NaSCN/NH3 systems for thermochemical energy storage,” *Heat Recover. Syst. CHP*, vol. 7, no. 3, pp. 203–212, 1987, doi: 10.1016/0890-4332(87)90133-5.

[55] U. Rockenfeller and L. Kirol, “Development of a Complex Compound Chill Storage System,” 1991.

[56] M. Selvidge and I. N. Miaoulis, “Evaluation of reversible hydration reactions for use in thermal energy storage,” *Sol. Energy*, vol. 44, no. 3, pp. 173–178, 1990, doi: 10.1016/0038-092X(90)90081-M.

[57] E. A. Levitskij, Y. I. Aristov, M. M. Tokarev, and V. N. Parmon, “‘Chemical Heat Accumulators’: A new approach to accumulating low potential heat,” *Sol. Energy Mater. Sol. Cells*, vol. 44, no. 3, pp. 219–235, 1996, doi: 10.1016/0927-0248(96)00010-4.

[58] K. E. N’Tsoukpoe, H. Liu, N. Le Pierrès, and L. Luo, “A review on long-term sorption solar energy storage,” *Renew. Sustain. Energy Rev.*, vol. 13, no. 9, pp. 2385–2396, 2009, doi: 10.1016/j.rser.2009.05.008.

[59] A. Hauer, “SORPTION THEORY FOR THERMAL ENERGY STORAGE,” in *Thermal Energy Storage for Sustainable Energy Consumption : Fundamentals, Case Studies and Design*, 2007, pp. 393–408.

[60] N. Yu, R. Z. Wang, and L. W. Wang, “Sorption thermal storage for solar energy,” *Prog. Energy Combust. Sci.*, vol. 39, no. 5, pp. 489–514, 2013, doi: 10.1016/j.pecs.2013.05.004.

[61] Y. Yuan, H. Zhang, F. Yang, N. Zhang, and X. Cao, “Inorganic composite sorbents for water vapor sorption: A research progress,” *Renew. Sustain. Energy Rev.*, vol. 54, pp. 761–776, 2016, doi: 10.1016/j.rser.2015.10.069.

[62] F. Kuznik, K. Johannes, C. Obrecht, and D. David, “A review on recent developments in physisorption thermal energy storage for building applications,” *Renew. Sustain. Energy Rev.*, vol. 94, no. March 2017, pp. 576–586, 2018, doi: 10.1016/j.rser.2018.06.038.

[63] R. M. Barrer and B. E. F. Fender, “The diffusion and sorption of water in zeolites-I. Sorption,” *J. Phys. Chem. Solids*, vol. 21, no. 1–2, pp. 1–11, 1961, doi: 10.1016/0022-3697(61)90206-2.

[64] J. E. Lennard-Jones, “Processes of adsorption and diffusion on solid surfaces,” *Trans. Faraday Soc.*, vol. 28, pp. 333–359, 1932, doi: 10.1039/tf9322800333.

[65] A. Züttel, “Materials for hydrogen storage,” *Mater. Today*, vol. 6, no. 9, pp. 24–33, 2003, doi: 10.1016/S1369-7021(03)00922-2.

[66] A. S. Ülkü and M. Mobedi, “Adsorption in Energy Storage,” *Energy Storage Syst.*, pp. 487–507, 1989, doi: 10.1007/978-94-009-2350-8_21.

[67] B. Mette, H. Kerskes, and H. Drück, “Concepts of long-term thermochemical energy storage for solar thermal applications - Selected examples,” *Energy Procedia*, vol. 30, pp. 321–330, 2012, doi: 10.1016/j.egypro.2012.11.038.

[68] G. A. Farulla, M. Cellura, F. Guarino, and M. Ferraro, “A review of thermochemical energy storage systems for power grid support,” *Appl. Sci.*, vol. 10, no. 9, 2020, doi: 10.3390/app10093142.

[69] F. Desai, J. Sunku Prasad, P. Muthukumar, and M. M. Rahman, “Thermochemical energy storage system for cooling and process heating applications: A review,” *Energy Convers. Manag.*, vol. 229, no. December 2020, p. 113617, 2021, doi: 10.1016/j.enconman.2020.113617.

[70] J. Cot-Gores, A. Castell, and L. F. Cabeza, “Thermochemical energy storage and conversion: A-state-of-the-art review of the experimental research under practical conditions,” *Renew. Sustain. Energy Rev.*, vol. 16, no. 7, pp. 5207–5224, 2012, doi: 10.1016/j.rser.2012.04.007.

[71] F. Kuznik, K. Johannes, and C. Obrecht, “Chemisorption heat storage in buildings: State-of-the-art and outlook,” *Energy Build.*, vol. 106, pp. 183–191, 2015, doi: 10.1016/j.enbuild.2015.07.002.

[72] K. E. N’Tsoukpoe, T. Schmidt, H. U. Rammelberg, B. A. Watts, and W. K. L. Ruck, “A systematic multi-step screening of numerous salt hydrates for low temperature thermochemical energy storage,” *Appl. Energy*, vol. 124, pp. 1–16, 2014, doi: 10.1016/j.apenergy.2014.02.053.

[73] W. R. Busing, “An interpretation of the structures of alkaline earth chlorides in terms of interionic forces.,” *Trans. Am. Crystallogr. Assoc.*, vol. 6, pp. 57–72, 1970, [Online]. Available: http://www.google.dk/search?q=An+interpretation+of+the+structures+of+alkaline+earth+chlorides+in+terms+of+interionic+forces.+&ie=utf-8&oe=utf-8&aq=t&rls=org.mozilla:da:official&client=firefox-a

[74] P. A. Leclaire and M. M. Borel, “Le Dichlorure de Calcium Dihydrate,” *Acta Crystallogr.*, vol. B33, no. 1, pp. 1608–1610, 1977, doi: doi.org/10.1107/S0567740877006645.

[75] J. Sherman, “Crystal energies of ionic compounds and thermochemical applications,” *Chem. Rev.*, vol. 11, no. 1, pp. 93–170, 1932, doi: 10.1021/cr60038a002.

[76] H. D. B. Jenkins, D. M. Hirst, E. Lagadianou, M. Patel, P. Herzig, and I. D. Brown, “Energetics of calcium dichloride hydrates; CaCl2·nH2O (n = 0, 2, 4, 6). Total lattice potential-energy calculations and the relation between the electrostatic and total energy of the hydrates,” *J. Chem. Soc. Faraday Trans. 2 Mol. Chem. Phys.*, vol. 81, no. 11, pp. 1607–1626, 1985, doi: 10.1039/F29858101607.

[77] H. D. B. Jenkins, H. K. Roobottom, J. Passmore, and L. Glasser, “Relationships among ionic lattice energies, molecular (formula unit) volumes, and thermochemical radii,” *Inorg. Chem.*, vol. 38, no. 16, pp. 3609–3620, 1999, doi: 10.1021/ic9812961.

[78] H. D. B. Jenkins, D. Tudela, and L. Glasser, “Lattice potential energy

estimation for complex ionic salts from density measurements," *Inorg. Chem.*, vol. 41, no. 9, pp. 2364–2367, 2002, doi: 10.1021/ic011216k.

[79] H. D. B. Jenkins and L. Glasser, "Ionic hydrates, MpXq·nH2O: Lattice energy and standard enthalpy of formation estimation," *Inorg. Chem.*, vol. 41, no. 17, pp. 4378–4388, 2002, doi: 10.1021/ic020222t.

[80] L. Glasser, "Thermodynamics of inorganic hydration and of humidity control, with an extensive database of salt hydrate pairs," *J. Chem. Eng. Data*, vol. 59, no. 2, pp. 526–530, 2014, doi: 10.1021/je401077x.

[81] S. Kiyabu, J. S. Lowe, A. Ahmed, and D. J. Siegel, "Computational Screening of Hydration Reactions for Thermal Energy Storage: New Materials and Design Rules," *Chem. Mater.*, vol. 30, no. 6, pp. 2006–2017, 2018, doi: 10.1021/acs.chemmater.7b05230.

[82] P. A. J. Donkers, L. C. Sögütoglu, H. P. Huinink, H. R. Fischer, and O. C. G. Adan, "A review of salt hydrates for seasonal heat storage in domestic applications," *Appl. Energy*, vol. 199, pp. 45–68, 2017, doi: 10.1016/j.apenergy.2017.04.080.

[83] R. J. Clark *et al.*, "Experimental screening of salt hydrates for thermochemical energy storage for building heating application," *J. Energy Storage*, vol. 51, no. March, p. 104415, 2022, doi: 10.1016/j.est.2022.104415.

[84] L. Scapino, H. A. Zondag, J. Van Bael, J. Diriken, and C. C. M. Rindt, "Energy density and storage capacity cost comparison of conceptual solid and liquid sorption seasonal heat storage systems for low-temperature space heating," *Renew. Sustain. Energy Rev.*, vol. 76, no. March, pp. 1314–1331, 2017, doi: 10.1016/j.rser.2017.03.101.

[85] L. C. Sögütoglu, P. A. J. Donkers, H. R. Fischer, H. P. Huinink, and O. C. G. Adan, "In-depth investigation of thermochemical performance in a heat battery: Cyclic analysis of K2CO3, MgCl2and Na2S," *Appl. Energy*, vol. 215, no. February, pp. 159–173, 2018, doi: 10.1016/j.apenergy.2018.01.083.

[86] A. Solé, L. Miró, C. Barreneche, I. Martorell, and L. F. Cabeza, “Corrosion of metals and salt hydrates used for thermochemical energy storage,” *Renew. Energy*, vol. 75, pp. 519–523, 2015, doi: 10.1016/j.renene.2014.09.059.

[87] A. Solé, C. Barreneche, I. Martorell, and L. F. Cabeza, “Corrosion evaluation and prevention of reactor materials to contain thermochemical material for thermal energy storage,” *Appl. Therm. Eng.*, vol. 94, pp. 355–363, 2016, doi: 10.1016/j.applthermaleng.2015.10.156.

[88] V. M. Van Essen *et al.*, “Characterization of MgSO4 hydrate for thermochemical seasonal heat storage,” *J. Sol. Energy Eng. Trans. ASME*, vol. 131, no. 4, pp. 0410141–0410147, 2009, doi: 10.1115/1.4000275.

[89] C. J. Ferchaud, R. A. A. Scherpenborg, H. A. Zondag, and R. De Boer, “Thermochemical seasonal solar heat storage in salt hydrates for residential applications - Influence of the water vapor pressure on the desorption kinetics of MgSO4·7H2O,” *Energy Procedia*, vol. 57, pp. 2436–2440, 2014, doi: 10.1016/j.egypro.2014.10.252.

[90] P. A. J. Donkers, S. Beckert, L. Pel, F. Stallmach, M. Steiger, and O. C. G. Adan, “Water Transport in MgSO4·7H2O during Dehydration in View of Thermal Storage,” *J. Phys. Chem. C*, vol. 119, no. 52, pp. 28711–28720, 2015, doi: 10.1021/acs.jpcc.5b08730.

[91] L. Okhrimenko, L. Favergeon, K. Johannes, and F. Kuznik, “New kinetic model of the dehydration reaction of magnesium sulfate hexahydrate: Application for heat storage,” *Thermochim. Acta*, vol. 687, no. February, p. 178569, 2020, doi: 10.1016/j.tca.2020.178569.

[92] K. E. N’Tsoukpoe *et al.*, “A review on the use of calcium chloride in applied thermal engineering,” *Appl. Therm. Eng.*, vol. 75, pp. 513–531, 2015, doi: 10.1016/j.applthermaleng.2014.09.047.

[93] M. Molenda, J. Stengler, M. Linder, and A. Wörner, “Reversible

hydration behavior of CaCl2 at high H2O partial pressures for thermochemical energy storage," *Thermochim. Acta*, vol. 560, pp. 76–81, 2013, doi: 10.1016/j.tca.2013.03.020.

[94] V. M. van Essen *et al.*, "Materials for thermochemical storage : characterization of magnesium sulfate," *Proc. Eurosun*, no. January, pp. 4–9, 2008.

[95] V. Mamani, A. Gutiérrez, and S. Ushak, "Development of low-cost inorganic salt hydrate as a thermochemical energy storage material," *Sol. Energy Mater. Sol. Cells*, vol. 176, no. November 2017, pp. 346–356, 2018, doi: 10.1016/j.solmat.2017.10.021.

[96] E. Vlieg *et al.*, "A Study of the Hydration and Dehydration Transitions of Srcl2 Hydrates for Use in Heat Storage," *SSRN Electron. J.*, pp. 1–20, 2022, doi: 10.2139/ssrn.4042750.

[97] L. Farcot, N. Le Pierrès, and J.-F. Fourmigué, "Experimental investigation of a moving-bed heat storage thermochemical reactor with SrBr2/H2O couple," *J. Energy Storage*, vol. 26, no. March, p. 101009, Dec. 2019, doi: 10.1016/j.est.2019.101009.

[98] M. A. J. M. Beving, A. J. H. Frijns, C. C. M. Rindt, and D. M. J. Smeulders, "Characterization and modelling of K2CO3 cycles for thermochemical energy storage applications," *Proc. Eurotherm Semin. 112*, no. 2019, pp. 1–10, 2019.

[99] K. E. N'Tsoukpoe, G. Restuccia, T. Schmidt, and X. Py, "The size of sorbents in low pressure sorption or thermochemical energy storage processes," *Energy*, vol. 77, pp. 983–998, 2014, doi: 10.1016/j.energy.2014.10.013.

[100] N. M. Ostrovskii, N. A. Chumakova, N. M. Bukhavtsova, N. V. Vernikovskaya, and Y. I. Aristov, "Modeling of the limiting step of water sorption by composite sorbents of the 'calcium chloride in porous matrix' type," *Theor. Found. Chem. Eng.*, vol. 41, no. 1, pp. 83–90, 2007, doi: 10.1134/S0040579507010095.

[101] H. P. Huinink and D. Zahn, “Elucidating water dynamics in MgCl2 hydrates from molecular dynamics simulation,” *Solid State Sci.*, vol. 69, pp. 64–70, 2017, doi: 10.1016/j.solidstatesciences.2017.05.011.

[102] A. D. Pathak, S. Nedea, H. Zondag, C. Rindt, and D. Smeulders, “Diffusive transport of water in magnesium chloride dihydrate under various external conditions for long term heat storage: A ReaxFF-MD study,” *Eur. J. Mech. B/Fluids*, vol. 64, pp. 93–101, 2017, doi: 10.1016/j.euromechflu.2016.12.011.

[103] A. D. Pathak *et al.*, “Mass diffusivity and thermal conductivity estimation of chloride-based salt hydrates for thermo-chemical heat storage: A molecular dynamics study using the reactive force field.,” *Int. J. Heat Mass Transf.*, vol. 149, p. 119090, 2020, doi: 10.1016/j.ijheatmasstransfer.2019.119090.

[104] H. P. Huinink, S. Sansotta, and D. Zahn, “Defect-driven water migration in MgCl2 tetra- and hexahydrates,” *J. Solid State Chem.*, vol. 277, no. May, pp. 221–228, 2019, doi: 10.1016/j.jssc.2019.06.010.

[105] M. A. J. M. Beving, A. J. H. Frijns, C. C. M. Rindt, and D. M. J. Smeulders, “Effect of cycle-induced crack formation on the hydration behaviour of K2CO3 particles: Experiments and modelling,” *Thermochim. Acta*, vol. 692, no. August, p. 178752, 2020, doi: 10.1016/j.tca.2020.178752.

[106] K. Heijmans, B. Klein Holkenborg, S. Gaastra-Nedea, and D. Smeulders, “Advanced diffusion methods for H2O in salt hydrates,” *Comput. Mater. Sci.*, vol. 205, no. February, 2022, doi: 10.1016/j.commatsci.2021.111154.

[107] D. G. Miller, J. A. Rard, L. B. Eppstein, and J. G. Albright, “Mutual diffusion coefficients and ionic transport coefficients lij of MgCl2-H2O at 25°C,” *J. Phys. Chem.*, vol. 88, no. 23, pp. 5739–5748, 1984, doi: 10.1021/j150667a056.

[108] L.-C. Sögütoglu, F. Birkelbach, A. Werner, H. Fischer, H. Huinink, and

O. Adan, “Hydration of salts as a two-step process: Water adsorption and hydrate formation,” *Thermochim. Acta*, vol. 695, no. November 2020, p. 178819, 2020, doi: 10.1016/j.tca.2020.178819.

[109] L.-C. Sögütoglu *et al.*, “Understanding the Hydration Process of Salts: The Impact of a Nucleation Barrier,” *Cryst. Growth Des.*, vol. 19, no. 4, pp. 2279–2288, Apr. 2019, doi: 10.1021/acs.cgd.8b01908.

[110] M. A. Stanish and D. D. Perlmutter, “Kinetics of hydration‐dehydration reactions considered as solid transformations,” *AIChE J.*, vol. 30, no. 4, pp. 557–563, 1984, doi: 10.1002/aic.690300405.

[111] K. Linnow, M. Niermann, D. Bonatz, K. Posern, and M. Steiger, “Experimental studies of the mechanism and kinetics of hydration reactions,” *Energy Procedia*, vol. 48, pp. 394–404, 2014, doi: 10.1016/j.egypro.2014.02.046.

[112] L. J. Mauer and L. S. Taylor, “Water-Solids Interactions: Deliquescence,” *Annu. Rev. Food Sci. Technol.*, vol. 1, no. 1, pp. 41–63, 2010, doi: 10.1146/annurev.food.080708.100915.

[113] R. Li, Y. Shi, L. Shi, M. Alsaedi, and P. Wang, “Harvesting Water from Air: Using Anhydrous Salt with Sunlight,” *Environ. Sci. Technol.*, vol. 52, no. 9, pp. 5398–5406, 2018, doi: 10.1021/acs.est.7b06373.

[114] A. G. Fernández, M. Fullana, L. Calabrese, V. Palomba, A. Frazzica, and L. F. Cabeza, “Corrosion assessment of promising hydrated salts as sorption materials for thermal energy storage systems,” *Renew. Energy*, vol. 150, pp. 428–434, 2020, doi: 10.1016/j.renene.2020.01.001.

[115] P. D’Ans, E. Courbon, M. Frère, G. Descy, T. Segato, and M. Degrez, “Severe corrosion of steel and copper by strontium bromide in thermochemical heat storage reactors,” *Corros. Sci.*, vol. 138, no. April, pp. 275–283, 2018, doi: 10.1016/j.corsci.2018.04.020.

[116] J. Xu, T. Li, T. Yan, J. Chao, and R. Wang, “Dehydration kinetics and thermodynamics of magnesium chloride hexahydrate for thermal energy

storage," *Sol. Energy Mater. Sol. Cells*, vol. 219, no. October 2020, p. 110819, 2021, doi: 10.1016/j.solmat.2020.110819.

[117] J. X. Xu, T. X. Li, J. W. Chao, T. S. Yan, and R. Z. Wang, "High energy-density multi-form thermochemical energy storage based on multi-step sorption processes," *Energy*, vol. 185, pp. 1131–1142, 2019, doi: 10.1016/j.energy.2019.07.076.

[118] S. Z. Xu, Lemington, R. Z. Wang, L. W. Wang, and J. Zhu, "A zeolite 13X/magnesium sulfate–water sorption thermal energy storage device for domestic heating," *Energy Convers. Manag.*, vol. 171, no. January, pp. 98–109, 2018, doi: 10.1016/j.enconman.2018.05.077.

[119] M. M. Tokarev and Y. I. Aristov, "Selective water sorbents for multiple applications, 1. CaCI2 CONFINED IN MESOPORES OF SILICA GEL: SORPTION PROPERTIES," *React. Kinet. Catal. Lett.*, vol. 62, no. 1, pp. 143–150, 1997, doi: 10.1007/BF02475725.

[120] L. Vinet and A. Zhedanov, "SELECTIVE WATER SORBENTS FOR MULTIPLE APPLICATIONS, 4. CaCI2 CONFINED IN SILICA GEL PORES: SORPTION/DESORPTION KINETICS," *React. Kinet. Catal. Lett.*, vol. 44, no. 8, pp. 1689–1699, 1997, doi: 10.1088/1751-8113/44/8/085201.

[121] I. S. Glaznev, I. V. Koptyug, and Y. I. Aristov, "A compact layer of alumina modified by CaCl2: The influence of composition and porous structure on water transport," *Microporous Mesoporous Mater.*, vol. 131, no. 1–3, pp. 358–365, 2010, doi: 10.1016/j.micromeso.2010.01.014.

[122] J. Mrowiec-Białoń, A. B. Jarzębski, and L. Pająk, "Water vapor adsorption on the SiO2-CaCl2 sol-gel composites," *Langmuir*, vol. 15, no. 19, pp. 6505–6509, 1999, doi: 10.1021/la990231n.

[123] C. Y. Tso and C. Y. H. Chao, "Activated carbon, silica-gel and calcium chloride composite adsorbents for energy efficient solar adsorption cooling and dehumidification systems," *Int. J. Refrig.*, vol. 35, no. 6, pp. 1626–1638, 2012, doi: 10.1016/j.ijrefrig.2012.05.007.

[124] D. Zhu, H. Wu, and S. Wang, “Experimental study on composite silica gel supported CaCl2 sorbent for low grade heat storage,” *Int. J. Therm. Sci.*, vol. 45, no. 8, pp. 804–813, 2006, doi: 10.1016/j.ijthermalsci.2005.10.009.

[125] J. Y. Wang, R. Z. Wang, and L. W. Wang, “Water vapor sorption performance of ACF-CaCl2 and silica gel-CaCl2 composite adsorbents,” *Appl. Therm. Eng.*, vol. 100, pp. 893–901, 2016, doi: 10.1016/j.applthermaleng.2016.02.100.

[126] E. Courbon *et al.*, “Further improvement of the synthesis of silica gel and CaCl2 composites: Enhancement of energy storage density and stability over cycles for solar heat storage coupled with space heating applications,” *Sol. Energy*, vol. 157, no. July, pp. 532–541, 2017, doi: 10.1016/j.solener.2017.08.034.

[127] Y. Liu and R. Wang, “Pore structure of new composite adsorbent SiO2 · xH 2O · yCaCl2 with high uptake of water from air,” *Sci. China, Ser. E Technol. Sci.*, vol. 46, no. 5, 2003, doi: 10.1360/02ye0480.

[128] I. Kanzaki, H. Suzuki, R. Hidema, Y. Komoda, and K. Fujioka, “Dynamic Characteristics of Calcium Chloride/Silica Nano-Holed Microcapsule Composites,” *J. Chem. Eng. Japan*, vol. 53, no. 8, pp. 457–462, 2020, doi: 10.1252/jcej.19we159.

[129] I. V. Ponomarenko, I. S. Glaznev, A. V. Gubar, Y. I. Aristov, and S. D. Kirik, “Synthesis and water sorption properties of a new composite ‘CaCl2 confined into SBA-15 pores,’” *Microporous Mesoporous Mater.*, vol. 129, no. 1–2, pp. 243–250, 2010, doi: 10.1016/j.micromeso.2009.09.023.

[130] Y. I. Aristov, I. S. Glaznev, A. Freni, and G. Restuccia, “Kinetics of water sorption on SWS-1L (calcium chloride confined to mesoporous silica gel): Influence of grain size and temperature,” *Chem. Eng. Sci.*, vol. 61, no. 5, pp. 1453–1458, 2006, doi: 10.1016/j.ces.2005.08.033.

[131] Y. I. Aristov, I. V. Koptyug, L. G. Gordeeva, L. Y. Il’ina, and I. S.

Glaznev, “Dynamics of water vapor sorption in a CaCl2/silica gel/binder bed: The effect of the bed pore structure,” *Kinet. Catal.*, vol. 47, no. 5, pp. 776–781, 2006, doi: 10.1134/S0023158406050181.

[132] A. Jabbari-Hichri, S. Bennici, and A. Auroux, “CaCl2-containing composites as thermochemical heat storage materials,” *Sol. Energy Mater. Sol. Cells*, vol. 172, no. July, pp. 177–185, 2017, doi: 10.1016/j.solmat.2017.07.037.

[133] A. Ristić and N. Z. Logar, “New composite water sorbents CaCl2-PHTS for low-temperature sorption heat storage: Determination of structural properties,” *Nanomaterials*, vol. 9, no. 1, 2019, doi: 10.3390/nano9010027.

[134] L. Silvester *et al.*, “Influence of Silica Functionalization on Water Sorption and Thermochemical Heat Storage of Mesoporous SBA-15/CaCl2 Composites,” *ACS Appl. Energy Mater.*, vol. 4, no. 6, pp. 5944–5956, Jun. 2021, doi: 10.1021/acsaem.1c00786.

[135] S. P. Casey, J. Elvins, S. Riffat, and A. Robinson, “Salt impregnated desiccant matrices for ‘open’ thermochemical energy storage - Selection, synthesis and characterisation of candidate materials,” *Energy Build.*, vol. 84, pp. 412–425, 2014, doi: 10.1016/j.enbuild.2014.08.028.

[136] L. G. Gordeeva, A. V. Gubar’, L. M. Plyasova, V. V. Malakhov, and Y. A. Aristov, “Composite water sorbents of the salt in silica gel pores type: The effect of the interaction between the salt and the silica gel surface on the chemical and phase compositions and sorption properties,” *Kinet. Catal.*, vol. 46, no. 5, pp. 736–742, 2005, doi: 10.1007/s10975-005-0130-8.

[137] J. Mrowiec-Białoń, A. B. Jarzębski, A. I. Lachowski, and J. J. Malinowski, “Two-component aerogel adsorbents of water vapour,” *J. Non. Cryst. Solids*, vol. 225, no. 1–3, pp. 184–187, 1998, doi: 10.1016/S0022-3093(98)00111-2.

[138] K. Posern, K. Linnow, M. Niermann, C. Kaps, and M. Steiger, “Thermochemical investigation of the water uptake behavior of MgSO4 hydrates in host materials with different pore size,” *Thermochim. Acta*, vol. 611, pp. 1–9, 2015, doi: 10.1016/j.tca.2015.04.031.

[139] Y. Zhang, V. Palomba, and A. Frazzica, “Development and characterization of LiCl supported composite sorbents for adsorption desalination,” *Appl. Therm. Eng.*, vol. 203, no. December 2021, p. 117953, 2022, doi: 10.1016/j.applthermaleng.2021.117953.

[140] A. Shkatulov, L. G. Gordeeva, I. S. Girnik, H. Huinink, and Y. I. Aristov, “Novel adsorption method for moisture and heat recuperation in ventilation: Composites ‘LiCl/matrix’ tailored for cold climate,” *Energy*, vol. 201, p. 117595, 2020, doi: 10.1016/j.energy.2020.117595.

[141] J. Jänchen, D. Ackermann, E. Weiler, H. Stach, and W. Brösicke, “Calorimetric investigation on zeolites, AlPO4’s and CaCl 2 impregnated attapulgite for thermochemical storage of heat,” *Thermochim. Acta*, vol. 434, no. 1–2, pp. 37–41, 2005, doi: 10.1016/j.tca.2005.01.009.

[142] T. Nonnen *et al.*, “A Thermochemical Long-Term Heat Storage System Based on a Salt/Zeolite Composite,” *Chem. Eng. Technol.*, vol. 39, no. 12, pp. 2427–2434, 2016, doi: 10.1002/ceat.201600301.

[143] T. Nonnen, H. Preißler, S. Kött, S. Beckert, and R. Gläser, “Salt inclusion and deliquescence in salt/zeolite X composites for thermochemical heat storage,” *Microporous Mesoporous Mater.*, vol. 303, no. January, p. 110239, 2020, doi: 10.1016/j.micromeso.2020.110239.

[144] S. Hongois, F. Kuznik, P. Stevens, and J. J. Roux, “Development and characterisation of a new MgSO4-zeolite composite for long-term thermal energy storage,” *Sol. Energy Mater. Sol. Cells*, vol. 95, no. 7, pp. 1831–1837, 2011, doi: 10.1016/j.solmat.2011.01.050.

[145] G. Whiting, D. Grondin, S. Bennici, and A. Auroux, “Heats of water sorption studies on zeolite-MgSO4composites as potential

thermochemical heat storage materials," *Sol. Energy Mater. Sol. Cells*, vol. 112, pp. 112–119, 2013, doi: 10.1016/j.solmat.2013.01.020.

[146] Q. Wang, Y. Xie, B. Ding, G. Yu, F. Ye, and C. Xu, "Structure and hydration state characterizations of MgSO4-zeolite 13x composite materials for long-term thermochemical heat storage," *Sol. Energy Mater. Sol. Cells*, vol. 200, no. February, p. 110047, 2019, doi: 10.1016/j.solmat.2019.110047.

[147] M. Gaeini, A. L. Rouws, J. W. O. Salari, H. A. Zondag, and C. C. M. Rindt, "Characterization of microencapsulated and impregnated porous host materials based on calcium chloride for thermochemical energy storage," *Appl. Energy*, vol. 212, no. May 2017, pp. 1165–1177, 2018, doi: 10.1016/j.apenergy.2017.12.131.

[148] R. Fisher, Y. Ding, and A. Sciacovelli, "Hydration kinetics of K2CO3, MgCl2 and vermiculite-based composites in view of low-temperature thermochemical energy storage," *J. Energy Storage*, vol. 38, no. November 2020, p. 102561, 2021, doi: 10.1016/j.est.2021.102561.

[149] Y. N. Zhang, R. Z. Wang, Y. J. Zhao, T. X. Li, S. B. Riffat, and N. M. Wajid, "Development and thermochemical characterizations of vermiculite/SrBr2 composite sorbents for low-temperature heat storage," *Energy*, vol. 115, pp. 120–128, 2016, doi: 10.1016/j.energy.2016.08.108.

[150] A. I. Shkatulov, J. Houben, H. Fischer, and H. P. Huinink, "Stabilization of K2CO3 in vermiculite for thermochemical energy storage," *Renew. Energy*, vol. 150, pp. 990–1000, 2020, doi: 10.1016/j.renene.2019.11.119.

[151] A. Jabbari-Hichri, S. Bennici, and A. Auroux, "Enhancing the heat storage density of silica–alumina by addition of hygroscopic salts (CaCl2, Ba(OH)2, and LiNO3)," *Sol. Energy Mater. Sol. Cells*, vol. 140, pp. 351–360, 2015, doi: 10.1016/j.solmat.2015.04.032.

[152] Y. Suwa, M. Kumita, R. Noki, A. Kodama, and Y. Otani, "Water vapor

sorption characteristics of calcium chloride-anodized alumina composites," *J. Chem. Eng. Japan*, vol. 49, no. 3, pp. 274–279, 2016, doi: 10.1252/jcej.14we286.

[153] S. Chumnanwat *et al.*, "Pore structure control of anodized alumina film and sorption properties of water vapor on CaCl2-aluminum composites," *Energy*, vol. 208, p. 118370, 2020, doi: 10.1016/j.energy.2020.118370.

[154] Y. N. Zhang, R. Z. Wang, and T. X. Li, "Thermochemical characterizations of high-stable activated alumina/LiCl composites with multistage sorption process for thermal storage," *Energy*, vol. 156, pp. 240–249, 2018, doi: 10.1016/j.energy.2018.05.047.

[155] K. Fujioka, K. Hatanaka, and Y. Hirata, "Composite reactants of calcium chloride combined with functional carbon materials for chemical heat pumps," *Appl. Therm. Eng.*, vol. 28, no. 4, pp. 304–310, 2008, doi: 10.1016/j.applthermaleng.2006.02.032.

[156] Z. Duan *et al.*, "CaCl2·6H2O/Expanded graphite composite as form-stable phase change materials for thermal energy storage," *J. Therm. Anal. Calorim.*, vol. 115, no. 1, pp. 111–117, 2014, doi: 10.1007/s10973-013-3311-0.

[157] K. Korhammer *et al.*, "Sorption and thermal characterization of composite materials based on chlorides for thermal energy storage," *Appl. Energy*, vol. 162, pp. 1462–1472, 2016, doi: 10.1016/j.apenergy.2015.08.037.

[158] Q. Zhao, J. Lin, H. Huang, Z. Xie, and Y. Xiao, "Enhancement of heat and mass transfer of potassium carbonate-based thermochemical materials for thermal energy storage," *J. Energy Storage*, vol. 50, no. February, p. 104259, 2022, doi: 10.1016/j.est.2022.104259.

[159] A. Zambotti *et al.*, "Thermochemical heat storage performances of magnesium sulphate confined in polymer-derived SiOC aerogels," *J. Alloys Compd.*, vol. 895, 2022, doi: 10.1016/j.jallcom.2021.162592.

[160] A. Entezari, M. Ejeian, and R. Wang, "Super Atmospheric Water

Harvesting Hydrogel with Alginate Chains Modified with Binary Salts," *ACS Mater. Lett.*, pp. 471–477, 2020, doi: 10.1021/acsmaterialslett.9b00315.

[161] T. Yan *et al.*, "Ultrahigh-Energy-Density Sorption Thermal Battery Enabled by Graphene Aerogel-Based Composite Sorbents for Thermal Energy Harvesting from Air," *ACS Energy Lett.*, pp. 1795–1802, 2021, doi: 10.1021/acsenergylett.1c00284.

[162] S. Afflerbach, M. Kappes, A. Gipperich, R. Trettin, and W. Krumm, "Semipermeable encapsulation of calcium hydroxide for thermochemical heat storage solutions," *Sol. Energy*, vol. 148, pp. 1–11, 2017, doi: 10.1016/j.solener.2017.03.074.

[163] M. Steiger, K. Linnow, H. Juling, S. Brüggerhoff, and D. Kirchner, "Hydration of MgSO4 ·H2O and Generation of Stress in Porous Materials," *Cryst. Growth Des.*, vol. 8, p. 336, 2008.

[164] A. Permyakova *et al.*, "Design of salt-metal organic framework composites for seasonal heat storage applications," *J. Mater. Chem. A*, vol. 5, no. 25, pp. 12889–12898, 2017, doi: 10.1039/c7ta03069j.

[165] J. Xu *et al.*, "Efficient Solar‐Driven Water Harvesting from Arid Air with Metal–Organic Frameworks Modified by Hygroscopic Salt," *Angew. Chemie Int. Ed.*, vol. 59, no. 13, pp. 5202–5210, Mar. 2020, doi: 10.1002/anie.201915170.

[166] R. Li, Y. Shi, M. Wu, S. Hong, and P. Wang, "Improving atmospheric water production yield: Enabling multiple water harvesting cycles with nano sorbent," *Nano Energy*, vol. 67, no. November 2019, p. 104255, 2020, doi: 10.1016/j.nanoen.2019.104255.

[167] A. Shkatulov, R. Joosten, H. Fischer, and H. Huinink, "Core–Shell Encapsulation of Salt Hydrates into Mesoporous Silica Shells for Thermochemical Energy Storage," *ACS Appl. Energy Mater.*, vol. 3, no. 7, pp. 6860–6869, 2020, doi: 10.1021/acsaem.0c00971.

[168] K. Yang *et al.*, "Hollow spherical SiO2 micro-container encapsulation of

LiCl for high-performance simultaneous heat reallocation and seawater desalination," *J. Mater. Chem. A*, vol. 8, no. 4, pp. 1887–1895, 2020, doi: 10.1039/c9ta11721k.

[169] B. G. P. Van Ravensteijn *et al.*, "Encapsulation of Salt Hydrates by Polymer Coatings for Low-Temperature Heat Storage Applications," *ACS Appl. Polym. Mater.*, vol. 3, no. 4, pp. 1712–1726, 2021, doi: 10.1021/acsapm.0c01186.

[170] R. Cuypers *et al.*, "Microencapsulation of Salts for Enhanced Thermochemical Storage Materials," *40th Annu. Meet. Expo. Control. Release Soc. Honolulu, Hawaii, USA*, vol. 24, no. 2, p. 212, 2013, [Online]. Available: http://ci.nii.ac.jp/naid/10016489498/

[171] S. Wei *et al.*, "Scalable Production of EP/CaCl2@C Multistage Core–Shell Sorbent for Solar-Driven Sorption Heat Storage Application," *Energy & Fuels*, vol. 35, no. 8, pp. 6845–6857, Apr. 2021, doi: 10.1021/acs.energyfuels.0c04021.

[172] S. Wei *et al.*, "Development of pomegranate-type CaCl2@C composites via a scalable one-pot pyrolysis strategy for solar-driven thermochemical heat storage," *Energy Convers. Manag.*, vol. 212, no. February, p. 112694, 2020, doi: 10.1016/j.enconman.2020.112694.

[173] S. Afflerbach, K. Afflerbach, R. Trettin, and W. Krumm, "Improvement of a semipermeable shell for encapsulation of calcium hydroxide for thermochemical heat storage solutions: Material design and evaluation in laboratory and reactor scale," *Sol. Energy*, vol. 217, no. September 2018, pp. 208–222, 2021, doi: 10.1016/j.solener.2021.02.005.

[174] A. Jamekhorshid, S. M. Sadrameli, and M. Farid, "A review of microencapsulation methods of phase change materials (PCMs) as a thermal energy storage (TES) medium," *Renew. Sustain. Energy Rev.*, vol. 31, pp. 531–542, 2014, doi: 10.1016/j.rser.2013.12.033.

[175] C. Liu, Z. Rao, J. Zhao, Y. Huo, and Y. Li, "Review on nanoencapsulated phase change materials: Preparation,

characterization and heat transfer enhancement,” *Nano Energy*, vol. 13, pp. 814–826, 2015, doi: 10.1016/j.nanoen.2015.02.016.

[176] E. M. Shchukina, M. Graham, Z. Zheng, and D. G. Shchukin, “Nanoencapsulation of phase change materials for advanced thermal energy storage systems,” *Chem. Soc. Rev.*, pp. 4156–4175, 2018, doi: 10.1039/C8CS00099A.

[177] E. Shchukina and D. G. Shchukin, “Nanocontainer-Based Active Systems: From Self-Healing Coatings to Thermal Energy Storage,” *Langmuir*, p. acs.langmuir.9b00151, 2019, doi: 10.1021/acs.langmuir.9b00151.

[178] H. Zhang, C. Xu, and G. Fang, “Encapsulation of inorganic phase change thermal storage materials and its effect on thermophysical properties: A review,” *Sol. Energy Mater. Sol. Cells*, vol. 241, no. February, p. 111747, 2022, doi: 10.1016/j.solmat.2022.111747.

[179] J. Huang, T. Wang, P. Zhu, and J. Xiao, “Preparation, characterization, and thermal properties of the microencapsulation of a hydrated salt as phase change energy storage materials,” *Thermochim. Acta*, vol. 557, pp. 1–6, 2013, doi: 10.1016/j.tca.2013.01.019.

[180] M. Graham, E. Shchukina, P. F. De Castro, and D. Shchukin, “Nanocapsules containing salt hydrate phase change materials for thermal energy storage,” *J. Mater. Chem. A*, vol. 4, no. 43, pp. 16906–16912, 2016, doi: 10.1039/c6ta06189c.

[181] M. Graham, J. A. Coca-Clemente, E. Shchukina, and D. Shchukin, “Nanoencapsulated crystallohydrate mixtures for advanced thermal energy storage,” *J. Mater. Chem. A*, vol. 5, no. 26, pp. 13683–13691, 2017, doi: 10.1039/c7ta02494k.

[182] A. Schoth, K. Landfester, and R. Muñoz-Espí, “Surfactant-free polyurethane nanocapsules via inverse pickering miniemulsion,” *Langmuir*, vol. 31, no. 13, pp. 3784–3788, 2015, doi: 10.1021/acs.langmuir.5b00442.

[183] M. Graham *et al.*, “Highly Stable Energy Capsules with Nano-SiO2 Pickering Shell for Thermal Energy Storage and Release,” *ACS Nano*, vol. 14, no. 7, pp. 8894–8901, Jun. 2020, doi: 10.1021/acsnano.0c03706.

[184] D. Saihi, I. Vroman, S. Giraud, and S. Bourbigot, “Microencapsulation of ammonium phosphate with a polyurethane shell. Part II. Interfacial polymerization technique,” *React. Funct. Polym.*, vol. 66, no. 10, pp. 1118–1125, 2006, doi: 10.1016/j.reactfunctpolym.2006.02.001.

[185] K. Bean, C. F. Black, N. Govan, P. Reynolds, and M. R. Sambrook, “Preparation of aqueous core/silica shell microcapsules,” *J. Colloid Interface Sci.*, vol. 366, no. 1, pp. 16–22, 2012, doi: 10.1016/j.jcis.2011.09.054.

[186] Z. Chen, Y. Zhao, Y. Zhao, H. Thomas, X. Zhu, and M. Möller, “Inclusion of Phase-Change Materials in Submicron Silica Capsules Using a Surfactant-Free Emulsion Approach,” *Langmuir*, vol. 34, no. 35, pp. 10397–10406, 2018, doi: 10.1021/acs.langmuir.8b02435.

[187] T. Bollhorst, K. Rezwan, and M. Maas, “Colloidal capsules: Nano- and microcapsules with colloidal particle shells,” *Chem. Soc. Rev.*, vol. 46, no. 8, pp. 2091–2126, 2017, doi: 10.1039/c6cs00632a.

[188] H. a Zondag, A. Kalbasenka, and M. Van Essen, “First studies in reactor concepts for Thermochemical Storage,” *ECN Energy Res.*, pp. 1–6, 2008.

[189] B. Fumey, R. Weber, and L. Baldini, “Sorption based long-term thermal energy storage – Process classification and analysis of performance limitations: A review,” *Renew. Sustain. Energy Rev.*, vol. 111, no. April, pp. 57–74, 2019, doi: 10.1016/j.rser.2019.05.006.

[190] A. H. Abedin and M. A. Rosen, “Closed and open thermochemical energy storage: Energy- and exergy-based comparisons,” *Energy*, vol. 41, no. 1, pp. 83–92, 2012, doi: 10.1016/j.energy.2011.06.034.

[191] M. Bouché, M. Richter, and M. Linder, “Heat transformation based on

CaCl2/H2O - Part B: Open operation principle," *Appl. Therm. Eng.*, vol. 102, no. mm, pp. 641–647, 2016, doi: 10.1016/j.applthermaleng.2016.03.102.

[192] H. Zondag, B. Kikkert, S. Smeding, R. de Boer, and M. Bakker, "Prototype thermochemical heat storage with open reactor system," *Appl. Energy*, vol. 109, pp. 360–365, 2013, doi: 10.1016/j.apenergy.2013.01.082.

[193] N. Yu, R. Z. Wang, and L. W. Wang, "Theoretical and experimental investigation of a closed sorption thermal storage prototype using LiCl/water," *Energy*, vol. 93, pp. 1523–1534, 2015, doi: 10.1016/j.energy.2015.10.001.

[194] A. Lass-Seyoum, D. Borozdenko, T. Friedrich, T. Langhof, and S. Mack, "Practical Test on a Closed Sorption Thermochemical Storage System with Solar Thermal Energy," *Energy Procedia*, vol. 91, pp. 182–189, 2016, doi: 10.1016/j.egypro.2016.06.200.

[195] M. Bouché, M. Richter, M. Linder, M. Bouché, and M. Linder, "Heat transformation based on CaCl2/H2O - Part A: Closed operation principle," *Appl. Therm. Eng.*, vol. 102, pp. 615–621, 2016, doi: 10.1016/j.applthermaleng.2016.03.076.

[196] B. Michel, P. Neveu, and N. Mazet, "Comparison of closed and open thermochemical processes, for long-term thermal energy storage applications," *Energy*, vol. 72, pp. 702–716, 2014, doi: 10.1016/j.energy.2014.05.097.

[197] J. Stengler and M. Linder, "Thermal energy storage combined with a temperature boost: An underestimated feature of thermochemical systems," *Appl. Energy*, vol. 262, no. February, p. 114530, 2020, doi: 10.1016/j.apenergy.2020.114530.

[198] Z. Y. Zeng, B. C. Zhao, and R. Z. Wang, "Passive day and night heating for zero energy buildings with solar-based adsorption thermal battery," *Cell Reports Phys. Sci.*, vol. 2, no. 9, p. 100578, 2021, doi:

10.1016/j.xcrp.2021.100578.

[199] Y. N. Zhang, R. Z. Wang, and T. X. Li, “Experimental investigation on an open sorption thermal storage system for space heating,” *Energy*, vol. 141, pp. 2421–2433, 2017, doi: 10.1016/j.energy.2017.12.003.

[200] B. Michel, N. Mazet, S. Mauran, D. Stitou, and J. Xu, “Thermochemical process for seasonal storage of solar energy: Characterization and modeling of a high density reactive bed,” *Energy*, vol. 47, no. 1, pp. 553–563, 2012, doi: 10.1016/j.energy.2012.09.029.

[201] S. P. Casey, D. Aydin, S. Riffat, and J. Elvins, “Salt impregnated desiccant matrices for ‘open’ thermochemical energy storage - Hygrothermal cyclic behaviour and energetic analysis by physical experimentation,” *Energy Build.*, vol. 92, pp. 128–139, 2015, doi: 10.1016/j.enbuild.2015.01.048.

[202] K. Johannes, F. Kuznik, J. L. Hubert, F. Durier, and C. Obrecht, “Design and characterisation of a high powered energy dense zeolite thermal energy storage system for buildings,” *Appl. Energy*, vol. 159, pp. 80–86, 2015, doi: 10.1016/j.apenergy.2015.08.109.

[203] M. Gaeini, M. R. Javed, H. Ouwerkerk, H. A. Zondag, and C. C. M. Rindt, “Realization of a 4kW thermochemical segmented reactor in household scale for seasonal heat storage,” *Energy Procedia*, vol. 135, pp. 105–114, 2017, doi: 10.1016/j.egypro.2017.09.491.

[204] B. Michel, N. Mazet, and P. Neveu, “Experimental investigation of an innovative thermochemical process operating with a hydrate salt and moist air for thermal storage of solar energy: Global performance,” *Appl. Energy*, vol. 129, pp. 177–186, 2014, doi: 10.1016/j.apenergy.2014.04.073.

[205] J. Woods, A. Mahvi, A. Goyal, E. Kozubal, A. Odukomaiya, and R. Jackson, “Rate capability and Ragone plots for phase change thermal energy storage,” *Nat. Energy*, vol. 6, no. 3, pp. 295–302, Mar. 2021, doi: 10.1038/s41560-021-00778-w.

[206] D. Aydin, S. P. Casey, X. Chen, and S. Riffat, “Novel ‘open-sorption pipe’ reactor for solar thermal energy storage,” *Energy Convers. Manag.*, vol. 121, pp. 321–334, 2016, doi: 10.1016/j.enconman.2016.05.045.

[207] S. P. Casey, D. Aydin, J. Elvins, and S. Riffat, “Salt impregnated desiccant matrices for ‘open’ thermochemical energy conversion and storage – Improving energy density utilisation through hygrodynamic & thermodynamic reactor design,” *Energy Convers. Manag.*, vol. 142, no. 2017, pp. 426–440, 2017, doi: 10.1016/j.enconman.2017.03.066.

[208] L. Farcot, N. Le Pierrès, B. Michel, J. F. Fourmigué, and P. Papillon, “Numerical investigations of a continuous thermochemical heat storage reactor,” *J. Energy Storage*, vol. 20, no. August, pp. 109–119, 2018, doi: 10.1016/j.est.2018.08.020.

[209] J. Wyttenbach *et al.*, “Performances and modelling of a circular moving bed thermochemical reactor for seasonal storage,” *Appl. Energy*, vol. 230, no. August, pp. 803–815, 2018, doi: 10.1016/j.apenergy.2018.09.008.

[210] R. J. Clark, A. Mehrabadi, and M. Farid, “State of the art on salt hydrate thermochemical energy storage systems for use in building applications,” *J. Energy Storage*, vol. 27, no. July 2019, p. 101145, 2020, doi: 10.1016/j.est.2019.101145.

[211] S. Flegkas, F. Birkelbach, F. Winter, N. Freiberger, and A. Werner, “Fluidized bed reactors for solid-gas thermochemical energy storage concepts - Modelling and process limitations,” *Energy*, vol. 143, pp. 615–623, 2018, doi: 10.1016/j.energy.2017.11.065.

[212] S. Padula, C. Tregambi, R. Solimene, R. Chirone, M. Troiano, and P. Salatino, “A novel fluidized bed ‘thermochemical battery’ for energy storage in concentrated solar thermal technologies,” *Energy Convers. Manag.*, vol. 236, 2021, doi: 10.1016/j.enconman.2021.113994.

[213] D. A. Bardy, C. A. Cruickshank, F. H. Tezel, Y. H. Carrier, and B. Wong,

"An experimental investigation of fixed and fluidized beds as adsorbers in compact thermal energy storage systems," *J. Energy Storage*, vol. 31, no. December 2019, p. 101648, 2020, doi: 10.1016/j.est.2020.101648.

[214] J. R. Howard, *Fluidized bed technology: principles and applications.* Bristol: Hilger, 1989. doi: 10.1016/0032-5910(90)80013-o.

[215] O. Skrylnyk, E. Courbon, N. Heymans, M. Frère, J. Bougard, and G. Descy, "Performance characterization of salt-in-silica composite materials for seasonal energy storage design," *J. Energy Storage*, vol. 19, no. August, pp. 320–336, Oct. 2018, doi: 10.1016/j.est.2018.08.015.

[216] T. Kodama, *High-temperature solar chemistry for converting solar heat to chemical fuels*, vol. 29, no. 6. 2003. doi: 10.1016/S0360-1285(03)00059-5.

[217] J. V. Briongos, J. Gómez-Hernández, P. A. González-Gómez, and D. Serrano, "Two-phase heat transfer model of a beam-down gas-solid fluidized bed solar particle receiver," *Sol. Energy*, vol. 171, no. June, pp. 740–750, 2018, doi: 10.1016/j.solener.2018.07.016.

[218] C. Tregambi, R. Chirone, F. Montagnaro, P. Salatino, and R. Solimene, "Heat transfer in directly irradiated fluidized beds," *Sol. Energy*, vol. 129, pp. 85–100, 2016, doi: 10.1016/j.solener.2016.01.057.

[219] M. Wuerth, M. Becker, P. Ostermeier, S. Gleis, and H. Spliethoff, "Development of a continuous fluidized bed reactor for thermochemical energy storage application," *J. Energy Resour. Technol. Trans. ASME*, vol. 141, no. 7, pp. 1–6, 2019, doi: 10.1115/1.4043629.

[220] K. Risthaus, M. Linder, and M. Schmidt, "Experimental investigation of a novel mechanically fluidized bed reactor for thermochemical energy storage with calcium hydroxide/calcium oxide," *Appl. Energy*, vol. 315, no. September 2021, p. 118976, 2022, doi: 10.1016/j.apenergy.2022.118976.

[221] M. Neises, S. Tescari, L. de Oliveira, M. Roeb, C. Sattler, and B. Wong,

“Solar-heated rotary kiln for thermochemical energy storage,” *Sol. Energy*, vol. 86, no. 10, pp. 3040–3048, 2012, doi: 10.1016/j.solener.2012.07.012.

[222] S. Tescari *et al.*, “Thermochemical solar energy storage via redox oxides: Materials and reactor/heat exchanger concepts,” *Energy Procedia*, vol. 49, pp. 1034–1043, 2013, doi: 10.1016/j.egypro.2014.03.111.

[223] H. Zheng *et al.*, “Dark calcium carbonate particles for simultaneous full-spectrum solar thermal conversion and large-capacity thermochemical energy storage,” *Sol. Energy Mater. Sol. Cells*, vol. 207, no. August 2019, p. 110364, 2020, doi: 10.1016/j.solmat.2019.110364.

[224] T. Kodama, S. Bellan, N. Gokon, and H. Seok, “Particle reactors for solar thermochemical processes,” *Sol. Energy*, vol. 156, pp. 113–132, 2017, doi: 10.1016/j.solener.2017.05.084.

[225] G. Krese, R. Koželj, V. Butala, and U. Stritih, “Thermochemical seasonal solar energy storage for heating and cooling of buildings,” *Energy Build.*, vol. 164, pp. 239–253, 2018, doi: 10.1016/j.enbuild.2017.12.057.

[226] L. F. Marie, S. Landini, D. Bae, V. Francia, and T. S. O. Donovan, “Advances in thermochemical energy storage and fluidised beds for domestic heat,” *J. Energy Storage*, vol. 53, no. December 2021, p. 105242, 2022, doi: 10.1016/j.est.2022.105242.

[227] C. Ferchaud, H. Zondag, R. de Boer, and C. Rindt, “Characterization of the sorption process in thermochemical materials for seasonal solar heat storage application,” in *The 12th International Conference on Energy Storag*, 2012, no. 2012.

[228] H. Kerskes, S. Asenbeck, F. Bertsch, H. Drück, and B. Mette, “Development of a thermo-chemical energy storage for solar thermal applications,” in *30th ISES Biennial Solar World Congress 2011, SWC 2011*, 2011, vol. 6, pp. 4679–4685. doi: 10.18086/swc.2011.29.14.

[229] S. Mauran, H. Lahmidi, and V. Goetz, “Solar heating and cooling by a thermochemical process. First experiments of a prototype storing 60 kW h by a solid/gas reaction,” *Sol. Energy*, vol. 82, no. 7, pp. 623–636, 2008, doi: 10.1016/j.solener.2008.01.002.

[230] K. M. Z. Hossain, L. Deeming, and K. J. Edler, “Recent progress in Pickering emulsions stabilised by bioderived particles,” *RSC Adv.*, vol. 11, no. 62, pp. 39027–39044, 2021, doi: 10.1039/d1ra08086e.

[231] A. Kabalnov, “Thermodynamic and theoretical aspects of emulsions and their stability,” *Curr. Opin. Colloid Interface Sci.*, vol. 3, no. 3, pp. 270–275, 1998, doi: 10.1016/S1359-0294(98)80071-X.

[232] K. L. Thompson, E. C. Giakoumatos, S. Ata, G. B. Webber, S. P. Armes, and E. J. Wanless, “Direct observation of giant pickering emulsion and colloidosome droplet interaction and stability,” *Langmuir*, vol. 28, no. 48, pp. 16501–16511, 2012, doi: 10.1021/la3025765.

[233] M. Mukherjee, M. G. Basavaraj, and N. Madhavan, “Porous ceramics via processable pickering emulsion stabilized by oppositely charged colloids,” *Langmuir*, vol. 36, no. 39, pp. 11645–11654, 2020, doi: 10.1021/acs.langmuir.0c02339.

[234] Q. Li, M. Hatakeyama, and T. Kitaoka, “Bioadaptive Porous 3D Scaffolds Comprising Cellulose and Chitosan Nanofibers Constructed by Pickering Emulsion Templating,” *Adv. Funct. Mater.*, vol. 2200249, p. 2200249, 2022, doi: 10.1002/adfm.202200249.

[235] B. Neirinck, J. Fransaer, O. Van Der Biest, and J. Vleugels, “Production of porous materials through consolidation of pickering emulsions,” *Adv. Eng. Mater.*, vol. 9, no. 1–2, pp. 57–59, 2007, doi: 10.1002/adem.200600191.

[236] B. P. Binks, “Particles as surfactants-similarities and differences,” *Curr. Opin. Colloid Interface Sci.*, vol. 7, pp. 21–41, 2002, [Online]. Available: http://www.firp.ula.ve/archivos/cuadernos/02_COCIS_Binks.pdf

[237] B. P. Binks and S. O. Lumsdon, “Influence of particle wettability on the

type and stability of surfactant-free emulsions," *Langmuir*, vol. 16, no. 23, pp. 8622–8631, 2000, doi: 10.1021/la000189s.

[238] A. M. Bago Rodriguez and B. P. Binks, "Capsules from Pickering emulsion templates," *Curr. Opin. Colloid Interface Sci.*, vol. 44, pp. 107–129, Dec. 2019, doi: 10.1016/j.cocis.2019.09.006.

[239] H. Jiang, Y. Sheng, and T. Ngai, "Pickering emulsions: Versatility of colloidal particles and recent applications," *Curr. Opin. Colloid Interface Sci.*, vol. 49, pp. 1–15, 2020, doi: 10.1016/j.cocis.2020.04.010.

[240] G. M. Radulova, T. G. Slavova, P. A. Kralchevsky, E. S. Basheva, K. G. Marinova, and K. D. Danov, "Encapsulation of oils and fragrances by core-in-shell structures from silica particles, polymers and surfactants: The brick-and-mortar concept," *Colloids Surfaces A Physicochem. Eng. Asp.*, vol. 559, no. July, pp. 351–364, 2018, doi: 10.1016/j.colsurfa.2018.09.079.

[241] J. W. O. Salari, J. Van Heck, and B. Klumperman, "Steric stabilization of pickering emulsions for the efficient synthesis of polymeric microcapsules," *Langmuir*, vol. 26, no. 18, pp. 14929–14936, 2010, doi: 10.1021/la1025284.

[242] J. Mathias and G. Wannemacher, "Basic characteristics and applications of aerosil," *J. Colloid Interface Sci.*, vol. 125, no. 1, pp. 61–68, 1988, doi: 10.1016/0021-9797(88)90054-9.

[243] J. G. Croissant, K. S. Butler, J. I. Zink, and C. J. Brinker, "Synthetic amorphous silica nanoparticles: toxicity, biomedical and environmental implications," *Nat. Rev. Mater.*, 2020, doi: 10.1038/s41578-020-0230-0.

[244] S. Jonat, "the Mechanism of Hydrophilic and Hydrophobic Colloidal Silicon Dioxide Types As Glidants," University of Tübingen, 2005.

[245] C. Chen, D. Weng, S. Chen, A. Mahmood, and J. Wang, "Development of Durable, Fluorine-free, and Transparent Superhydrophobic Surfaces for Oil/Water Separation," *ACS Omega*, vol. 4, no. 4, pp. 6947–6954, 2019, doi: 10.1021/acsomega.9b00518.

[246] T. Hielscher, “Ultrasonic Production of Nano-Size Dispersions and Emulsions,” no. December, pp. 14–16, 2007, [Online]. Available: http://arxiv.org/abs/0708.1831

[247] J. S. Taurozzi, V. A. Hackley, and M. R. Wiesner, “Ultrasonic dispersion of nanoparticles for environmental, health and safety assessment issues and recommendations,” *Nanotoxicology*, vol. 5, no. 4, pp. 711–729, 2011, doi: 10.3109/17435390.2010.528846.

[248] V. S. Nguyen, D. Rouxel, and B. Vincent, “Dispersion of nanoparticles: From organic solvents to polymer solutions,” *Ultrason. Sonochem.*, vol. 21, no. 1, pp. 149–153, 2014, doi: 10.1016/j.ultsonch.2013.07.015.

[249] K. Larson-Smith, A. Jackson, and D. C. Pozzo, “SANS and SAXS analysis of charged nanoparticle adsorption at oil-water interfaces,” *Langmuir*, vol. 28, no. 5, pp. 2493–2501, 2012, doi: 10.1021/la204513n.

[250] Y. Zhao, Y. Li, D. E. Demco, X. Zhu, and M. Möller, “Microencapsulation of hydrophobic liquids in closed all-silica colloidosomes,” *Langmuir*, vol. 30, no. 15, pp. 4253–4261, 2014, doi: 10.1021/la500311y.

[251] H. Wang, X. Zhu, L. Tsarkova, A. Pich, and M. Möller, “All-silica colloidosomes with a particle-bilayer shell,” *ACS Nano*, vol. 5, no. 5, pp. 3937–3942, 2011, doi: 10.1021/nn200436s.

[252] H. Jiang, L. Hong, Y. Li, and T. Ngai, “All-Silica Submicrometer Colloidosomes for Cargo Protection and Tunable Release,” *Angew. Chemie - Int. Ed.*, vol. 57, no. 36, pp. 11662–11666, 2018, doi: 10.1002/anie.201805968.

[253] J. D. Berry, M. J. Neeson, R. R. Dagastine, D. Y. C. Chan, and R. F. Tabor, “Measurement of surface and interfacial tension using pendant drop tensiometry,” *J. Colloid Interface Sci.*, vol. 454, pp. 226–237, 2015, doi: 10.1016/j.jcis.2015.05.012.

[254] V. N. Paunov, “Novel method for determining the three-phase contact angle of colloid particles adsorbed at air-water and oil-water interfaces,” *Langmuir*, vol. 19, no. 19, pp. 7970–7976, 2003, doi:

10.1021/la0347509.

[255] L. N. Arnaudov, O. J. Cayre, M. A. Cohen Stuart, S. D. Stoyanov, and V. N. Paunov, “Measuring the three-phase contact angle of nanoparticles at fluid interfaces,” *Phys. Chem. Chem. Phys.*, vol. 12, no. 2, pp. 328–331, 2010, doi: 10.1039/b917353f.

[256] E. L. Sharp, H. Al-Shehri, T. S. Horozov, S. D. Stoyanov, and V. N. Paunov, “Adsorption of shape-anisotropic and porous particles at the air-water and the decane-water interface studied by the gel trapping technique,” *RSC Adv.*, vol. 4, no. 5, pp. 2205–2213, 2014, doi: 10.1039/c3ra44563a.

[257] J. F. Miller, K. Schätzel, and B. Vincent, “The determination of very small electrophoretic mobilities in polar and nonpolar colloidal dispersions using phase analysis light scattering,” *J. Colloid Interface Sci.*, vol. 143, no. 2, pp. 532–554, 1991, doi: 10.1016/0021-9797(91)90286-H.

[258] W. T. Liu and Y. R. Shen, “Surface vibrational modes of α-quartz(0001) probed by sum-frequency spectroscopy,” *Phys. Rev. Lett.*, vol. 101, no. 1, pp. 1–4, 2008, doi: 10.1103/PhysRevLett.101.016101.

[259] I. Umezu, H. Minami, H. Senoo, and A. Sugimura, “Synthesis of photoluminescent colloidal silicon nanoparticles by pulsed laser ablation in liquids,” *J. Phys. Conf. Ser.*, vol. 59, no. 1, pp. 392–395, 2007, doi: 10.1088/1742-6596/59/1/083.

[260] D. Boldridge, “Morphological characterization of fumed silica aggregates,” *Aerosol Sci. Technol.*, vol. 44, no. 3, pp. 182–186, 2010, doi: 10.1080/02786820903499462.

[261] A. Mulderig, G. Beaucage, K. Vogtt, H. Jiang, and V. Kuppa, “Quantification of branching in fumed silica,” *J. Aerosol Sci.*, vol. 109, no. January, pp. 28–37, 2017, doi: 10.1016/j.jaerosci.2017.04.001.

[262] L. Hohl, S. Röhl, D. Stehl, R. von Klitzing, and M. Kraume, “Influence of Nanoparticles and Drop Size Distributions on the Rheology of w/o

Pickering Emulsions," *Chemie-Ingenieur-Technik*, vol. 88, no. 11, pp. 1815–1826, 2016, doi: 10.1002/cite.201600063.

[263] B. P. Binks and R. Murakami, "Phase inversion of particle-stabilized materials from foams to dry water," *Nat. Mater.*, vol. 5, no. 11, pp. 865–869, 2006, doi: 10.1038/nmat1757.

[264] M. Destribats *et al.*, "Pickering emulsions: What are the main parameters determining the emulsion type and interfacial properties?," *Langmuir*, vol. 30, no. 31, pp. 9313–9326, 2014, doi: 10.1021/la501299u.

[265] K. D. Danov, P. A. Kralchevsky, K. P. Ananthapadmanabhan, and A. Lips, "Particle-interface interaction across a nonpolar medium in relation to the production of particle-stabilized emulsions," *Langmuir*, vol. 22, no. 1, pp. 106–115, 2006, doi: 10.1021/la052273j.

[266] H. Wang, V. Singh, and S. H. Behrens, "Image charge effects on the formation of pickering emulsions," *J. Phys. Chem. Lett.*, vol. 3, no. 20, pp. 2986–2990, 2012, doi: 10.1021/jz300909z.

[267] W. Stöber, A. Fink, and E. Bohn, "Controlled growth of monodisperse silica spheres in the micron size range," *J. Colloid Interface Sci.*, vol. 26, no. 1, pp. 62–69, 1968, doi: 10.1016/0021-9797(68)90272-5.

[268] E. J. A. Pope and J. D. Mackenzie, "Sol-gel processing of silica. II. The role of the catalyst," *J. Non. Cryst. Solids*, vol. 87, no. 1–2, pp. 185–198, 1986, doi: 10.1016/S0022-3093(86)80078-3.

[269] C. L. Chang and H. S. Fogler, "Kinetics of Silica Particle Formation in Nonionic w/o Microemulsions from TEOS," *AIChE J.*, vol. 42, no. 11, pp. 3153–3163, 1996, doi: 10.1002/aic.690421115.

[270] P. P. Ghimire and M. Jaroniec, "Renaissance of Stöber method for synthesis of colloidal particles: New developments and opportunities," *J. Colloid Interface Sci.*, vol. 584, pp. 838–865, 2021, doi: 10.1016/j.jcis.2020.10.014.

[271] Y. J. Wong *et al.*, "Revisiting the Stöber method: Inhomogeneity in silica

shells," *J. Am. Chem. Soc.*, vol. 133, no. 30, pp. 11422–11425, 2011, doi: 10.1021/ja203316q.

[272] T. Nemoto, T. Sakai, and T. Okada, "Unimodal sized silica nanocapsules produced through water-in-oil emulsions prepared by sequential irradiation of kilo- And submega-hertz ultrasounds," *RSC Adv.*, vol. 11, no. 37, pp. 22921–22928, 2021, doi: 10.1039/d1ra03384k.

[273] J. L. Heidman, C. Tsonopoulos, C. J. Brady, and G. M. Wilson, "High-Temperature Mutual Solubilities of Hydrocarbons and Water Ii. Ethylbenzene, Ethylcyclohexane, and N-Octane.," *Annu. Meet. - Am. Inst. Chem. Eng.*, vol. 29, no. 6, pp. 990–999, 1983.

[274] R. Danon, M. C. Kroon, and F. Banat, "Mutual Solubilities of Cyclohexane and Water in Aqueous Methyldiethanolamine /Cyclohexane Liquid-Liquid Equilibria," *J. Chem. Eng. Data*, vol. 63, no. 4, pp. 1123–1131, 2018, doi: 10.1021/acs.jced.7b00873.

[275] C. J. Beverung, C. J. Radke, and H. W. Blanch, "Protein adsorption at the oil/water interface: Characterization of adsorption kinetics by dynamic interfacial tension measurements," *Biophys. Chem.*, vol. 81, no. 1, pp. 59–80, 1999, doi: 10.1016/S0301-4622(99)00082-4.

[276] H. Fan and A. Striolo, "Nanoparticle effects on the water-oil interfacial tension," *Phys. Rev. E - Stat. Nonlinear, Soft Matter Phys.*, vol. 86, no. 5, pp. 1–11, 2012, doi: 10.1103/PhysRevE.86.051610.

[277] L. Alison, A. F. Demirörs, E. Tervoort, A. Teleki, J. Vermant, and A. R. Studart, "Emulsions Stabilized by Chitosan-Modified Silica Nanoparticles: PH Control of Structure-Property Relations," *Langmuir*, vol. 34, no. 21, pp. 6147–6160, 2018, doi: 10.1021/acs.langmuir.8b00622.

[278] B. Derjaguin and L. Landau, "Theory of the stability of strongly charged lyophobic sols and of the adhesion of strongly charged particles in solutions of electrolytes," *Prog. Surf. Sci.*, vol. 43, no. 1–4, pp. 30–59, 1993, doi: 10.1016/0079-6816(93)90013-L.

[279] E. J. W. Verwey, “Theory of the stability of lyophobic colloids,” *Journal of Physical and Colloid Chemistry*, vol. 51, no. 3. pp. 631–636, 1947. doi: 10.1021/j150453a001.

[280] J. C. Everts, S. Samin, and R. Van Roij, “Tuning Colloid-Interface Interactions by Salt Partitioning,” *Phys. Rev. Lett.*, vol. 117, no. 9, pp. 1–5, 2016, doi: 10.1103/PhysRevLett.117.098002.

[281] P. Linse, “Image charge effects in spherical symmetry with applications to micellar systems,” *J. Phys. Chem.*, vol. 90, no. 26, pp. 6821–6828, Dec. 1986, doi: 10.1021/j100284a022.

[282] R. Messina, “Image charges in spherical geometry: Application to colloidal systems,” *J. Chem. Phys.*, vol. 117, no. 24, pp. 11062–11074, 2002, doi: 10.1063/1.1521935.

[283] H. C. Hamaker, “The London-van der Waals attraction between spherical particles,” *Physica*, vol. 4, no. 10, pp. 1058–1072, 1937, doi: 10.1016/S0031-8914(37)80203-7.

[284] J. Israelachvili, *Intermolecular and Surface Forces*, Third. Elsevier, 2011. doi: 10.1016/C2009-0-21560-1.

[285] N. F. Owens and P. Richmond, “Hamaker constants and combining rules,” *J. Chem. Soc. Faraday Trans. 2 Mol. Chem. Phys.*, vol. 74, no. 2, pp. 691–695, 1978, doi: 10.1039/F29787400691.

[286] P. Richmond, “The theory and calculation of van der waals forces,” in *Colloid Science*, D. H. Everett, Ed. 1975. doi: 10.1039/9781847555847-00130.

[287] G. Kokot, M. I. Bespalova, and M. Krishnan, “Measured electrical charge of SiO2 in polar and nonpolar media,” *J. Chem. Phys.*, vol. 145, no. 19, 2016, doi: 10.1063/1.4967401.

[288] A. L. Loeb, J. T. G. Overbeek, and P. H. Wiersema, *The Electrical Double Layer Around a Spherical Colloid Particle: Computation of the Potential, Charge Density, and Free Energy of the Electrical Double Layer Around a Spherical Colloid Particle*. 1961.

[289] A. Delgado, F. González-Caballero, and J. M. Bruque, “On the zeta potential and surface charge density of montmorillonite in aqueous electrolyte solutions,” *J. Colloid Interface Sci.*, vol. 113, no. 1, pp. 203–211, 1986, doi: 10.1016/0021-9797(86)90220-1.

[290] C. P. Royall, M. E. Leunissen, A. P. Hynninen, M. Dijkstra, and A. Van Blaaderen, “Re-entrant melting and freezing in a model system of charged colloids,” *J. Chem. Phys.*, vol. 124, no. 24, 2006, doi: 10.1063/1.2189850.

[291] M. N. Van Der Linden *et al.*, “Charging of poly(methyl methacrylate) (PMMA) colloids in cyclohexyl bromide: Locking, size dependence, and particle mixtures,” *Langmuir*, vol. 31, no. 1, pp. 65–75, 2015, doi: 10.1021/la503665e.

[292] I. M. Smallwood, “Handbook of Organic Solvent Properties,” *Handbook of Organic Solvent Properties*. Elsevier, pp. 1–306, 2012. doi: 10.1016/C2009-0-23646-4.

[293] R. M. Fuoss, “Dependence of the Walden Product on Dielectric Constant,” *Proc. Natl. Acad. Sci.*, vol. 45, no. 6, pp. 807–813, 1959, doi: 10.1073/pnas.45.6.807.

[294] R. Hogg, T. W. Healy, and D. W. Fuerstenau, “Mutual coagulation of colloidal dispersions,” *Trans. Faraday Soc.*, vol. 62, no. 615, pp. 1638–1651, 1966, doi: 10.1039/tf9666201638.

[295] J. E. Sader, S. L. Carnie, and D. Y. C. Chan, “Accurate Analytic Formulas for the Double-Layer Interaction between Spheres,” *J. Colloid Interface Sci.*, vol. 171, no. 1, pp. 46–54, Apr. 1995, doi: 10.1006/jcis.1995.1149.

[296] B. Derjaguin, “On the repulsive forces between charged colloid particles and on the theory of slow coagulation and stability of lyophobe sols,” *Trans. Faraday Soc.*, vol. 35, pp. 203–215, 1940, doi: 10.1039/tf9403500203.

[297] G. M. Bell, S. Levine, and L. N. McCartney, “Approximate methods of

determining the double-layer free energy of interaction between two charged colloidal spheres," *J. Colloid Interface Sci.*, vol. 33, no. 3, pp. 335–359, 1970, doi: 10.1016/0021-9797(70)90228-6.

[298] H. Afsaneh and J. A. W. Elliott, "Charge-Dipole Attraction as a Surface Interaction between Water Droplets Immersed in Organic Phases," *Langmuir*, vol. 38, no. 43, pp. 13121–13138, 2022, doi: 10.1021/acs.langmuir.2c01828.

[299] Y. Uematsu and H. Ohshima, "Electrophoretic Mobility of a Water-in-Oil Droplet Separately Affected by the Net Charge and Surface Charge Density," *Langmuir*, vol. 38, no. 14, pp. 4213–4221, 2022, doi: 10.1021/acs.langmuir.1c03145.

[300] Y. Sun, X. Huang, and S. Soh, "Solid-to-Liquid Charge Transfer for Generating Droplets with Tunable Charge," *Angew. Chemie Int. Ed.*, vol. 55, no. 34, pp. 9956–9960, Aug. 2016, doi: 10.1002/anie.201604378.

[301] W. Albers and J. T. G. Overbeek, "Stability of emulsions of water in oil. I. The correlation between electrokinetic potential and stability," *J. Colloid Sci.*, vol. 14, no. 5, pp. 501–509, 1959, doi: 10.1016/0095-8522(59)90015-7.

[302] A. M. Schoeler, D. N. Josephides, S. Sajjadi, C. D. Lorenz, and P. Mesquida, "Charge of water droplets in non-polar oils," *J. Appl. Phys.*, vol. 114, no. 14, pp. 0–9, 2013, doi: 10.1063/1.4824180.

[303] D. Choi *et al.*, "Spontaneous electrical charging of droplets by conventional pipetting," *Sci. Rep.*, vol. 3, pp. 1–7, 2013, doi: 10.1038/srep02037.

[304] H. Böhm and J. Lindorfer, "Techno-economic assessment of seasonal heat storage in district heating with thermochemical materials," *Energy*, vol. 179, pp. 1246–1264, 2019, doi: 10.1016/j.energy.2019.04.177.

[305] T. Yang, W. Liu, G. J. Kramer, and Q. Sun, "Seasonal thermal energy storage: A techno-economic literature review," *Renew. Sustain. Energy*

Rev., vol. 139, no. December 2020, p. 110732, 2021, doi: 10.1016/j.rser.2021.110732.

[306] L. Scapino, C. De Servi, H. A. Zondag, J. Diriken, C. C. M. Rindt, and A. Sciacovelli, “Techno-economic optimization of an energy system with sorption thermal energy storage in different energy markets,” *Appl. Energy*, vol. 258, no. June, p. 114063, 2020, doi: 10.1016/j.apenergy.2019.114063.

[307] W. Li, J. J. Klemeš, Q. Wang, and M. Zeng, “Salt hydrate–based gas-solid thermochemical energy storage: Current progress, challenges, and perspectives,” *Renew. Sustain. Energy Rev.*, vol. 154, no. October 2020, p. 111846, 2022, doi: 10.1016/j.rser.2021.111846.

[308] W. Li, J. J. Klemeš, Q. Wang, and M. Zeng, “Development and characteristics analysis of salt-hydrate based composite sorbent for low-grade thermochemical energy storage,” *Renew. Energy*, vol. 157, pp. 920–940, 2020, doi: 10.1016/j.renene.2020.05.062.

[309] B. Dawoud and Y. Aristov, “Experimental study on the kinetics of water vapor sorption on selective water sorbents, silica gel and alumina under typical operating conditions of sorption heat pumps,” *Int. J. Heat Mass Transf.*, vol. 46, no. 2, pp. 273–281, 2003, doi: 10.1016/S0017-9310(02)00288-0.

[310] A. Terzis, A. Ramachandran, K. Wang, M. Asheghi, K. E. Goodson, and J. G. Santiago, “High-Frequency Water Vapor Sorption Cycling Using Fluidization of Metal-Organic Frameworks,” *Cell Reports Phys. Sci.*, vol. 1, no. 5, p. 100057, 2020, doi: 10.1016/j.xcrp.2020.100057.

[311] S. Bellan, T. Kodama, K. Matsubara, N. Gokon, H. S. Cho, and K. Inoue, “Heat transfer and particulate flow analysis of a 30 kW directly irradiated solar fluidized bed reactor for thermochemical cycling,” *Chem. Eng. Sci.*, vol. 203, pp. 511–525, 2019, doi: 10.1016/j.ces.2018.09.012.

[312] J. A. Almendros-Ibáñez, M. Fernández-Torrijos, M. Díaz-Heras, J. F. Belmonte, and C. Sobrino, “A review of solar thermal energy storage in

beds of particles: Packed and fluidized beds," *Sol. Energy*, vol. 192, no. May 2018, pp. 193–237, 2019, doi: 10.1016/j.solener.2018.05.047.

[313] B. Du *et al.*, "One-pot preparation of hollow silica spheres by using thermosensitive poly(N-isopropylacrylamide) as a reversible template," *Langmuir*, vol. 25, no. 20, pp. 12367–12373, 2009, doi: 10.1021/la902531p.

[314] S. Narayanan, S. Yang, H. Kim, and E. N. Wang, "Optimization of adsorption processes for climate control and thermal energy storage," *Int. J. Heat Mass Transf.*, vol. 77, pp. 288–300, 2014, doi: 10.1016/j.ijheatmasstransfer.2014.05.022.

[315] T. Kano, Y. Aota, and K. Maruoka, "Rate Acceleration of Solid-Liquid Phase-Transfer Catalysis by Rotor-Stator Homogenizer," *Adv. Synth. Catal.*, vol. 358, no. 18, pp. 2996–2999, 2016, doi: 10.1002/adsc.201600425.

[316] Y. Singh *et al.*, "Nanoemulsion: Concepts, development and applications in drug delivery," *J. Control. Release*, vol. 252, pp. 28–49, 2017, doi: 10.1016/j.jconrel.2017.03.008.

[317] A. B. Subramaniam, M. Abkarian, L. Mahadevan, and H. A. Stone, "Colloid science: Non-spherical bubbles," *Nature*, vol. 438, no. 7070, p. 930, 2005, doi: 10.1038/438930a.

[318] J. W. Kim, D. Lee, H. C. Shum, and D. A. Weitz, "Colloid surfactants for emulsion stabilization," *Adv. Mater.*, vol. 20, no. 17, pp. 3239–3243, 2008, doi: 10.1002/adma.200800484.

[319] H. A. Stone, "Dynamics of Drop Deformation and Breakup in Viscous Fluids," *Annu. Rev. Fluid Mech.*, vol. 26, no. 1, pp. 65–102, Jan. 1994, doi: 10.1146/annurev.fl.26.010194.000433.

[320] Y. W. Kruijt-Stegeman, F. N. van de Vosse, and H. E. H. Meijer, "Droplet behavior in the presence of insoluble surfactants," *Phys. Fluids*, vol. 16, no. 8, pp. 2785–2796, 2004, doi: 10.1063/1.1756168.

[321] H. Y. Sohn and C. Moreland, "The effect of particle size distribution on

packing density," *Can. J. Chem. Eng.*, vol. 46, no. 3, pp. 162–167, Jun. 1968, doi: 10.1002/cjce.5450460305.

[322] D. J. French, P. Taylor, J. Fowler, and P. S. Clegg, "Making and breaking bridges in a Pickering emulsion," *J. Colloid Interface Sci.*, vol. 441, pp. 30–38, 2015, doi: 10.1016/j.jcis.2014.11.032.

[323] M. N. Lee, H. K. Chan, and A. Mohraz, "Characteristics of pickering emulsion gels formed by droplet bridging," *Langmuir*, vol. 28, no. 6, pp. 3085–3091, 2012, doi: 10.1021/la203384f.

[324] M. Kaganyuk and A. Mohraz, "Non-monotonic dependence of Pickering emulsion gel rheology on particle volume fraction," *Soft Matter*, vol. 13, no. 13, pp. 2513–2522, 2017, doi: 10.1039/c6sm02858f.

[325] F. Vult Von Steyern, J. O. Josefsson, and S. Tågerud, "Rhodamine B, a fluorescent probe for acidic organelles in denervated skeletal muscle," *J. Histochem. Cytochem.*, vol. 44, no. 3, pp. 267–274, 1996, doi: 10.1177/44.3.8648087.

[326] J. H. J. Thijssen, A. B. Schofield, and P. S. Clegg, "How do (fluorescent) surfactants affect particle-stabilized emulsions?," *Soft Matter*, vol. 7, no. 18, pp. 7965–7968, 2011, doi: 10.1039/c1sm05968h.

[327] M. E. Leunissen, J. Zwanikken, R. van Roij, P. M. Chaikin, and A. van Blaaderen, "Ion partitioning at the oil–water interface as a source of tunable electrostatic effects in emulsions with colloids," *Phys. Chem. Chem. Phys.*, vol. 9, no. 48, p. 6405, 2007, doi: 10.1039/b711300e.

[328] K. G. Marinova *et al.*, "Charging of oil-water interfaces due to spontaneous adsorption of hydroxyl ions," *Langmuir*, vol. 12, no. 8, pp. 2045–2051, 1996, doi: 10.1021/la950928i.

[329] L. Alison *et al.*, "Pickering and Network Stabilization of Biocompatible Emulsions Using Chitosan-Modified Silica Nanoparticles," *Langmuir*, vol. 32, no. 50, pp. 13446–13457, 2016, doi: 10.1021/acs.langmuir.6b03439.

[330] S. Ghosh, T. Tran, and D. Rousseau, "Comparison of pickering and

network stabilization in water-in-oil emulsions," *Langmuir*, vol. 27, no. 11, pp. 6589–6597, 2011, doi: 10.1021/la200065y.

[331] J. Heintzenberg, "Properties of the log-normal particle size distribution," *Aerosol Sci. Technol.*, vol. 21, no. 1, pp. 46–48, 1994, doi: 10.1080/02786829408959695.

[332] S. Sihler, A. Schrade, Z. Cao, and U. Ziener, "Inverse Pickering Emulsions with Droplet Sizes below 500 nm," *Langmuir*, vol. 31, no. 38, pp. 10392–10401, 2015, doi: 10.1021/acs.langmuir.5b02735.

[333] M. Graham and D. Shchukin, "Formation Mechanism of Multipurpose Silica Nanocapsules," *Langmuir*, vol. 37, no. 2, pp. 918–927, 2021, doi: 10.1021/acs.langmuir.0c03286.

[334] R. Aveyard, "Can Janus particles give thermodynamically stable Pickering emulsions?," *Soft Matter*, vol. 8, no. 19, pp. 5233–5240, 2012, doi: 10.1039/c2sm07230k.

[335] E. R. A. Lima, B. M. De Melo, L. T. Baptista, and M. L. L. Paredes, "Specific ion effects on the interfacial tension of water/hydrocarbon systems," *Brazilian J. Chem. Eng.*, vol. 30, no. 1, pp. 55–62, 2013, doi: 10.1590/S0104-66322013000100007.

[336] A. D. Pathak, S. Nedea, H. Zondag, C. Rindt, and D. Smeulders, "A DFT-based comparative equilibrium study of thermal dehydration and hydrolysis of CaCl2 hydrates and MgCl2 hydrates for seasonal heat storage," *Phys. Chem. Chem. Phys.*, vol. 18, no. 15, pp. 10059–10069, 2016, doi: 10.1039/c6cp00926c.

[337] A. Mehari, Z. Y. Xu, and R. Z. Wang, "Thermal energy storage using absorption cycle and system: A comprehensive review," *Energy Convers. Manag.*, vol. 206, no. December 2019, 2020, doi: 10.1016/j.enconman.2020.112482.

[338] S. Lan, M. Gaeini, H. Zondag, A. van Steenhoven, and C. Rindt, "Direct numerical simulation of the thermal dehydration reaction in a TGA experiment," *Appl. Therm. Eng.*, vol. 128, pp. 1175–1185, 2018, doi:

10.1016/j.applthermaleng.2017.08.073.

[339] F. Trausel, A. J. De Jong, and R. Cuypers, “A review on the properties of salt hydrates for thermochemical storage,” *Energy Procedia*, vol. 48, pp. 447–452, 2014, doi: 10.1016/j.egypro.2014.02.053.

[340] A. Khawam and D. R. Flanagan, “Solid-state kinetic models: Basics and mathematical fundamentals,” *J. Phys. Chem. B*, vol. 110, no. 35, pp. 17315–17328, 2006, doi: 10.1021/jp062746a.

[341] K. L. Mampel, “Zeitumsatzformeln für heterogene Reaktionen an Phasengrenzen fester Körper,” *Zeitschrift für Phys. Chemie*, vol. 187A, no. 1, pp. 43–57, 1940, doi: 10.1515/zpch-1940-18705.

[342] E. Alpay and D. M. Scott, “The linear driving force model for fast-cycle adsorption and desorption in a spherical particle,” *Chem. Eng. Sci.*, vol. 47, no. 2, pp. 499–502, 1992, doi: 10.1016/0009-2509(92)80041-A.

[343] S. I. Nakao and M. Suzuki, “Mass transfer coefficient in cyclic adsorption and desorption,” *J. Chem. Eng. Japan*, vol. 16, no. 2, pp. 114–119, 1983, doi: 10.1252/jcej.16.114.

[344] Y. Ding and E. Alpay, “Equilibria and kinetics of CO2 adsorption on hydrotalcite adsorbent,” *Chem. Eng. Sci.*, vol. 55, no. 17, pp. 3461–3474, 2000, doi: 10.1016/S0009-2509(99)00596-5.

[345] P. A. J. Donkers, L. Pel, and O. C. G. Adan, “Experimental studies for the cyclability of salt hydrates for thermochemical heat storage,” *J. Energy Storage*, vol. 5, pp. 25–32, 2016, doi: 10.1016/j.est.2015.11.005.

[346] M. Schmidt and M. Linder, “A Novel Thermochemical Long Term Storage Concept: Balance of Renewable Electricity and Heat Demand in Buildings,” *Front. Energy Res.*, vol. 8, no. July, pp. 1–12, 2020, doi: 10.3389/fenrg.2020.00137.

[347] M. Chen *et al.*, “Caking of crystals: Characterization, mechanisms and prevention,” *Powder Technol.*, vol. 337, pp. 51–67, 2018, doi: 10.1016/j.powtec.2017.04.052.

[348] K. Kuwata *et al.*, “Durability of thermochemical heat storage demonstrated through long-term repetitive CaCl2/H2O reversible reactions,” *J. Renew. Sustain. Energy*, vol. 9, no. 2, 2017, doi: 10.1063/1.4978351.

[349] Y. I. Aristov, M. M. Tokarev, G. Restuccia, and G. Cacciola, “Selective water sorbents for multiple applications, 2. CaCl2 confined in micropores of silica gel: Sorption properties,” *React. Kinet. Catal. Lett.*, vol. 59, no. 2, pp. 335–342, 1996, doi: 10.1007/BF02068131.

[350] Y. I. Aristov, G. Restuccia, G. Cacciola, and V. N. Parmon, “A family of new working materials for solid sorption air conditioning systems,” *Appl. Therm. Eng.*, vol. 22, no. 2, pp. 191–204, 2002, doi: 10.1016/S1359-4311(01)00072-2.

[351] J. Xu *et al.*, “Ultrahigh solar-driven atmospheric water production enabled by scalable rapid-cycling water harvester with vertically aligned nanocomposite sorbent,” *Energy Environ. Sci.*, vol. 14, no. 11, pp. 5979–5994, 2021, doi: 10.1039/d1ee01723c.

[352] T. S. Yan, T. X. Li, J. X. Xu, and R. Z. Wang, “Water sorption properties, diffusion and kinetics of zeolite NaX modified by ion-exchange and salt impregnation,” *Int. J. Heat Mass Transf.*, vol. 139, pp. 990–999, 2019, doi: 10.1016/j.ijheatmasstransfer.2019.05.080.

[353] M. Fasano *et al.*, “Interplay between hydrophilicity and surface barriers on water transport in zeolite membranes,” *Nat. Commun.*, vol. 7, pp. 1–8, 2016, doi: 10.1038/ncomms12762.

[354] H. Shan *et al.*, “High-yield solar-driven atmospheric water harvesting with ultra-high salt content composites encapsulated in porous membrane,” *Cell Reports Phys. Sci.*, vol. 2, no. 12, 2021, doi: 10.1016/j.xcrp.2021.100664.

[355] Y. Wang *et al.*, “Heterogeneous wettability and radiative cooling for efficient deliquescent sorbents-based atmospheric water harvesting,” *Cell Reports Phys. Sci.*, vol. 3, no. 5, p. 100879, 2022, doi:

10.1016/j.xcrp.2022.100879.

[356] S. Vyazovkin, A. K. Burnham, J. M. Criado, L. A. Pérez-Maqueda, C. Popescu, and N. Sbirrazzuoli, “ICTAC Kinetics Committee recommendations for performing kinetic computations on thermal analysis data,” *Thermochim. Acta*, vol. 520, no. 1–2, pp. 1–19, 2011, doi: 10.1016/j.tca.2011.03.034.

[357] S. Arditty, C. P. Whitby, B. P. Binks, V. Schmitt, and F. Leal-Calderon, “Some general features of limited coalescence in solid-stabilized emulsions,” *Eur. Phys. J. E*, vol. 11, no. 3, pp. 273–281, 2003, doi: 10.1140/epje/i2003-10018-6.

[358] B. P. Binks, P. D. I. Fletcher, B. L. Holt, J. Parker, P. Beaussoubre, and K. Wong, “Drop sizes and particle coverage in emulsions stabilised solely by silica nanoparticles of irregular shape,” *Phys. Chem. Chem. Phys.*, vol. 12, no. 38, pp. 11967–11974, 2010, doi: 10.1039/c0cp00581a.

[359] J. Van Wijk, J. W. O. Salari, J. Meuldijk, and B. Klumperman, “Determination of the shell growth direction during the formation of silica microcapsules by confocal fluorescence microscopy,” *J. Mater. Chem. B*, vol. 3, no. 39, pp. 7745–7751, 2015, doi: 10.1039/c5tb01232e.

[360] Dow Chemical Company, “CALCIUM CHLORIDE HANDBOOK A Guide to Properties, Forms, Storage and Handling,” 2003.

[361] Y. Zhang and R. Wang, “Sorption thermal energy storage: Concept, process, applications and perspectives,” *Energy Storage Mater.*, vol. 27, no. February, pp. 352–369, 2020, doi: 10.1016/j.ensm.2020.02.024.

[362] R. Alfonsetti, L. Lozzi, M. Passacantando, P. Picozzi, and S. Santucci, “XPS studies on SiOx thin films,” *Appl. Surf. Sci.*, vol. 70/71, pp. 222–225, 1993, [Online]. Available: https://orproxy.lib.utk.edu:2135/016943329390431A/1-s2.0-016943329390431A-main.pdf?_tid=18913ea3-ef73-4c0d-af2a-1533f4d96e85&acdnat=1535635022_92ed4629200cce9cad86d995da3f

57f1

[363] L. A. O'Hare, B. Parbhoo, and S. R. Leadley, "Development of a methodology for XPS curve-fitting of the Si 2p core level of siloxane materials," *Surf. Interface Anal.*, vol. 36, no. 10, pp. 1427–1434, 2004, doi: 10.1002/sia.1917.

[364] C. J. Howard, B. J. Kennedy, and C. Curfs, "Temperature-induced structural changes in CaCl2, CaBr2, and CrCl2: A synchrotron x-ray powder diffraction study," *Phys. Rev. B*, vol. 72, no. 21, p. 214114, 2005, doi: 10.1103/PhysRevB.72.214114.

[365] L. M. Uriarte, J. Dubessy, P. Boulet, V. G. Baonza, I. Bihannic, and P. Robert, "Reference Raman spectra of synthesized CaCl2·nH2O solids (n=0, 2, 4, 6)," *J. Raman Spectrosc.*, vol. 46, no. 10, pp. 822–828, 2015, doi: 10.1002/jrs.4730.

[366] L. Garzón-Tovar, J. Pérez-Carvajal, I. Imaz, and D. Maspoch, "Composite Salt in Porous Metal-Organic Frameworks for Adsorption Heat Transformation," *Adv. Funct. Mater.*, vol. 27, no. 21, pp. 1–10, 2017, doi: 10.1002/adfm.201606424.

[367] S. Wang *et al.*, "A robust large-pore zirconium carboxylate metal-organic framework for energy-efficient water-sorption-driven refrigeration," *Nat. Energy*, pp. 1–10, 2018, doi: 10.1038/s41560-018-0261-6.

[368] T. X. Li, R. Z. Wang, and H. Li, "Progress in the development of solid-gas sorption refrigeration thermodynamic cycle driven by low-grade thermal energy," *Prog. Energy Combust. Sci.*, vol. 40, no. 1, pp. 1–58, 2014, doi: 10.1016/j.pecs.2013.09.002.

[369] P. A. Kallenberger and M. Fröba, "Water harvesting from air with a hygroscopic salt in a hydrogel–derived matrix," *Commun. Chem.*, vol. 1, no. 1, pp. 6–11, 2018, doi: 10.1038/s42004-018-0028-9.

[370] S. Vyazovkin *et al.*, "ICTAC Kinetics Committee recommendations for analysis of multi-step kinetics," *Thermochim. Acta*, vol. 689, no. March,

p. 178597, 2020, doi: 10.1016/j.tca.2020.178597.

[371] S. Y. Misyura, “The crystallization behavior of the aqueous solution of CaCl2 salt in a drop and a layer,” *Sci. Rep.*, vol. 10, no. 1, pp. 1–10, 2020, doi: 10.1038/s41598-019-57169-1.

[372] J. Aarts *et al.*, “Diffusion limited hydration kinetics of millimeter sized salt hydrate particles for thermochemical heat storage,” *J. Energy Storage*, no. September, p. 103554, 2021, doi: 10.1016/j.est.2021.103554.

[373] C. Zhu, Q. Yu, R. N. Dave, and R. Pfeffer, “Gas fluidization characteristics of nanoparticle agglomerates,” *AIChE J.*, vol. 51, no. 2, pp. 426–439, 2005, doi: 10.1002/aic.10319.

[374] A. Anantharaman, R. A. Cocco, and J. W. Chew, “Evaluation of correlations for minimum fluidization velocity (Umf) in gas-solid fluidization,” *Powder Technol.*, vol. 323, pp. 454–485, 2018, doi: 10.1016/j.powtec.2017.10.016.

[375] L. De Martín, W. G. Bouwman, and J. R. Van Ommen, “Multidimensional nature of fluidized nanoparticle agglomerates,” *Langmuir*, vol. 30, no. 42, pp. 12696–12702, 2014, doi: 10.1021/la502987e.

[376] X. Zhu, Q. Zhang, Y. Wang, and F. Wei, “Review on the nanoparticle fluidization science and technology,” *Chinese J. Chem. Eng.*, vol. 24, no. 1, pp. 9–22, 2016, doi: 10.1016/j.cjche.2015.06.005.

[377] D. Geldart, “Types of Gas FLuidization,” *Powder Technol.*, vol. 7, pp. 285–292, 1973.

[378] J. R. Hirschey, N. Kumar, T. Turnaoglu, K. R. Gluesenkamp, and S. Graham, “Review of Low-Cost Organic and Inorganic Phase Change Materials with Phase Change Temperature between 0°C and 65°C,” in *International High Performance Buildings Conference*, 2021, p. 389.

[379] A. Odukomaiya *et al.*, “Addressing energy storage needs at lower cost via on-site thermal energy storage in buildings,” *Energy Environ. Sci.*, vol. 14, no. 10, pp. 5315–5329, 2021, doi: 10.1039/D1EE01992A.

[380] Y. Wu, X. Huang, L. Huang, and J. Chen, “Strategies for Rational Design of High-Power Lithium-ion Batteries,” *Energy Environ. Mater.*, vol. 4, no. 1, pp. 19–45, 2021, doi: 10.1002/eem2.12088.

[381] M. S. Ziegler and J. E. Trancik, “Re-examining rates of lithium-ion battery technology improvement and cost decline,” *Energy Environ. Sci.*, vol. 14, no. 4, pp. 1635–1651, 2021, doi: 10.1039/d0ee02681f.

[382] Z. Zhang, J. Wang, X. Feng, L. Chang, Y. Chen, and X. Wang, “The solutions to electric vehicle air conditioning systems: A review,” *Renew. Sustain. Energy Rev.*, vol. 91, no. February, pp. 443–463, 2018, doi: 10.1016/j.rser.2018.04.005.

[383] M. Gaeini, R. van Alebeek, L. Scapino, H. A. Zondag, and C. C. M. Rindt, “Hot tap water production by a 4 kW sorption segmented reactor in household scale for seasonal heat storage,” *J. Energy Storage*, vol. 17, pp. 118–128, 2018, doi: 10.1016/j.est.2018.02.014.

[384] S. Bellan, T. Kodama, K. Matsubara, N. Gokon, H. S. Cho, and K. Inoue, “Thermal performance of a 30 kW fluidized bed reactor for solar gasification: A CFD-DEM study,” *Chem. Eng. J.*, vol. 360, no. April 2018, pp. 1287–1300, 2019, doi: 10.1016/j.cej.2018.10.111.

[385] M. Abdelrahman, P. Fumeaux, and P. Suter, “Study of solid-gas-suspensions used for direct absorption of concentrated solar radiation,” *Sol. Energy*, vol. 22, no. 1, pp. 45–48, 1979, doi: 10.1016/0038-092X(79)90058-6.

[386] Y. Li *et al.*, “Solution-Processed All-Ceramic Plasmonic Metamaterials for Efficient Solar–Thermal Conversion over 100–727 °C,” *Adv. Mater.*, vol. 2005074, pp. 14–17, 2020, doi: 10.1002/adma.202005074.

[387] Timothy J. Johnson, Tanya L. Myers, Yin-Fong Su, Russell G. Tonkyn, Molly Rose K. Kelly-Gorham, and Tyler O. Danby, *IARPA / PNNL Solid Phase IR Spectra*, vol. 69. Gaithersburg MD, 20899: National Institute of Standards and Technology, 2022. doi: /10.18434/T4D303.